A Multimodal Imaging Platform to enable Hyperspectral Coherent Raman Spectroscopy

Dissertation

by

Henning Maximilian Hachmeister

Research group Biomolecular Photonics
Faculty of Physics
University of Bielefeld

supervised by

Prof. Dr. Thomas Huser

and

Prof. Dr. Dario Anselmetti

March 30, 2021

Printed on non-aging paper DIN ISO 9706

Contents

List of Figures

1 Introduction

One of the most basic principles in natural sciences is the observation of a closed system and describing it in its simplest way. Therefore, there is a need to develop tools that are able to take a snapshot of a process in order to analyze and study that particular phenomenon. Imaging techniques have evolved throughout the last half millennium starting from simple light microscopy and photography to sophisticated techniques such as fluorescence imaging, electron microscopy [1][2][3], or radiography [4][5] to name a few. Simultaneously, the field of biomedical research emerged and evolved by studying genetic modifications of cells [6], cell-to-cell interactions [7][8] as well as biopsy tissue analysis [9], among other things. Especially, for live-cell imaging on the sub-cellular level, confocal laser scanning microscopy [10][11] and super-resolution imaging techniques [12][13][14][15][16][17] have proven themselves to be powerful tools.
However, when utilizing fluorescence imaging techniques, it is necessary to label the molecules of interest with exogenous labels which could lead to unintended interference with the cell's response [18]. This means the labeling method itself has to be verified in advance before the study can be conducted. This verification process very often involves the use of another imaging technique that will provide complementary results [19]. In addition, fluorophores can only produce a certain number of photons until they photobleach. Thus the balance between the acquisition speed, observation time and spatial accuracy has to be optimized [20]. In order to study a system as an independent observer, there is a need for imaging techniques that involve less labor-intensive sample preparation and at the same time are label-free.
Raman scattering spectroscopy is a promising candidate that meets these requirements. It is a label-free, nondestructive and noninvasive method that comes naturally with the provision of information about the chemical composition and

structure of the sample in question. Since Raman scattering based techniques exploit the sample's chemical bonds for information generation, the observation time is not limited by bleaching effects. Theoretically the acquisition time is independent of the imaging method. Spontaneous Raman spectroscopy is a widely used technique that has already been used in studies involving cells [21][22][23] and tissue [24][25]. However, spontaneous Raman scattering suffers from a low scattering cross section resulting in slow spectral acquisition speed and long signal integration time. Therefore, when utilized as an imaging technique, it is unable to acquire highly dynamic sample movements [26]. Coherent Raman imaging such as coherent anti-Stokes Raman scattering (CARS) [27][28] and stimulated Raman scattering (SRS) [29][30][31] are offering improved signal intensities allowing fast image acquisition speeds [32]. These techniques are based on the coherent interaction of two laser beams, the pump laser and the Stokes laser, with a sample e.g. a molecule. When the energy difference between the pump and Stokes beam is tuned in such a way that it efficiently drives a vibrational resonance, the cross section is enhanced. This interaction alters the refractive index of the sample that can be probed by another laser beam e.g. the pump beam generating the anti-Stokes signal. Since all molecules inside the sample are coherently driven, the signal interferes constructively at the detector. Within the last decade, these techniques have been developed further and improved in various aspects [33][34][35]. However, narrowband laser systems utilizing picosecond pulses are offering high imaging-speed capabilities at the cost of low chemical information content [36]. In order to recover the amount of chemical information, the probe resonance is shifted by altering the exciting wavelengths and thereby generating a hyperspectral data set. Alternatively, broadband laser systems utilizing femtosecond pulses can be employed for generating hyperspectral data sets [37][38][39][40][41]. Here, the two broadband pulses are chirped and overlapped in time [41]. By varying the temporal overlap between the two pulses, the hyperspectral data can be acquired. However, because these imaging systems are bulky and expensive, they are limited to only a small number of research institutes. To overcome these limitations and making them accessible for medical purposes, fiber laser technology has been utilized in recent years in order to generate compact and versatile optical systems for clinical applications [42][43][44].

In this thesis I will present a custom-built coherent Raman microscope that is capable of imaging CARS and SRS simultaneously. Furthermore, the system is extended with custom-written software that allows stable and reproducible acquisition of hyperspectral data sets. At the beginning of the thesis, I will briefly highlight the theoretical background. Starting in chapter 2 with the interaction of a photon with matter, the remaining parts are illustrating the foundation of Raman scattering, occurring scattering effects present in coherent Raman imaging and finally the basic principles of optical fiber technology. In the subsequent chapter 3, I will describe the optical laser system suitable for coherent Raman imaging as well as the spontaneous Raman systems that have been utilized throughout the studies for sample characterization and analyses. Chapter 4 will summarize the experimental results of this thesis. After a short introduction to capturing high-resolution Raman spectra (subsection 4.1), the multimodal imaging capabilities and the system's versatility will be showcased in a variety of biomedical problems such as the effect of nitrogen starvation on algae (subsection 4.2) and the analysis of differentiating stem cells (subsection 4.3). In the subsequent chapter I will focus on the generation and evaluation of hyperspectral CARS data sets. First, I will describe the method that will be used to tune two narrowband lasers in order to acquire a hyperspectral data set, focusing on the reproducible and stable acquisition of the data (subsection 4.4.2). Next, I will introduce two unsupervised algorithms that will be utilized for the analysis of the data sets (subsection 4.4.3). Finally, these approaches are showcased when the similarities between stem cells lines (subsection 4.4.4), effects of pollutants on the metabolism of nematodes (subsection 4.4.5) and the evolution of alveolar epithelial cells (subsection 4.4.6) are investigated. In the last subsection (4.5), I will present a newly designed all-fiber laser system as a source for coherent Raman spectroscopy and multimodal imaging. This system will be a preliminary stage for a cost-efficient and compact fiber laser system suitable for the application in a clinical environment. The development of such a system has been the collaborative effort with the research group of Prof. K.K.Y. Wong of Hong Kong University. Finally, I will summarize the main results of the thesis and give an outlook on future efforts that will push the boundaries of coherent Raman spectroscopy even further.

2 Theory

In this chapter I will provide a short overview about the fundamentals of the Raman process as well as a brief description of fiber laser technology. Starting with a short introduction to light-matter interactions and highlighting the role of the dipole moment of the molecule in Raman scattering, I will provide the classical mathematical foundation of this process and show how the Raman scattering process evolves [45].

2.1 Light-matter interactions

In order to describe the interaction of light with matter, the fundamental question of what light actually is needs to be answered. This question is not easy to answer since light can be described as a quasi-particle e.g. photon or as a wave. In the following light will be described as a wave. This wave is of electro-magnetic nature which means that it interacts with charged particles - positive and negative. Matter consists of atoms, in the simplest case of a proton and an electron. When a light wave interacts with this atom, both charges experience a force and are getting displaced from their equilibrium position. However, when considering light in the visible range, only the electron is light enough to follow this force. Thus the interaction induces a dipole moment, that depends on the electron's displacement. Considering an atom with multiple electrons, the summation of all dipole moments yields the macroscopic polarization. In the case of weak light waves that only slightly alters the equilibrium state of the molecule, the binding potential between electron and nucleus can be approximated as an harmonic potential resulting in a proportional relation between the electric field $E(t)$ and electron displacement.

$$P(t) = \epsilon_0 X E(t) \tag{2.1}$$

The ϵ_0 resembles the electric permittivity in vacuum and X stands for the susceptibility of the material. If the influence of a short light pulse on an atom is considered, the equation 2.1 has to be expanded into a power series that leads to

$$\begin{aligned} P(t) &= \epsilon_0[X^{(1)}E(t) + X^{(2)}E(t)E(t) + X^{(3)}E(t)E(t)E(t) + ...] \\ &= P^{(1)}(t) + P^{(2)}(t) + P^{(3)}(t) \end{aligned} \tag{2.2}$$

In equation 2.2, $X^{(n)}$ describes the nth order of susceptibility and $P^{(n)}$ the contribution of the nth order to the polarization. Linear light-matter interactions such as Rayleigh scattering or refraction can be described by the first order $P^{(1)}$. The higher order terms are describing effects of nonlinear optics. Note that equation 2.2 may also describe the interaction between multiple electric fields. For example, such an interaction can occur in a parametric medium such as a β-barium borate (BBO) crystal into which two laser beams with frequencies ω_1 and ω_2 are focused in. The material is parametric so that any energy transfer from the electric field to the material can be neglected. The interaction of the two light waves can be described by the second order polarization $P^{(2)}$ of equation 2.2. Application of the energy conservation yields

$$\omega_1 + \omega_2 = \omega_3 \tag{2.3}$$

This effect is called sum frequency generation (SFG) since the frequencies of both incoming lasers are added up resulting in a higher frequency component ω_3. In the degenerated case when $\omega_1 = \omega_2$, the newly generated frequency is exactly twice the original frequency ($\omega_3 = 2 \cdot \omega_2$), which is known as second harmonic generation (SHG). Next to the energy conservation, the momentum conservation has also to be satisfied ($k_3 = k_1 + k_2$), which can be accomplished by using birefringent materials.

Aside from the participating electric fields from the laser pulses, a polarization does depend on the (non)linear susceptibility. The susceptibility is directly related to the electron displacement. Whenever the electron displacement is enhanced e.g. when the electron experiences a resonance, the susceptibility is increased. This effect is particularly exploited in coherent Raman scattering, a $X^{(3)}$ process. Here, the presence of nuclear modes enhances the electron's displacement and

thereby leads to an increase in susceptibility. By carefully tuning the frequency of two incident laser pulses, the resulting difference frequency drives a specific nuclear mode. Since each nuclear mode is unique to a molecular bond, coherent Raman scattering can be efficiently applied in investigating chemical composition of molecules.

2.2 Spontaneous Raman scattering

In the last section it was stated, that only the electrons are 'light' enough to follow an applied electric field. However, the motion of the electron and the nucleus are coupled to each other so that the motion of the nucleus affects the electron and vice versa. Considering an incoming electric field $E(t)$ with a frequency far away from any electronic resonance, the dipole moment can be written as

$$\mu(t) = \alpha(t)E(t), \tag{2.4}$$

with $\alpha(t)$ the time dependent polarizability. In order to describe the influence of nuclear modes on the polarizability, equation 2.4 has to be expanded in a Taylor series in terms of the nuclear coordinate $Q(t)$. Thus, the dipole moment can be found as

$$\mu(t) = \alpha_0 A e^{-i\omega_1 t} + A\left(\frac{\partial\alpha}{\partial Q}\right)_0 Q_0(e^{-i(\omega_1-\omega_v)t+i\phi} + e^{-i(\omega_1+\omega_v)t-i\phi}) + c.c \tag{2.5}$$

Here, the nuclear modes are assumed to act as harmonic oscillators and the incoming electric field is approximated as $E(t) = Ae^{-i\omega_1 t} + c.c.$. The first term of this equation is unaltered in its frequency and thus describes Rayleigh scattering. The second and the third term are showing a frequency shift. The interaction between electron motion and the nuclear modes forces a frequency shift on the incident field. The second term of equation 2.5 describing a red-shift of $-\omega_v$ is called the Stokes shift ($\omega_s = \omega_1 - \omega_v$) (see figure 2.1). The third term experiences a blue-shift $+\omega_v$ and represents the anti-Stokes contribution ($\omega_{as} = \omega_1 + \omega_v$). If the polarizability is unaltered by the nuclear coordinate ($\left(\frac{\delta\alpha}{\delta Q}\right)_0 = 0$), Raman scattering does not take place. This expression is called the selection rule in Raman spectroscopy.

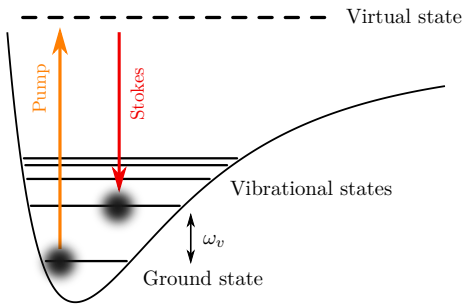

Figure 2.1: **Jablonski diagram of spontaneous Raman scattering**
The spontaneous Raman scattering process is shown in the Jablonski diagram. Excited by a photon, an electron is lifted from the ground state to a virtual state of the molecule. Here, it remains for a couple of fs before relaxing into a vibrational state. While this process takes place, a photon containing the energy difference between those two states is emitted. Analyzing the energy of this photon with a spectrometer results in the information about the molecular bond structure.

In order to analyze the spatial distribution of the spontaneous Raman signal, a single oscillating dipole is considered. The Raman signal is emitted parallel to the dipole axis. Integrating the signal flux over a unit sphere results in

$$I(\omega_s) = \frac{\omega_s^4}{12\pi\epsilon_0 c^3} Q_0^2 |A|^2 \left| \frac{\partial \alpha}{\partial Q} \right|^2 \tag{2.6}$$

with $I(\omega_s)$ the total radiated energy. The ω_s^4 dependency indicates that the Raman signal is stronger when using a blue laser than a red laser as the pump beam. However, sample damage and the creation of spurious background signals such as auto-fluorescence is very likely when utilizing a blue laser, especially in the case of biological samples.

Considering a bulk material, it can be assumed that each molecule can be seen as an individual Raman emitter. Even though all molecules emit a signal with the same frequency, no interference can be observed at the detector due to the incoherent nature of the signal. Revisiting equation 2.5 reveals that each molecule has its own phase $e^{i\phi}$ that is unaffected by other molecules. Thus, two Raman emitters in the material have no phase relation to each other. The overall generated intensity is then calculated by summing up all Raman emitters and multiplying the number with equation 2.6.

2.3 Coherent Raman scattering

Coherent Raman scattering belongs to the field of four-wave mixing processes in nonlinear optics. It occurs whenever three electric fields interact with a molecule and produce a fourth signal. For example in the case of CARS, the newly generated signal would be blue-shifted compared to the three fundamental beams. In the following section, I will introduce the mathematical description for coherent Raman scattering.

To simplify things, the three fundamental laser pulses interact with a molecule that exhibits only one nuclear mode. Since three electric fields are participating in this interaction, it depends on the third order polarization $P^{(3)}$ and can be divided into a two-step process. In the first step, two of the three laser pulses are interacting with the molecular bond (figure 2.2). Here, the laser pulse with the higher frequency ω_1 is called pump pulse while the other pulse ω_2 is referred to as Stokes pulse. If the difference frequency $\Omega_{12} = \omega_1 - \omega_2$ approaches the resonance frequency of the nuclear mode ω_v, the mode is actively driven. This interaction can be described with the model of a driven harmonic oscillator so that the nuclear displacement can be derived as

$$Q(\Omega_{12}) = \frac{1}{m}\left(\frac{\partial\alpha}{\partial Q}\right)_0 \frac{A_1 A_2^*}{\omega_v^2 - \Omega_{12}^2 - 2i\Omega_{12}\gamma} \tag{2.7}$$

m stands for the reduced mass of the oscillator, γ for the damping parameter, Q the nuclear displacement, A_i for the amplitude of the incident fields. As it can be seen, the nuclear displacement depends on the driving force e.g. the field amplitudes of the laser pulses as well as the difference between the driving frequency Ω_{12} and the resonance frequency ω_v.

In the second step, the interaction between the third laser pulse with frequency ω_3 and the molecule is considered. Since the molecule has been excited in the first step, it can be described as an oscillating dipole. Due to the induced oscillations, the optical properties of the molecule change. The resulting macroscopic polarization is the sum of all participating dipoles. This modified polarization affects the third laser pulse as well as the the other two laser pulses that initially drive the nuclear mode. If the frequency of the third laser pulse is equal to the

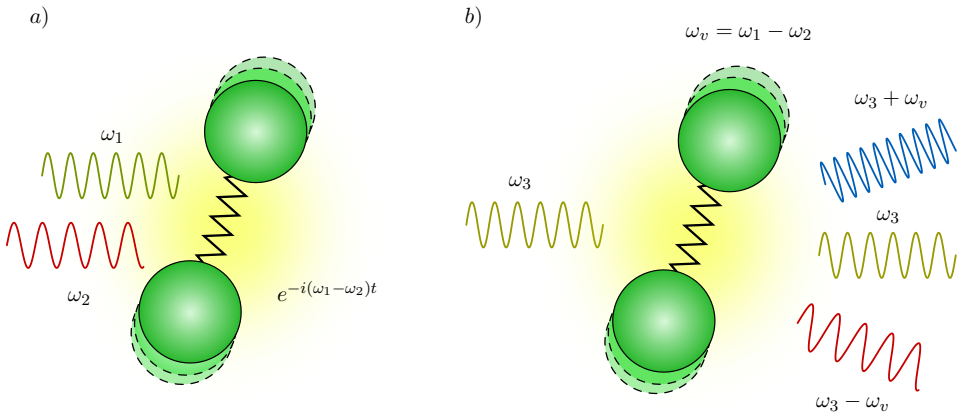

Figure 2.2: **Coherent Raman scattering of a molecule**
The two-step process of coherent Raman scattering begins with a molecule whose electrons are excited to a specific molecular bond (a). Unlike spontaneous Raman scattering, there are now two waves (pump (ω_1) and Stokes (ω_2) wave) that interact with the molecule. The frequency difference $\Omega = \omega_1 - \omega_2$ with $\omega_1 > \omega_2$ is tuned in such a way that it matches the energy difference between the ground state and an excited vibrational state. Thus, the pump photon is absorbed by the molecule and a Stokes photon is emitted through stimulated emission. In the second step (b) a third wave interacts with the previously excited molecule and lifts the electron from a vibrational state into a virtual state. In this case, the emitted photon provides a higher energy than the latter resulting in a blue-shift. If $\omega_1 = \omega_3$, the emitted photon is called the anti-Stokes photon. However, instead of coherent Raman scattering, Rayleigh and spontaneous Raman scattering can also occur.

first e.g. $\omega_3 = \omega_1$, the resulting nonlinear polarization can be found as

$$\begin{aligned} P_{NL}^{(3)}(t) = P^{(3)}(\omega_{cs})e^{-i\omega_{cs}t} + P^{(3)}(\omega_2)e^{-i\omega_2 t} + P^{(3)}(\omega_1)e^{-i\omega_1 t} \\ + P^{(3)}(\omega_{as})e^{-i\omega_{as}t} + c.c \end{aligned} \tag{2.8}$$

with $\omega_{cs} = 2\omega_2 - \omega_1$ as the coherent Stokes frequency and $\omega_{as} = 2\omega_1 - \omega_2$ as the coherent anti-Stokes frequency. Theses two components describe the newly generated frequencies at which the dipole oscillates in addition to the fundamental ones. $P^{(3)}(\omega_{cs})$ stands for the coherent Stokes Raman scattering (CSRS), $P(\omega_2)$ for stimulated Raman gain scattering (SRS), $P^{(3)}(\omega_1)$ for stimulated Raman loss scattering (SRS) and $P^{(3)}(\omega_{as})$ for the coherent anti-Stokes Raman scattering (CARS). The amplitude for e.g. the anti-Stokes frequency component can be calculated by

$$P^{(3)}(\omega_{as}) = 6\epsilon_0 X_e(\Omega_{12}) A_1^2 A_2^* \tag{2.9}$$

with

$$X_e(\Omega_{12}) = \frac{N}{6m\epsilon_0}\left(\frac{\partial\alpha}{\partial Q}\right)_0^2 \frac{1}{\omega_v^2 - \Omega_{12}^2 - 2i\gamma\Omega_{12}} \tag{2.10}$$

For the sake of completeness, the amplitudes of the other frequency components can be written as

$$P^{(3)}(\omega_{cs}) = 6\epsilon_0 X_e^*(\Omega_{12}) A_2^2 A_1^* \tag{2.11}$$

$$P^{(3)}(\omega_2) = 6\epsilon_0 X_e^*(\Omega_{12}) |A_1|^2 A_2 \tag{2.12}$$

$$P^{(3)}(\omega_1) = 6\epsilon_0 X_e(\Omega_{12}) |A_2|^2 A_1 \tag{2.13}$$

Before the newly generated electric field E_4 and its propagation is calculated, some assumptions have do be made in order to simplify the mathematical description. First, it is assumed that the material is homogeneous and that the incoming electric fields possess a constant wave front so that the approximation as plane waves is valid. Furthermore, the polarization of these fields are in the x-direction. Now, with these assumptions, we can now insert each polarization contribution of equation 2.8 into the inhomogeneous wave equation.

$$\nabla^2 E_4 - \frac{n^2}{c^2}\frac{\partial^2}{\partial t^2}E_4 = \frac{1}{\epsilon_0 c^2}\frac{\partial^2}{\partial t^2}P^{(3)} \tag{2.14}$$

The nonlinear polarization can be rewritten as

$$P^{(3)}(z,t) = \frac{1}{8}\epsilon_0 X_e^{(3)}(\Omega) A_1(z) A_2^*(z) A_3(z) e^{i[(k_1-k_2+k_3)z-\omega_4 t]} + c.c \tag{2.15}$$

with $\omega_4 = \omega_1 - \omega_2 + \omega_3$. This equation shows that the newly generated signal is propagating in the forward and in the backward direction. When assuming that also the generated signal is polarized in the x-direction

$$E_4(z,t) = \frac{1}{2} A_4 e^{i(k_4 z-\omega_4 t)} + c.c. \tag{2.16}$$

it can be shown, that after we have inserted equations 2.15 and 2.16 into equation 2.14 and integrated along the length of the parametric material, the amplitude A_4 can be found as

$$A_4(L) = \frac{\omega_4}{8 n_4 c} X_e^{(3)}(\Omega_{12}) A_1 A_2^* A_3 L sinc\left(\frac{\Delta k L}{2}\right) e^{i\Delta k L/2} \tag{2.17}$$

This equation describes the signal build up inside the material. The amplitude of the newly generated component is the highest when the wave vector mismatch $\Delta k = k_4 - k_1 + k_2 - k_3$ is rather small, ideally 0. When there is no mismatch, the phase of the nonlinear polarization and the phase of the newly generated signal are always in phase with each other. However, due to dispersion the mismatch is always nonzero. Sooner or later, the induced polarization will run out of phase so that only on a specific length scale a significant build-up takes place (figure 2.3). This specific length is called coherence length and can be calculated through $L_c = \frac{2\pi}{|\Delta k|}$. For the forward propagating signal, the coherence length can be in the range of several hundreds of micrometers. Whereas in the backward direction, the signal is significantly smaller compared to the forward direction due to the increased wave vector mismatch of $L_c = \frac{\lambda_4}{2n_4}$. However, when investigating heterogeneous samples such as cells and tissue, the destructive interference caused by the phase mismatch might be incomplete yielding a non-vanishing signal in the backward direction.

In the following, I will describe the fundamental concepts of coherent Raman scattering with a focus on coherent anti-Stokes Raman scattering (CARS) and stimulated Raman scattering (SRS). The foundation of coherent Raman scat-

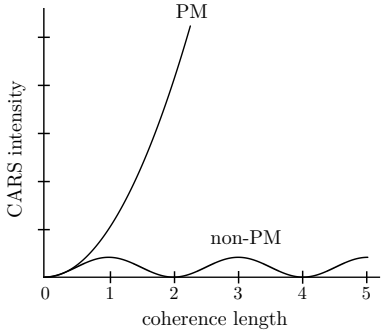

Figure 2.3: **Effects of phase matching on the CARS signal generation**
The diagram displays the effect of phase matching on the CARS signal generation. The two curves are resembling the signal growth if phase matching (PM) is considered and when it is not (non-PM). When optimizing the phase matching conditions the signal grows exponentially since no destructive interference occurs. If it is neglected, the signal strength depends on the interaction length. When the interaction length is equal or an odd multiple of the coherence length, the signal is maximized. Therefore, the most efficient way of generating a CARS signal is when phase matching conditions are considered (adapted from [46]).

tering is the way intense light pulses interact with molecules. In general, the interaction of light with an electron causes a change in its equilibrium position resulting in a change in the molecule's polarization. This change is coupled to the nuclear modes and contains information about the chemical properties of the molecule. When two intense light pulses are tuned in their spectral frequencies so that their energy difference matches such a vibration resonance, the molecule's polarization is efficiently altered. The coherent Raman signal is the result of the modulation of another light pulse by the induced polarization.

2.3.1 Coherent anti-Stokes Raman scattering

Coherent anti-Stokes Raman scattering is a four wave-mixing process that offers chemical sensitivity and holds great potential for the analysis of chemical compounds and biological samples. Since there is no energy exchange with the target molecule, CARS is considered to be a parametric process. As described previously, three incoming light waves interact with the molecule producing a

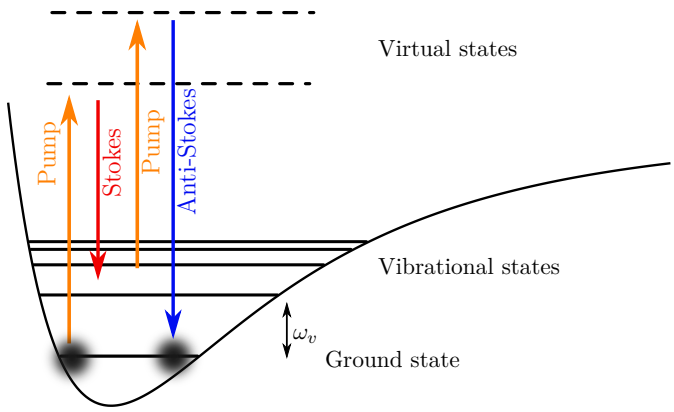

Figure 2.4: **Jablonski diagram of the CARS process**
In the CARS process a total of three photons interact with the molecule that, in the end, emits a fourth photon. As figure 2.2 displays, in the first step, the pump and the Stokes photon interact coherently with the molecule exciting an electron to a vibrational state. Now, a second pump photon lifts that particular electron to a higher virtual state from where it relaxes back to the ground state. The thereby generated photon is called the anti-Stokes photon since unlike the Stokes photon that has less energy than the pump photon, the anti-Stokes photon contains more energy and is thus blue-shifted.

blue-shifted photon ω_{as}, the CARS signal. Figure 2.4 visualizes this process in a Jablonski diagram. The pump photon, depicted in orange, excites an electron of the target molecule from the ground state to a virtual energy level. Note, that the energy of a single pump photon is not sufficient enough to excite the electron into the first excited state. Now, a Stokes photon interacts with this electron and it relaxes into a vibrational level that is defined by the energy difference Ω_{12} between the pump and Stokes photon.

$$\Omega_{12} = \omega_1 - \omega_2 \qquad with \quad \omega_1 > \omega_2 \tag{2.18}$$

Then, the electron is again excited into a second virtual state by absorbing another pump photon. Since there is no further photon-electron interaction, the electron relaxes to the ground state and releases a photon. Compared to the initial pump and Stokes photons, the newly generated photon is blue-shifted. The second pump photon, that excites the electron from a vibrational state into a virtual level, can possess any possible frequency as long as it still interacts with the electron. This process, however would then simply be called a four-wave mixing

process since CARS defines exactly the degenerated case when ω_3 equals ω_1. The CARS signal frequency ω_{as} can be calculated as follows

$$\begin{aligned} \omega_{as} &= \omega_1 - \omega_2 + \omega_1 \\ \omega_{as} &= \Omega_{12} + \omega_1 \end{aligned} \tag{2.19}$$

The blue-shift of the CARS signal can be spectrally separated from the fundamental beams and thus allows for an easy homodyne detection. In order to analyze the spatial CARS generation inside a material, the CARS polarization of equation 2.9 is utilized and the expression is inserted into the inhomogeneous wave equation (eq. 2.14). For the CARS intensity $I(\omega_{as})$ it can be found

$$I(\omega_{as}) = |X_e^{(3)}(\Omega_{12})|^2 I_1^2 I_2 L^2 sinc^2\left(\frac{\Delta k L}{2}\right) \tag{2.20}$$

Here, it can be seen that the intensity depends quadratically on the pump intensity and only linearly on the Stokes intensity due to the twofold interaction of the electron with the pump photon. However, the intensity also depends quadratically on the nonlinear susceptibility which has a major influence on the formation of the CARS signal. The nonlinear susceptibility consists of a resonant and a non-resonant contribution. The resonant amount comes directly from the resonance itself while the non-resonant part describes the influence of all resonances inside the sample that are not resonantly driven. Even though their resonant part is zero, they produce a non-zero (constant) background signal.

$$\begin{aligned} X_e^{(3)}(\Omega_{12}) &= X_r^{(3)}(\Omega_{12}) + X_{nr}^{(3)}(\Omega_{12}) \\ |X_e^{(3)}(\Omega_{12})|^2 &= \left(X_r^{(3)}(\Omega_{12})\right)^2 + \left(X_{nr}^{(3)}(\Omega_{12})\right)^2 + 2Re\left\{X_r^{(3)}(\Omega_{12})\right\} X_{nr}^{(3)}(\Omega_{12}) \end{aligned} \tag{2.21}$$

Here, the first two terms stand for the quadratic contribution of the resonant and the non-resonant part of the nonlinear susceptibility. The last part is the result of the squaring of the nonlinear susceptibility and describes the interference between the resonant and the non-resonant components. This interference term is the cause for the dispersive lineshape of the CARS resonance. A typical lineshape can be seen in figure 2.5. Here, the real (red line), the imaginary (blue line) and the

resulting absolute value (black line) of the nonlinear susceptibility are displayed under different conditions. Going from (a) to (c) it can be seen, that while increasing the non-resonant background from initially 0 to a constant value of 0.15, the lineshape is going from a symmetric one to a non-symmetric one. Figure 2.5(d) displays the CARS lineshape for various background values and shows that the peak position shifts with an increasing background. These two effects of the non-resonant background make the interpretation of a CARS image very complex. In the analysis of biological samples or a mixture of chemical compounds, the amount of non-resonant background contributions may vary across the field of view. Thus, a peak position change of the nonlinear susceptibility is inevitable as well as the dispersive lineshape.

2.3.2 Stimulated Raman scattering

Another powerful tool of coherent Raman spectroscopy is stimulated Raman scattering (SRS). Similar to CARS, it is a four-wave mixing process whose signal provides information about the chemical structure of a sample. Compared to CARS, it has the advantage to provide a coherent, non-distorted signal since the non-resonant background has no influence on the signal's lineshape. The fundamental process of SRS is a dissipative coherent interaction of two light waves with the molecule. It is dissipative because during the interaction an energy exchange between the light waves and the molecule takes place. The occurring process can again be separated into a two-step action. In the first step, the pump photon ω_1 excites the molecule from the ground state into a virtual energy level (figure 2.6). The Stokes photon ω_2 ($\omega_2 < \omega_1$) then probes the molecule which leads to a stimulated emission of a Stokes photon while the electron is relaxing into an excited vibrational state. Now, in the next step, a Stokes photon excites the electron from the excited vibrational state to a virtual energy level. Finally, a pump photon leads to a relaxation of the electron back to the ground state and to the stimulated emission of a pump photon. At first glance it seems that the number of pump and Stokes photons is unchanged. While in the first step, one pump photon is destroyed and one Stokes photon is generated, the second step inverts the generation and destruction of pump and Stokes photon. However, looking closely at the newly generated photons reveals that these photons exhibit

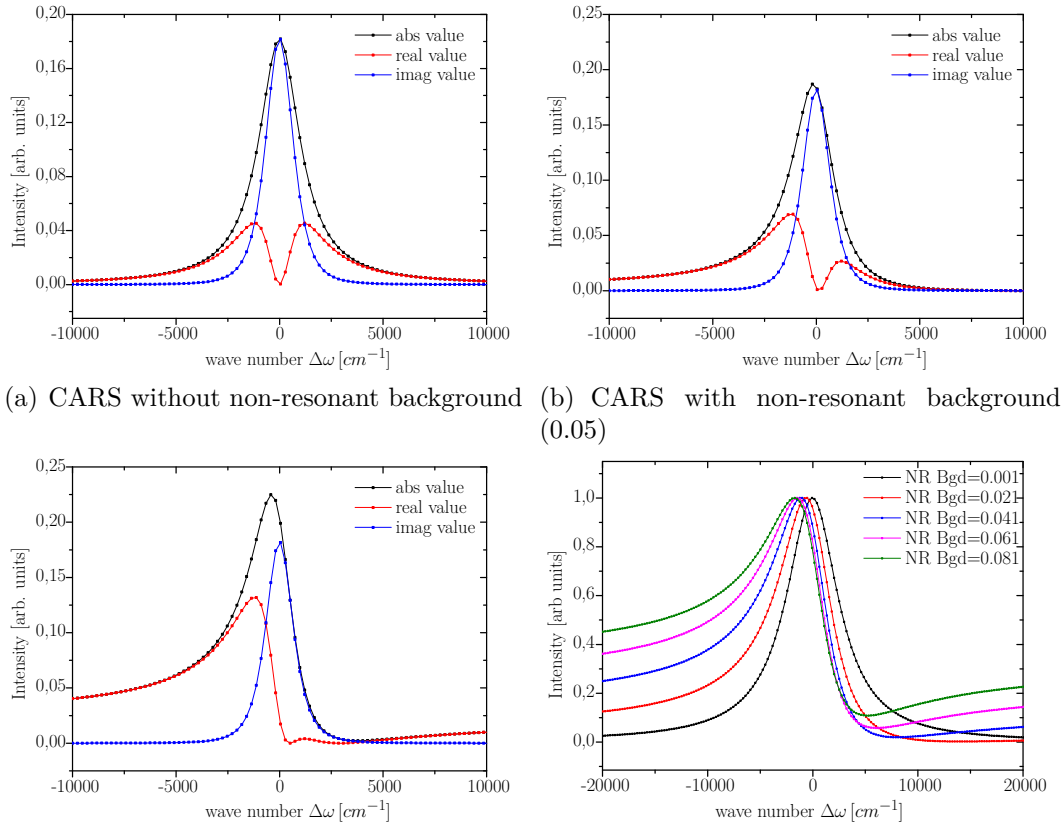

(a) CARS without non-resonant background

(b) CARS with non-resonant background (0.05)

(c) CARS with non-resonant background (0.15)

(d) CARS with variable background

Figure 2.5: **Simulation of CARS lineshapes**
In figures (a) to (d), simulations of the CARS lineshape are displayed. In figure (a), the imaginary (*blue*), the real part (*red*) and the absolute value (*black*) of the CARS signal are shown in relation to the mismatch of the combination of pump and Stokes and the resonance ($\Delta\omega = (\omega_1 - \omega_2) - \omega_v$). The lineshape is symmetric to the resonance and no distortion takes place. The situation changes when a non-resonant background contribution is added. Figure (b) and (c) illustrate the strong influence of the non-resonant background on the CARS signal. Even though the overall generated signal is stronger, the lineshapes are getting distorted while the non-resonant background is increased. Apart from the lineshape, the position of the maximum CARS intensity changes according to the amount of non-resonant background. Figure (d) shows the simulated CARS lineshape for different amounts of background signal. As can be clearly seen, the position of the maximum signal shifts slightly to the red side of the resonance.

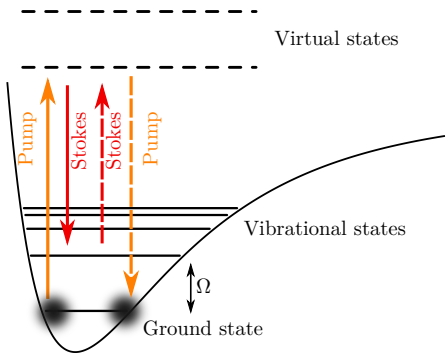

Figure 2.6: **Jablonski diagram of the stimulated Raman scattering process** The stimulated Raman process is just like the CARS process a two-step process. First, an electron is excited by a pump photon and a Stokes photon is emitted. In the second step this electron is excited by a Stokes photon and a pump photon is emitted. When performing a SRS experiment, one of the waves is intensity modulated which is indicated by the dashed lines. Depending on which beam is modulated, one performs either stimulated Raman loss or stimulated Raman gain spectroscopy. In the end, the SRS signal is the result of the temporal behavior of the Stokes and pump beam intensities.

a phase shift in relation to the initial light waves which leads to interference. The newly generated pump photons possess a total phase shift of π and interfere destructively with the fundamental beam, whereas the Stokes photons have no phase shift and interfere constructively. In order to understand the origin of this phase shift, the nonlinear polarization for these two processes (eq. 2.12 & eq. 2.13) needs to be revisited.

$$\begin{aligned} P(\omega_2) &= 6\epsilon_0 X^*_{NL}(\Omega)|A_1|^2 A_2 \\ P(\omega_1) &= 6\epsilon_0 X_{NL}(\Omega)|A_2|^2 A_1 \end{aligned} \tag{2.22}$$

The first equation describes the stimulated Raman gain (SRG) process. Note, that the nonlinear susceptibility is complex conjugated so that only the imaginary part of the generated waves undergoes a phase shift of π. The second equation stands for the stimulated Raman loss (SRL) process, in which this phase shift is not present. To calculate the amplitude of the forward-propagating wave, the

polarization is inserted into the wave equation (eq. 2.14)

$$\begin{aligned} A_2^{stim}(L) &= i\frac{\omega_2}{8n_2c}\{X_e^{(3)}(\Omega_{12})\}^* A_1^* A_2 A_1 L \\ A_1^{stim}(L) &= i\frac{\omega_1}{8n_1c}\{X_e^{(3)}(\Omega_{12})\} A_2^* A_1 A_2 L \end{aligned} \tag{2.23}$$

Interestingly, the wave vector mismatch Δk for the forward-propagating signal wave is always zero. Since the newly generated photons originate in the stimulated emission of the previously described two-step process, they exhibit a constant phase relation to the fundamental wave. Equation 2.23 shows that both amplitudes experience a phase advance of $\pi/2$ ($i = e^{i\pi/2}$). Calculating the intensity of the stimulated Raman gain signal leads to

$$\begin{aligned} I(\omega_2) &= |A_2(L) + A_2^{stim}(L)|^2 \\ &= I_2 + |X_e^{(3)}|^2 I_1^2 I_2 L^2 \\ &+ 2I_1 I_2 L \left[Re\left\{X_e^{(3)}(\Omega_{12})\right\} cos(\phi_{gm}) + Im\left\{X_e^{(3)}(\Omega_{12})\right\} sin(\phi_{gm}) \right] \end{aligned} \tag{2.24}$$

Here, the geometric phase shift ϕ_{gm} is introduced. The origin of this phase shift lies in the way the light wave interacts with the sample. There are two ways how the light wave might interact with the sample. If a homogeneous material is considered which is excited by a plane wave, the signals from all emitters interfere with each other resulting in a constant phase shift. If a light wave is focused on a single dipole emitter, the Gouy phase shift of a Gaussian beam introduces a constant phase difference. In both cases the phase shift is the same and amounts to $-\pi/2$ for the stimulated Raman gain/loss signal.

Equation 2.24 describes the intensity of the stimulated Raman gain signal after the light wave passes the sample. The first two terms represent the intensities from the fundamental and the generated stimulated Raman wave, respectively. The third and the fourth term are the interference terms. If we assume, that the fundamental wave is orders of magnitude stronger than the stimulated Raman signal ($A_2 \gg A_2^{stim}$), the second term of equation 2.24 can be neglected. Now, only the interference terms depend on the nonlinear susceptibility and thus contain significant information about the sample. Recasting the interference term shows that only the imaginary part of the stimulated Raman signal is in phase with the

fundamental wave and that the real part, being out-of phase, does not contribute.

$$I(\omega_2) = 2I_1 I_2 L \left[Re\left\{X_e^{(3)}(\Omega_{12})\right\} cos(\phi_{gm}) + Im\left\{X_e^{(3)}(\Omega_{12})\right\} cos(\phi_{gm} + \pi/2)\right] \tag{2.25}$$

Equation 2.25 visualizes the spectral phase shift through the conversion of sine to cosine. If the geometric phase shift is inserted into the equation, it is becoming apparent that the real part of the susceptibility has no influence on the signal strength and that solely the imaginary part contributes to the signal. Finally, when utilizing modulation techniques in which the pump beam is modulated, the detected signal on a far-field detector can be found as the intensity change of the Stokes beam

$$\Delta I(\omega_2) = 2Im\left\{X_e^{(3)}(\Omega_{12})\right\} I_1 I_2 L \tag{2.26}$$

Thus, the signal intensity is proportional to the imaginary part of the nonlinear polarization and independent from the non-resonant contributions. The sign in front of the equation shows that the Stokes signal experiences a gain in intensity. Analogously, the signal intensity for the stimulated Raman loss signal can be derived.

$$\Delta I(\omega_1) = -2Im\left\{X_e^{(3)}(\Omega_{12})\right\} I_2 I_1 L \tag{2.27}$$

Here, the sign changes indicates the loss in intensity of the detected signal.

2.4 Other scattering effects

Light scattering effects always occur whenever a sample is analyzed that consists of different refractive indices. In the case of CARS and SRS, where only a small volume is analyzed, the spatial resolution is unaltered because it only depends on the focal volume in which the four-wave mixing signal is generated. However, scattering does influence the signal strength and thus the contrast of the image. In order to analyze the influence of scattering, we will divide it into linear and nonlinear scattering events.

Light that travels through a sample experiences linear scattering whenever it passes materials with different refractive indices. In the case of CARS and SRS, the forward detected signal is scattered at each interface resulting in an intensity

loss. This effect can be exploited when investigating strongly scattering biological samples such as tissue because simultaneously to the signal loss in the forward direction, the backward scattered signal experiences a signal growth independently from the phase matching criteria [36].
The nonlinear scattering has its origin in the coherence of the generated signal. Compared to spontaneous Raman scattering, the coherence leads to a signal strength that is orders of magnitude stronger and thus enables faster signal acquisition. However, when the phase relation between two emitters is unfavorable the signal strength at the detector decreases due to destructive interference. Nonlinear scattering is a purely phase related effect and is quite prominent in CARS imaging. The effect can be divided into two separate mechanisms that take place inside the sample.
The first effect is related to the spectral properties of the nonlinear susceptibility. If the resonance is driven on the blue side, the generated CARS signal is experiencing a phase shift of π compared to the non-resonant part. The non-resonant contribution of the neighboring material interferes destructively with the resonant signal. Especially at interfaces this effect can be predominantly observed. To visualize the effect on a CARS signal, a comparison of the CARS and SRS signals is shown in figure 2.7. Here, Chinese ovary hamster (CHO) cells have been axially imaged. The left side displays the acquired CARS image and the right side the corresponding SRS image. The white circle in the image indicates the region in which destructive interference in the CARS image occurs. Because the SRS signal solely depends on the resonant background, no interference with the non-resonant background takes place.
The second mechanism takes place in CARS as well as in SRS. Whenever a Gaussian beam is focused onto a single dipole emitter, the newly generated field experiences an additional phase shift, the Gouy phase. This effect leads to interference between the target molecule and the surrounding media. The amount of additional phase depends on the position of the focus compared to the object. This situation is illustrated in figure 2.8. The figure depicts two situations, in which the object is located below the focus (left side) or above the focus (right side). The black line indicates the evolution of the phase shift. This phase shift ranges between $-\pi$ and $+\pi$. The actual phase shift of the molecule (ϕ_d) at a spe-

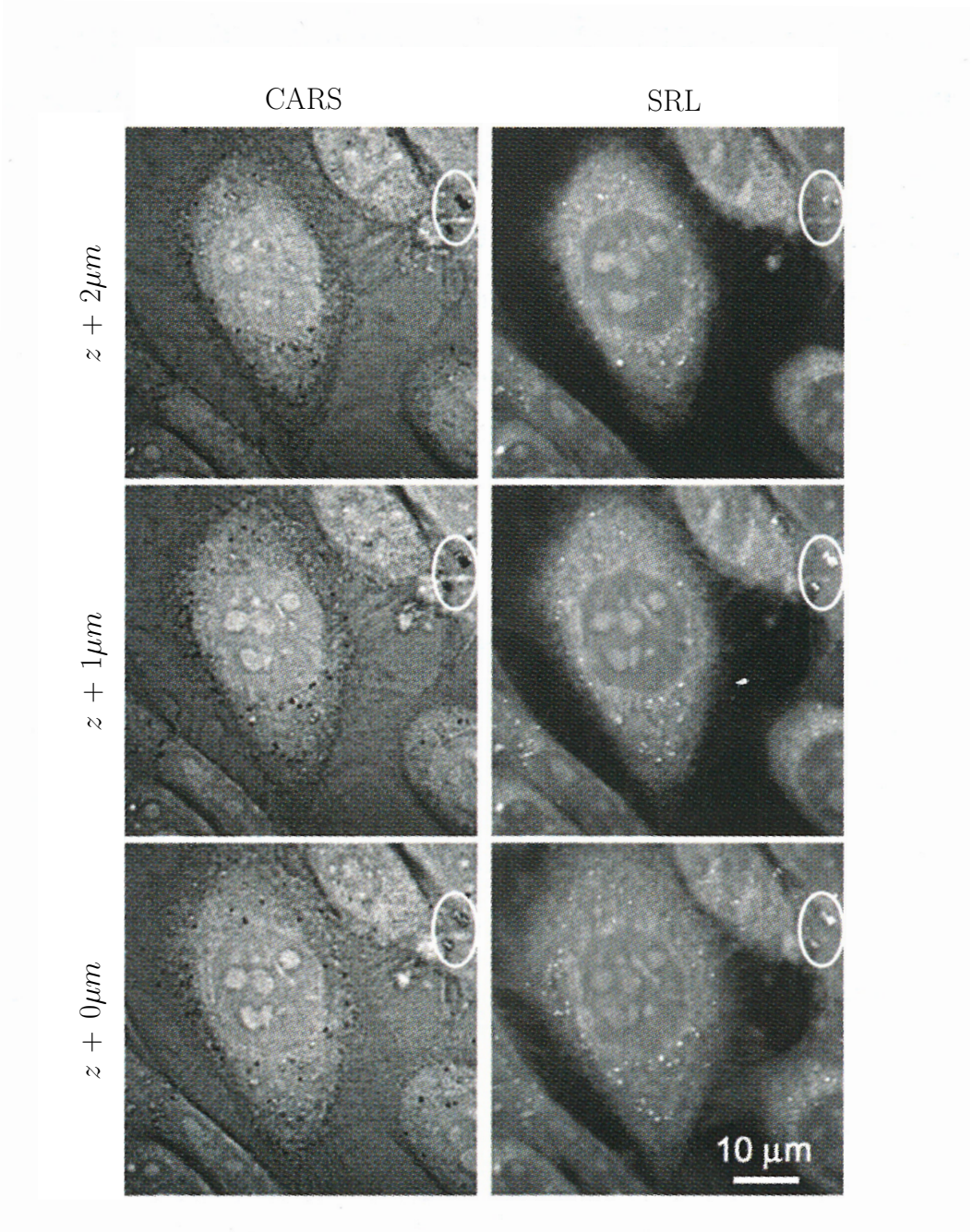

Figure 2.7: **Comparison of CARS and SRS images when axially scanning a cell** When scanning a cell axially, the effect of constructive and destructive interference between the resonant and non-resonant contributions of the CARS signal becomes visible. As an example, CARS images (left side) and SRS images (right side) of chinese hamster ovary cells (CHO) are compared to each other at different scanning depth z. The white circle highlights the region in which the effects can easily be identified. Keeping in mind that ideally, the SRS image should be the same as the CARS image, the images taken at 2 μm differ due to the occurring destructive interference in the CARS image (image taken from [45]).

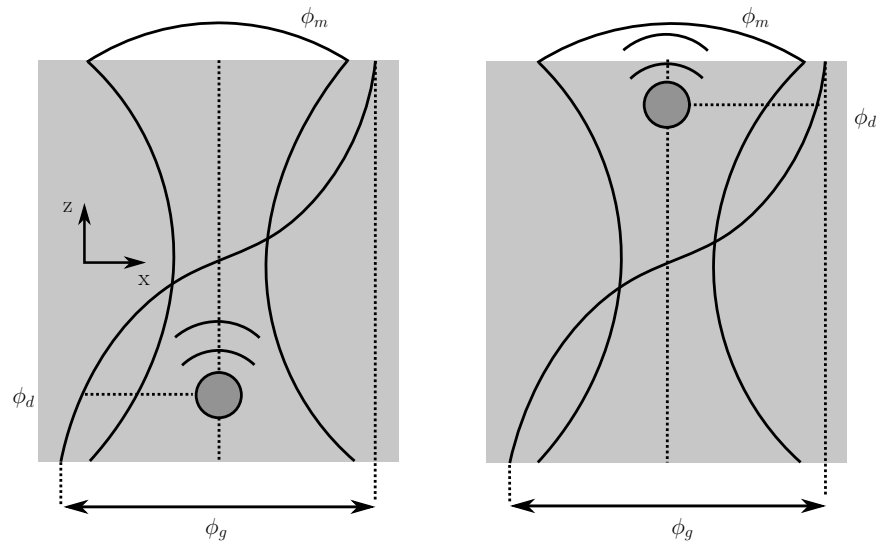

Figure 2.8: **Effects of the Gouy phase shift**
When imaging small objects with CARS, the location of the object in relation to the focus plays an important role in CARS microscopy. The figure displays two possible situations. One in which the object is below the focus and the other above the focus. The generated non-resonant background is independently from the focus position and has the fixed phase ϕ_m. The molecule however, experiences the Gouy phase shift ϕ_d. The black line displays the phase progression of the Gouy phase. Below the focus, the phase shift ranges from $-\pi$ to 0, above the focus between 0 and $+\pi$. Therefore, depending on the position of the molecule, destructive or constructive interference between the CARS signal of the molecule and the non-resonant background occurs due to the Gouy phase shift (adapted from [45]).

cific position is indicated by the black dotted line. The grey rectangle indicates the area of non-resonant background contribution, which exhibits a fixed phase (ϕ_m). As it can be seen, destructive interference occurs when the molecule is below the focus point, while constructive interference occurs above the focus. Even though this effect is very prominent in CARS, this phase shift also influences the contrast of a SRS image to a small amount. Due to this effect, the SRS signal is not completely independent of the non-resonant background [47].

2.5 Optical fibers

The utilization of fiber optics facilitates the construction of small and compact optical systems. Since light is confined in a small space and guided by the fiber itself it is applicable to medical technology e.g. endoscopy [42][43]. Moreover, utilizing fiber technology results in portable and cost-efficient optical systems often designed as turn-key systems [48].

2.5.1 Basic working principle of an optical fiber

The basic physical principle of an optical fiber is the total internal reflection of light. Total internal reflection describes the light-matter interaction when light is traveling from one medium with optical density n_1 to another medium n_2 with $n_2 < n_1$ [49]. If the angle of incidence is greater than the critical angle, the light is reflected back into the denser medium. A step-index fiber is basically constructed from two media: a round core with n_1 and a surrounding medium n_2 with the same relation of optical density as previously shown. Figure 2.9 illustrates a step-index fiber and the light path within it. The NA of the fiber describes the acceptance angle under which light can be coupled into the fiber (illustrated as the grey area). The NA can be tuned by the relation of n_1 and n_2. However, when light enters the fiber under various angles, the optical path of a pulse depends on the angle of incidence. Therefore, the pulses exhibit a time delay between each other. When analyzing the fiber output, interference patterns resulting from the additional phase are visible on a screen. This effect is called modal dispersion and plays an important role in data transferring through the

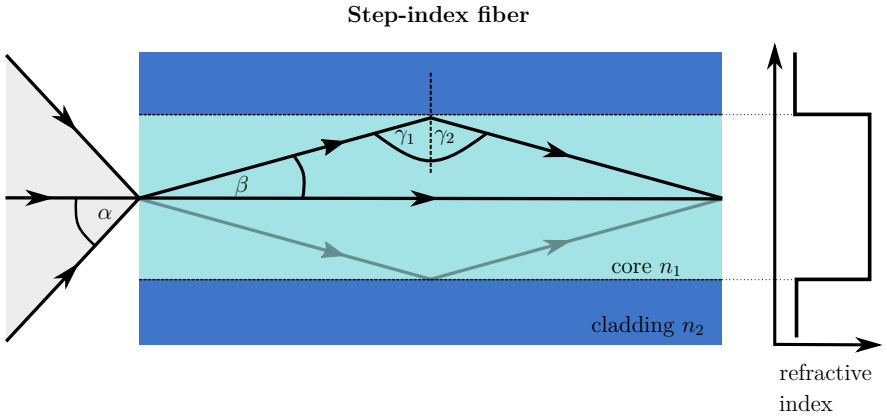

Figure 2.9: **Sideview of a step-index fiber**
The fiber consists of two materials with optical densities n_1 and n_2. As can be seen in the diagram, the optical density of the core n_1 is higher than that of the cladding n_2. The numerical aperture (NA) describes the cone of light (grey area), that is still guided inside the fiber. Every ray of light entering the fiber with a greater angle is not supported and is affected by loss.

fiber since it limits the maximum data rate. Assuming a time delay between the pulses of 10 ns would result in a maximum data rate of 10 MHz. For higher data rates, the signals are mixed with each other so that the information is unresolvable. Instead of utilizing a step-index fiber, the gradient of the optical density n_1 can be modified in order to compensate for the additional optical path. These fibers are hence called gradient index fibers and are designed to reduce the optical density towards the edges of the fiber so that the optical path length of the pulses traveling straight and under an angle is ideally identical. This effect is only taking place when multiple optical modes are participating within the fiber. If the fiber core is reduced to a critical size, only one mode is allowed to travel through the fiber. However, this singlemode fiber possesses a degenerated mode since the polarization allows two configurations. In an ideal fiber the state of polarization is maintained over the entire length of the fiber. But due to naturally occurring impurities within the fiber and also external stress such as bending or even temperature changes, the polarization states are mixing with each other. This effect is continuously evolving so that after a certain path length, the beat length, the polarization ratio is back to the initial state. The effect of polarization mixing is called polarization mode dispersion. In order to maintain the polarization state of an optical pulse while traveling through a fiber, a special fiber design has to

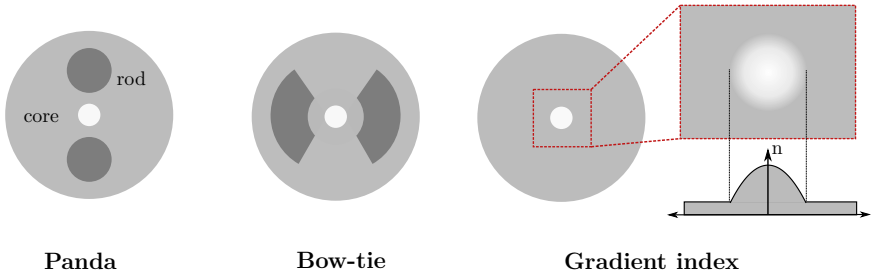

Figure 2.10: **Optical fiber layouts for maintaining the state of polarization and compensating modal dispersion**
In order to maintain the polarization of an optical pulse upon propagation through a fiber, specially designed fibers are utilized. Here, the cross-sections of a bow-tie and a panda fiber are visualized that maintain the polarization. This is accomplished by introducing two rods of a different material than fused silica into the cladding so that stress is induced. The stress leads to stress-induced birefringence so that the polarization state is maintained. The last cross-section belongs to a gradient index fiber which can be utilized to reduce the effect of modal dispersion. As it is shown in the small inset, the optical density of the core is smaller towards the edges than in the middle. Thus, the optical path of the rays traveling e.g. on a helical beam path is ideally identical to the rays traveling in the middle of the fiber without an angle.

be chosen. Figure 2.10 illustrates a small collection of fiber shapes that can be utilized in order to reduce the modal dispersion and the polarization dispersion. The panda and the bow-tie fiber are able to maintain the state of polarization of the incoming pulse due to stress-induced birefringence [50]. The birefringence is produced by introducing a small rod of a different material into the cladding of the fiber. Compensation of the modal dispersion is accomplished by the gradient index fiber. As stated earlier, due to the varying optical density towards the edges of the fiber core, the helical traveling beams are experiencing the same optical path length as the light traveling in the very core of the fiber.

When dealing with short pulses chromatic dispersion plays an important role, especially when designing a fiber laser cavity. Since light is guided through a material, dispersion is always present. Depending on the type of material, the dispersion is either negative or positive. The spectral components of the pulse e.g. the blue and red components experience a different refractive index and are thus traveling with a different speed through the fiber so that the overall pulse is broadened. When designing a fiber cavity, the net dispersion for the desired central wavelength should ideally be zero. This is achieved by carefully combining

fibers with negative dispersion e.g. highly nonlinear fibers with fibers possessing a positive dispersion. A pulse that is stable in its shape upon traveling within a cavity is named a soliton.

2.5.2 Nonlinear effects within an optical fiber

Guiding light through a fiber results in confining the energy to a very small volume leading to high energy densities. Dealing with short pulses increases this energy density to a manifold extent. Thus, nonlinear effects that occur within the fiber have to be taken into account. A prominent effect is the generation of stimulated Raman scattering. The fiber material itself possesses Raman-active modes that are excited when a pulse travels through the fiber. Thus, the optical pulse is always accompanied by a Raman pulse. When a Raman mode is excited by the initial pulse, the present Raman pulse interacts with the mode and stimulated emission takes place increasing the Raman pulse further. When utilizing a fiber for spectroscopy purposes e.g. Raman spectroscopy one has to block the red-shifted Raman pulse before focusing the beam into a sample (see also section 3.8.2).
The second effect that occurs within the fiber due to the high energy density is self-phase modulation (SPM). Since the refractive index of the material is not strictly linear, the temporal high energy results in an instant and local modification of the refractive index leading to a temporal phase shift of the pulse. When performing a Fourier transformation on the pulse, it can be seen that the spectral components are directly affected by the temporal phase shift. This effect is exploited for supercontinuum generation when a short-pulse is traveling through a small piece of fiber generating new frequency components. In addition to a temporal shift, the polarization state of the pulse might shift. Assuming a Gaussian pulse, the polarization change would affect the middle of the pulse more than the edges due to the higher intensity in the center. Within a cavity, this effect can be utilized for passive mode locking a laser cavity by placing an analyzer in the cavity that only allows high intensity regions to pass and rejects lower intensity portions of the pulse [51].
But not only the pulse itself can lead to self-phase modulation. When two beams

coincide within the fiber, they can interact with each other. Since the material experiences the resulting energy density of both beams, the same effects that occur in SPM are taking place. This effect is called cross-phase modulation (XPM). In contrast to SPM, the pulses may modulate each others temporal phase and polarization state in the overlapping regions. Exploiting the XPM effect leads to many fascinating effects such as building an optical shutter or performing additive pulse mode locking [52][53].

2.5.3 Fiber optical elements

In the following the basic working principle of a small selection of fiber optical elements will be analyzed and discussed. The first element that I will present is the fiber-based polarization controller. This controller consists of two or even more fiber loops packed together in a disk. Because the fiber is sensitive to external stress e.g. bending and twisting the fiber, the polarization state of the light traveling through that fiber can be modified. Depending on the amount of fiber on which the stress is induced, the polarization change equals that of a quarter-wave plate or a half-wave plate. Thus, a polarization controller can fully control the polarization of the guided light [54].
Another fiber-based element is the optical isolator. Isolators are exploiting the Faraday effect in which a strong magnetic field interacts with the fiber material. When light travels past this element, its polarization is turned in relation to the interaction length and efficiency of the material. The efficiency depends on the Verdet's constant of the material and the wavelength of the light. That is why for visible light terbium gallium garnet (TGG) is utilized and yttrium iron garnet (YIG) for infrared light. Placing the Faraday rotator between two analyzers results in a polarization sensitive optical diode. In order to achieve a polarization independent Faraday rotator, the two polarizations of the light are split by a birefringent polarizer, directed into two separate Faraday rotators and recombined afterwards.
Designing a fiber based beam splitter is accomplished by fusing two fibers within well defined distance together. When the light is totally reflected inside the fiber, there is always an evanescent field present in the cladding. In general, there is

no energy flow, since the field cannot couple to anything within the cladding. However, with the second fiber being in the vicinity of the first, efficient coupling is possible. Depending on the distance and the interaction length, the energy transfer from one fiber to the other can be tuned. Therefore, it is possible to create fiber-based beam splitters with an arbitrary splitting ratio e.g. 50:50.
Lastly, the active fiber based amplifier is investigated. An active amplifier consists of a highly-nonlinear fiber such as an Ytterbium-doped (Yb-doped) fiber and a pump diode. The pump diode is a standard cw laser source that is coupled into the highly-nonlinear fiber. The wavelength of the laser diode should match the maximum absorption cross-section of the nonlinear fiber e.g. for a Yb-fiber the ideal wavelength would be 980 nm. Pumping leads to a population inversion within the nonlinear fiber. The incoming pulses are then amplified by a certain amount depending on the fiber length and the pumping intensity. A side effect that can arise is the formation of amplified spontaneous emission (ASE). When the pumping is too strong and thus the population inversion is high, ASE might be generated and contributes to the signal output of the fiber amplifier. In addition, the amplification yield of the signal is reduced due to the presence of the ASE. Since amplifying the signal results in a higher energy density, nonlinear effects as discussed earlier have to be considered. Especially SPM and self-focusing of the pulse have a dramatic effect on the pulse shape and the condition of the fiber itself. While SPM leads to undesired broadening of the spectrum, self-focusing might lead to the destruction of the fiber due to the increasing energy density. This effect can be circumvented by a simple and yet very efficient method. Before introducing the pulse into the amplifier, second order dispersion (group velocity dispersion (GVD)) is introduced to the pulse e.g. by adding 5 m of additional fiber. Thus, the blue and the red side of the spectrum experience an additional time delay reducing the local energy density within the fiber. Consequently, the amplification of the separate spectral components can be higher without the short-comings of considering nonlinear effects (see also section 4.5.4). After amplification, the pulse can be compressed again ideally yielding a transform-limited pulse with high energy. This method is called chirped pulse amplification (CPA) and is a ground-breaking method for achieving high-intensity optical pulses [55].

3 Optical setup for coherent Raman imaging

In this chapter, I will give a general overview about the experimental setups that are utilized in the experimental section. The coherent Raman setup consists of a ps laser source, an optical parametric oscillator and a custom-built microscope (figure 3.1). It is capable of capturing coherent anti-Stokes Raman scattering signals and stimulated Raman scattering signals simultaneously. Furthermore, it provides the possibility to perform two-photon emission fluorescence (TPEF) as well as second harmonic generation (SHG) imaging. In the following subsections, I will focus on selected elements of this complex optical instrument and highlight their unique properties and characteristics.
After that we will have a closer look at the commercial Raman setup and the custom-built spontaneous Raman microscope. I will discuss three different arrangements of light illumination and how the Raman scattering signal can efficiently be directed into the spectrometer.

3.1 The laser system

The essential element of every coherent Raman microscope is the laser system. Since CARS and SRS are four-wave mixing processes, the use of short-pulse laser systems is inevitable. To address these non-linear processes picosecond (ps) or femtosecond (fs) lasers have to be employed. The choice of the laser system defines whether only a single resonance is addressed or multiple ones. A typical resonance has a bandwidth of 10 cm^{-1}, leading to an ideal pulse width of roughly 2 ps. When addressing only a single resonance, the chemical contrast is high

and finer differences can be resolved. However, utilizing picosecond pulses reduces the signal intensity and thus leads to a longer integration time compared to femtosecond pulses. Also scanning a wider range of wavenumbers consumes more time which might finally lead to sample damage. Femtosecond pulses offer rapid scanning capabilities due to higher peak intensities and thus higher signal intensities. The drawback of using spectral broad femtosecond pulses is the poor chemical contrast which makes complex post-processing routines necessary [39]. The optical system employes a solid-state Nd:YVO_4 picosecond laser with a repetition rate of 80 MHz and a fundamental wavelength of 1064 nm. The pulse width of the laser is 6.5 ps which is slightly longer than the ideal pulse ensuring that only a single resonance is being addressed. Due to a lower absorption cross-section and thus a deeper penetration depth, near-infrared light was chosen above light in the visible regime. An image of the solid-state laser interior can be seen in figure 3.2.

The laser is build in a Master Oscillator Power Amplifier (MOPA) design and can be divided into three different parts of signal generation: The laser cavity, the amplifier and finally the SHG stage. The laser cavity hosts a pump diode that pumps the oscillator crystal. The crystal is made of Nd:YVO_4 which generates photons with a wavelength of 1064 nm that run inside the cavity. Passive mode locking is achieved by a semiconductor saturable absorber mirror (SESAM). The cavity length is 3.75 m in total leading to the repetition rate of 80 MHz. The cavity output is then directed into the amplifier. Here, a second diode laser pumps the amplifier crystal, into which the 1064 nm photons are directed. The maximum achievable output power can go as high as 16 W. Finally, the photons are directed into the SHG stage. Here, the polarization is changed by a motorized half-wave plate and directed to a thin-film polarizer. Only the horizontal part is being transmitted, the other is reflected and directed into a SHG crystal (e.g. BBO). The fundamental 1064 nm beam is then doubled in its frequency to 532 nm by a type 1 SHG process and its polarization is changed to horizontal. Again, this beam is split up in two parts by a half-wave plate and a thin-film polarizer. This means the laser provides three laser beams exiting the housing through separate exits: one fundamental horizontal polarized beam at 1064 nm and two beams at 532 nm, one horizontally polarized, one vertically. The ratio

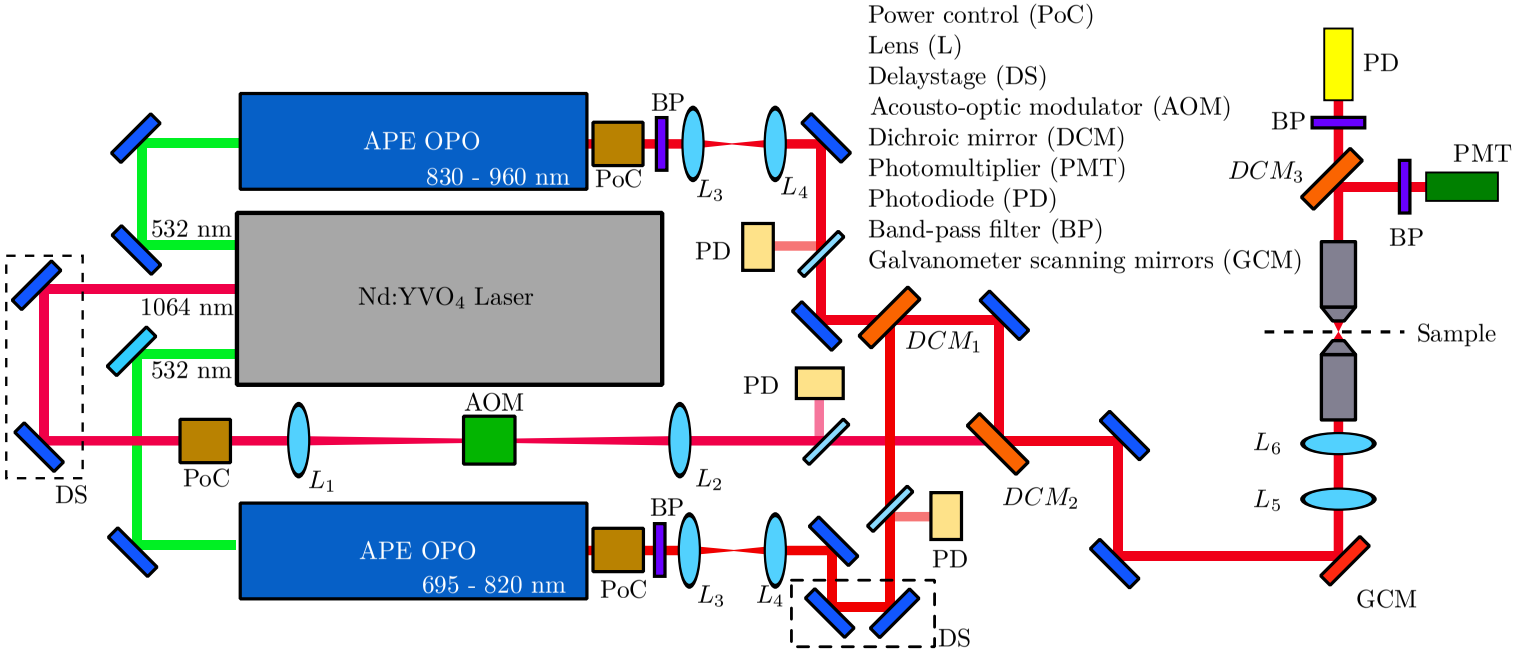

Figure 3.1: **Schematic sketch of the setup**
The center piece of the laser system is a Nd:YVO_4 laser system that provides the setup with three laser ports: one 1064 nm and two 532 nm laser beams. The two 532 nm beams are directed to two OPOs in which the wavelength can be altered through a parametric operation. The power can be adapted through the use of a power control consisting of a $\lambda/2$ wave plate and a polarizer. The output of the OPO passes a band-pass filter and a telescope that expands the beam in order to match the diameter to the back focal plane of the utilized objective lens. Both beams are then combined by a dichroic mirror (DCM_1) until they are combined with the fundamental 1064 nm beam through a second dichroic mirror (DCM_2). Right after the fundamental beam emerges the laser it passes a power control and is focused into an acousto-optic modulator (AOM) which will be utilized for SRS imaging. Then, the 1064 nm beam is combined with the other two beams and directed to a set of galvanometer scanning mirrors (GCM). They provide a 2D pattern that is projected onto the back focal plane of the objective lens. The objective lens focuses the set of beams into the sample and a second objective lens collects the signals. The signals are then split and directed on a detector. In the case of blue-shifted signals such as CARS the signal is directed on a photomultiplier tube (PMT). For SRS imaging, the pump beam is directed on a photodiode. Further information about the signal detection can be found in figure 3.10.

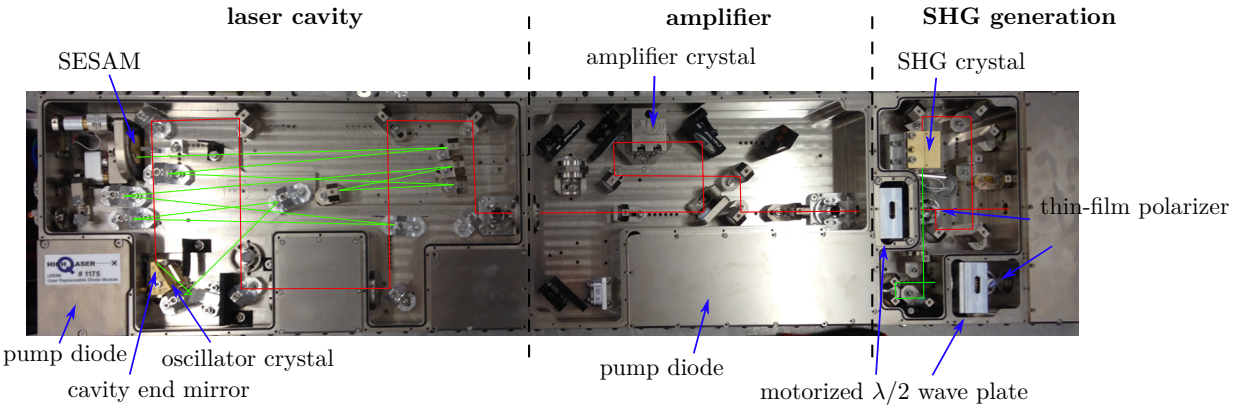

Figure 3.2: **Schematic sketch of the Nd:YVO_4 laser**
The laser consists of three parts going from left to right: the laser cavity, the amplifier and finally the SHG stage. In the laser cavity the fundamental 1064 nm beam is generated. Mode locking is achieved by utilizing a SESAM mirror. The cavity output is then amplified to an average output power of 16 W. Finally, the beam is divided into two portions: one part for the fundamental output and the second for generating the frequency doubled output. Here, a SHG crystal is utilized to generate the 532 nm beam which is subsequently subdivided into two portions and sent to individual outputs. Due to splitting, both outputs possess opposing polarization orientations.

of these beams can be adjusted by the motorized half-wave plates in front of the polarizers that can be controlled via the control software provided by HighQ.
In summary, the laser source for the narrowband coherent Raman microscope is a picosecond laser. It is operating with a repetition rate of 80 MHz and has a fundamental wavelength of 1064 nm. The beam is later divided into three portions. Two of these portions are frequency doubled. The maximum output power of the near-infrared output is 16 W, the maximum output of the frequency doubled outputs is 11 W. The pulse width is 7.4 ps and 6.2 ps for the 1064 nm and 532 nm beam, respectively. Due to the SHG process, the pulse width of the 532 nm beam is slightly shorter. The beam diameter of all three beams is in the range of 1.2 mm. Analyzing the intensity of the 1064 nm beam with a fast photodiode (DET36A/M, Thorlabs) reveals the temporal behavior (see figure 3.3). As it turns out, the laser exhibits a laser noise that is particularly strong at around 30 kHz. When acquiring images with long integration time, this effect becomes rather important. These images will carry a periodic pattern that is independent of the sample structure. The source of this noise is yet unknown and might be

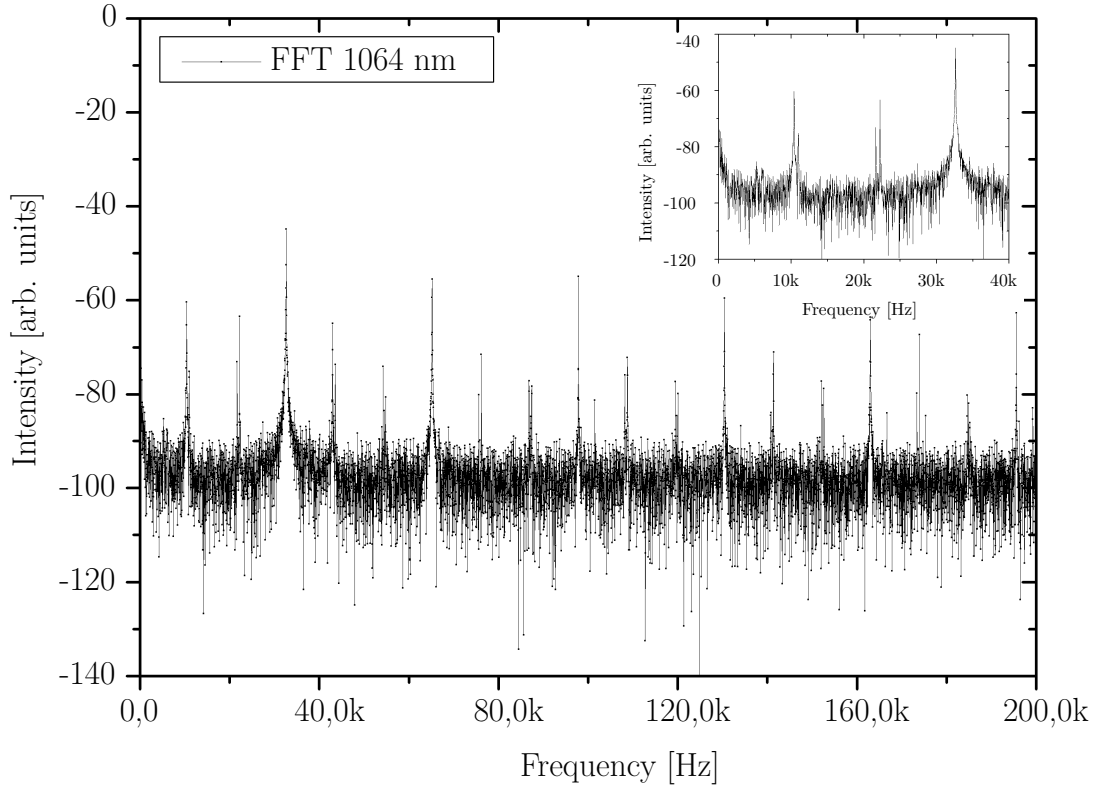

Figure 3.3: **Fast-Fourier transform of the laser intensity**
In order to verify the laser performance, the fundamental beam intensity was monitored with a photodiode. Applying a Fourier transformation on the data set reveals the participating frequency components. For CARS imaging and especially for SRS imaging it is mandatory to provide a noise-free laser source in order to achieve the best signal-to-noise ratio. The observed frequency components in the lower frequency range e.g. 30 kHz are very likely to cause strips in the final CARS image.

associated with aging of the laser (electronic noise, SESAM, misalignment of the laser cavity, pumping diodes).

3.2 Optical parametric oscillator

In order to address different molecular vibrations, we need an element that is capable of varying the pump wavelength. In general, either the pump or the Stokes beam can be varied in its wavelength. In the presented optical system, the pump wavelength is tuned. The tuning of the pump beam is accomplished by utilizing an optical parametric oscillator (OPO).

The OPO exploits the parametric process in order to produce the tunable output. In a parametric process, one photon of a high frequency ω_1 is being destroyed while two other photons of lower frequency e.g. ω_2 & ω_3 are being generated. By convention, the newly generated photon with the higher frequency is called the signal, the other the idler. The parametric process has to satisfy the conservation of energy and momentum. This leads to the energy relation $\omega_1 = \omega_2 + \omega_3$ and the phase-matching criteria $k_1 = k_2 + k_3$. In order to fulfill the momentum conservation, the parametric process takes place inside a crystal. Depending on the type of crystal, there are two different approaches to meet the requirements. The OPO used in this thesis utilizes the type 1 phase matching arrangement. Hence, a photon of ordinary polarization is being destroyed and two photons of extraordinary polarization are generated. Alternatively, the process can occur with reversed polarizations.

Figure 3.4 depicts a sketch of the OPO. It is pumped by the frequency doubled output of the laser source. The photons with a wavelength of 532 nm pass the Brewster window at the entrance of the OPO. The Brewster window ensures that no dirt enters the OPO but also that mostly vertical polarized light enters the cavity. Then, the photons are focused into the lithium triborate (LBO) crystal generating the signal and idler photons. These photons travel through the cavity that is constructed by four concave mirrors and four plane mirrors. To form a stationary wave inside the cavity, the cavity length can be modified by a piezo stage underneath mirror (M2). After one round trip, they are again focused into the crystal supporting the parametric process. When photons are reflected from the confocal mirror CM2, a small part exits the cavity and is collimated by L2. Two small portions are then reflected at the interface and the backside of the beam splitter (BS). One portion is directed to the spectrometer, the other to a photodiode. The photons which pass the beam splitter travel to a long-pass filter that splits the beam into two components: signal and idler. The idler passes the filter and the signal is reflected and leaves the OPO through the second output. For the generation of the coherent Raman signal, only the signal photons are utilized so that the idler beam is blocked inside the OPO housing.

Controlling the parametric process is accomplished by carefully tuning the temperature of the crystal. This way, the beam paths are unaltered. When the OPO

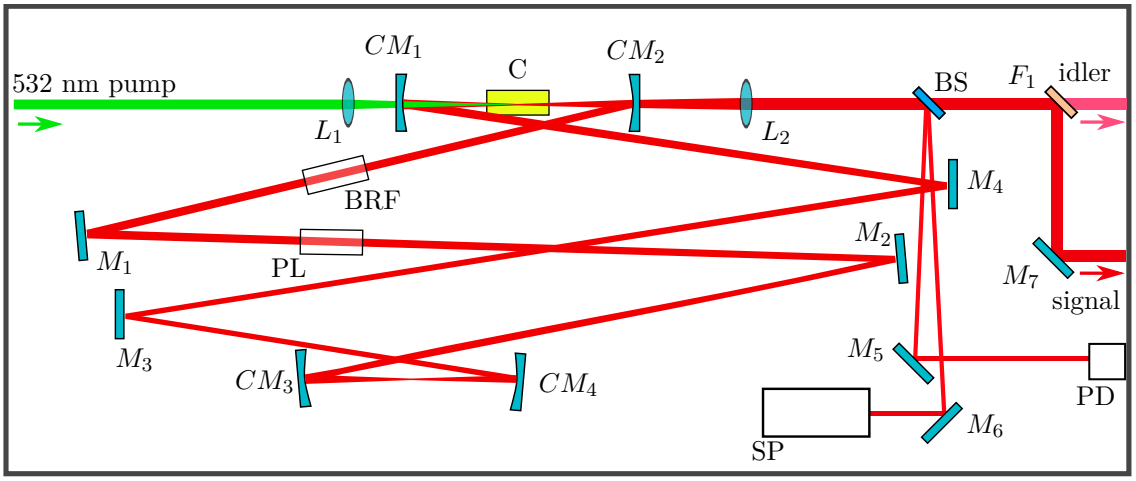

Focusing lens (L_1)	Lyot Filter (BRF)	Collimating lens (L_2)	Photodiode (PD)
Concave mirror (CM)	Plane mirror (M)	Beam splitter (BS)	Long-pass filter (F_1)
LBO crystal (C)	Polarizer (PL)	Spectrometer (SP)	

Figure 3.4: **Schematic sketch of an OPO**
The OPO consists of a laser cavity with a lithium triborate (LBO) crystal in the center. The 532 nm pump beam enters the cavity and is focused into the crystal. The crystal splits the pump photon into two parts: the signal and the idler. After generation, the photons travel through the cavity and are focused into the crystal in which they interact with the next pump photon. After a certain number of round trips, the photons pass through the confocal mirror (CM_2) and are collimated by a lens (L2). In order to have a feedback about the parametric process, two small portions are deflected from the main beam by utilizing a beam splitter (BS). One part is directed to a spectrometer, the other part to a photodiode. The main beam is divided into signal and idler beam and then exits the OPO through the signal or idler port. The parametric process can be controlled by adjusting the crystal temperature, the cavity length and the Lyot filter position enabling a tuning range of 680 nm to 1000 nm.

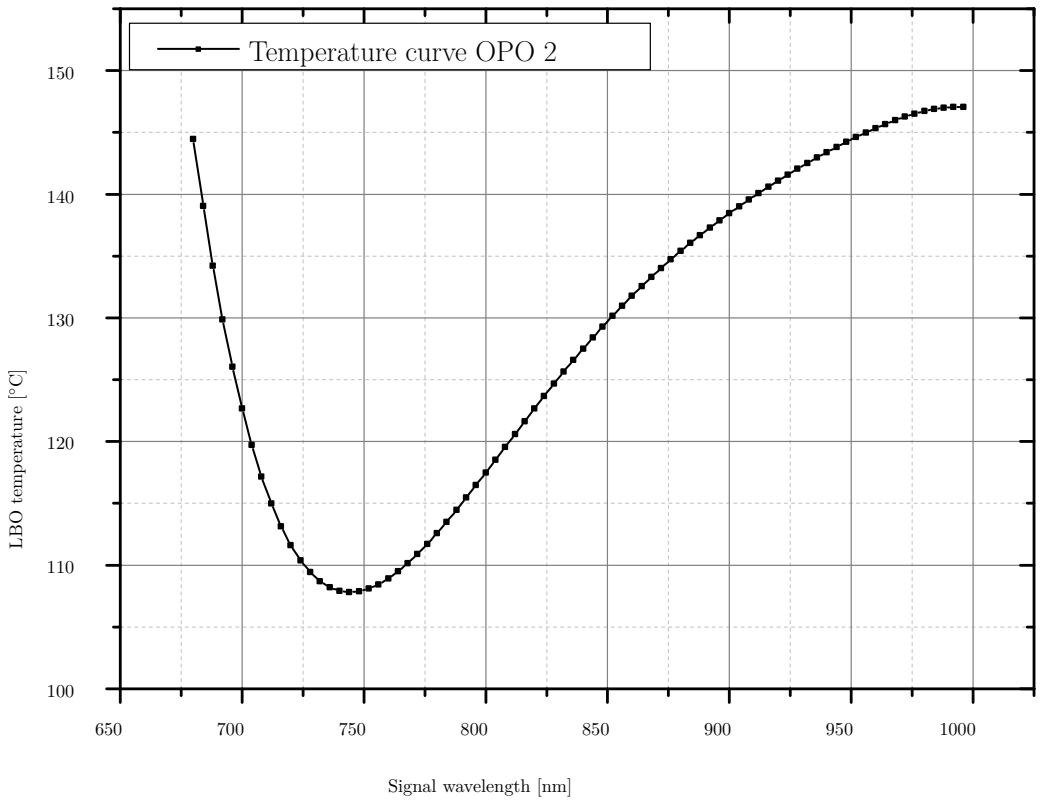

Figure 3.5: **Relation between temperature and wavelength**
The figure demonstrates the relation between the OPO's crystal temperature and the signal wavelength. For a certain temperature, the crystal provides two wavelength windows that can be utilized for generating a signal. By tuning the cavity length and the Lyot filter, the wavelength can be selected. Each OPO crystal has a unique temperature curve. As it can be seen, this curve plays an important role in maintaining a stable operation of the OPO (see section 4.4.2).

is not in operation, the crystal temperature is kept at $100\,°C$ to avoid entry of water which would lead to a reduced OPO efficiency. For each wavelength, there is a specific temperature that supports the chosen wavelength. Figure 3.5 illustrates the relation of wavelength and temperature. The tuning bandwidth of the signal wavelength goes from 690 nm to 980 nm and from 1150 nm to 2200 nm in the case of signal and idler, respectively. However, for one temperature, there are two possible signal wavelengths that can be selected by adjusting the cavity length and the Lyot filter. At a specific temperature, the crystal produces photons in a range of 6-10 nm. To address only a single Raman resonance, the width needs to be reduced by a Lyot filter and a polarizer. Each round trip, the Lyot filter reduces the spectral width of the photons passing the polarizer until finally, in the steady state operation, the spectral width of the exiting photons reaches 0.3 nm. The steady state operation is reached when the photons have traveled a couple of hundred round trips. Accordingly, the OPO is seen as a slow optical element in terms of wavelength tuning. Fast switching can only be employed within the spectral window of the crystal at a specific temperature. Within this range, the Lyot filter can vary the wavelength in the order of nm. However, it turns out that running an OPO with non ideal parameters leads to a change in the pulse length of the pump pulses (see also subsection 4.4.2).

3.3 Acousto-optic modulator

In order to perform stimulated Raman scattering, one of the participating beams has to be modulated. In the presented optical setup, an acousto-optic modulator (AOM) is utilized to modulate the Stokes beam in the MHz regime. The idea of modulating at such a high frequency is that it is well above the shot noise of the laser.

The 1064 nm beam leaving through one of the ports of the laser is attenuated by using a half-wave plate and a polarizing beam splitter. After the polarization has been adjusted by another half-wave plate, the Stokes beam is focused into the AOM. This AOM (MT-200-A0.5-1064, Pegasus Optics) is specially designed to modulate a 1064 nm beam with high efficiency. It consists of a TeO_2 crystal to which a high-frequency piezo transducer is attached. The transducer produces

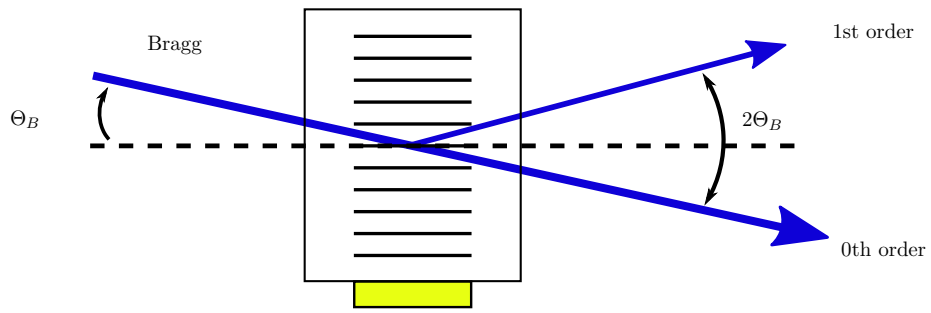

Figure 3.6: **Schematic view of a Bragg cell**
In order for the crystal to act as a Bragg cell, the incoming beam must have an entrance angle of θ_B. The standing wave generated from the high-frequency piezo transducer deflects a portion of the beam by an angle of $2\theta_B$ (1st order). The remaining portion travels unaltered through the crystal (0th order).

a 200 MHz acoustic wave that travels through the crystal. It causes a density modulation so that regions with higher density result in a higher refractive index. Thus, an acoustic grating is generated by the modulation deflecting the beam. The strength of this deflection can be controlled by the strength of the acoustic wave. As it can be seen from figure 3.6, the unaltered beam passes the crystal on the zeroth order while some portion is deflected to the first order. For creating a Bragg cell, the beam has to interact with the acoustic wave at a specific angle (Θ_B). This angle depends on the RF frequency and the incoming wavelength. The grid size of the crystal is 21 μm which leads to a separation angle (2Θ) of 1.32°. The diffraction efficiency depends on how the beam interacts with the acoustic waves and accordingly on the beam size. Here, a 300 mm lens was employed to create a spot size of 0.12 mm inside the AOM leading to a maximum efficiency of 76 %. The amount of diffraction can be adjusted by applying a voltage of 0-5 V to the RF generator. The rise time of the AOM for a 0.12 mm beam is 20 ns enabling a maximum modulation of 50 MHz.
For the application of stimulated Raman scattering it is important that preferably most of the beam is modulated at an exact frequency. However, many modulators exhibit a nonlinearity that produces higher harmonics but may also lead to other frequency contributions. To characterize the diffraction efficiency for a constant voltage, an external power supply (E3620A, Hewlett Packard) was utilized to apply a constant voltage to the RF generator and the beam intensity was measured in the 1st order of diffraction. Figure 3.7 displays the resulting intensity

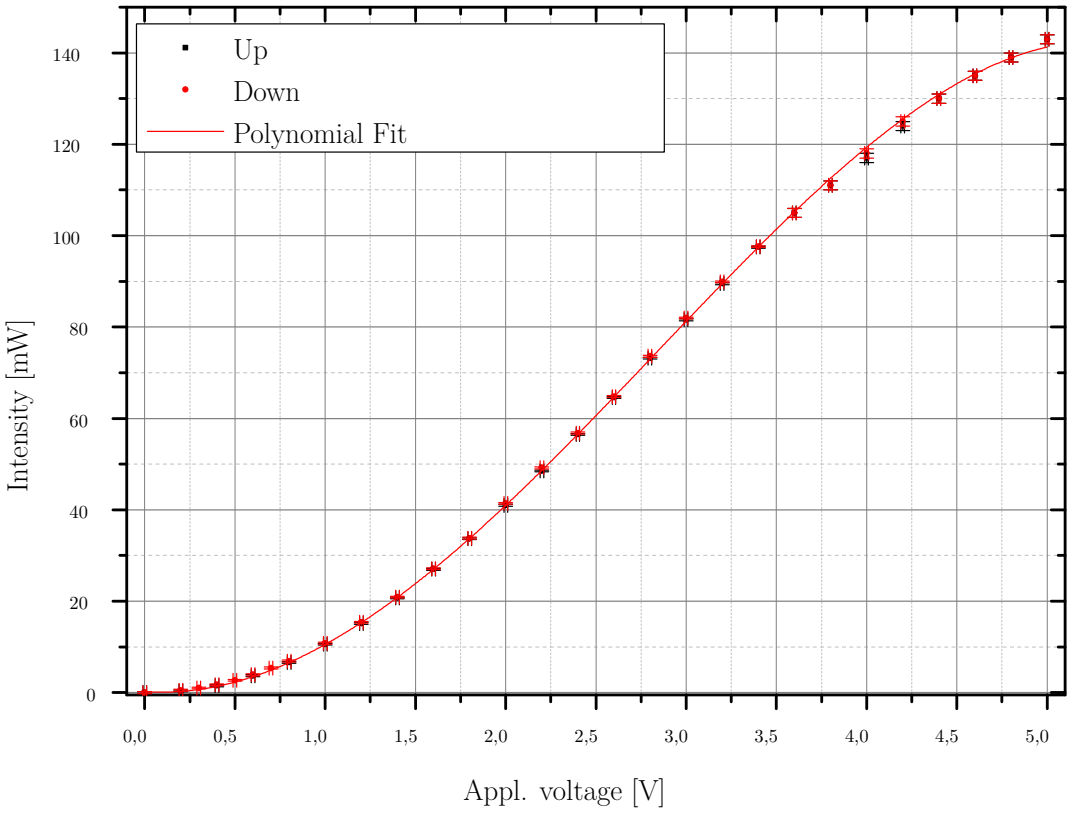

Figure 3.7: **Diffraction profile of the AOM**
The diagram illustrates the relation between the applied voltage and the amount of signal intensity, that is being deflected into the 1st order. In order to achieve the best performance, the frequency translation between the modulated voltage and the signal intensity should yield a linear relation. As it can be seen, that is only the case for a small tuning range between 2 V and 4 V. At the edges of the tuning range of 0 V and 5 V the slope decreases which facilitates the generation of other frequency components. Furthermore, it can be seen that no hysteresis is presented in the tuning curve since the red and black curve coincide.

measurement when tuning the voltage from 0 to 5 V (black dots) and back again (red dots). The ideal case would be that the intensity linearly depends on the applied voltage. Then the frequency that is applied to the RF generator would be directly translated to the intensity of the beam. However, this is only true for the region between 2 V and 4 V. At the edge of the tuning range, the curve converges to 0 or the maximum diffraction intensity. So when the full tuning range is utilized, new frequencies are very likely to be introduced. Since the red and the black dots coincide along the full curve, no hysteresis is present. For the use of the AOM it is therefore important to balance the modulation depth and the generation of new frequencies. For SRS experiments, the newly generated frequencies may not contribute to the demodulated signal.

3.4 Spatio-temporal overlap of excitation laser beams

After generation of the Stokes and the pump beams, the photons have to be delivered to the microscope. In general, there are two possibilities to generate a coherent Raman signal: the wide-field and the collinear approach. When generating a CARS signal utilizing the wide-field arrangement, the challenging part is to satisfy the momentum conservation of the four-wave mixing process and still having a suitable photon density producing nonlinear signals [56][57]. The advantage is the possibility to collect a two dimensional image in one shot. In this thesis, the collinear approach has been utilized in which both the Stokes and the pump beam are overlapped temporally and spatially and then focused on the sample. That way only a small fraction of the sample is illuminated and due to the strong focusing the phase-matching criterion can be neglected since the interaction length is small.

Figure 3.1 shows the current optical setup. Here, delay stages in the beam path of the Stokes and the second pump beam from OPO 2 are used to control the temporal overlap of the beams. Each delay stage is adjusted so that the maximum overlap with the pump beam from OPO 1 is achieved. To spatially overlap the three beams, two dichroic mirrors (DCM) are employed. The first DCM (830LP, Semrock) combines the signal beam of OPO 1 with the one from

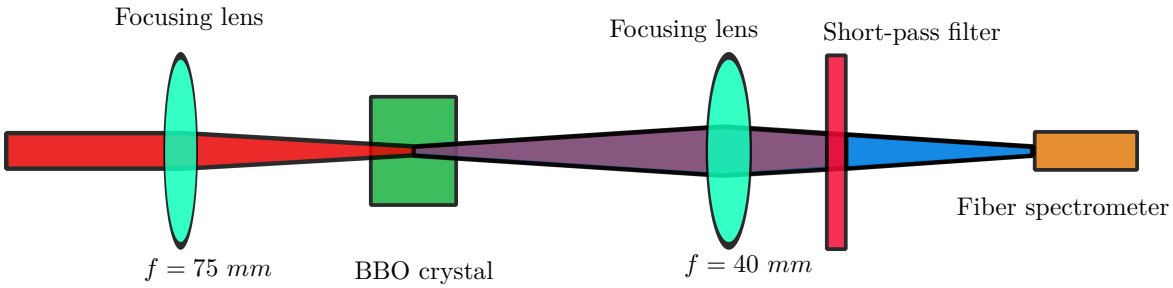

Figure 3.8: **Optimizing the temporal overlap**
In order to check the temporal overlap between all three beams, a BBO crystal is employed. The beams are focused into the BBO crystal and the resulting signals directed into a spectrometer. A short-pass filter blocks the fundamental wavelength in order to prevent the spectrometer from overfilling. The temporal overlap is optimized for each pair of laser beams through optimizing the generated sum-frequency (SFG) signal. Since the SFG signal is blue-shifted to the fundamental beams, it passes the short-pass filter and is coupled into the spectrometer. By changing the incidence angle of the BBO crystal, three SFG signals as well as three SHG signals can be found.

OPO 2. The second DCM (950LP, Semrock) superimposes the two signal beams from the OPO with the fundamental laser at 1064 nm. Here, each beam only transmits a DCM one time at maximum. Thus, the influence of the DCM on the beam shape and phase front is negligible. However, this action reduces the maximum tuning range of the OPOs. OPO 1 can only be tuned between 850 nm and 950 nm and OPO 2 in the range of 800 nm and 825 nm. Accordingly, OPO 1 is mainly used to address deuterated chemical substances with a Raman resonance located at round 2100 cm^{-1}.
In the following, the possible Raman resonances that can be addressed with the combinations of signals and the fundamental laser beam will be calculated. The combination of the fundamental beam and OPO 1 can tune in the range of 1120 cm^{-1} to 2650 cm^{-1}. Combining the OPO 2 with the 1064 nm beam yields a tuning range of 2700 cm^{-1} to 3100 cm^{-1}. Finally, using both OPOs vibrational resonances with wavenumbers ranging from 73 cm^{-1} to 1950 cm^{-1} are achievable. In addition, the first DCM can be replaced by a 50:50 beam splitter in order to freely choose the combination of OPO and fundamental laser by the cost of loosing 50 % of maximum laser power.
Controlling the laser intensity is accomplished by the combination of a half-wave plate and a polarizer. Furthermore, a telescope is present in every beam path.

Each telescope controls the divergence of the beam and matches the diameter to the fundamental laser output.
The correct temporal overlap was adjusted in a two-step action. First, a fast photodiode (DET10*A*, Thorlabs) with a rise time of 1 ns was utilized resulting in an accuracy of 10 cm. Next, the beams are focused into a BBO crystal and then collected and directed into a spectrometer (see figure 3.8). Within the BBO crystal, the sum-frequency signal is being generated under a certain angle. Its signal strength can then be optimized by adjusting the temporal overlap. Further improvement can be achieved by replacing the focusing lens with an air objective lens.

3.5 Control of the galvanometer scanning mirrors

In this subsection I focus on the sample illumination and discuss two different approaches to generate a coherent Raman image from a sample. Since when using a collinear alignment, the pump and Stokes beam need to be focused into the sample, the illuminated sample volume is very small because only if the intensity is very high e.g. when both foci are at the same spot, the coherent Raman signal is generated efficiently. This yields a high spatial resolution but also the need to scan the sample in order to generate a 2D image. In general, one can either move the sample with a motorized stage or scan the beam across the sample. Utilizing a stage has advantages in terms of reproducibility, long integration times and easier signal collection. However, scanning a sample with a stage is not applicable to fast scanning needs. Here, scanning the beam across the sample by a pair of galvanometer scanning mirrors (GCMs) is a good choice. The mirrors are small in their physical dimensions resulting in acquisition times of 2 frames per second. Figure 3.9 illustrates the implementation of the GCMs into the optical setup. The GCMs are located directly in front of the objective lens. The GCMs (6220H, Cambridge Technology) consist of two mirrors with a diameter of 5 mm. Thus, to avoid clipping effects the beam diameter should match the mirrors' accessible area. In the simplest configuration, one of the mirrors resembles the fast scanning axis producing the horizontal lines while the second mirror is comparably slower resulting in the vertical lines. However, also

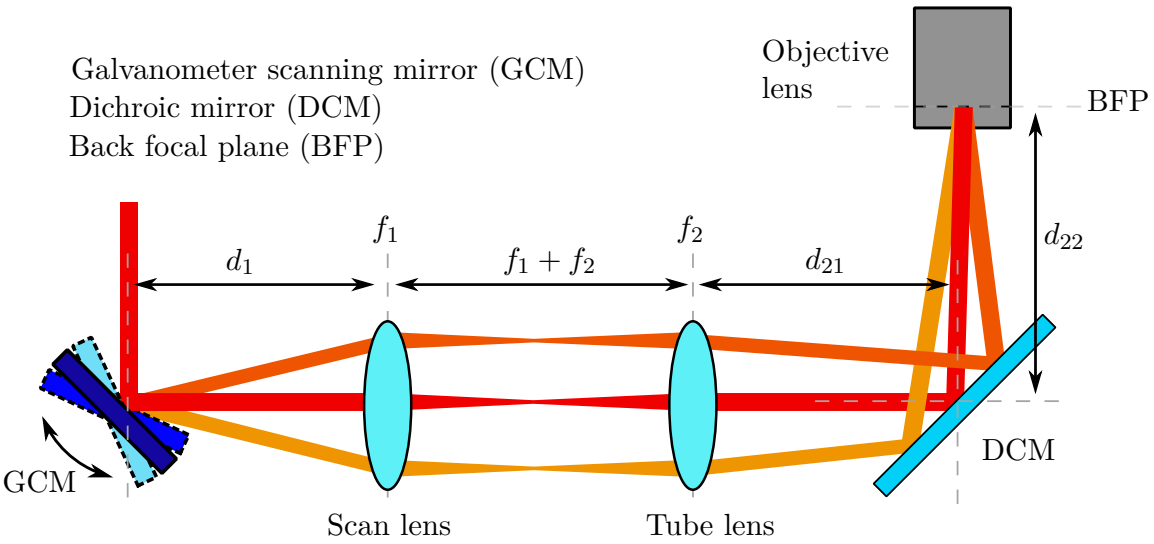

Figure 3.9: **Sketch of the 2D scanning telescope**
Scanning the sample is accomplished by utilizing a pair of galvanometer scanning mirrors (GCMs) in combination with a telescope. The mirror pair produces a pattern that is projected by a telescope onto the back focal plane (BFP) of the objective lens. Due to the limited diameter of the mirrors, the telescope is designed for magnifying the beam in order to match the beam diameter to the diameter of the BFP.

a combined movement of both mirrors is possible.

Adjacent to the GCMs, a telescope is utilized accomplishing two tasks. One task is to project the movement of the scanning mirrors onto the back focal plane of the objective lens. The second is to magnify the beam diameter to match the back focal plane of the objective lens ensuring the best possible focus size. However, when performing SRS imaging, it is crucial not to overfill the back focal plane which would result in artificial signals in the SRS image afterwards. In the presented setup, the telescope is constructed by two lenses (f_1=150 mm and f_2=200 mm). Taking the diameter of the scanning mirrors as the starting value, the final beam diameter at the back focal plane is 6.5 mm, matching the 7 mm back aperture of the objective lens.

In order to correctly align the telescope it is mandatory to exactly know where the back focal plane of an objective lens is located. When focusing a beam in the right position of the objective lens, the resulting beam exiting the objective lens is parallel. Thus varying the focus position until the resulting beam is parallel yields the exact position of the back focal plane of the objective lens. In the case of a 60x water-immersion objective lens (60x UPLANSAPO, Olympus), the ideal

position coincides with the height of the adjustment collar.
For producing a sharp image, it is mandatory to generate a spot on the back focal plane, that is not moving while the scanning mirrors are scanning. Since trying to image the mid position between the mirrors onto the objective lens' plane, small movements are inevitable. The position of the telescope in comparison to the objective lens and the GCMs can be calculated utilizing the following formula.

$$d_1 = \frac{f_1}{f_2}\Big(f_1 + f_2 - \frac{f_1}{f_2} d_{20}\Big) \tag{3.1}$$

f_1 stands for the focal length of the scan lens and f_2 for the focal length of the tube lens. The distance between the two lenses is the combination of both focal lengths. The distance between the GCMs and the scan lens is denoted as d_1. d_{20} is the summation of d_{21} and d_{22} and describes the path of the tube lens to the back focal plane of the objective lens.
Controlling the GCMs is accomplished by utilizing the open-source software ScanImage from Janelia Farm (HHMI) [58]. ScanImage is a MATLAB based program that interacts with the GCMs via a National Instruments PCI card (PCI-6110, National Instruments) and a breakout box (BNC-2110, National Instruments). The PCI card is equipped with two analogue output channels with a maximum sampling rate of 4 MS/s in single channel mode and 2.5 MS/s in dual channel mode. The maximum control voltage is ± 10 V. In addition, it has two counters and eight digital I/O ports with a sampling rate of 5 MS/s. This results in a maximum analogue output resolution of 400 ns. The ready-to-use aspect of ScanImage is a great advantage. It controls the mirrors in a very versatile way and many aspects such as the number of pixels or the integration time that can be chosen to match the user's requirement. It also offers the possibility to zoom into regions of interest and to rotate the beam pattern. Here, if a motorized stage is combined with the scanning mirrors, it has proven quite advantageous to align the pattern along the primary axis of the stage. That way, stitching multiple images to one big image can be accomplished easier. Another advantage of ScanImage is the possibility to extend the functionality of ScanImage by incorporating customized scripts.

3.6 Detection scheme

After the coherent Raman scattering signal is being generated inside the sample, it needs to be detected by a suitable measurement system. In this setup, two versions of a compact photomultiplier tubes (PMTs) (H9565-20, Hamamatsu) are utilized. One with the ordinary internal resistance and one with a lower internal resistance (called H9565-20 MOD). The modified internal resistance results in faster signal acquisitions at the cost of lower overall signal detection. The active area of these PMTs is 8 mm. When using a motorized stage for scanning the sample, the illuminating beam and the signal beam are not moving which makes the detection straight forward. Here, the signal beam describes the coherent Raman signal. However, in the present setup, a pair of GCMs are primarily employed to scan the pump and Stokes beam across the sample. On the one hand it is an elegant way to scan the sample without moving it, but on the other hand it results in a more complex arrangement of the detection path. Due to this scanning movement, the collected coherent Raman signal is scanning across the active area of the PMTs. In order to reduce the scanning area of the signal after collection, a telescope is inserted into the detection path that restricts the scanning area of the signal to the active area of the PMT. Figure 3.10 displays the detection arrangement for the forward and backward scattered Raman signal. In the backward detection path, a suitable beam splitter is implemented directly before the 60x objective lens. The backward scattered signal is reflected and directed to a 120 mm lens that sits in a distance of 240 mm from the objective lens. This lens images the back focal plane onto the active area of a PMT which is located again 240 mm after the lens. Ensuring that the scanning area of the signal matches the diameter of the lens, the back focal plane of the objective lens is imaged on the active area of the PMT canceling out the effect of beam movement.
The forward scattered signal is collected by a second objective lens. Here, a long working distance condenser has been utilized which is mounted on a customized linear stage. If using a high numerical aperture objective lens instead of the condensor, the thickness of the sample is limited to the combined working distance from both objective lenses. Since the sample is scanned with the pair of GCMs, a second telescope has to be implemented in order to reduce the beam movement and to ideally restrict it to the size of the PMT's active area. This is achieved by

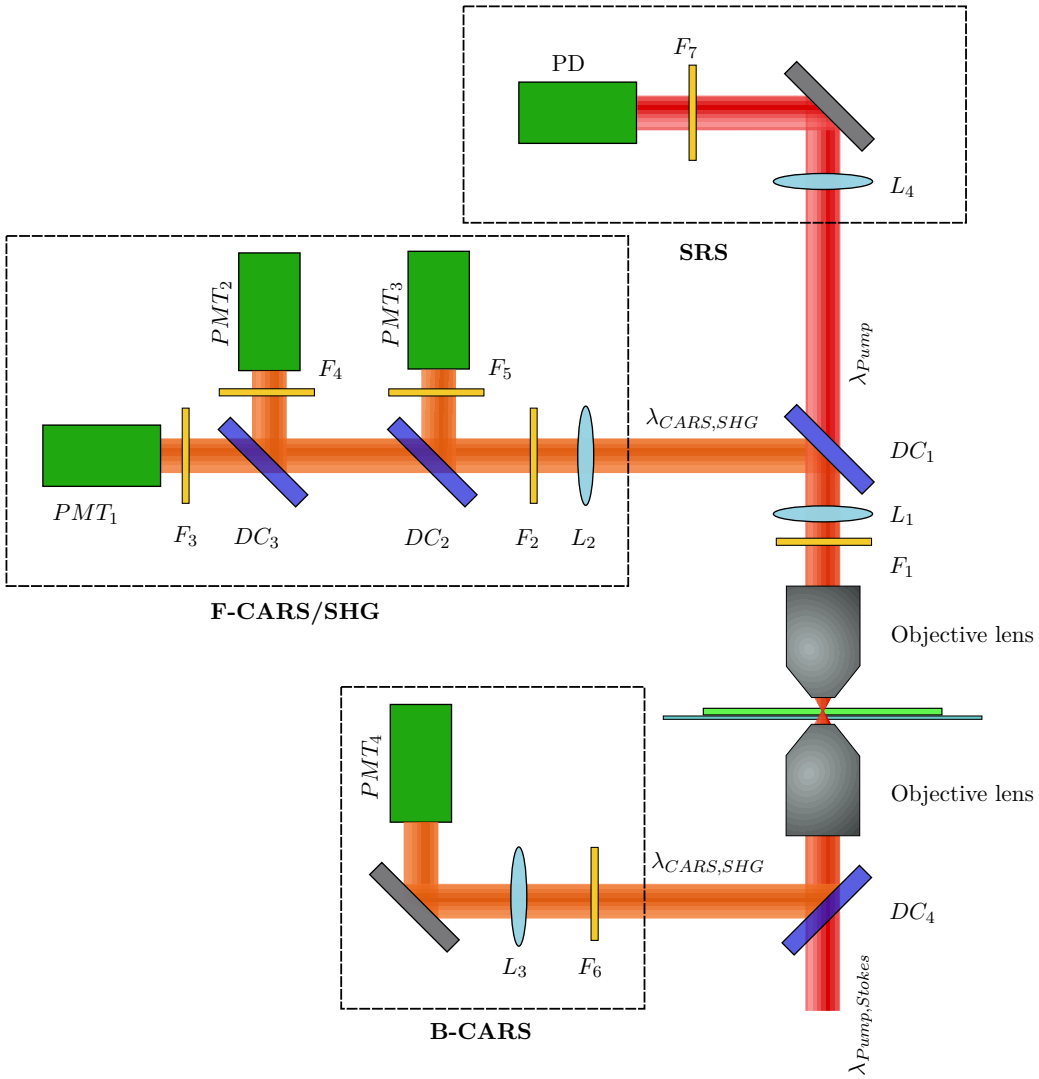

Figure 3.10: **Detection scheme for simultaneous CARS and SRS imaging**
In order to simultaneously detect CARS and SRS images, the following scheme was developed. The incoming pump and Stokes beams are focused into the sample by an objective lens and collected by a second objective lens. Right after the signals are collected, a filter (F_1) is employed to block the Stokes beam. A dichroic mirror (DC_1) splits the pump beam from all blue shifted signals such as SHG and CARS. The pump beam passes the dichroic mirror and is directed towards a photodiode (PD) that is optimized for SRS imaging. A band-pass filter (F_7) ensures that only the pump beam is detected by the photodiode. The blue-shifted signals that are collected by the second objective lens, are reflected from the dichroic mirror and directed towards three individual photomultiplier tubes (PMT). Here, the signal is split up into its spectral components so that each PMT detects a specific signal such as SHG or CARS. In order to detect the newly generated signals that are collected by the first objective lens in the epi direction, a second dichroic mirror (DC_4) is utilized to filter out the blue-shifted components and direct them to a fourth PMT. Since the beam is scanned over the sample in a line per line manner, a telescope is employed in the forward direction in order to minimize beam movements. In the epi direction, the back focal plane is projected on the PMT's photosensitive area by utilizing a single lens.

simply copying the telescope of the illumination path. However, due to spatial restrictions the choice of the lens is changed to keep the overall length small. Furthermore, instead of having only one PMT, a total of three PMTs are utilized to collect all possible generated signals. One PMT is mostly used to detect the CARS signal while the others can be used to collect fluorescence signals or even a second CARS signal. For CARS detection, a narrow band-pass filter is utilized since any possible occurring fluorescence has a comparable low spectral intensity. However, sometimes the fluorescent signals can become so strong that even with these precautions, the fluorescence is still too high. In this case, special detection arrangements have to be met as will be demonstrated in section 4.2 in the case of capturing CARS signals in the presence of strong auto-fluorescence originating from a chloroplast.

An advantage of utilizing a customized microscope body is that it can be specially designed for multimodal imaging. The signal acquisition is not restricted to fluorescent signals, CARS and SHG signals. The system is designed in such a way that it is capable of capturing SRS signals simultaneously to the previously mentioned signals. For this purpose, the microscope is divided into two areas divided by a dichroic mirror. In the first area, any signal that is blue-shifted to the fundamental beams is being reflected at the dichroic mirror and is later detected by a suitable detector. As mentioned before, that applies to SHG signals, CARS and even two-photon fluorescence. The signal that has a similar wavelength to the fundamental photons passes the dichroic mirror and is directed towards a photodetector in the second area. For SRS imaging, a customized photodiode (SRS photodiode, APE Berlin) is utilized to measure the intensity of the pump beam. The photodiode's signal is fed into a lock-in amplifier (LIA) together with the reference signal from the modulator. Finally, the LIA's output is integrated for a certain time and the signal is collected by the NI acquisition card.

Instead of using the commercial photodiode, a customized photodetector was developed. To fully understand the critical points in designing the SRS detection, figure 3.11 depicts the general electronic working principle of the photodetector as well as of the lock-in amplifier. The customized photodetector utilizes a commercial photodiode that is powered by a custom-built power supply. In between, a 1.25 MHz low-pass filter is used to ensure that no noise pick-up in the region

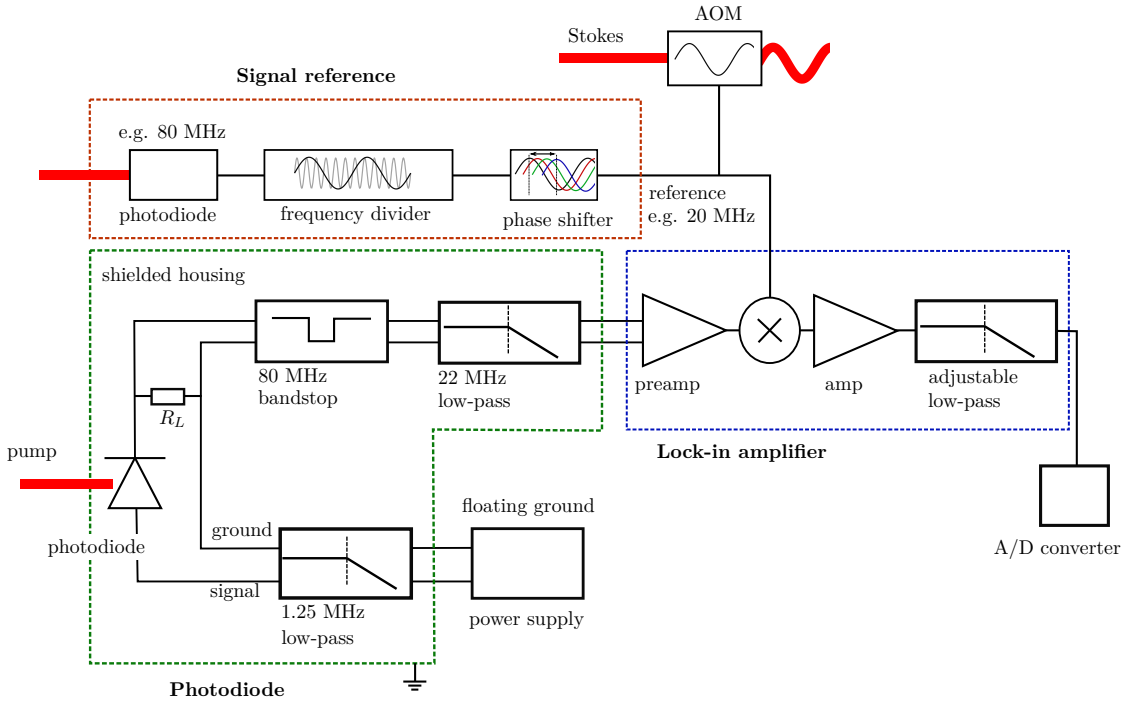

Figure 3.11: **Signal processing for SRS imaging**
The photodiode is powered by a power supply with a floating ground such as a battery. The power passes a 1.25 MHz low-pass filter ensuring that no higher frequency components are coupling in. The photodiode itself detects the modulated pump beam and produces a current. The load resistance R_L is 50 Ω. The signal then passes an 80 MHz band-stop and a 22 MHz low-pass filter. Those two filters make sure that the fundamental signal of the laser e.g. the repetition rate of 80 MHz is efficiently suppressed. Within the lock-in amplifier, the signal is first amplified, demodulated and finally amplified and integrated. The resulting signal is then directed to an A/D converter card. As the reference, the signal of either the pump or the Stokes beam is detected. In order to get a modulation reference of 20 MHz, the fundamental 80 MHz signal is divided by a factor of 4. A phase shifter controls the phase of the reference signal. The signal is then sent to the lock-in amplifier and to the AOM acting as the modulation frequency.

of the modulation frequency e.g. 20 MHz occurs. The power supply is producing a low noise 70 V voltage. Directly after the photodiode, a 50 Ω resistor has been placed for signal generation. Next, because the signal is expected to have a modulation at 20 MHz, the remaining frequencies components have to be filtered out. Hence a 80 MHz band-stop filter is utilized in combination with a 22 MHz low-pass filter. The low-pass filter is designed utilizing a Butterworth configuration, the possible attenuation of the 80 MHz fundamental laser frequency would range between -60 to -80 dB. Since the signal we hope to measure is on the order of 1/1000 of the measured electric intensity, a 19 dB low-noise pre-amplifier is inserted. To further increase the signal intensity a variable gain amplifier is utilized that can enhance the signal up to 44 dB. This amplification stage would not be possible if the fundamental 80 MHz laser frequency would still be present. The signal is then mixed with the reference signal that comes from the modulator. The mixer acts as a cross-correlation. That means, that the frequency parts that have the same frequency as the reference signal are shifted to 0 MHz e.g. DC. The amplifier enhances the signal and the integrator acts as a short-pass filter. Finally, the signal is sent to the acquisition card.
The filtering effect of the lock-in amplifier strongly depends on the signal quality of the reference signal. In order to generate a good quality reference signal that is phase sensitive to the laser, the laser pulse train is captured with a photodiode. The resulting signal is directed to a signal generator to which it is acting as the reference signal. The signal generator provides the 20 MHz sinusoidal waveform that is sent to the AOM and the lock-in amplifier. A critical factor in SRS imaging is the phase relation between the photodiode signal and the signal generator. Tuning the phase relation results in a shift in the supporting points of the 20 MHz waveform that is forced on the fundamental 80 MHz signal. Optimizing these supporting points yields an optimized SRS signal. Alternatively to the 20 MHz modulation of the Stokes beam, the signal generator can be set to 10 MHz or 5 MHz.
When dealing with low signal intensities, the grounding and shielding of the components detecting and guiding the signal is of great importance. The shielding of the components resembles a star shaped configuration. Every shielding is connected to this central point. The ground reference of the SRS signal is defined by

the ground of the PC. That is because neither the power supply of the photodetector or the lock-in amplifier nor the sinusoidal signal generator are connected to the ground. Only through the lock-in amplifier that is directly connected to the DAQ card and to the RS232 port, the instruments are connected to the reference ground of the PC. This prevents the generation of ground loops that could contaminate the sensitive SRS signal through the addition of frequency components.

3.7 Noise reduction approach

Since our laser system exhibits a temporal frequency in the kHz regime, we extended our laser system by three photodiodes that measure the laser intensity of each beam with high temporal resolution (see figure 3.1) [59]. Inserting the photodiodes into the beam path is accomplished by utilizing pellicle beam splitters (8R/92T, Edmund Optics) that only reflect a small portion of the laser beam. In a previous version, a small portion of the laser beam was directed onto the photodiodes by the reflection of a glass coverslip. As it turns out the front and back reflection of the glass produces a wavelength dependent interference that influences the measured intensity. Switching to pellicle beam splitters greatly reduces this effect due to a smaller thickness compared to glass coverslip. The photodiodes consist of a commercial available photodiode (PDB-C613-2, Lunar Optoelectronics) that is powered by a custom-built power supply. By inserting a low-pass filter, the power supply introduces only a very small amount of noise. A data acquisition card (PCIe-6363, National Instruments) detects the photodiodes' signals. This data is used in a post-processing step to compensate the laser noise of up to 100 kHz and to normalize sequentially acquired images to each other. The importance of these photodiodes becomes apparent when acquiring hyperspectral CARS and SRS images (see figure 4.18). Here, the OPO is automatically controlled via our software that optimizes the OPO's output to the maximum intensity. In order to post-process the data, the mean value of the photodiodes is utilized to correct for the wavelength dependent intensity changes.

3.8 Confocal Raman scattering microscope

In the following section, I will give a quick overview on the two Raman scattering setups which have been utilized for various measurements in this thesis. Prior to performing coherent Raman imaging on an unknown sample, it will be characterized by spontaneous Raman scattering spectroscopy. First, I will describe the commercial Raman scattering setup and in the second part we will look closer at the custom-built Raman scattering system. Initially, the custom-built system was part of the doctoral thesis of Ms. Elina Oberlander [60] but was optimized to meet the necessary resolution and performance requirements. The presented systems are utilizing different kind of illumination schemes and laser. Thus, it is possible to switch the excitation wavelength in order to reduce the auto-fluorescence of a sample or exploit a sample's absorption as it is the case in resonance Raman spectroscopy.

3.8.1 Commercial Raman scattering system

The Raman scattering microscope that utilizes an up-right configuration for Raman signal collection is a commercial system (Labram Aramis, Horiba Jobin Yvon). A sketch of the system is displayed in figure 3.12. It utilizes two cw laser sources, a 632 nm Helium Neon (HeNe) laser and a diode-pumped solid-state (DPSS) laser that operates at 473 nm. The maximum intensity is 13 mW and 25 mW for the HeNe and the DPSS laser respectively. The overall optical layout resembles a confocal Raman scattering microscope. A motorized mirror can be used to select the suitable laser source. A shutter, that is connected to the software and to the microscope's enclosure, controls the laser output. To adjust the power output, neutral density filters can be used to reduce the intensity. The light is then reflected from an interference filter and directed to the objective lens. Here, the system typically operates with either a 10x, a 50x or a 100x objective lens. The generated Raman signal is then collected with the same objective lens and passes the interference filter. A lens focuses the signal on an iris. A telescope matches the divergence to the f-number of the spectrometer. The signal is directed towards a grating that diffracts the signal into its spectral components

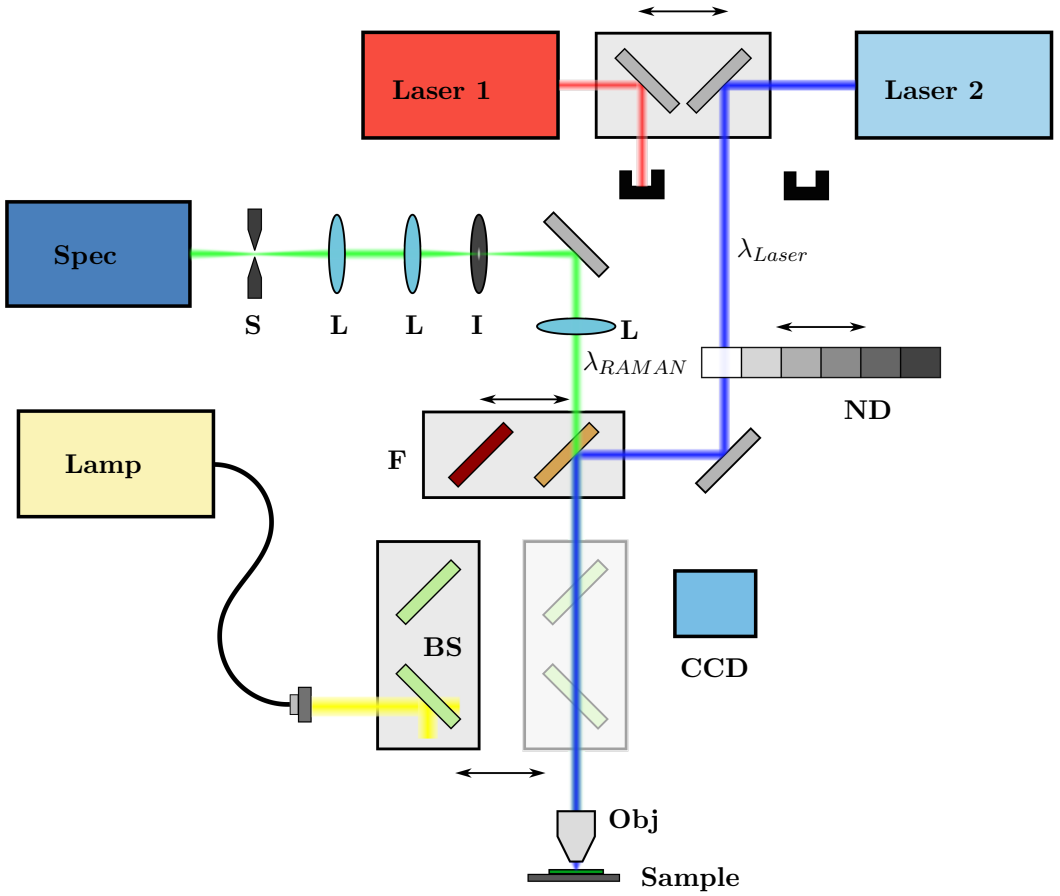

Figure 3.12: **Scheme of a commercial Raman scattering microscope**
The sketch shows a simplified view of a commercial Raman scattering microscope. The system is equipped with two lasers that can be selected via the software by moving a stage back and forth. The laser then passes a selectable neutral density filter that can adjust the laser power. The beam is then reflected from a steep Raman filter (F) and focussed onto the sample by an objective lens. The generated Raman signal is then collected with the same objective lens and passes the Raman filter. The signal is then focused by a lens (L) on an adjustable pinhole (I) and a slit (S) before it is coupled into the spectrometer. In addition, the system offers the use of a whitelight source e.g. a lamp to be coupled in via a fiber. Selected by the software, a stage is moved into the light path so that the light from the lamp is directed on the sample and the reflected light can be detected by a built-in CCD camera (adapted from [61]).

which are imaged with a CCD camera. The spectrometer is equipped with four different gratings with the following line numbers: 300 l/mm, 600 l/mm, 1200 l/mm and 1800 l/mm.
Orientating on the sample is accomplished by a light source e.g. a lamp and a second CCD camera that can be moved into the light path when needed. The light is guided into the microscope by a fiber and is coupled into the beam path by a couple of beam splitters. The light that is reflected from the sample or the surface passes the mirror pair and is directed onto the CCD.
For calibration, the build-in calibration program is being used which utilizes the distinct Raman peak of silicon and the Rayleigh signal to calibrate itself. The calibration has been repeated a couple of times until the subsequent calibration differs minimally from the previous. Through this procedure, a reproducibility of 4 cm^{-1} can be achieved.

3.8.2 Custom-built Raman scattering system

The custom-built Raman scattering system that will be presented in the following has two modes of light illumination. One type of illumination is an inverted confocal microscope in which the sample is illuminated from below. The second method also utilizes the epi illumination but from the side of the sample. Compared to the commercial system, the spectroscopy system is easier to handle and can be extended easier. When it comes to the analysis of chemical components that have an even distribution but might be sensitive to light or even should be kept at a certain temperature, this epi illumination from the side is superior to the two other approaches.

Figure 3.13 displays the inverted confocal Raman scattering system utilizing a 785 nm diode laser with a maximum output power of 200 mW. The laser output is directed through a Faraday rotator that ensures that no reflected light damages the laser diode. For efficient fiber coupling the beam diameter is expanded. The telescope consists of a defocusing lens and a focusing lens and expands the beam by a factor of 6.25. Utilizing a 10x objective lens, the beam is coupled into a singlemode high-power fiber. The use of a singlemode fiber has the advantage that the mode profile of the pump beam is predominantly TEM_{00}. However, the high energy density within the fiber can lead to stimulated Raman contributions from

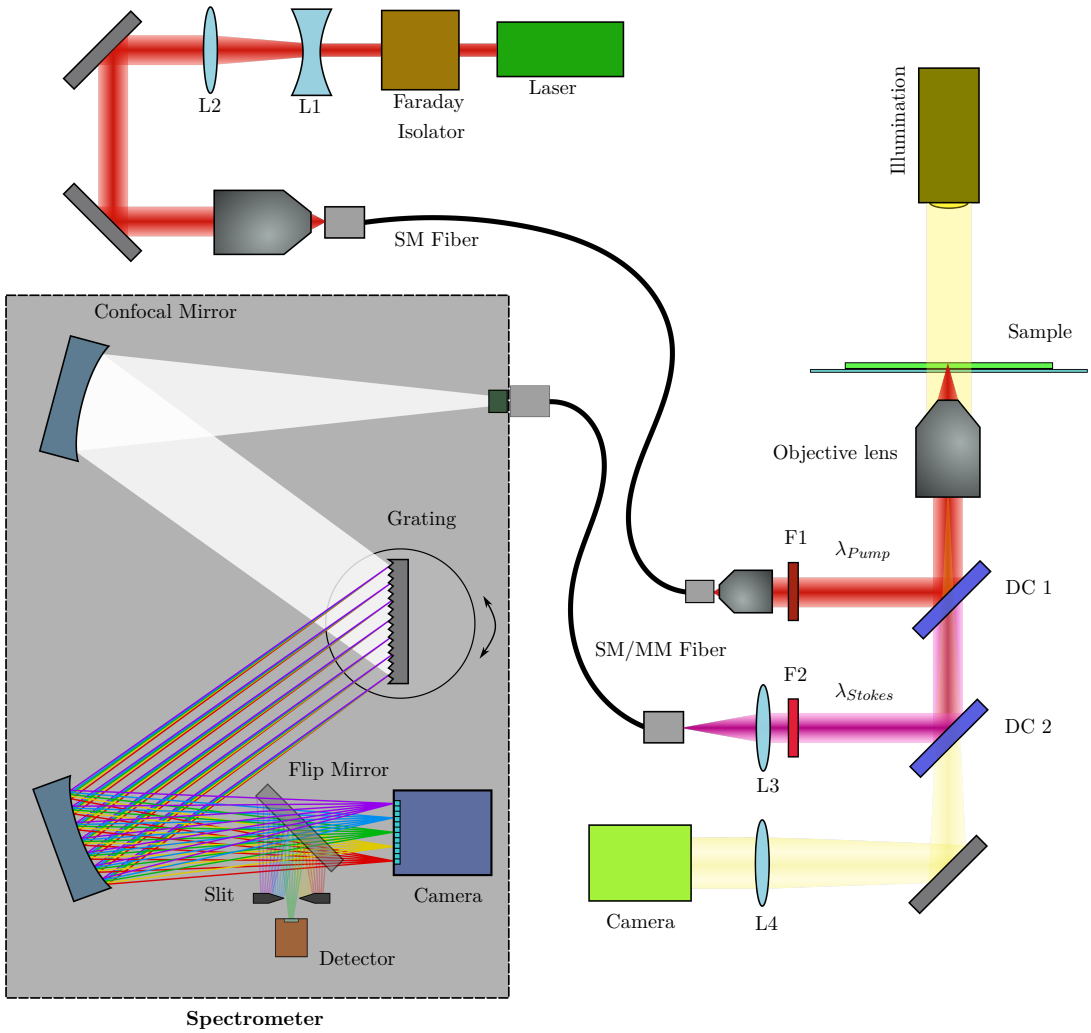

Figure 3.13: **Custom-built inverted Raman scattering microscope**
The Raman scattering microscope is equipped with a 785 nm laser. The laser beam passes a Faraday isolator and is expanded with a telescope. In order to provide perfect focusing conditions, the beam is coupled into a high-power singlemode fiber. The outcoupled beam is then reflected from a dichroic mirror and focused into the sample with an objective lens. The generated Raman signal is collected with the same objective lens and passes the first dichroic mirror. The second dichroic mirror is a 90:10 mirror, that reflects the major part of the signal towards a multimode fiber. The multimode fiber guides the signal to the spectrometer. The spectrometer, consisting of two confocal mirrors and a grating disperses the signal into its spectral components and directs it on a camera. A flip mirror can be utilized in order to allow fast intensity measurements of a small spectral window that can be selected with an adjustable slit. A Köhler illumination source is located above the sample. The light that passes the 90:10 beam splitter is collected by a CCD camera generating a microscopic image.

the silica (see also section 2.5). Therefore, a laser-line filter is inserted after the collimator. The beam is then reflected from the dichroic mirror and directed to the objective lens that focuses the beam into the sample. The generated Raman signal is then again collected by the same objective lens. Since the Raman signal is red-shifted it passes the dichroic mirror. After being reflected from a 90:10 beam splitter, the beam is focused by a 100 mm lens into a multimode fiber. The multimode fiber guides the signal into the spectrometer ensuring that the signal incoupling is stable.
The spectrometer is a Czerny-Turner spectrograph (Acton SP-2300i) and is equipped with three reflection gratings (resolution : blaze wavelength: 300 l/mm : 500 nm , 300 l/mm : 750 nm and 600 l/mm : 1000 nm). Figure 3.13 depicts the layout of such a spectrometer. Since the beam is divergent when leaving the fiber, the confocal mirror parallelizes the signal and directs it on the grating. The grating diffracts the signal into its spectral components along the horizontal axis. The diffracted beam is then reflected from the second confocal mirror and directed on the CCD camera (Newton DU 920P BR-DD, Andor). The camera leverages a deep-depletion detector that offers higher quantum efficiencies in the infra-red region. Because the spectrometer's f number is f/4, the utilized multimode fiber should have a matching NA ensuring that the signal is not over- or underfilling the grating. Underfilling the grating would lead to a decreased spectral resolution and overfilling results in a loss of signal intensity. Furthermore, the choice of the multimode fiber for incoupling into the spectrometer has two impacts. One is that the diameter of the fiber limits the resolution of the spectrometer since a smaller aperture in the beginning results in finer structures on the camera. The second is that the combination of incoupling lens and fiber diameter limits the confocal resolution of the Raman setup.
In addition, a white light source and a CCD camera are added to the inverted microscope. Typically, the white light source that operates in the Köhler illumination scheme is set above the sample so that the CCD camera can see the transmitted light. For that purpose, the 90:10 beam splitter is built into the setup so that 10% of the light is being directed towards the camera.
The other type of epi illumination is the side illumination of the sample (figure 3.14). Here, a low NA objective lens with a long working distance is employed to

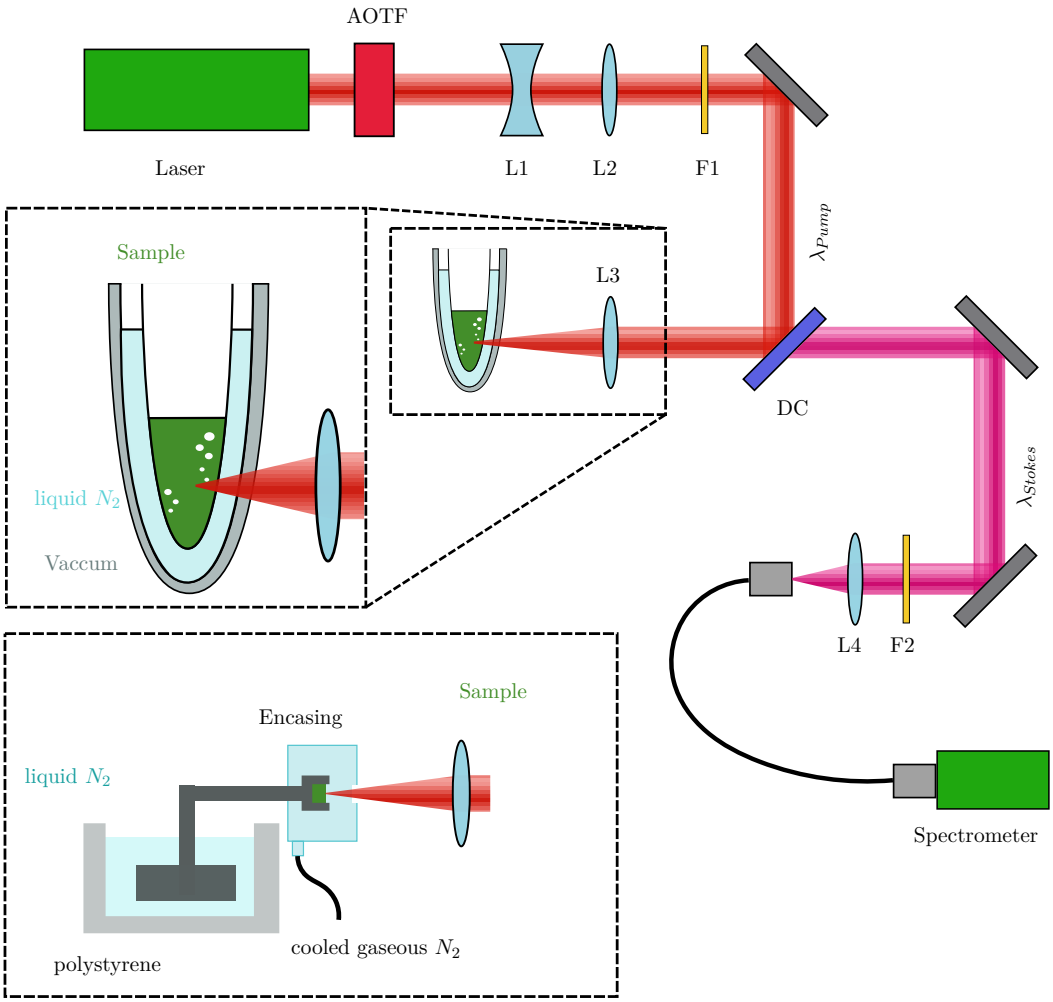

Figure 3.14: **Raman scattering microscope in the side illumination scheme**
The side illumination Raman scattering system is utilizing an Ar:Kr laser as the pump laser. The wavelength can be selected with an AOTF. The beam is then expanded and filtered so that only the desired wavelength is directed to the dichroic mirror that reflects the beam towards the sample. A lens e.g. 100 mm is focusing the pump beam into the sample and collects the Raman signal. The Raman signal then passes the dichroic mirror and, after filtering the beam from any residual pump signal, the beam is coupled into a multimode fiber and analyzed by the spectrometer. The system is capable to penetrate the outer layer of a cold-finger and to collect only the Raman signal of a temperature-sensitive sample. A second sample holder can be employed for analyzing solid temperature-sensitive samples. Here, the sample is cooled by the holder that is immersed in liquid nitrogen. In addition, the sample is protected from the surrounding air by cooled gaseous nitrogen that fills the encasing around the sample preventing the sample from condensation.

focus the pump beam into the sample. This opens up the possibility to efficiently collect Raman signals from samples that need to be stored inside a container e.g. a glass bottle or a cold finger. A cold finger is a Dewar vessel made of glass and filled with liquid nitrogen that supports temperatures down to $-196\,°C$. For generating the Raman signal, an Argon:Krypton (Ar:Kr) laser is being utilized to produce a tunable output. A specific laser line such as 515 nm or 647 nm can be readily selected with an acusto-optic tunable filter (AOTF). The output passes a telescope in order to expand the beam by a factor of 2.8 and a laser-line filter to filter out residual light. The beam is then reflected at a dichroic mirror and is focused with a 10x long working distance objective lens into the sample. Alternatively, a 100 mm lens can be employed. The generated Raman signal is collected by the same objective lens and passes the dichroic mirror. Finally, it is focused into the multimode fiber by a 100 mm lens that leads into the spectrometer, similar to the previously presented inverted microscope. If working with solid cooled samples, a different approach can be used. The sample can be prepared and frozen on the sample holder itself. The holder is then transported to the Raman microscope and immersed in liquid nitrogen in order to cool the sample. Since the air humidity would condensate on the sample very rapidly and thus corrupts the Raman measurement, an encasing was designed. The encasing is filled with cooled gaseous nitrogen that protects the sample from condensation. Cooling is accomplished by using a cooling coil that lies in a vessel filled with liquid nitrogen. In the case of temperature-sensitive materials, a lens with a long working distance should be used in order to disperse the energy on a bigger area and thus keeping the local heat-up rate low. Also the cold stream of nitrogen leads to condensation on the lens if it would be too close to the opening.
For daily operation, the system is tested with toluene, a standard chemical substance that offers various Raman resonances between 800 cm^{-1} and 2000 cm^{-1}. The camera is typically operated at around $-90\,°C$ in order to reduce the dark current. The toluene spectrum is used in a post-processing step as calibration of the spectrometer's x-axis. The intensity of the original spectrum remains unchanged since only the location and not the peak ratios are of interest in the following Raman experiments. For calibrating the peak intensity, the transmission and quantum efficiencies of the various components such as the grating or the

camera have to be accounted for. Furthermore, when performing the calibration, also the peak intensities need to undergo a Jacobian transformation in order to satisfy the energy conservation.

4 Experimental Results

In this chapter I will present the experimental studies that have been conducted on the presented microscope. In the beginning I will give a short overview about the prior characterization of a sample by spontaneous Raman scattering spectroscopy. The main aspects for acquiring high resolution Raman spectra such as the influence of the camera and the choice of substrate will be highlighted and discussed. In the next section I will present the analysis of the lipid metabolism of oleaginous microalgae under nitrogen starvation. The study will showcase the flexibility in signal generation and acquisition of the custom-built microscope when dealing with strong background signals. The ability of multimodal imaging will be demonstrated when I will present an approach to study stem cell differentiation with label-free imaging techniques. Subsequently, I will show the system's capabilities when acquiring hyperspectral data sets. The section is subdivided into five subsections. The first of these subsections will emphasize the reproducible collection of hyperspectral data sets. The second subsection will deal with the computational analysis of these data sets. The final three subsections will showcase the hyperspectral data collection and its computational analysis within three distinct projects. Finally in the last section, an alternative laser source based on fiber laser technology will be presented. In combination with the custom-built laser scanning microscope it is representing a powerful tool for imaging samples with CARS and SRS simultaneously.

4.1 Characterization of the spontaneous Raman scattering microscope

The following section will highlight some technical aspects that have a severe influence on the shape and the quality of the Raman spectrum. Finally, I will

give a quick outlook on temperature sensitive spontaneous Raman spectroscopy that is conducted at low temperatures. In the current version of the custom-built inverted Raman microscope (see also figure 3.13), the pump beam is delivered through a high-power singlemode fiber. Introducing a fiber is beneficial since it offers a degree of flexibility as well as improving the beam quality of the pump beam since only the TEM_{00} mode is efficiently supported in the fiber. However, utilizing a fiber has the drawback, that a lot of power is lost when coupling the light into the fiber. Therefore, the laser diode needs to provide a suitable amount of power. Due to the high amount of power that is transported through the fiber, one has to care for non-linear effects occurring in the fiber even though the pump beam is a continuous wave. While the light travels through the fiber, it stimulates the generation of Raman signals originating from the silica core (see also section 2.5). Because the signal travels through the whole fiber, the power of the stimulated Raman signal can be high. Since this signal is already red-shifted, it has to be filtered out by a suitable clean-up filter before focusing the light into the sample. If this Raman signal is allowed to be reflected from the sample, it will pass all filters and will therefore corrupt the Raman signal of the sample.
The Raman signals are collected with a spectrometer that employs a cooled EMCCD camera. Thermo-electric cooling is employed in order to reduce the dark current allowing high-sensitivity measurements. Figure 4.1 illustrates the effect of cooling at different temperatures and with a changed central wavelength. As it can be seen, when the temperature of the sensor is set to $-75°C$, the dark current of the camera is not uniform for all pixels. The structure of the current and the overall level of dark current can be reduced by cooling the camera down to $-90°C$. The previously seen structure of the dark current is reduced and can only be identified as a straight line. In addition the overall amount of dark current is reduced by 19% when cooling at the lowest achievable temperature of the camera. In order to cancel out stray light or other effects that might originate in the spectrometer itself, we turned the grating by a small angle. As it turned out, the structure that is observed for a cooling temperature of $-75°C$ is unchanged. Therefore, this effect is coming from the EMCCD camera itself and has to be considered especially when comparing spectra with different cooling temperatures of the camera.

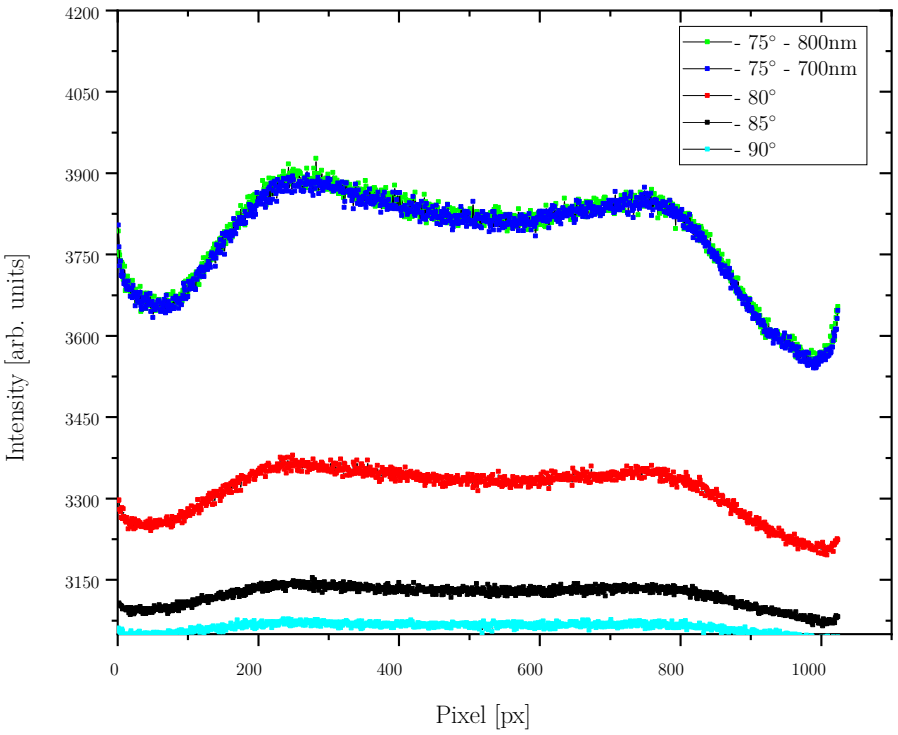

Figure 4.1: **Influence of cooling temperature on camera pixel values**
The figure displays various spectra taken for different cooling temperatures of the EMCCD camera. As it can be seen, the spectrum shows some distinct features that can be reduced by further cooling down the temperature of the chip. Ultimately, the best results are achieved for temperatures at around $-90°$ C.

When starting the Raman scattering system and adjusting the optical system, the Raman collection efficiency is changed from day to day as well as the position of the center wavelength of the spectrometer. Since the grating inside the spectrometer is turned by a stepper motor, the spectrum's absolute position is changed. Therefore, a calibration sample e.g. pure silica or toluene can be utilized for daily operation. Analyzing the Raman spectrum of the calibration sample leads to an efficient calibration of the camera's pixel and allows the detection of small shifts in the Raman spectrum. This precision is necessary when analyzing for example isotope-labeled samples that differ by only a few wavenumbers.
The final aspect for high-sensitivity Raman scattering experiments is the choice of the substrate [62]. The choice of the substrate influences the resolution of the acquisition its contribution to the background signal. The substrate-dependent auto-fluorescence is detected by the optical system along with the Raman signal of the sample. Therefore it is very likely that the Raman signal is hidden on top of the fluorescent signal and thus unresolvable. For near-infrared (NIR) spectroscopy e.g. with a laser wavelength of 785 nm, a substrate consisting of calcium fluoride is the best choice for acquiring high-quality Raman spectra [63]. In order to illustrate the contribution of the substrate to the background of the Raman spectrum, the spectrum of a 2 μm polystyrene bead was captured under two different acquisition conditions. In one case the polystyrene's Raman spectrum was captured directly on a glass coverslip, in the other it was captured in an optical trap. For the optical trap the pump beam was utilized to trap the bead in the focus of the beam away from the coverslip.
Figure 4.2 shows the basic working principle of an optical trap [64]. The bead is floating in a medium, that has a lower refractive index than the bead. This criteria is necessary in order for refraction to occur. To efficiently capture the bead, the focus of the beam should be located above it. Since the bead itself is larger than the wavelength, the principle of an optical trap can be explained utilizing ray optics. Here, at the interface between the bead and the surrounding media refraction takes place introducing a direction change of the beam. As a consequence, a momentum is acting on the bead due to this change. Since the beam is refracted two times, entering and exiting the bead, a beam interacts two times with the bead. Calculating the overall applied momentum on the bead

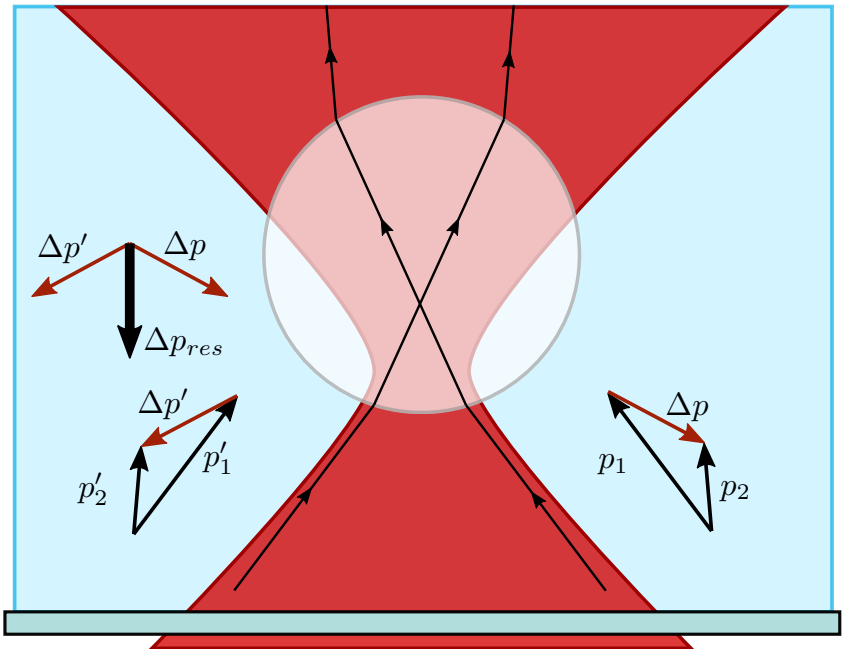

Figure 4.2: **Sketch of an optical trap**
A polystyrene bead floating in distilled water is captured by the focus of a laser beam. Due to the refractive index difference between the bead and the surrounding media e.g. water, the light is refracted twice at the surface of the bead, illustrated by the light rays coming from left and right. Each time the ray is diffracted, there is a change in momentum. For the right beam, the momentum change is displayed by Δp and for the left beam by $\Delta p'$. Calculating the resulting momentum that interacts with the bead results in Δp_{res}. Thus the bead experiences a momentum down towards the focus of the beam.

from one beam results in Δp. In the presented situation, it can be assumed that for every beam coming from the right side there is an identical beam coming from the left so that the direction of the momentum can be calculated to Δp_{res}. As it can be seen, the direction of the momentum draws the bead closer to the focus. This is repeated until no momentum is acting on the bead. When the bead is displaced perpendicular to the beam direction, the bead also experiences a momentum towards the focus of the beam. Thus, the bead is trapped in the focus of the beam and is not moving, which allows for high-resolution Raman spectra to be captured. The resulting Raman spectra from two acquisition conditions are shown in figure 4.3. The left spectrum belongs to the acquisition of the Raman spectrum of the bead which is directly on the glass coverslip. The right

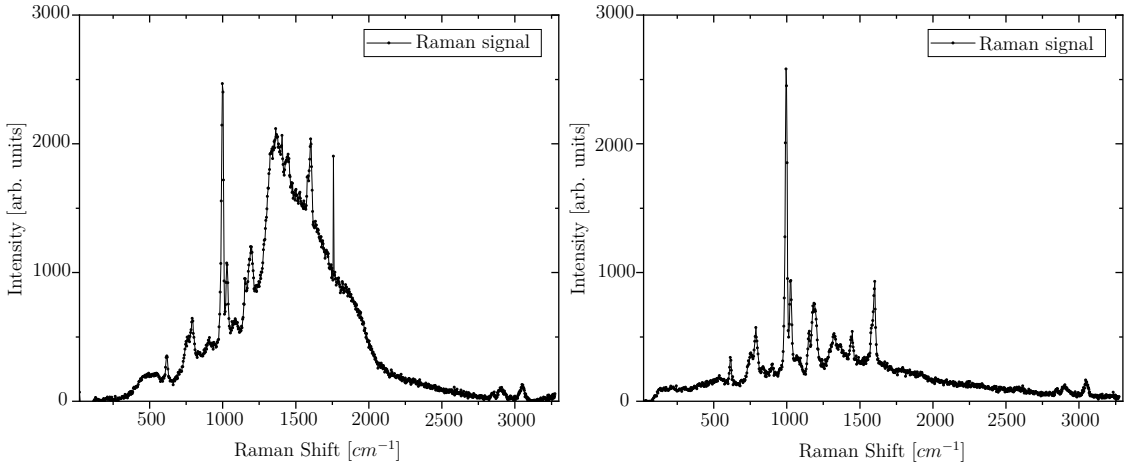

Figure 4.3: **Influence of the substrate's auto-fluoresence**
The figure demonstrates the influence of the substrate's auto-fluorescence. The left image displays the case, when a polystyrene bead is located directly on top of a glass coverslip. The distinct features of the bead are mixed with the broad fluorescence signal. The right image shows the outcome of the bead when trapped within an optical trap and moved away from the glass surface. As it can be seen, the features of the bead's Raman spectrum have a higher signal-to-noise ratio due to the absence of background signals.

spectrum shows the Raman spectrum of the bead that is captured in the optical trap. Comparing the two spectra indicates that the right spectrum is free of any spectral contributions of the substrate. The spectral features of the polystyrene bead are easily identified. In the left spectrum, the substrate produces an irregular background that is mixed with the bead's spectrum. This experiment shows the importance of the samples substrate in terms of background contributions. New promising substrate materials for Raman spectroscopy of nanoparticles are for example self-assembling monolayers (SAMs) that have been cross-linked to carbon nanomembranes (CNMs) and analyzed in a study conducted by Zhang et al. [65]. It was found, that this new material is suitable for Raman spectroscopy due to the absence of any background contribution.

As we have seen, there are a few factors in confocal spontaneous Raman scattering spectroscopy that have an impact on the Raman spectrum of a sample. For high-resolution spontaneous Raman spectroscopy, one has to minimize the background contributions of the optical setup e.g. of the incoming laser or the background signal of the camera as well as the sample preparation in terms of the

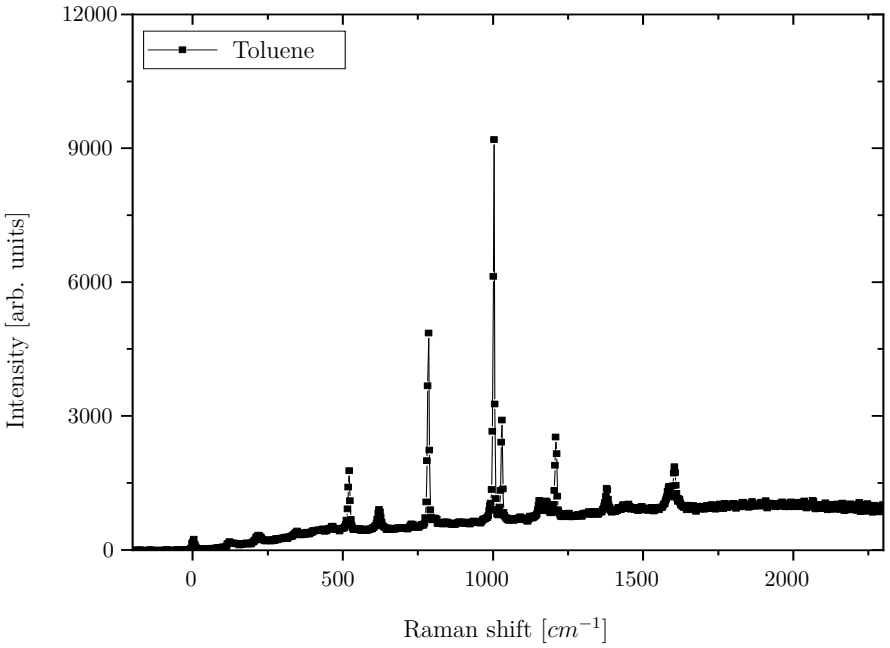

Figure 4.4: **Raman spectrum of toluene within a cold finger**
The figure shows the Raman spectrum of toluene within a cold finger. Note, that the background signal of the surrounding glass is reduced due to the confocal acquisition.

substrate. Furthermore, choosing a suitable objective lens will strongly reduce out-of-focus contributions as well as improving the depth resolution [66][67]. Taking all these factors into account, the presented system is suitable for analyzing molecular systems that require low temperatures as well as for samples that are sealed within a glass container. As an example for a sample located inside a glass container, the Raman spectrum of toluene was captured within a cold finger as it is shown in figure 4.4. Even though the pump beam has to penetrate many layers of glass, the background contribution of it is reduced due to the confocal aperture. Comparing the background with the contribution of a glass coverslip that is multiple times thinner (figure 4.3) demonstrates the influence of the improved signal acquisition. The signal collection efficiency could be optimized further by utilizing adaptive optics that account for spherical distortions introduced by the strongly curved glass. Modifying the wavefront would result in an optimized focus that is not spread out within the sample but still allows for efficient confocal acquisition.

In an ongoing study the Raman spectra of (hydro-)peroxo diferric complexes are

being analyzed. These chemical compounds play an important role in many biological oxygenases [68]. When producing isotopes that possess shifted Raman resonances, these compounds are only stable at very low temperatures around $-100°C$. In order to efficiently generate Raman spectra from the chemical compound, resonance Raman (RR) spectroscopy was exploited as it has been previously demonstrated in [68]. Therefore, the commercial Raman microscope (see section 3.8.1) as well as the custom-built Raman microscope (see section 3.8.2) have been utilized in order to cover the absorption bands around 439 nm, 530 nm and 561 nm.

In the following sections, these Raman microscopes will be utilized for the prior characterization of the sample. Depending on the sample's properties, either the commercial Raman microscope or the custom-built Raman microscope will be employed.

4.2 Intracellular lipid analysis of oleaginous microalgae

4.2.1 Introduction

Throughout the recent decade, microalgae have gained importance in the area of pharmaceuticals and petrochemistry. For instance, oleaginous algae are containing very long-chain $\omega - 3$ polyunsaturated fatty acids which play an important role in human nutrition [69]. The main characteristics of algae are that they thrive in a wide range of environmental conditions e.g. unfavorable conditions for conventional agriculture and, depending on these conditions, can contain a relatively high lipid content [70]. In fact, the amount of neutral lipids in oleaginous algae that plays an important role in the generation of biofuels can range between $20 - 50\%$ of the alga's cellular dry weight (CDW), mainly in the form of triacylglycerol (TAG) [70]. Thus, algae-related research has been focused on increasing the neutral lipids' CDW amount further by altering the alga's metabolism through genetic modification [69][71][72] or by identifying environmental conditions for the alga to efficiently generate lipids [73][74]. It has been found that under certain stress conditions such as nitrogen starvation or excessive light [69], the alga's metabolism is changing drastically accumulating in higher amounts of neutral lipids. Within a short time period, the recycling of the photosynthetic membrane into TAG takes place which are then stored in densely packed lipids [70]. Simultaneously, new TAG molecules are synthesized and accumulated. The intensity of these two processes depends on the environmental conditions and the kind of stress [69][75].

Compared to other methods for a sustainable production of biofuels e.g. soybeans, the efficiency of algae is theoretically 100-fold higher utilizing suitable culture vessels [70]. In general there are two main approaches for efficiently cultivating algae for production: raceway pond systems and photobioreactors (PBRs). PBRs have the advantage of an improved control of the algae culture environment but are consuming more energy than they produce. Raceway pond systems produce biomass at lower cost but these ponds have higher requirements on the location of the installation [75]. The most important goal when utilizing algae as a feedstock for production e.g. biofuels is to find the most efficient conditions

under which the algae is producing the highest amount of sugars and TAGs. This also involves the consideration of upscaling possibility for large-scale production and the stability of the algae culture in such an environment. For example, the alga Chlamydomonas reinhardtii (C.reinhardtii) is a well understood model organism for oil accumulation. Compared to other algae strands, the genome is fully sequenced and its physiology is well understood [69]. However, when upscaling the production to the industrial scale, the culture is not as easy to control as e.g. the algae species Monoraphidium Neglectum (M. Neglectum). M. Neglectum is characterized by a more stable upscaling performance as well as more specific production of TAG making it a promising candidate for industrial production [76].

4.2.2 Project outline

To further optimize the production of biomass, we investigated in our study the intracellular lipid formation in oleaginous microalgae M. Neglectum through the application of CARS and Raman spectroscopy. The results were published in *Scientific Reports* with the title "Label-free in vivo analysis of intracellular lipid droplets in the oleaginous microalga Monoraphidium neglectum by coherent Raman scattering microscopy" [77].

So far, the lipid content of microalgae can be readily analyzed by high-performance liquid chromatography (HPLC) or gas chromatography-mass spectroscopy (GC-MS) measurements. Staining of lipids with Nile Red is also used to access the lipid formation. However, these techniques are often laborious or require a higher amount of biomass. In the case of some algae species, the dye cannot even penetrate the rigid cell wall [78][79]. CARS microscopy and spontaneous Raman spectroscopy are operating without the need for additional contrast agents. Instead, they access the lipid content directly and might become a valuable tool for the analysis of microalgae.

The main obstacle when analyzing algae by optical spectroscopy is the strong fluorescence from the chlorophyll in the chloroplast. To overcome the fluorescence, a modulation scheme was used that has been presented in Garbacik et al. [80]. Here, the group performed in planta analysis with CARS in the presence of strong fluorescence. To efficiently suppress the influence of the fluorescence they

applied a modulation scheme to the Stokes and pump beam and demodulated the generated signal with a lock-in amplifier.
In the presented study, this approach was adapted and modified in order to access the lipid distribution. The project was structured as follows. The algae M. Neglectum were cultivated under the conditions presented in [77] and subjected to nitrogen starvation. It has been reported that nitrogen starvation triggers the formation of lipid inside the algae. On day 0, 1, 2, 4 and 8 we analyzed the lipid content by Raman spectroscopy, CARS imaging and traditional chromatography methods. Here, the lipids were extracted by modified Folch extraction [81], separated into polar and neutral lipids and determined gravimetrically. Finally, the results of the gravimetric analysis were compared to the CARS and Raman scattering data.

4.2.3 Pre-experiments

To demonstrate the successful suppression of the two-photon excited fluorescence from the chlorophyll, first the influence of the pump and Stokes beam on the algae at day 0 was tested. Figure 4.5(a,c) illustrates the generated signal when only the Stokes or the pump beam is present on the sample. While the two-photon signal from the pump beam is rather strong, the signal contribution of the Stokes beam is ten times lower and nearly negligible. In order to get rid of the two-photon excited fluorescence, we therefore slightly modified the approach of Garbacik et al. [80]. Instead of modulating both, the pump and the Stokes beam, only the Stokes beam is modulated. Thus, the detection scheme becomes easier. When modulating the Stokes beam with the AOM at 3 MHz, the contribution of the Stokes beam is slightly smaller due to the reduced mean intensity that naturally comes with the modulation (4.5(b)). The constant contribution of the pump beam that remains unmodulated, is successfully rejected by demodulating the collected signal at 3 MHz (4.5(d)). Signal collection is accomplished by utilizing the modified version of the PMT that offers a greater acquisition bandwidth. This effect is becoming more obvious when comparing the CARS signal without modulating the Stokes beam (figure 4.5(e)) to the CARS signal with the Stokes beam modulation (figure 4.5(f)). Here, we addressed the 2845 cm^{-1} Raman res-

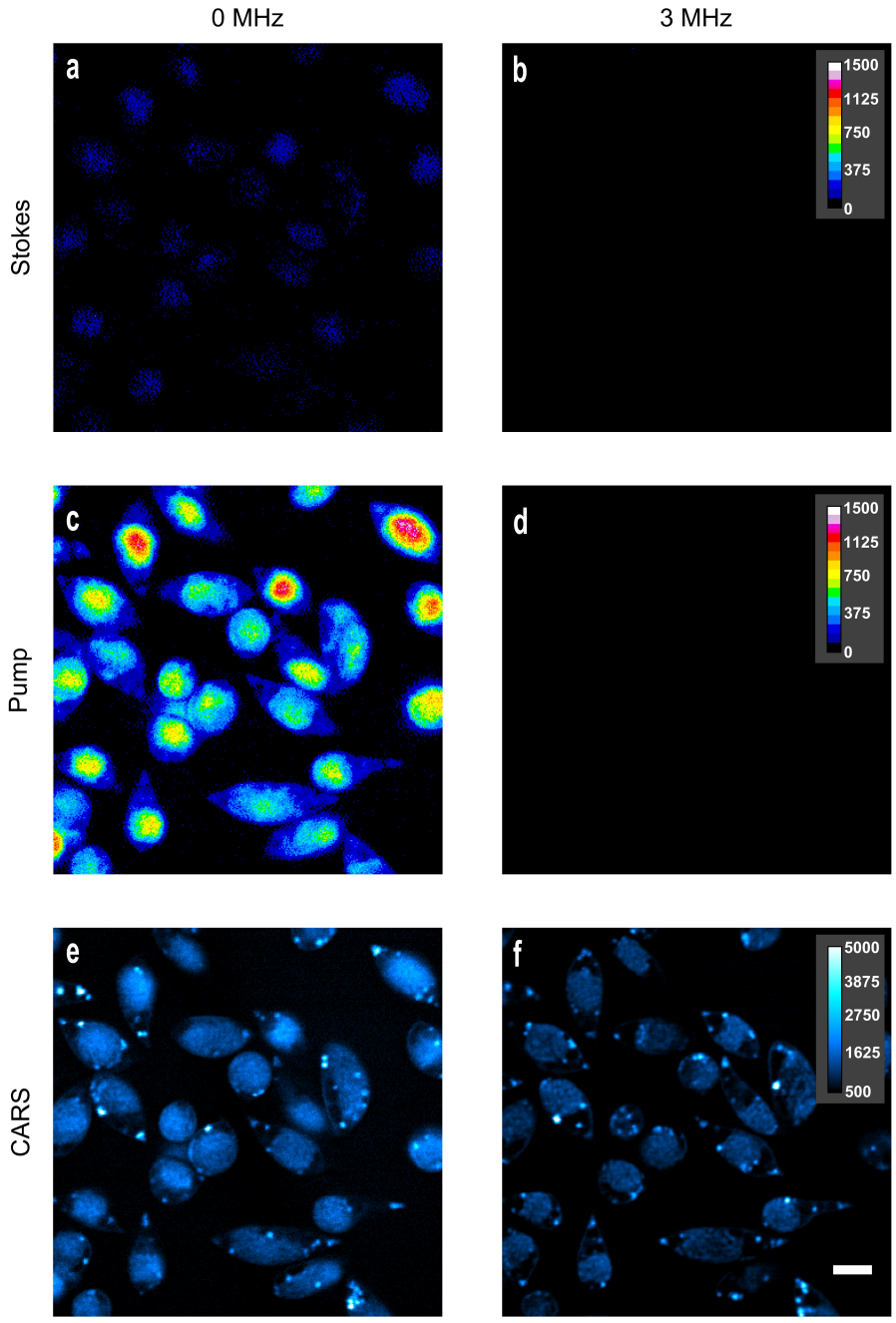

Figure 4.5: **Validation of the modulation approach**
As a validation of the modulation approach we acquired six images with different illumination schemes. The first column demonstrates the signal generation, when the Stokes beam is unmodulated and the second column when it is modulated and the CARS signal is fed into a lock-in amplifier. When only the Stokes beam is present, there is a small signal in the unmodulated case (a) however it nearly vanishes in the modulated case (b). When only the pump beam is present, the static signal (c) is intense due to the excited auto-fluorescence of the algae. The unmodulated signal at 3 MHz is, however, free of this parasitic signal. When finally performing CARS and both beams are present on the sample, the resulting demodulated signal (f) appears dimmer than the static signal (e) resulting in the efficient rejection of the fluorescence. The scale bar depicts 5 μm (images taken from [77]).

onance that is mainly associated with lipids. As it can be seen, the overall signal level inside the cell that is rather unspecific and mainly located directly in the middle of the cell vanishes by applying the modulation scheme.

4.2.4 Analyzing the impact of nitrogen starvation on the formation of lipid droplets

After demonstrating the efficient reduction of the fluorescence signal in the images, we performed CARS measurements on the cells that underwent nitrogen starvation for a certain time period. In total we captured three images per sample position. Besides the CARS image we also collected an image with only the pump beam present on the sample and one with only the modulated Stokes beam. The last two images served as background images that are subsequentially subtracted from the CARS image in order to get rid of any contribution of the fluorescence. Figure 4.6(a-e) shows the CARS images of the algae that underwent the nitrogen starvation for $0, 1, 2, 4$ and 8 days. From these five images it is obvious, that lipid droplets are formed after the first day of starvation. Furthermore, the amount of lipids as well as the individual size is increasing with each day of starvation until on day 8 the cell seems to be completely filled with lipid droplets. Figure 4.6(f) is a merged image visualizing the position of the two-photon fluorescence and the CARS signals. Here, the chloroplast is located in the middle of the cell while the lipid droplets are formed around it. When performing a z-scan this effect is becoming more apparent. Figure 4.6(g) shows three CARS images, each taken at different height positions of the same cell that underwent nitrogen starvation for about 8 days. It can be seen that even on top and on the bottom of the chloroplast lipid droplets are arranged. Therefore, it is necessary to perform 3D CARS microscopy on the algae in order to be able to calculate the whole amount of lipid content within the cell.

The obtained images can now be used to support the impression that the lipid droplets grow in size and that the amount of lipids inside the cell increases with each day of starvation. These findings can then be compared to the results of the traditional gravimetric measurements. Figure 4.7 compares gravimetric results and CARS calculations to each other. Figure 4.7(a) shows the dependence

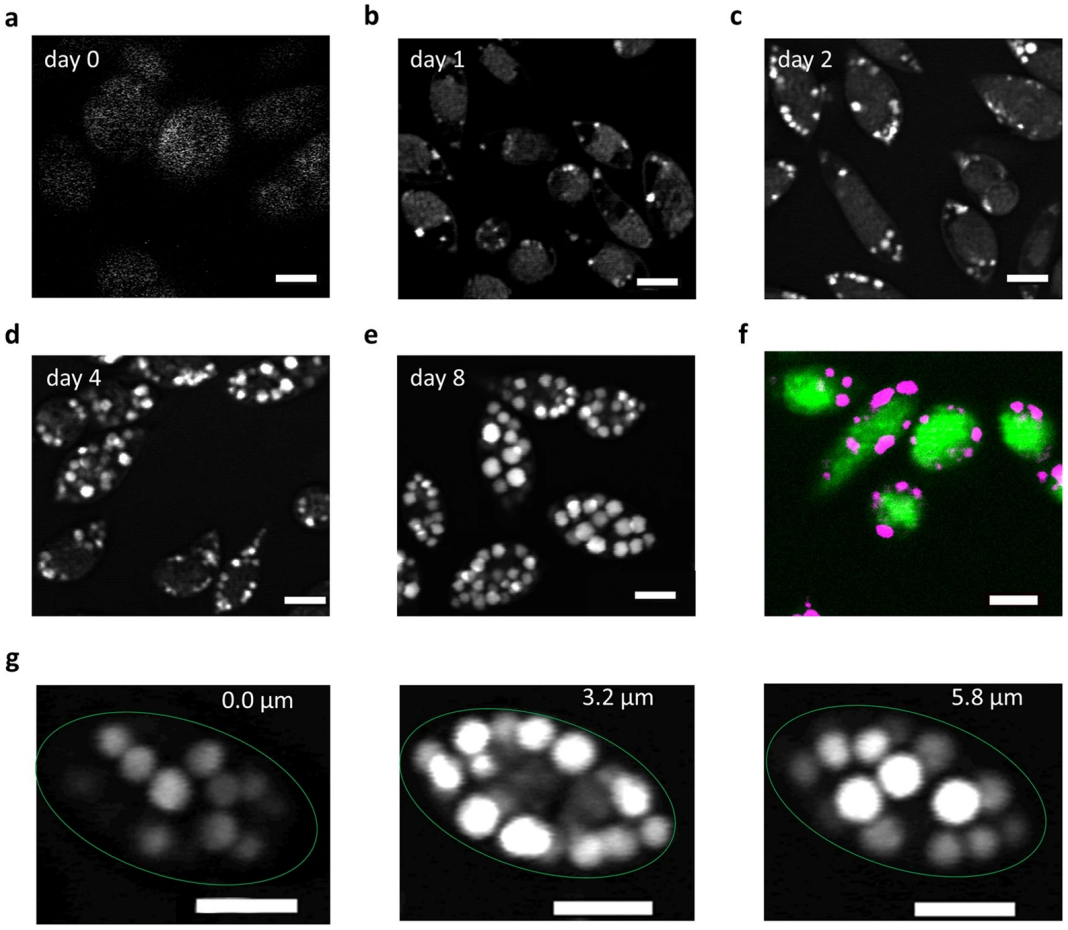

Figure 4.6: **Lipid droplet formation under nitrogen starvation**
The figure shows CARS images of the algae' evolution under nitrogen starvation (a-e) from day 0 to day 8. The targeted Raman resonance has been 2845 cm^{-1} which is mainly associated with lipids. The formation of individual lipid vesicles is clearly visible. Figure (f) displays an overlay image of the CARS signal (magenta) and the fluorescence (green) of the chloroplast. Figure (g) consists of three images displaying a z-stack at different heights from the algae after 8 days of nitrogen starvation. This information can be utilized to calculate the volume of the lipid vesicles. The scale bar is 5 μm (images taken from [77]).

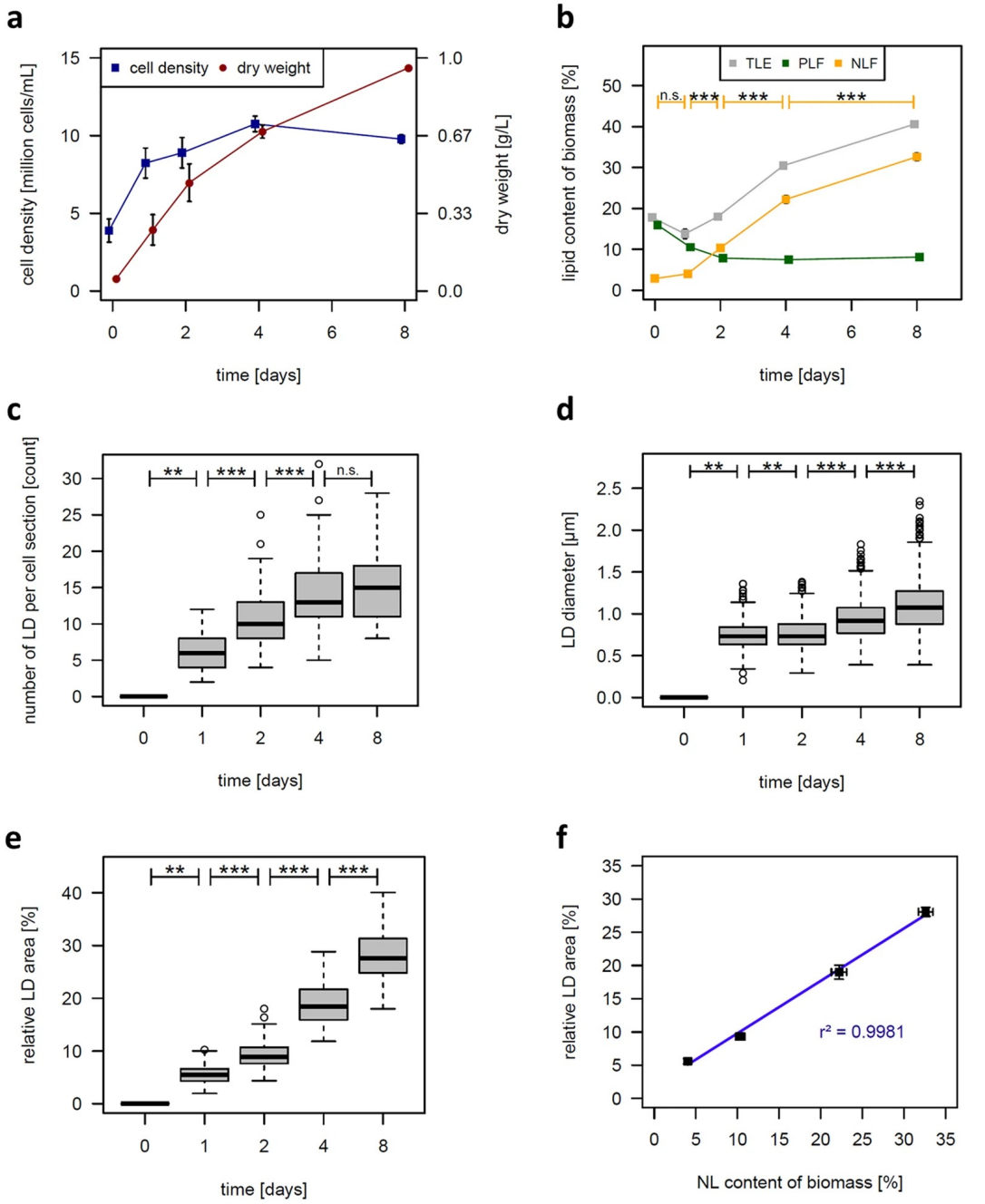

Figure 4.7: **Acquiring growth parameters and lipid accumulation characteristics** Figure (a) displays the cell count (blue) and the dry weight (red) of the algae after eight days of nitrogen starvation. Figure (b) shows the evolution of the total lipid contents (TLE), polar lipid fractions (PLF) and neutral lipid fractions (NLF) determined by gravimetric measurements. The number of lipid vesicles and their diameter of random sections within the algae are shown in figure (c) and (d). Figure (e) displays the relation of lipid area to cell area. Figure (f) is finally the correlation between the relative lipid area compared to the neutral lipid amount of the algae. $n.s. = not\ significant$, $^{*} = p < 0.05$, $^{**} = p < 0.01$, $^{***} = p < 0.001$ (images taken from [77]).

between the cell density and the dry weight in relation to the day of starvation. The cell density as well as the dry weight increases in the first four days. After that the dry weight increases further while the cell density remains constant and even slightly decreases. Figure 4.7(b) demonstrates the results from the gravimetric measurements. Here, the lipids are divided into polar and neutral lipids. The overall lipid amount (TLE) decreases in the first days of starvation but then starts growing until the end of the observation. The fraction of polar lipids (PLF) is decreasing and then from day 4 on remains unchanged while the neutral lipid fraction (NLF) is increasing through the whole eight day period. Figure 4.7(c-e) shows the statistic analysis of the CARS data. In 4.7(c) the number of lipid vesicles in a cell is counted while in 4.7(d) the diameter of the lipids are listed. These two graphs indicate that with each day of starvation the number of lipids as well as their size increases. Calculating the ratio of lipid area per cell area leads to figure 4.7(e). The relative lipid vesicles amount increases with each day of starvation supporting the results from the gravimetric analysis. Putting both analyses in relation to each other results in figure 4.7(f). Here, the straight line marks a clear correlation between both types of analyses.

Since the two dimensional data set is just a cut through the cell and thus a rough approximation of the overall lipid content, a three-dimensional scan of the algae at different time periods of starvation is more accurate. In order to derive the lipid content and the cell volume from the CARS images we assumed that the lipid vesicle can be approximated as a sphere while the cell is resembling an elliptical body (figure 4.8(a)). On the basis of this data we redid the analysis as previously shown for the two dimensional data set. Due to the longer acquisition time of about 30 min per three dimensional image stack, the data set is greatly reduced to just a few lipid droplets (46 - 205). Figure 4.8(b-d) displays the results on the basis of the three dimensional data set. The data shows a similar trend as the two dimensional data set but experiences a higher variance due to the reduced sampling number. We hereby demonstrated that the two- and three-dimensional data sets are showing similarities and can thus be utilized as an approximation of the mean lipid distribution.

Finally, spontaneous Raman spectroscopy was applied to the algae in order to observe the lipid composition in regard to the level of saturation. By carefully

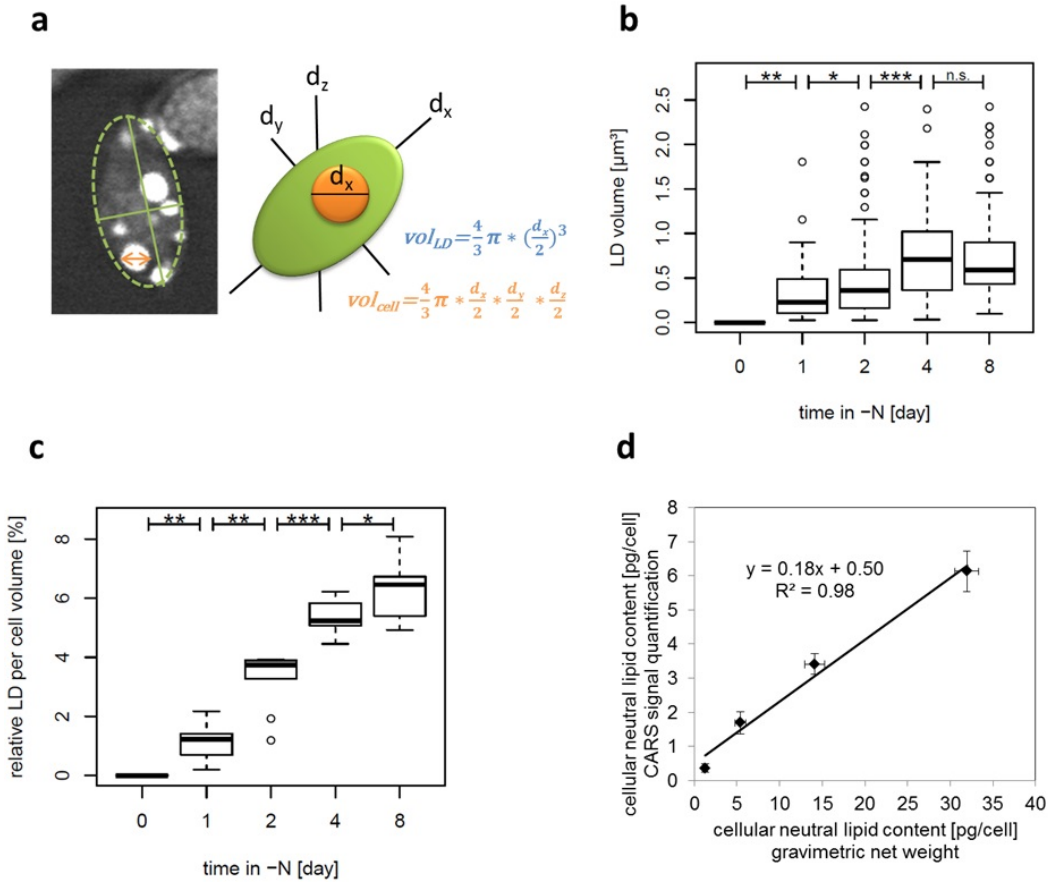

Figure 4.8: **3D cell volume calculation and comparison to gravimetric measurement** For a more exact estimation of the lipid content within the cell, the 3D CARS stacks are evaluated following the approximation in figure (a). Figure (b) shows the overall lipid content in relation to the days of nitrogen starvation. Figure (c) then relates this volume to the overall cell volume. The results are then correlated with the gravimetric measurements (d) (images taken from [77]).

focusing on individual lipid droplets a Raman spectrum was acquired that can be used to identify the level of saturation by calculating the intensity ratio of the Raman resonances at 1660 cm^{-1} and 1442 cm^{-1}. The 1660 cm^{-1} resonance is associated to the $C = C$ vibration and the 1442 cm^{-1} to CH_2 groups. Due to a low signal-to-noise ratio, only the Raman spectra from day 4 and 8 show a suitable signal intensity. We compared these results with the analysis by fatty acid methyl ester analysis (FAME) combined with gas chromatography - mass spectrometry (GC-MS). Figure 4.9 summarizes the results of the three analyses. The Raman data shows that no change in the amount of saturated lipids occurs from day 4 to day 8 of nitrogen starvation. The FAME analysis and the GC-MS measurement support this observation.

4.2.5 Conclusion

In this study we successfully demonstrated the ability to access the lipid distribution of algae in the presence of a strong fluorescent background. The strong fluorescence that was very dominant in the first days of nitrogen starvation was canceled out by applying a modulation scheme on the exciting lasers. As a result we have been able to calculate the ratio of lipids and the overall cell area and referred it to gravimetric measurements of the algae. Here, while being subject to nitrogen starvation, the algae undergoes a change in its lipid metabolism. The composition of intracellular lipids changes in a two-step process. At first, in the early period of nitrogen starvation, polar lipids are metabolized to neutral lipids while the overall lipid content stays the same. In the next phase (day 4 and 8), the algae synthesizes new neutral lipids and thereby increasing the overall lipid content [69]. During this period the amount of polar lipids remains unchanged. The results from Raman spectroscopy and the FAME analysis confirm that the level of unsaturated lipids reaches a steady state. Consequently, the optimal harvesting time point with a high lipid content was found to be after 4 days of nitrogen starvation. Furthermore, we demonstrated the ability to utilize coherent Raman imaging as live monitoring technique for culturing vessels in order to yield the ideal time point for harvesting the algae.

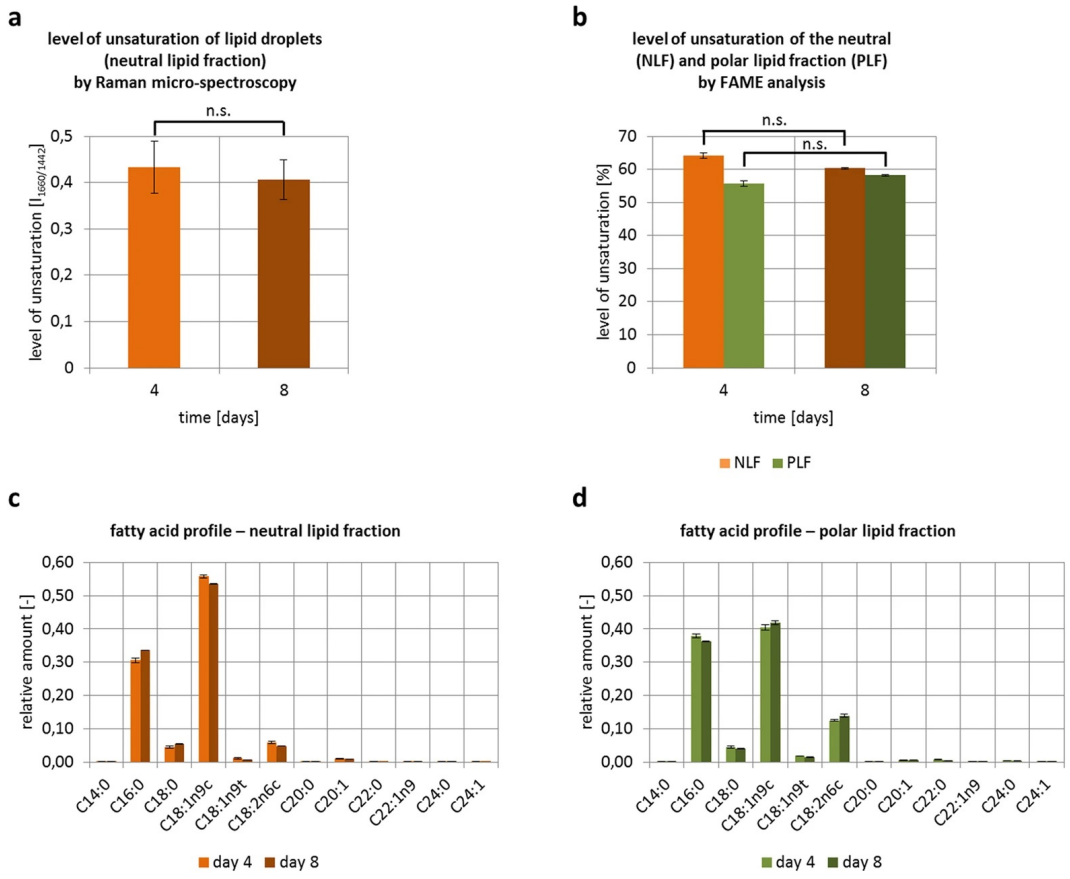

Figure 4.9: **Analysis of lipid composition by spontaneous Raman scattering and FAME**
Figure (a) shows the results of the Raman analysis of individual lipid droplets. The level of unsaturation was determined by calculating the ratio of unsaturated fatty acids with a Raman resonance around 1660 cm^{-1} with the intensity of saturated fatty acids. Figure (b) displays the result of the FAME analysis. Here, the fraction of neutral and polar lipids can be discriminated and set into relation. Both analyses show no significance (n.s.). Finally, the fatty acid profile is shown in (c) and (d) resulting from the FAME and GC-MS analysis (images taken from [77]).

4.3 Following stem cell differentiation with label-free imaging techniques

4.3.1 Introduction

An essential step towards tissue engineering and stem cell therapies is the controlled differentiation of stem cells. To follow such a differentiation most of the established techniques that are currently used are invasive. Either by adding fluorescent dyes such as Alizaring Red S to follow the calcification or by destroying the cells and isolating their DNA such as in reverse transcription-polymerase chain reaction (rt-PCR), the cells are not anymore suitable for any therapeutic application afterwards.
The following study was published in the journal *Scientific Reports* "Label-free nonlinear optical microscopy detects early markers for osteogenic differentiation of human stem cells" [82].
Here, the potential of label-free techniques such as Raman spectroscopy and multimodal imaging in the analysis of stem cell differentiation was investigated. The general project idea was to follow the osteogenic differentiation of inferior turbinate stem cells (ITSCs) for a period of three weeks. Stem cells are generally divided into different types of stem cells according to their differentiation potential. ITSC are adult stem cells and belong to neural crest-derived stem cells that are unable to form germ cells or to develop into every cell type of the three germ layers [83]. Nevertheless, ITSC have gained a broad interest in the area of cell therapy due to their differentiation potential and possibility of autologous therapies [84][85]. These stem cells can efficiently be stimulated to undergo osteogenic differentiation by adding a so called induction medium. More details about the different components inside the medium that induces the differentiation can be found in [86][85].
The project was divided into two steps. In the first step, the chemical induction method was verified through the application of rt-PCR. Simultaneously, we tested the multimodal imaging capabilities. For this purpose, we prepared three samples that will prove the chemical specificity of the CARS setup and the capability of capturing the osteogenic differentiation. In the second step, after successful verification, the cells are cultivated and analyzed on every seventh day by spon-

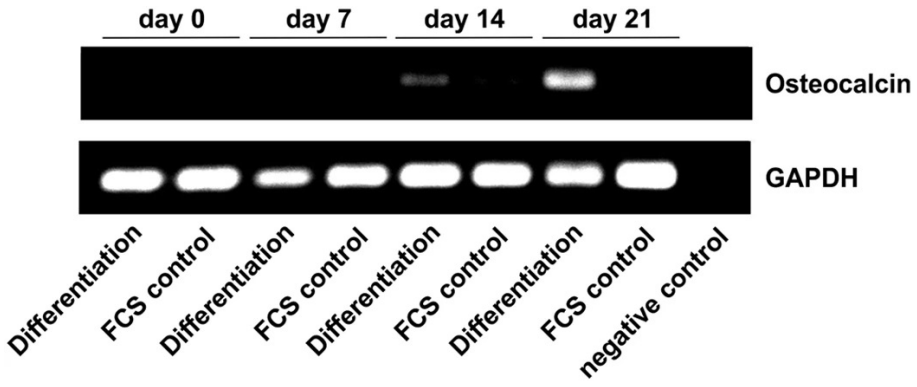

Figure 4.10: **Process verification of successful cell differentiation**
The process of cell differentiation was verified by rt-PCR. After 14 and 21 days, the expression of osteocalcin indicates the successful differentiation of the ITSCs. ITSCs treated only with a medium show no signs of direct osteogenic differentiation. Glyceraldehyde-3-phosphate-Dehydrogenase (GAPDH) is utilized as the reference housekeeping gene (image taken from [82]).

taneous Raman spectroscopy and CARS and SHG imaging.

4.3.2 Pre-experiments

To test the chemically induced osteogenic cell differentiation, cells were cultivated for three weeks. Every week, a rt-PCR was performed to reveal the expression of the characteristic marker osteocalcin. Figure 4.10 shows the rt-PCR of the ITSCs that have been treated with the induction medium (Differentiation) and with fetal calf serum (FCS control). After 14 and 21 days, osteocalcin is expressed by the cells meaning that the ITSC are differentiating. The cells that have only been treated with fetal calf serum show no expression. Glyceraldehyde-3-phosphate-Dehydrogenase (GAPDH) [87] has been utilized as the housekeeping gene due to its stable expression across all cells regardless of their nature [88]. Based on this fact, we expect to be able to observe changes in the morphology of the cells as well as to detect signals from the calcium if it is produced to a certain extend.
To verify the multimodal imaging capabilities, we tested the imaging system on collagen from a mouse tail, murin skull bone and finally on a fragment of human bone material.
In order to have a verified source for collagen fibers, we analyzed a mouse tail by

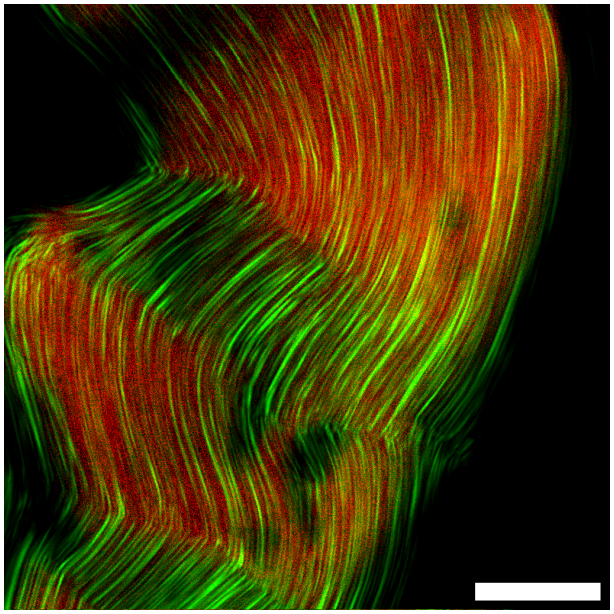

Figure 4.11: **CARS and SHG imaging of a mouse tail**
In order to verify the successful imaging of collagen, a mouse tail was utilized as a reference. The mouse tail is known to be consisting of collagen to a very high degree. The SHG signal originating from highly ordered collagen strands (green) can be easily seen. The CARS signal (red) resembling the Raman resonance around 1662 cm^{-1} belongs to collagen type I as well as lipids and is comparably weak. The scale bar corresponds to 30 μm (image taken from [82]).

means of CARS and SHG imaging. The fibers are closely aligned along the mouse tail forming a characteristic fibrous structure that is known to provide a strong SHG signal [89]. To generate the SHG signal, we utilized the 1064 nm beam with an intensity of 50 mW on the sample. A filter set composed of a 950 SP, 2x 842 SP, and a 514 LP was inserted in front of the photomultiplier to suppress the fundamental beam. In addition, we also collected the CARS signal at 1662 cm^{-1} which is associated with lipids as well as collagen type I. Here, we tuned the pump beam to 904.1 nm and chose the intensity of 16 mW and 8 mW for the pump and Stokes beam respectively. To efficiently collect the CARS signal at around 785 nm, we added a tunable band-pass filter (785/20 nm) to the existing filter stack. Figure 4.11 displays the overlay image of the CARS (red) and SHG signal (green). As it can be seen, the CARS signal is fairly weak compared to the strong SHG signal. The collagen fibers are strongly aligned along the tail and even produce a signal in the absence of the CARS signal. Typically, both signals

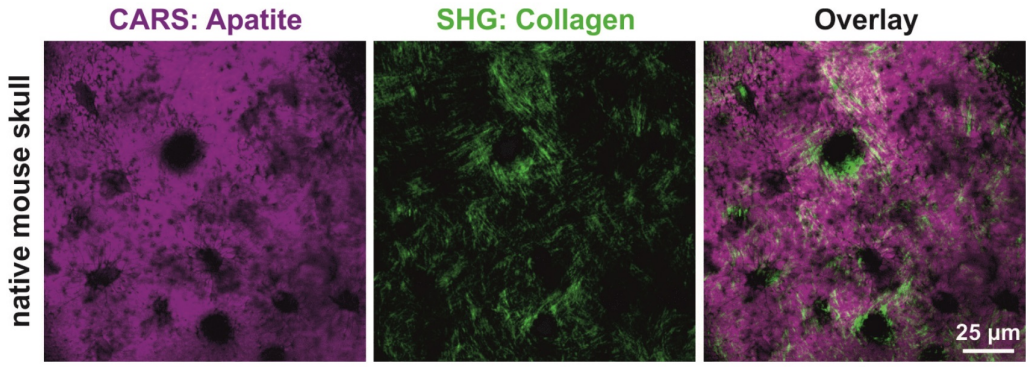

Figure 4.12: **CARS and SHG imaging of a mouse skull**
As a verification for imaging calcium hydroxyapatite, a freshly prepared mouse skull has been imaged. The CARS resonance was chosen to be 959 cm^{-1} corresponding to PO_4^{-3}. As it can be seen, the collagen seems to be forming some kind of structure around the bone material (images taken from [82]).

should coincide in every part of the sample but the most likely explanation is that since the CARS signal is strongly dependent on the incoming polarization, the target molecules are just as strictly aligned as the collagen fibers which results in an undetectably low signal.

In the next step we applied this analysis to a murin skull. Because the skull was freshly extracted, we assumed that the collagen fibers would still be intact. Here, we changed the targeted Raman resonance from 1662 cm^{-1} to the stretching vibration of PO_4^{3-} at 959 cm^{-1} that is present in the calcium hydroxyapatite of the bone. In order to be able to address this resonance, we utilized the signal beams from the OPOs for generating the CARS signal. One OPO was tuned to 860.6 nm and the other to 796.0 nm acting as Stokes and pump beam respectively. The earlier mentioned filter set was changed accordingly (e.g. 785 SP, 775 SP, 514 LP). Again, a tunable band-pass filter was set around the CARS signal wavelength of 740 nm. The power levels were 10 mW for the pump and 6 mW for the Stokes beam. For SHG imaging the Stokes beam's power was set to 40 mW. Figure 4.12 displays the CARS signal from the calcium hydroxyapatite (magenta), the SHG signal from the collagen (green) and an overlay image of the CARS and SHG image. Except for a few areas, the CARS signal from the calcium hydroxyapatite is uniformly distributed whereas the collagen fibers are strongly correlated around the areas with no CARS signal present. As it seems,

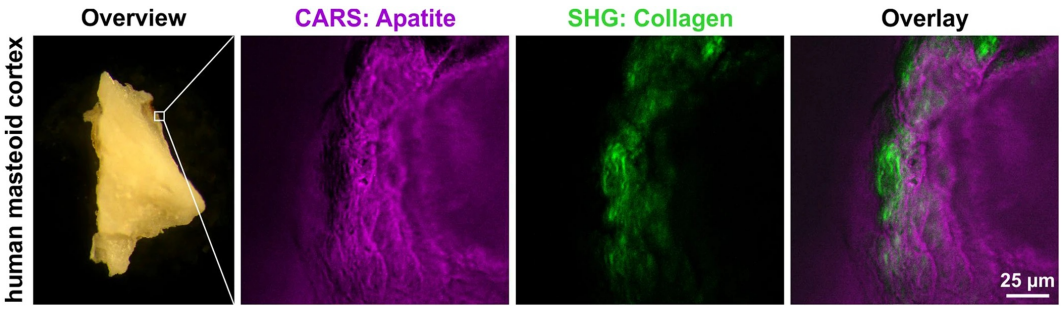

Figure 4.13: **CARS and SHG imaging of human bone material**
As a second verification, human bone material has been utilized in order to generate CARS and SHG images. The CARS signal of the calcium hydroxyapatie is depicted in magenta, the SHG signal of the collagen in green (image taken from [82]).

the collagen forms some kind of supporting layer around the bone material. A possible explanation of the circular holes is that here the cells are located that produce the bone material as well as the collagen.
As the last test sample, we imaged the collagen and calcium hydroxyapatite distribution of a human skull fragment in order to verify our approach for the analysis of human material. Compared to the previous samples, the bone fragment is rather rough and uneven which makes the analysis of the sample challenging since only a small part of the sample can be found to lie in the focus plane. At the edges we did efficiently collect CARS and SHG signals on a bigger area. Figure 4.13 shows an image of the fragment and the associated CARS and SHG images as well as an overlay. The collagen signal seems to be located at the very edge of the sample while the CARS signal is present throughout the whole sample. Just like before, the SHG signal and the CARS signal seem to coincide in most parts in which a SHG signal is efficiently generated. With this result we can state that in case of a cell differentiation and assuming that a suitable amount of material is being produced, we can follow the chemically induced cell differentiation of the ITSCs.

4.3.3 Following cell differentiation of induced ITSCs

Before presenting the experimental results, a small summary about the experimental procedure will be given. Eight wells with ITSCs were prepared. Four of which underwent the forced differentiation process through the application of an

induction medium, the other four were treated with fetal calf serum as it has been the case for the rt-PCR. We followed the differentiation for a period of 3 weeks and analyzed the cells every week. Including the initial day, we had four observation time points. For the analysis an induced and a control sample were fixed by adding 4% paraformaldehyde (PFA) and analyzed in the following sequence. First, we applied spontaneous Raman spectroscopy on certain points of interests, then imaged small regions with CARS microscopy and finally performed Alizarin Red S staining on the cells. That way, the staining doesn't interfere with Raman spectra and CARS measurements since otherwise the dye is very likely to produce some kind of background signal.

The images of the stained ITSCs that were exposed to the induction medium are displayed in figure 4.14 together with the Raman spectra. Here, it can be seen that the cells did undergo an osteogenic differentiation. Alizarin Red S primarily stains calcium accumulations. After 14 days, the staining indicates the first deposits of calcium in the sample. The amount of calcium is then increased further after an additional week. When looking closely at the formation of the cells, it can be seen that the cells arrange themselves around specific regions in a star-shaped manner after day 7. This effect can be exploited when performing spontaneous Raman spectroscopy on the cells. Since the likelihood of having calcium in center position of this star-shaped arrangement is very high, we performed Raman spectroscopy at this position. After 7 days, a peak in the Raman spectrum appears at around 959 cm^{-1} belonging to the stretching mode of PO_4^{3-}. The control samples showed no sign of differentiation (not shown) which is in good accordance to the previously presented rt-PCR result.

When performing CARS imaging on the cells, we also used the star-shaped arrangement of the cells to guide the analysis. Compared to spontaneous Raman spectroscopy, CARS acquires an image highlighting a certain resonance and thus reducing the spatial influence. Just like the verification, we detected the CARS signal at the Raman resonance of 959 cm^{-1} as well as the SHG signal from the collagen. In addition, we acquired the CARS signal at 2845 cm^{-1} which is mainly associated to lipids. This CARS signal serves as proof that we are in the right focal plane where we also expect to detect the CARS signal from calcium hydroxyapatite. Figure 4.15 displays the acquired signals of the control sample.

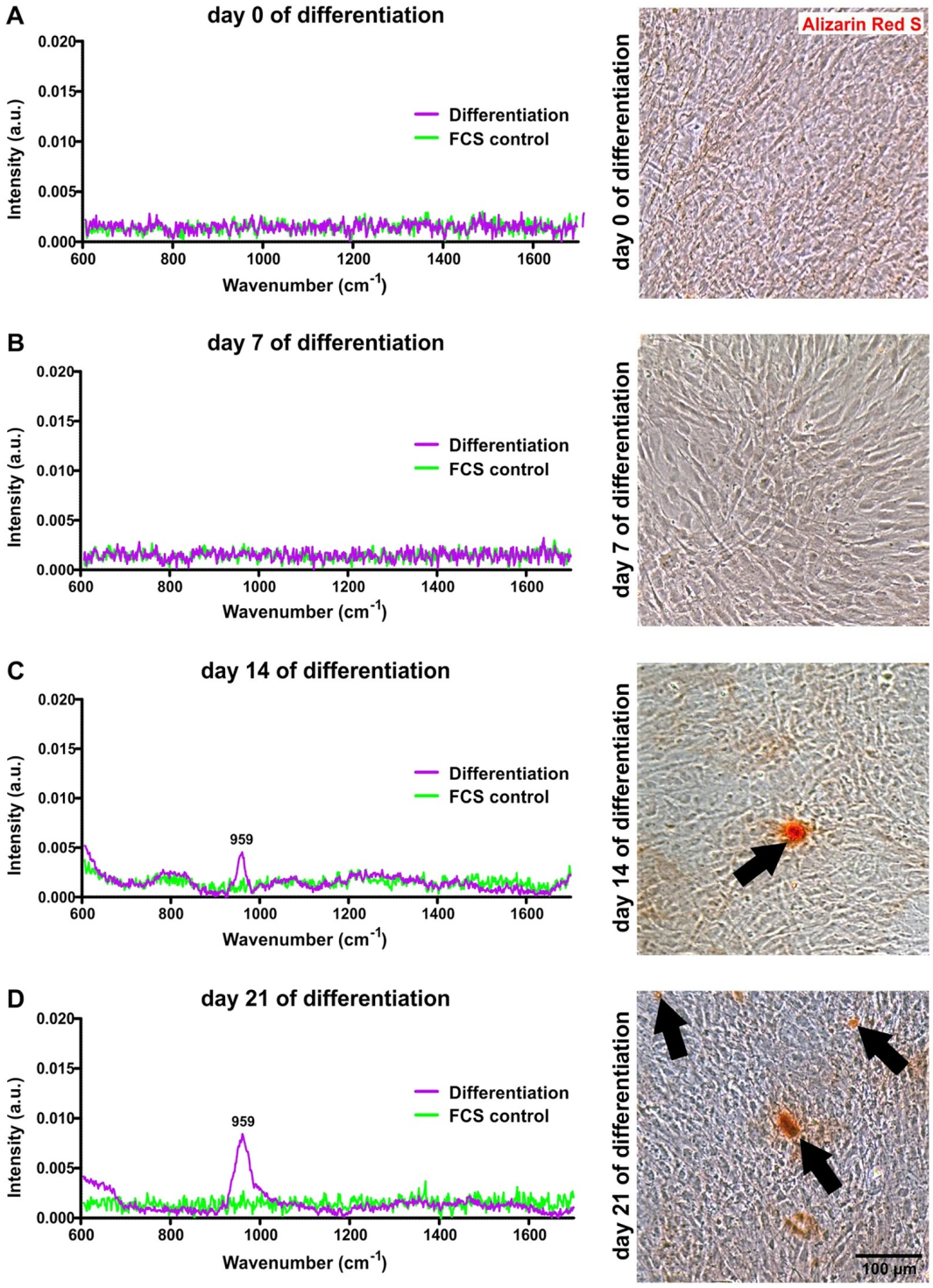

Figure 4.14: **Following cell-differentiation with spontaneous Raman spectroscopy and Alizarin Red S coloring**
On every seventh day of differentiation, spontaneous Raman scattering microspectroscopy and Alizarin Red S coloring was conducted after initialization. Figures (a) and (b) demonstrate that neither of the two techniques indicate successful differentiation in the early observation time points. After 14 days, a small peak at around 959 cm^{-1} appears in the Raman spectrum indicating the presence of calcium hydroxyapatite. Likewise, the staining specifically shows spots with accumulations of calcium. The intensity of these signals is amplified after 21 days (image taken from [82]).

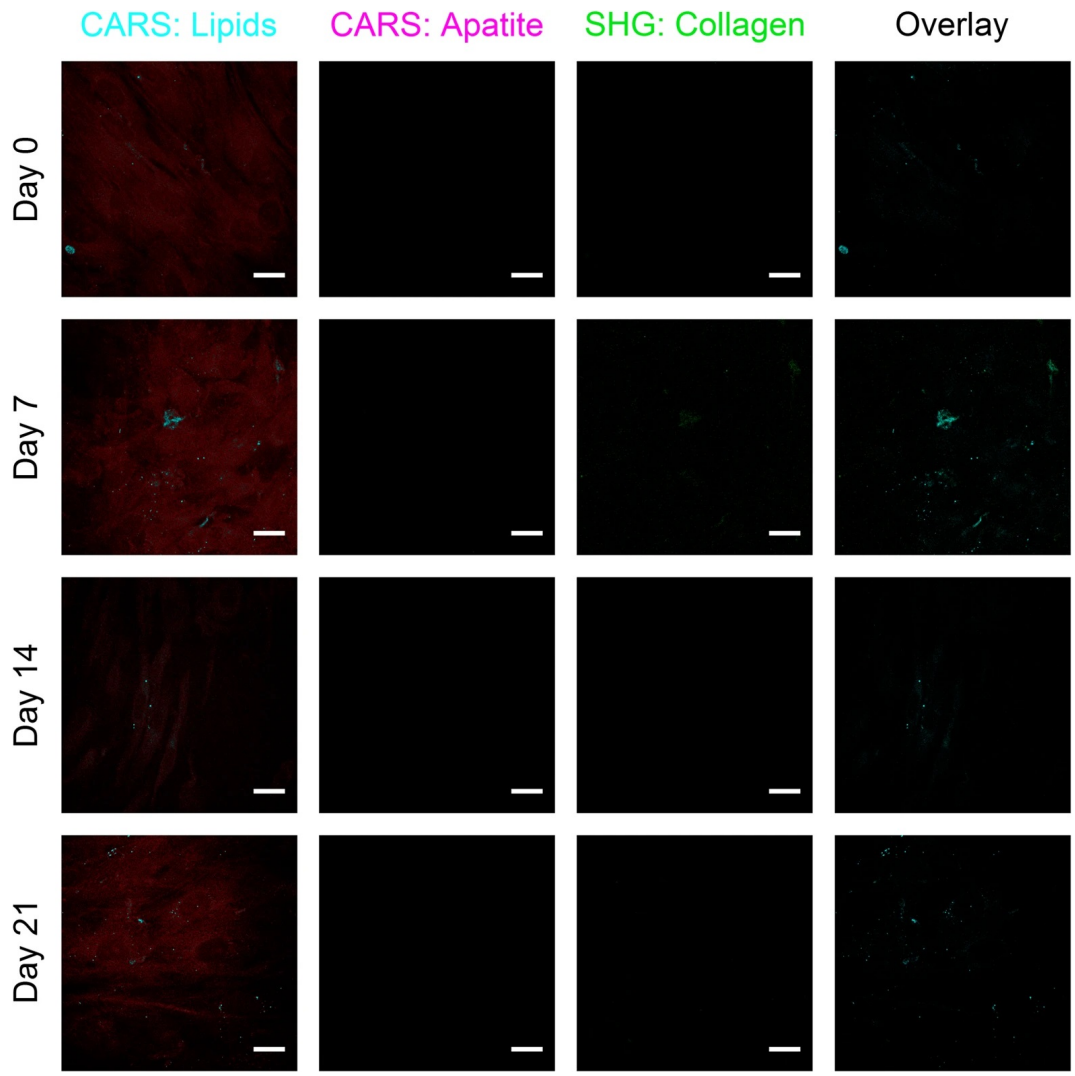

Figure 4.15: **Control samples show no sign of differentiation**
Simultaneous to the analysis with spontaneous Raman microspectroscopy and Alizarin Red S staining, multimodal imaging was conducted on the samples. On every seventh day, images were acquired targeting the 2845 cm^{-1} resonance, the 959 cm^{-1} resonance as well as the SHG signal of collagen. The intensity in the lipid channel was split into two parts: the lower intensity level resembling mainly the non-resonant background providing a light-microscopy-like image and the higher intensity levels indicating the presence of lipids. The scale bar equals 20 μm (images taken from [82]).

In the first column, the CARS signal associated to lipids is depicted. For easier interpretation, we divided the signal level according to its intensity into two color channels. The dark red channel indicates the always-present non-resonant background while in cyan the local lipid accumulations are shown. Thus the dark-red channel is resembling a light-microscopy-like image showing the location of the cells. In the second and third column, the CARS signal from calcium hydroxyapatite and the SHG signal of collagen are displayed respectively. Finally, in the fourth column, an overlay image is created to visualize the distribution of all signals. As it can be seen, the control only provides a contrast at 2845 cm^{-1} but neither a CARS signal at 959 cm^{-1} nor a SHG signal is present. Figure 4.16 demonstrates that after 14 days the induced ITSCs provide a very prominent CARS signal at 959 cm^{-1} that is co-localized with the SHG signal (indicated by the arrow). Similar to the results of spontaneous Raman spectroscopy and Alizarin Red S staining, the images on day 0 and day 7 show no sign of a possible ongoing differentiation. On day 21, the amount of collagen and calcium hydroxyapatite is further increased compared to day 14.

Finally, we collected a three dimensional image of a calcium hydroxyapatite particle that was generated by the induced ITSCs after 21 days. For that purpose we utilized the piezo stage and scanned through the sample by simply varying the focus plane in 1 μm steps. The sample was previously already stained with Alizarin Red S in order to efficiently identify the free calcium sites inside the sample. Since the presence of the staining might corrupt the imaging process so special care has to be taken in the interpretation of the signals. Figure 4.17 shows the three dimensional reconstructed image of the calcium hydroxysapatite. The color coding of the three signals (CARS lipids (blue), CARS calcium hydroxyapatite (magenta) and SHG collagen (green)) is the same as in the previous images. From the top view image one can see that the collagen is oriented around the calcium hydroxyapatite accumulation. The third image, which is rotated by 80°, reveals that even on top of the hydroxyapatite a SHG signal can be detected. This result supports the interpretation, that the collagen structure acts as some kind of supporting material for the calcium hydroxyapatite. Comparing the signal levels around the calcium with the signal levels on the calcium could lead to the guess that also on top there is a thin layer of collagen. This observation is

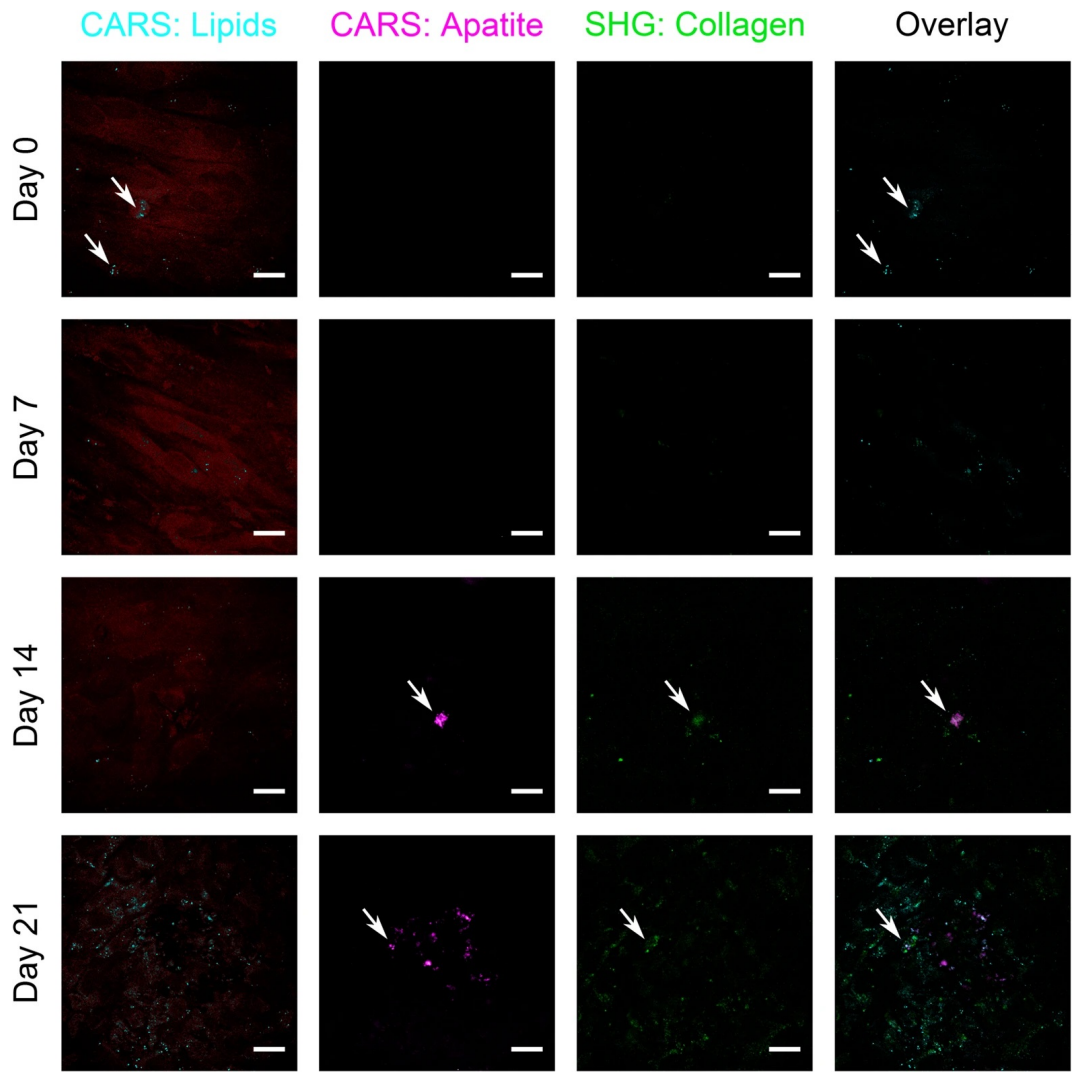

Figure 4.16: **Induced cells show first signs of formation of hydroxyapatite after 14 days.**
The figure is constructed in the same manner as the control experiment shown in figure 4.15. Every seventh day, an experiment was performed imaging the 2845 cm^{-1}, the 959 cm^{-1} resonance as well as capturing the SHG signal from the sample. On day 0, in the absence of any signal from collagen and calcium hydroxyapatite, a CARS signal of lipids was found, indicated by white arrows. After 14 days, the first signal of hydroxyapatite was found. After 21 days, the signal is increased and distributed across the sample. As it can be seen, the gathered signals don't necessarily coincide. The scale bar equals 20 μm (images taken from [82]).

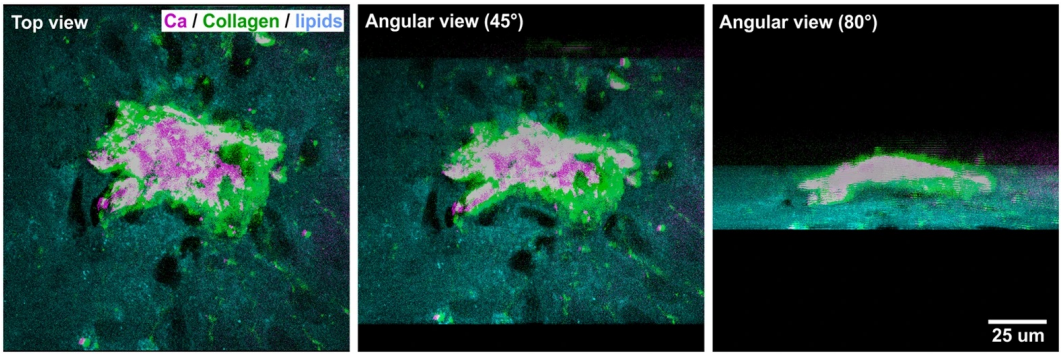

Figure 4.17: **3D image of differentiated cells producing calcium hydroxyapatite and collagen**
In the last step, a 3-dimensional image of an accumulation of hydroxyapatite was constructed. It can be seen in the top view, that the collagen (green) is located predominantly at the boarder of the calcium hydroxyapatite (magenta) and thus is forming a layer around it (images taken from [82]).

in good accordance with the investigation of Davies et al. [90] utilizing scanning electron microscopy.

4.3.4 Conclusion

In the presented study, we demonstrated the ability to follow an osteogenic differentiation of adult stem cells by means of label-free imaging methods. CARS imaging, SHG imaging and spontaneous Raman spectroscopy were utilized to analyze the state of differentiation of ITSCs that were exposed to an induction medium. After 14 days of treatment, we were able to verify the successful cell differentiation into osteoblasts by identifying the presence of calcium hydroxyapatite and collagen. Furthermore, we verified our findings by traditional biochemical analysis methods such as Alizarin Red S staining and rt-PCR. Both methods support our experimental results. In addition, we provided a three dimensional image of a calcium hydroxyapatite accumulation that is covered and surrounded by a layer of collagen. Thus, we demonstrated that label-free imaging and spectroscopy modalities hold a big potential in the non-invasive analysis of stem cell differentiation. This method can even be used in-vivo through the application of endoscopy within clinical procedures [43][44].

4.4 Hyperspectral CARS imaging

4.4.1 Introduction

Label-free methods such as CARS and SRS are employed for the analysis of biological samples or for gaining structural information about chemical or even pharmaceutical compounds. Utilizing picosecond or femtosecond pulsed lasers leads to the efficient generation of CARS and SRS signals due to the high density of photons at a specific time point. Picosecond pulses are characterized by their ideal balance between signal yield and chemical specificity. However, compared to spontaneous Raman spectroscopy, picosecond based coherent Raman imaging lacks the information content of a Raman spectrum. Instead only a single vibrational resonance is excited at a time. There are approaches that overcome this limitation e.g. combining a picosecond and a femtosecond laser. Otherwise the wavelength of one of the participating beam has to be varied in order to tune the targeted vibrational resonance.
In this section I will present our implementation of hyperspectral CARS on the basis of a picosecond laser system. In particular I will focus on signal distortions that might occur when an OPO is utilized for tuning the wavelength. Then I will highlight ways to analyze the hyperspectral data set by means of multivariate analysis methods such as principal component analysis (PCA) and non-negative matrix factorization (NNMF). Finally, the methods are showcased in the studies of nematodes and primary human alveolar epithelial cells.

4.4.2 Effect of varying pulse length on the CARS signal

Within our study that has been published in *Optics Express* under the title "Pulse length variation causing spectral distortions in OPO-based hyperspectral coherent Raman scattering microscopy" [91], we utilized the laser system that has been presented in section 3.1. In order to change the targeted vibrational resonance, the pump wavelength is tuned. A custom-written MATLAB-based algorithm (HyperSpectrum) that communicates with the OPO via a RS-232 interface is utilized for tuning the wavelength. Figure 4.18 visualizes the different steps of the MATLAB algorithm and of the necessary post-processing step [92][93]. As

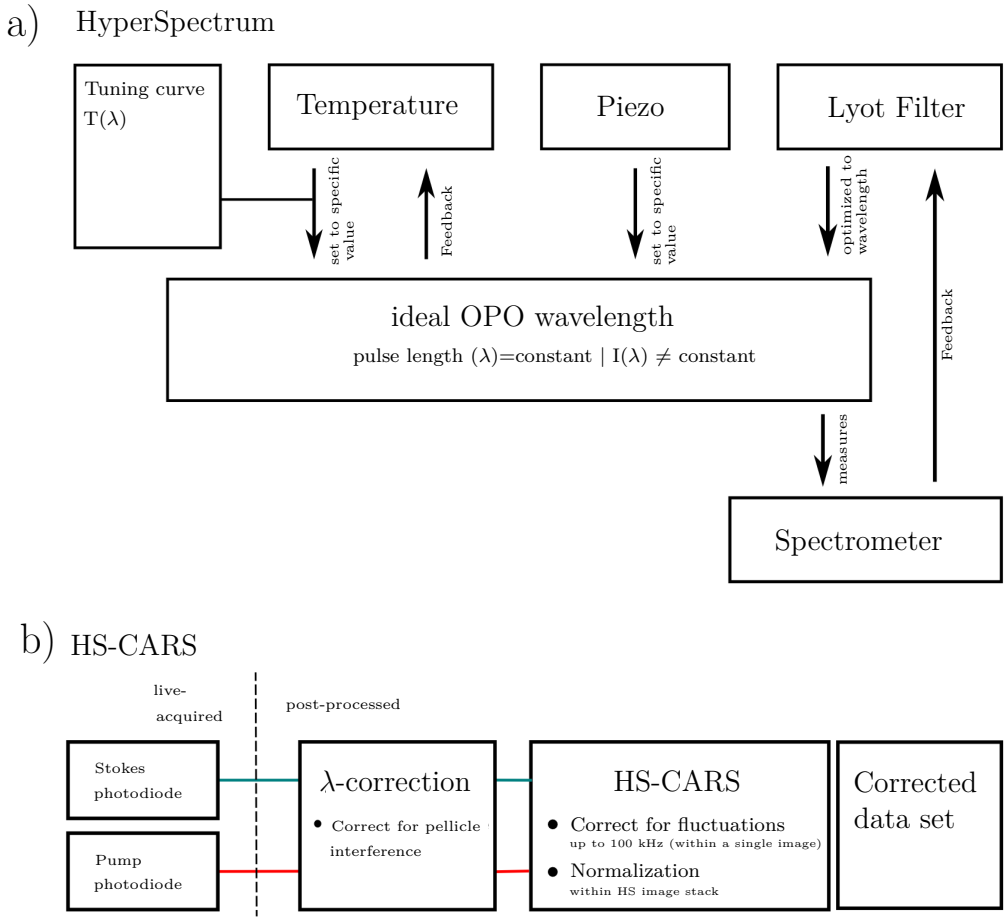

Figure 4.18: **Sketch of OPO control software and image post-processing**
(a) describes the custom-written HyperSpectrum software that is utilized for automatic wavelength tuning of the OPO. In order to adjust the OPO's performance the temperature, the piezo position and the Lyot filter can be tuned. Prior to operating the software, a temperature tuning curve has to be recorded which is exclusive for every OPO. When targeting a specific tuning range, the OPO is optimized for each selected wavelength by setting the correct temperature and the piezo position. When the temperature reaches a steady-state, the Lyot filter is tuned in order to access the wavelength. For that purpose, the internal spectrometer is utilized to measure the spectrum and feedbacks the currently selected wavelength. Note, that for an ideal OPO operation, the pulse length will be kept constant for all selected wavelengths while the output power depends on the selected wavelength and is in general not constant. Therefore, (b) shows a way to compensate for this effect. In every beam path of the three beams that can participate in the CARS process e.g. as pump and Stokes beam, we introduced a pellicle and a photodiode that records the intensity every couple of ms while performing a measurement. This data is then used in the post-processing step in order to correct for the pellicle's spectral response due to interference effects. In addition the data is utilized to compensate intensity fluctuations in the order of 100 kHz for every image. By calculating the mean value of the the photodiode throughout the acquisition, the image is normalized (adapted from [91]).

prior information, the algorithm needs a wavelength tuning table of the OPO. Even though each OPO consists of the same components, the crystal's behavior differs from OPO to OPO. This table combines the wavelength with the ideal temperature that results in the maximum output power. The cavity length that is controlled by the piezo position is set to a specific position according to the wavelength shift. Solely the Lyot filter is adjusted to the target wavelength. By measuring the current wavelength the Lyot filter position is further optimized until the correct wavelength is found. The algorithm is designed in such a way that wavelength tuning is limited to one nm. Otherwise the risk of losing the signal or even switching into another mode is too high. Wavelength tuning across multiple nm is accomplished by dividing the tuning range into smaller steps in the range of a nm. This limitation results in slower but robust wavelength tuning.
In the post-processing step in figure 4.18(b), the images are corrected for the influence of the pellicle and for the laser noise of up to 100 kHz. Since the beam is reflected on both sides of the pellicle, the spectral dependent influence of the pellicle caused by interference effects needs to be analyzed. The resulting dependence of wavelength and intensity can then be used to correct the images. It is advised that this calibration needs to be redone every couple of weeks since the orientation of the laser beam compared to the pellicle changes on a day to day basis. For correcting the laser noise, the data set of the three photodiodes needs to be adjusted to the image pixels. Since the photodiodes also detect a signal in the time period when the laser beam is switching back to the first position of an image row (also called flyback time), these redundant pixels need to be identified. This is accomplished by acquiring the trigger signal that indicates that ScanImage starts the acquisition of a new line. Since ScanImage does not provide an end-of-line trigger signal, one has to clearly identify the actual relevant data. For this purpose a correlation function is implemented that compares the diode data set with the image. After correcting the temporal effects of the laser fluctuations, the mean intensity between two sequentially acquired images need to be compensated. Since the tuning program only accounts for the correct wavelength and tries to reach the maximum output power of the OPO, the signal intensity depends on the signal wavelength. For normalization, the mean value is calculated from the photodiode data and divided from the image. When correcting

the data one has to account for the power dependencies of the CARS signals e.g. dividing the squared pump intensity from the CARS image.

There is one parameter that cannot be controlled directly: the pulse length of the signal beam. The OPO's pulse length depends on the mode of operation and strongly influences the CARS signal intensity. Furthermore, when performing hyperspectral CARS, the ratios of the vibrational resonances can be misleading when neglecting the influence of the pulse length. Figure 4.19 visualizes the effect of varying pulse length on the vibrational profile of an U2OS cell's nucleus. The diagram depicts two modes of operation which are called static and dynamic OPO setting and their corresponding acquired hyperspectral Raman spectrum. This spectrum is the result of 47 images that have been taken from an U2OS cell each time varying the wavelength. Each data point in the diagram is the mean value of the nucleus' CARS signal as shown in the white dashed line in the inset images. The static mode is referred to the mode of operation when the OPO is optimized to one specific wavelength. The dynamic mode optimizes the performance of the OPO in such a way that the pulse length stays constant. For that purpose, the pulse length is simultaneously captured with an autocorrelator (pulseCheck 50, APE). It is apparent that both curves suggest a different intensity ratio due to a varying pulse length.

In order to identify the parameters that have an impact on the pulse length, the LBO temperature and the cavity length was changed. The temperature was detuned starting from the ideal set point that provides the maximum output power by 3.5°C. Figure 4.20 (a-b) visualize the pulse length in dependence to the LBO temperature and the CARS intensity of DMSO, respectively. The starting temperature resulting in the highest OPO signal output is 119.5°C. While measuring the wavelength, the piezo position is kept constant. Figure 4.20(a) indicates that the longest pulse length is achieved when the temperature is reached that provides the highest OPO signal output. Going above or below this temperature results in a decrease of the pulse length from initially 5.3 ps down to 3.6 ps. The corresponding CARS intensity is experiencing a gain by roughly 50%. Surprisingly, the relation of CARS intensity and the pulse length seems to exhibit a linear behavior. Here, two mechanisms could lead to this observation. On one hand the pump's pulse width is reduced leading to a higher temporal intensity but on the

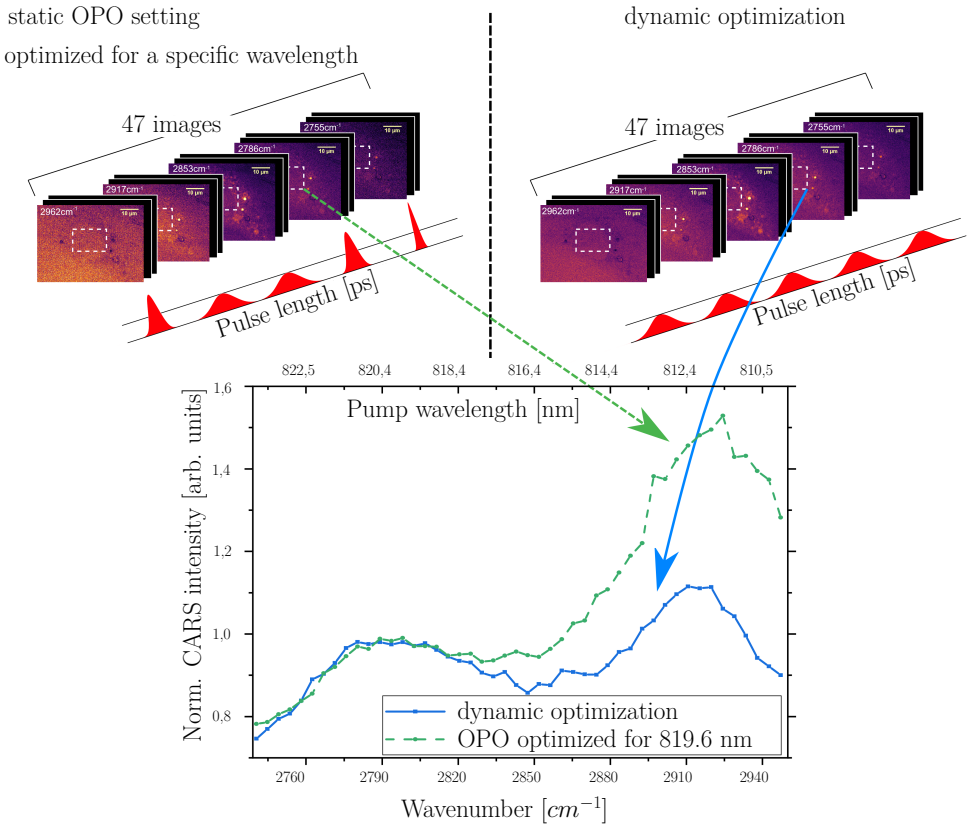

Figure 4.19: **Experimental procedure to access the effect of pulse length distortions** Every diagram highlights two spectra that have been acquired in two distinct procedures. When acquiring CARS images with static OPO settings, the OPO is optimized for one particular wavelength. The dynamic approach optimizes the OPO's settings for every wavelength and is thus maintaining a constant pulse length. This effect is illustrated in the diagram by imaging the nucleus of an U2OS cell. Comparing the green (static optimization) with the blue (dynamic optimization) curve highlights the importance of having a constant pulse length (adapted from [91]).

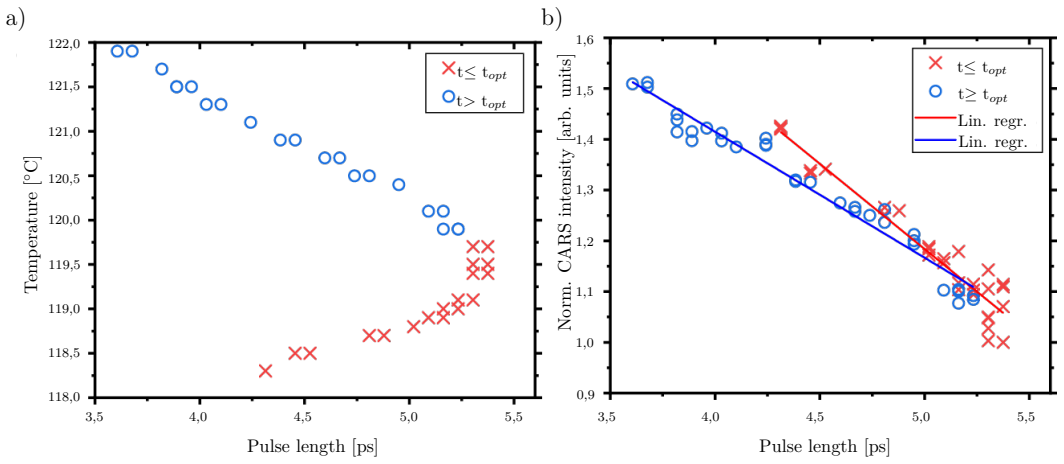

Figure 4.20: **Influence of crystal temperature on OPO's pulse length**
(a) shows the influence of the crystal temperature on the pulse length. The piezo position is kept constant in this experiment. The temperature varies from 118.0°C to 122.0°C. The ideal temperature producing the maximum laser power was found to be 119.5°C. As it turns out, it is also the position with the longest pulse length (5.4 ps). The corresponding CARS intensity of the DMSO sample is depicted in (b). It can be seen that with decreasing pulse length, the CARS signal intensity is rising. Thus by detuning the temperature, an intensity shift of 50 % can be enforced. Linear regression lines are added for the temperature below 119.5°C (red crosses) and above 119.5°C (blue circles) (adapted from [91]).

other hand simultaneously decreases the temporal overlap between the pump and Stokes beam which has a fixed pulse length. Since the higher temporal intensity scales quadratically in the CARS process, the result is a linear dependence on the pulse length within the observed range.

The experiment was redone with varying piezo position and constant LBO temperature. Again starting from the ideal piezo position that provides the maximum signal output of the OPO and detuning the cavity length in the range of 20 μm results in the CARS intensity of DMSO shown in Figure 4.21(a). As before, the longest pulse length is achieved when the OPO cavity provides the maximum signal power. Decreasing or increasing the piezo position results in a decrease in the pulse length. Consequently, the CARS intensity is increased by about 40%. Since changing the cavity length has a severe influence on the timing between the pulse and Stokes beam, the introduced timing mismatch has to be compensated for. Figure 4.21(b) displays the result when the temporal mismatch of pump and Stokes beam is being compensated. The pulse length varies between 4.8 ps for the ideal piezo position and 3.0 ps while the signal experiences a growth by

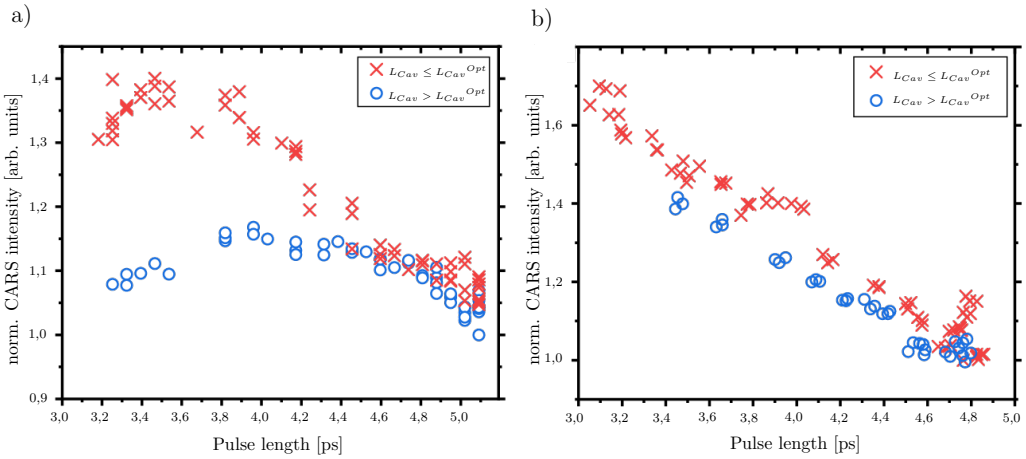

Figure 4.21: **Influence of piezo position on OPO's pulse length**
(a) shows the CARS intensity of the DMSO sample with a fixed crystal temperature and varying piezo position. The ideal piezo position is indicated by the maximum output power of the OPO. The corresponding pulse length was found to be 5.1 ps. Reducing (red crosses) or increasing (blue circles) the piezo position results in a decrease in pulse length and therefore an increase in CARS intensity. (b) shows the same CARS intensity however the temporal mismatch between pump and Stokes beam that originates from the changed cavity length is compensated for (adapted from [91]).

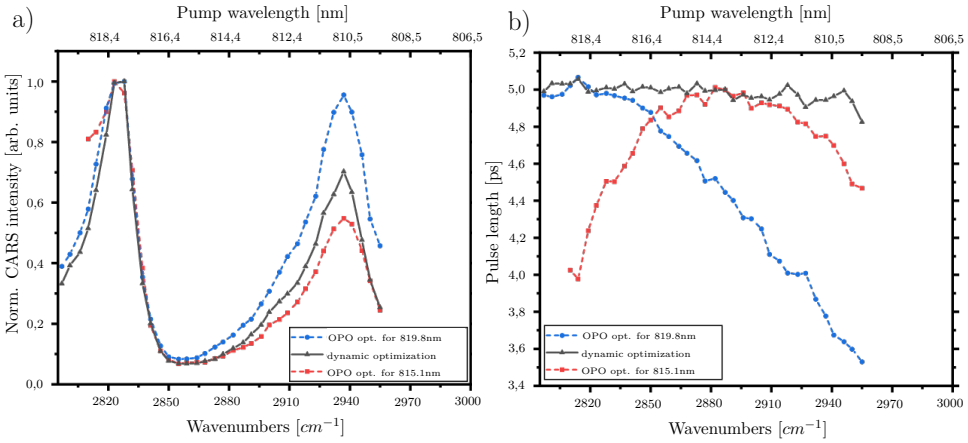

Figure 4.22: **Effect of pulse length variations when calculating CARS intensity ratios** (a) shows the CARS spectrum of methanol for three different acquisition types. The blue curve corresponds to a static optimization for the left peak at around 2800 cm^{-1} wavenumber (blue), the red curve when optimizing the OPO output for the mid position between the two peaks at around 2870 cm^{-1} (red). The third method (black) employs the developed algorithm for controlling the OPO. (b) shows the captured pulse length throughout the experiment. While the dynamic optimization routine yields a constant pulse length, the variation in the red curve and in the blue curve are quiet prominent yielding the observed distortion of the CARS spectrum (adapted from [91]).

70%. Thus, both experiments indicate that tuning the OPO in such a way that it provides the maximum signal output, the pulse length stays the same and is the longest. This observation was implemented into our OPO tuning software that controls the OPO during the hyperspectral data acquisition.

In order to test the software, a hyperspectral scan on methanol was performed in the Raman region going from 2800 cm^{-1} to 2955 cm^{-1} that employs the dynamic optimization. For comparison, two hyperspectral scans were conducted with static OPO parameters. These parameters correspond to the ideal OPO settings for signal wavelengths of 819.8 nm (2800 cm^{-1}, blue curve) and 815.1 nm (2870 cm^{-1}, red curve). In addition, the pulse length was simultaneously captured in order to verify the performance of the tuning software. Figure 4.22 displays the results of the CARS intensity and the pulse length of the three hyperspectral scans. In figure 4.22(a), the intensity curves are normalized to the 2823 cm^{-1} resonance. The black curve resembling the dynamic optimized hyperspectral scan exhibits a constant pulse length throughout the whole scan. The blue curve and

the red curve however both decrease in their pulse lengths. The variation is very prominent which leads to the observed distortion of the CARS spectrum in figure 4.22(a). Thus we can see the importance of taking hyperspectral scans with a constant pulse length. Calculating the relation of the two resonances at 2823 cm^{-1} and 2935 cm^{-1} from the blue curve would yields a misleading interpretation of the Raman resonances. Furthermore, when not taking care of the pulse length parameter, the reproducibility of the experiment is corrupted due to changing factors in the selection of the assumed ideal parameters of the OPO.

Finally, a hyperspectral scan from an U2OS cell in the range of 2738 cm^{-1} and 2947 cm^{-1} was acquired consisting of 47 images. The blue curve indicates the dynamic optimization of the OPO tuning software and the green curve resembles the OPO tuning optimized for the output at around 819.6 nm (2800 cm^{-1}). Again, the pulse length was captured simultaneously to the CARS signal of the cell. Figure 4.23(a) shows the result of a principle component analysis (PCA) of the hyperspectral scan resembling the cell. The color coding is according to the intensity of the loadings found by the PCA. Figure 4.23(b) shows the pulse length while the image has been taken. Again, the dynamic optimization ensures that the pulse length stays constant. In contrast, when the OPO is optimized for a wavelength of 819.6 nm the pulse length variation goes from 4.8 ps down to 3.5 ps. In figure 4.23(c-d) the results of the hyperspectral scan are depicted for two specific areas ROI A and ROI B. In both graphs the data points indicate the mean value and the standard deviation of three sequentially acquired images. The spectrum is the mean value of ROI A and visualizes a lipid droplet while ROI B stands for the Raman response of the nucleus. Figure 4.23(c) shows only a small difference between the static and dynamic optimized method while in figure 4.23(d) it is more prominent. Here, the intensity ratio between the 2845 cm^{-1} and the 2920 cm^{-1} are quite different between the dynamic and the static optimization of the OPO. Dividing the blue curve from the green yields figure 4.24. Here the difference between both methods is getting more prominent. As it can be seen the overall trend indicates that the further away the optimization of the static method is from the target resonance, the more severe the pulse length difference (up to 50%) is getting.

In summary, the importance of a constant pulse length in CARS measurements

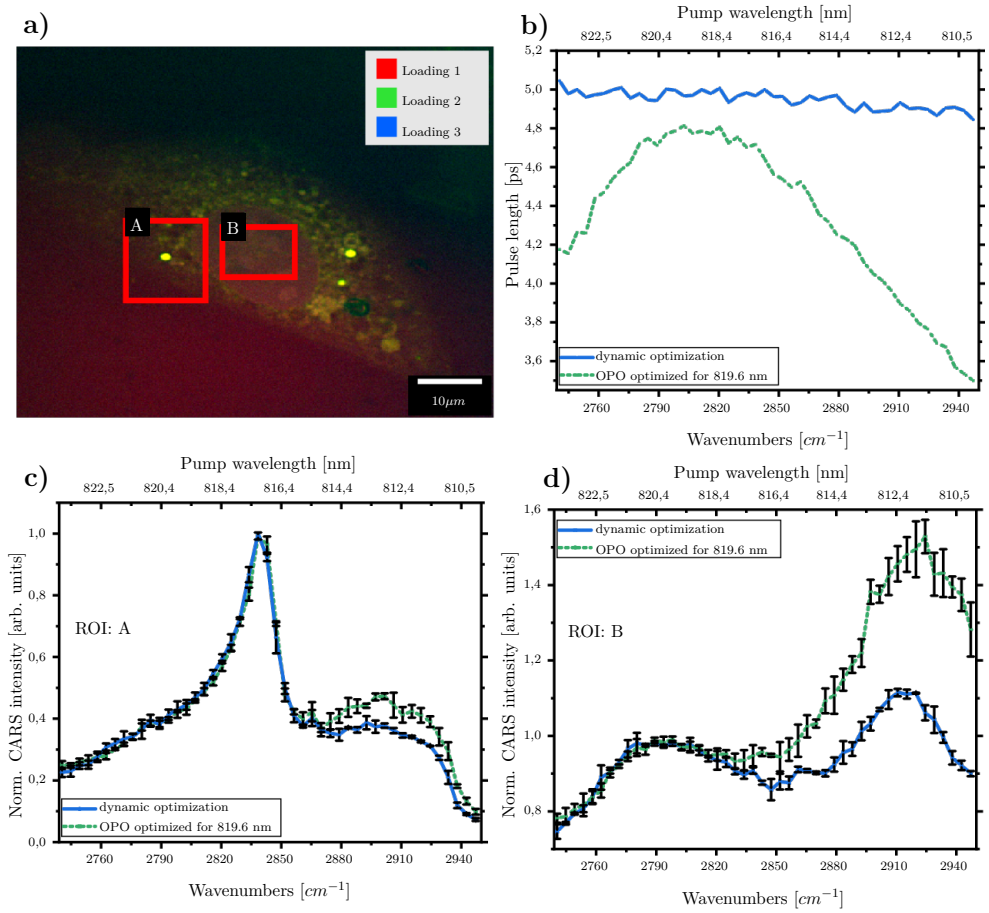

Figure 4.23: **Analyzing a hyperspectral data set of an U2OS cell**
(a) displays the result of analyzing the hyperspectral data set with the PCA. The false color image corresponds to the three loadings of the PCA. Marked within the image are two regions: ROI A highlighting a lipid droplet and ROI B the cell's nucleus. (b) shows the acquired pulse lengths for the dynamic optimization and static scanning. As it can be seen, the variation of the static approach varies between 3.5 ps to 4.8 ps. (c) and (d) illustrate the spectrum of the lipid droplet and the nucleus for the two approaches. The effect of the varying pulse length is prominent, especially for ROI B (adapted from [91]).

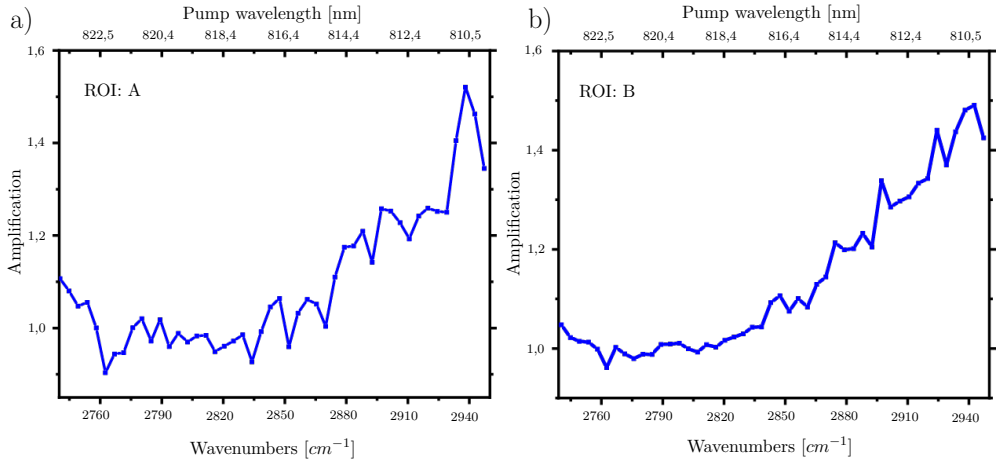

Figure 4.24: **False signal amplification resulting from varying pulse length**
(a) and (b) are highlighting the ratio between the two spectral curves from fig. (4.23). Ideally, when no difference between static and dynamic optimization is present, the curve would be a straight line around 1. Because in the statics approach the OPO was optimized for 2800 cm^{-1} wavenumbers, the curves diverge as it can be seen from the amplification factor being constantly above 1. The maximum amplification factor was found to be around 1.5 (adapted from [91]).

has been successfully demonstrated. Incorrect wavelength tuning without optimizing the OPO to its maximum output will lead to misinterpretations due to distorted intensity profiles as shown in figure 4.24. The herein described program is designed specifically for optimizing the OPO output ensuring a constant pulse length. Therefore, simultaneous tracking of the pulse length is not required which simplifies the acquisition and interpretation of hyperspectral data sets.

4.4.3 Computational analysis of hyperspectral data sets

Big data sets such as hyperspectral data sets are rich in information and details. Analyzing these data manually is labor-intensive since most of them consist of many thousands and even millions of data sets. In order to get an idea of the data and to make it accessible for the user, this data is processed by machine learning algorithms or multivariate analysis methods. Multivariate methods find patterns within the data and combine similar features so that the overall dimension of the data is reduced. Every method differs in the way they look for and find these similarities. In this section I will focus on two methods in order to analyze such

data sets. In both cases I will highlight the fundamental working principle of both methods and their varying characteristics. Finally, I will shortly present the successful implementations of these methods by applying them to hyperspectral CARS data sets.

4.4.3.1 Principal component analysis (PCA)

The principal component analysis (PCA) is one of the oldest methods in multivariate analysis. The basic idea of PCA is to reduce the dimensionality n of the data set [94] [95]. In general, the dimensionality is equal to the number of parameters present in the data set. It is assumed that some of these parameters are coupled to each other. PCA tries to identify the linked parameters by calculating the covariance. The ambition of the PCA is to describe most of the variation in the data set with only a small number of parameters. This is accomplished by generating new parameters from the interrelated parameters of the original data set. Geometrically, this can be understood as having a n-dimensional vector space. However, the vector space's eigen values are yet unknown since some of the parameters are interrelated. The PCA now tries to find these eigen values by generating a covariance matrix. The newly found parameters, also known as principle components (PCs), form new eigen values that can be used to generate a new vector space since these PCs are orthogonal to each other. In the case of PCA, typically the first couple of newly found eigen values are sufficient to represent most of the original data's variation. Thus, by utilizing these few eigen values the original data set can be represented to a certain degree and the overall dimensionality is reduced. Multiplying the eigen values with a certain vector that is called loading, the original data can be retrieved e.g. the pixel values within a hyperspectral image.

4.4.3.2 Non-negative matrix factorization (NNMF)

An alternative to PCA is the non-negative matrix factorization. As the name of the method already implies, the method tries to find two matrices W and H that when multiplied with each other should yield the original matrix V [96][97]. Non-negative means that both matrices W and H have the constrain of not having negative values. Especially, when e.g. analyzing spectrometric data it is desirable

that the algorithm's result only consists of positive values to ease the interpretation. The basis vectors of W for example can be used for identification of patterns inside the spectrum. Imagine a Raman spectrum of a chemical compound that consists of many different chemical elements. When having a big data set with a suitable variance and on which NNMF is applied, the resulting basis vectors of W represent the unique Raman signatures of the chemical elements the compounds consists of. Since this method is a dimensional reducing algorithm the rank of W and H is m x k and k x n, respectively, with $k < min(m, n)$. Thus, the product WH resembles a compressed version of V instead of being a perfect copy. The measure that is later on used in order to optimize the algorithm only approaches 0 but not necessarily equals 0. If we revisit the example with the chemical compounds constructed from different chemical elements, we could set the rank k to the assumed number chemical elements present inside the sample. However, in the presence of impurities, the method will not completely reach 0 unless the Raman signature of these impurities scales with one or more chemical elements. Comparing the derived Raman signatures from NNMF with the Raman spectrum of the pure substance to identify the cause of these impurities offers another potential. Within our studies we utilized the NNMF method that has been implemented in MATLAB [98]. In order to find the matrices W and H the method provides the user with two optimization algorithms: a multiplicative update (MULT) algorithm and an alternating least squares (ALS) algorithm. Both methods are explained in detail elsewhere [99][100]. What can be said about the algorithms is that depending on the implementation of the ALS algorithm, it holds the potential to converge faster than the MULT method. Both methods only work with positive entries in their matrices. When a negative value is calculated it will be set to 0. Unlike the MULT method that sets this value to 0 until the algorithm has converged, the ALS approach does not set the value to 0 permanently. Thus, it offers a higher degree in flexibility and it is not as prone to run into a local minimum as the MULT algorithm. However, since the vector space of H and W is not convex meaning that there is not only one (global) minimum but instead many local minima, the results of the algorithms strongly depend on the starting value. Prior knowledge can efficiently help reducing the vector space to only a small number of local minima. When providing the algorithm with

external information, the real challenge is to know how much information is necessary to proof one's assumption without constraining the algorithm's flexibility too much.
Within the following sections, we will apply these unsupervised learning algorithms to high rank data sets as well as to hyperspectral CARS data sets in order to discern between e.g. cell types or lipids and proteins.

4.4.4 Applying PCA on ITSC and iPSC data sets

Investigating the differentiation process of stem cells into different kinds of cell types is a very important topic in regeneration medicine. Among the various stem cell types the neural-crest derived stem cells (NCSC) are described as the fourth germ layer [101] and are thus considered to be promising candidates for clinical applications due to their extraordinary differentiation potential. NCSC can be found at various sites inside the human body [102][103][104]. In the presented study that has been published in *bioRxiv* under the title "Identification of a human adult cardiac stem cell population with neural crest origin" [105], human cardiac stem cells (hCSC) are investigated regarding their differentiation potential and their possible relation to NCSCs.
It is considered that the various cardiac stem cells (CSC) [106][107] populations differ in their differentiation potential depending on the development origin [108][109]. Therefore, in this study we utilized the hCSC that can be found in the left atrial appendage. In order to verify this assumption, the RNAs of cultured cells from hCSC and inferior turbinate stem cells (ITSC), a well characterized NCSC population, were isolated and sequenced by Novogene (Beijing, China). Here, we performed a PCA on the RNA data set and compared it to literature values. First, we took both, the literature values [110] and the RNA data set from the hCSC and ITSC and compared the data entries. Only when a gene expression was found in all data sets, it was used in the PCA analysis. The PCA was performed within MATLAB utilizing the build-in PCA function.
When performing the PCA only on the data set of the ITSC and the hCSC, we found that both cell types can be easily differentiated when comparing PC 1 and PC 2 (figure 4.25(a)). Only the fifth datapoint of the hCSC seems to be an outlier. Again, when making the comparison between PC1 and PC3, the fifth data

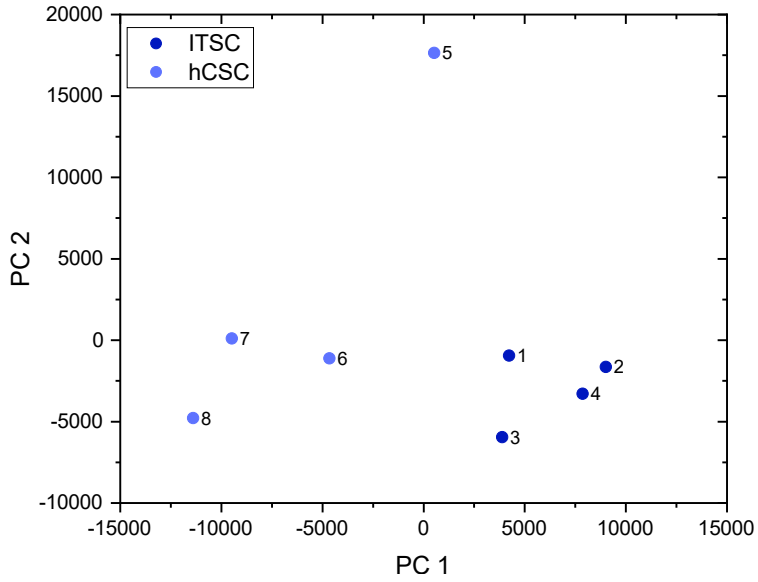

Figure 4.25: **PCA analysis on RNA data set**
PCA on the RNA data set without external reference reveals clustering into two different groups of cells (ITSC and hCSC) (adapted from [105]).

point seems to be off. The other data points can be clearly differentiated. However, when analyzing the behavior of PC2 to PC3 or PC2 to PC4 (figure 4.26), both cell types seem to have similar gene expression. This finding is in good accordance with our assumptions that the hCSC population belongs to NCSC. Now, comparing the ITSC and hCSC to literature results in figure 4.27. Note, that in this case, the number of gene expressions that take part in the PCA is reduced to the same base of gene expressions that could be found in both data sets. Again, a clear clustering is observable for all three kind of cells when comparing PC1 with PC2 or PC3.

This study is a great example of the successful implementation of PCA to a huge data set. The PCA was able to find certain patterns and differentiate the data sets into two kinds of cell types. Furthermore, it showed similarities between the ITSCs and hCSCs which would not be directly apparent by looking at the result of the RNA sequencing. As a result, the similarity indicates that the hCSC that have been found in the left atrial appendage are belonging to NCSCs and are thus favorable for clinical applications.

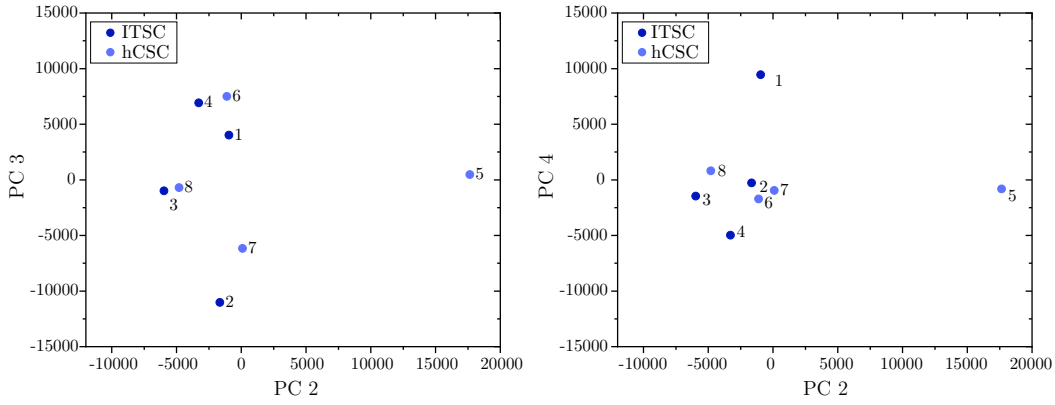

Figure 4.26: **PC2 reveals no clustering**
The second PC shows no clustering when being plotted against PC3 and PC4 leading to the assumption that the ITSC and hCSC have similiar gene expressions that are forming the PC2.

4.4.5 Analyzing the impacts of pollutants on early environmental markers

In order to detect pollutants that have an impact on an ecologic system there is a need for sensors [111]. Caenorhabditis elegans (C. elegans) are free-living nematodes that live in the liquid phase of soils and have already been subject of many toxicology studies [112]. For example at low concentrations Cu plays an important role in many cellular processes. However, increasing the concentration induces stress and therefore affects the nematode's metabolism [113]. As a result, the reproduction, feeding, and lifetime is altered [112][114]. In the recent years, the metabolism of C. elegans has been widely studied by utilizing fluorescence microscopy. Here, the lipids are stained with Nile Red and analyzed with a confocal microscope. However, utilizing fluorescent dyes alters the cellular environment in terms of the hydrophilic/hydrophobic environment [115]. Also Nile Red staining is not specific to lipids but also labels autofluorescent granules [116][117] which results in a higher lipid count compared to label-free methods such as CARS [114]. CARS has already been utilized as a tool to access the lipid distribution of nematodes [118][114]. Since no labeling is required, the specificity of CARS is superior to fluorescence imaging [119]. In addition, when analyzing live worms, Nile Red is unable to enter the cytoplasm in order to stain the lipid droplets [114]. Accordingly it is recommended to use label-free methods such as CARS in

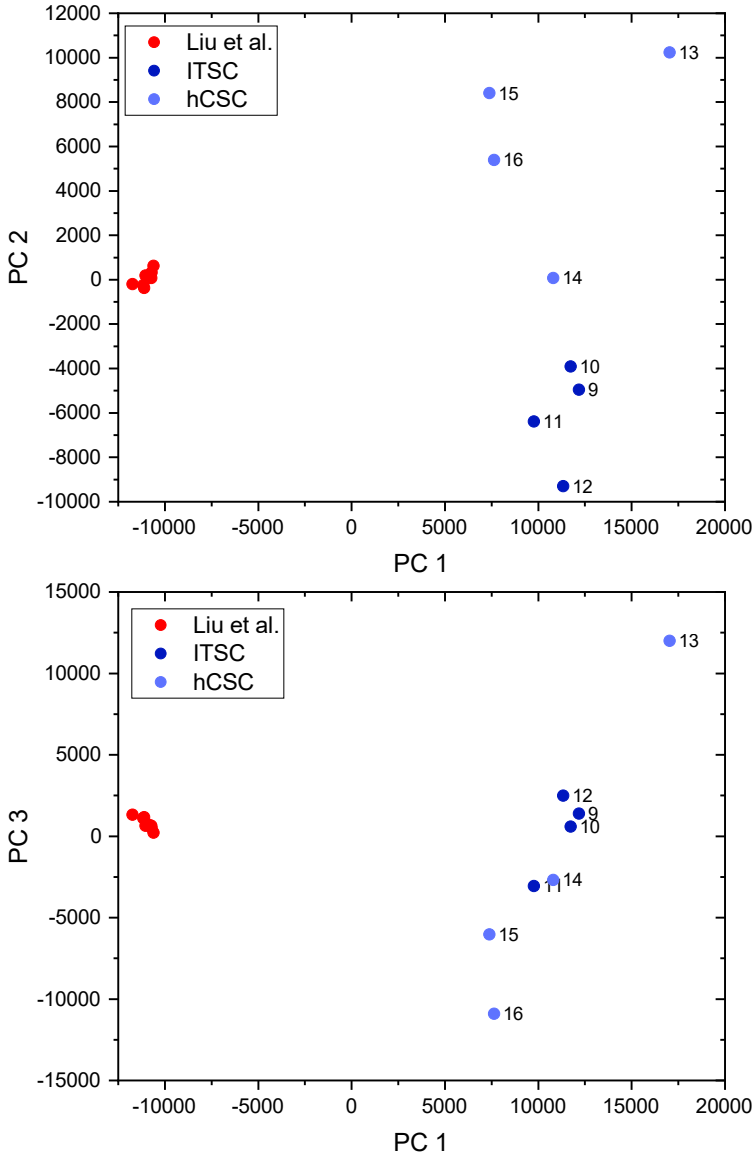

Figure 4.27: **PCA analysis on data set combined with reference**
PCA analysis of the RNA data set including an external reference data set. For comparison, the original data set was reduced to the markers present in both data sets (images taken from [105]).

order to study the lipid metabolism.

4.4.5.1 Project outline

Thus in this study we investigated the impact of copper (Cu) on C. elegans in a sub-lethal concentration. The study has been published in *Ecotoxicology and Environmental Safety* with the title "Analyzing life-history traits and lipid storage using CARS microscopy for assessing effects of copper on the fitness of Caenorhabditis elegans" [120].
In order to follow the influence of chronic Cu exposure in C. elegans, we analyzed the formation of lipid vesicles in a life-cycle experiment by CARS microscopy. The concentration of Cu was EC20 which stands for a concentration that was reported to inhibit the reproduction of C. elegans by 20%. The nematodes were cultivated utilizing the hanging-drop method in which every worm was set in its own drop [121].
Analyzing the life span of the nematodes shows that EC20-exposed worms die 10 days earlier than those of the control group. For the CARS analysis, we took 8 (4 of them exposed to EC20 and 4 control) adult nematodes that died of natural causes and which were then fixed with 4% paraformaldehyde. Furthermore, we collected 20 juvenile (10 control and 10 EC20-exposed) right after hatching. For imaging, we utilized the 2845 cm^{-1} resonance that is mainly associated with lipids. A 60x immersion objective lens (UPlanSApo, NA=1.2, Olympus) was used for focusing and a condensor lens (U-AAC, NA=1.4, Olympus) for collection. The CARS signal, originating at 660 nm, was separated from the fundamental beams by applying suitable short-pass and band-pass filters (950 SP, 2x 775 SP, 785 SP, 514 LP and a 660/40 BP). Intensity corrections as previously described (see section 4.4.2) were applied to the data. The resulting CARS images are displayed in figure 4.28. When imaging the juvenile nematodes, only a single image of the worm was taken due to its small size. For imaging the adult nematodes, we selected two distinct regions inside the nematode (figure 4.28(a)): the vulva region and the tail region. The vulva region is of particularly interesting because that's where the eggs are developed. Here, z-stacks of the nematodes were collected utilizing a piezo stage and taking every 500 nm a CARS image of the region. Finally, a projection of the z-stacks was calculated utilizing FIJI. As it turns out,

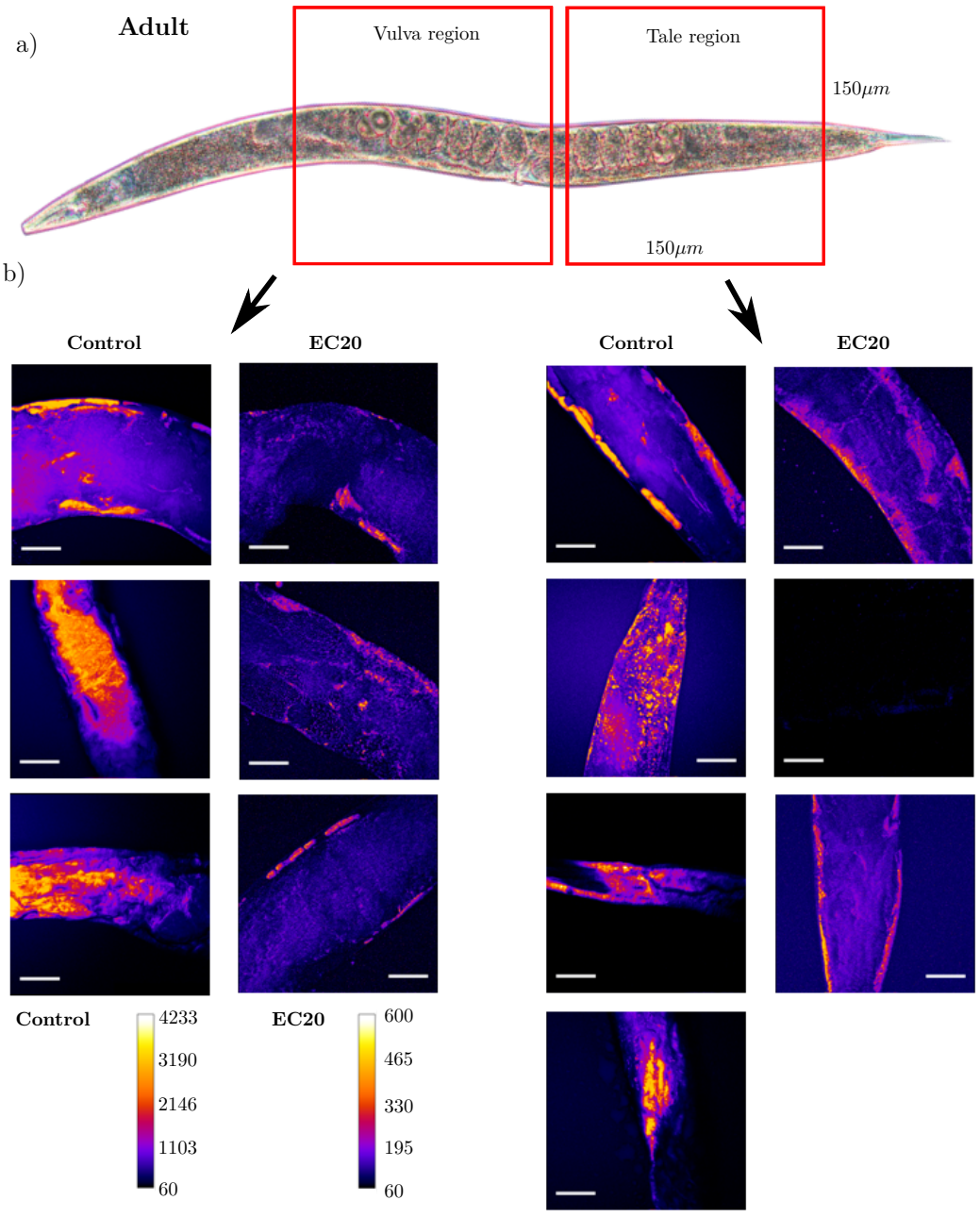

Figure 4.28: **CARS images of adult nematodes**
(a) illustrates a microscopic image of an adult nematode. Here, the two distinct regions e.g. the vulva and tail region are illustrated that are targeted throughout the analysis. (b) shows the images taken from the control and the exposed adult nematodes. As it can be seen, the overall lipid content seems to be higher in the control group than in the nematodes exposed to copper. Also the lipids in the exposed group are predominantly distributed at the outer parts of the nematode. The scale bar corresponds to 30 μm (image taken from [120]).

no significant difference has been found between the two regions within the control or the EC20-exposed nematodes. However, when comparing the control with the exposed worms, the lipid distribution differs significantly from each other. While the control group has a homogeneous lipid distribution, the lipids of the other group were predominantly found near the body wall and also in a smaller amount (figure 4.28(b)). To further analyze the lipid distribution, the program FIJI [122] was utilized and the analysis was conducted following [119][114][118]. In short, first a background value was subtracted from the slices before summing up all z-stacks. These images were then thresholded and converted into a binary image. This binary image was finally utilized to quantify the lipid distribution. Here, the total area of all lipids (figure 4.29(a)) as well as the average area of the lipids (figure 4.29(b)) were calculated. The lipid area fraction (figure 4.29(c)) describes the amount of lipids in comparison to the nematode's size. Finally, the lipids were segmented into different sizes (figure 4.29(d)). From this analysis, it is apparent that the chronic exposure to copper has a significant impact on the nematode's metabolism. The overall lipid content is reduced compared to the control group and at the same time the distribution of lipids is altered. It can be seen from figure 4.29(d) that the nematode has a tendency to form smaller lipid droplets instead of bigger ones. There are many possibilities how the copper might interact with the nematode's metabolism. One is that the nematode has a higher rate of energy consumption making the formation of smaller lipid droplets more favorable than bigger ones. This is due to the lesser surface-to-volume ratio which favors lipolysis [123].

4.4.5.2 Hyperspectral CARS imaging of nematodes

In the next step, we performed hyperspectral CARS on the vulva region of the nematode in order to test whether it is possible to distinguish between proteins and lipids since both share the same Raman resonance at around 2845 cm^{-1}. For that purpose we scanned the Raman resonance of both lipids and proteins going from 800 nm to 830 nm which corresponds to 3100 cm^{-1} to 2650 cm^{-1}. This hyperspectral data set is then inserted into the PCA. Our assumption is that since proteins and lipids have distinct Raman spectra, the PCA should be able to

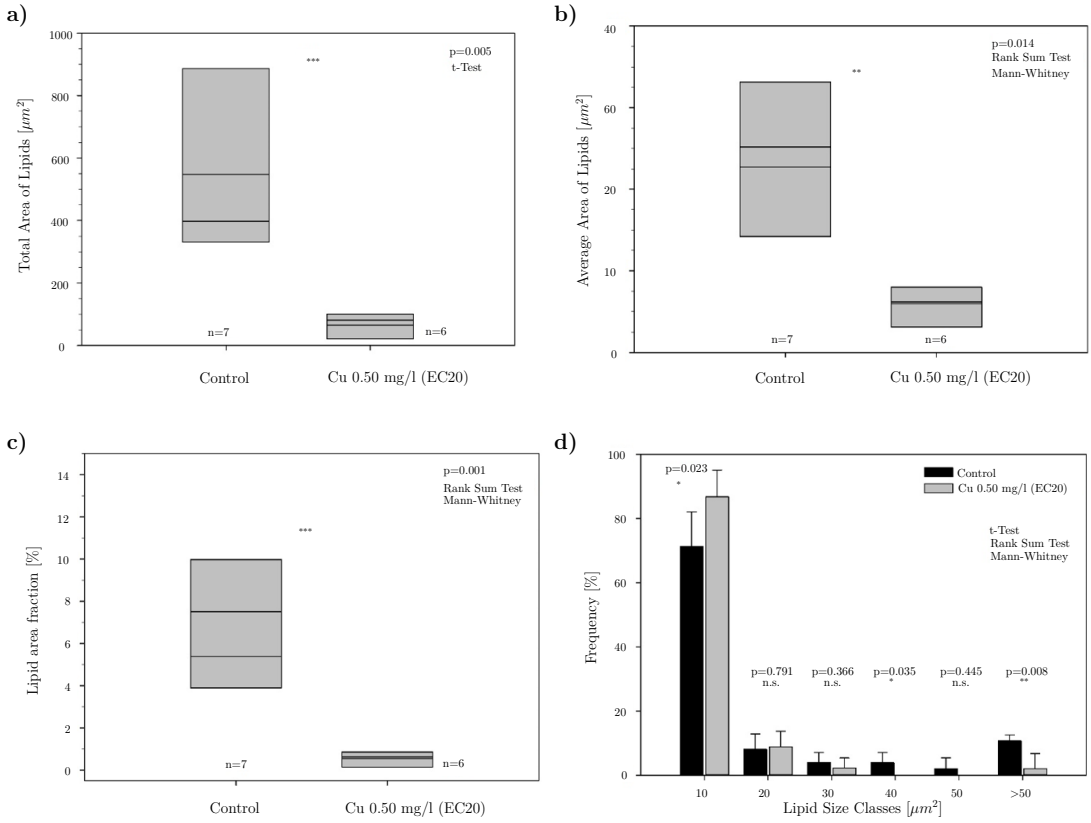

Figure 4.29: **Quantitative results of the CARS images regarding the effect of Cu** (a) describes the total area of lipids within the CARS images which is higher in the control than in the exposed group. The diagram (b) compares the average area of lipids between the two groups. In diagram (c) the relative area that is covered by lipids and finally is shown, in the last diagram (d) the lipids are clustered into classes regarding their size. As it can be seen, the exposed group tends to form smaller lipid vesicles instead of bigger ones that occur more frequently in the control group (image taken from [120]).

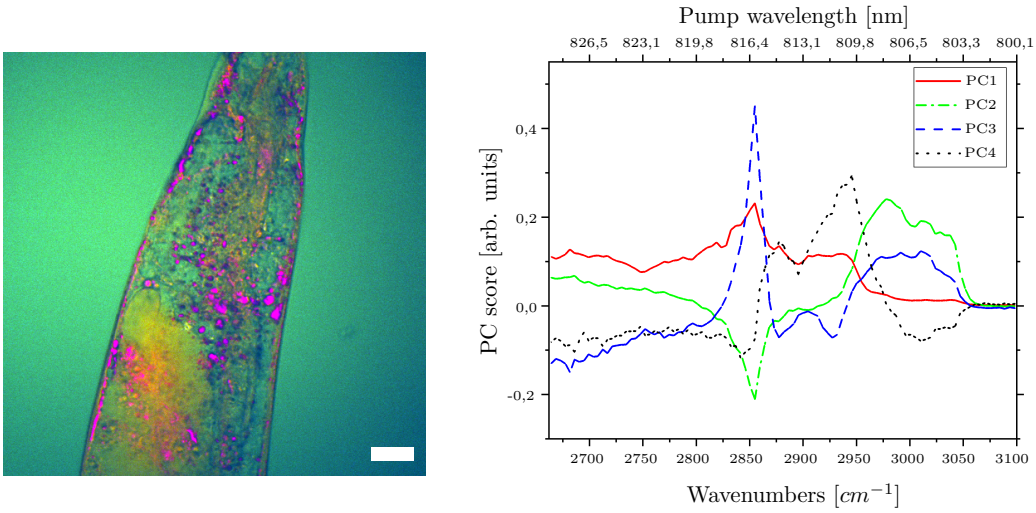

Figure 4.30: **PCA of an hyperspectral data set**
The left image shows the false color image of a nematode. The right side shows the eigenvector of the nematode. The false-colors in the image are a superposition of the spectra found by the PCA. The scale bar equals 15 μm.

differentiate their signal contributions. The resulting spectrum of the first four PCA components are shown in figure 4.30. When looking at the spectrum, the interpretation is not intuitive due to the presence of negative values. What can be said is that the blue curve that belongs to PC3 strongly correlates with the characteristic curve progression of lipids and the black curve strongly resembles the one of proteins. Since the green curve has high contributions in the higher wavenumber range (3000 cm^{-1}) it might belong to the Raman signal of water. Thus, the red curve consists of some lipid signal due to the peak at around 2850 cm^{-1} but also to the non-resonant background which should have a uniform value. Because the PCA is a variance-driven decomposition, the first component refers to the contribution that causes most of the variance. Within our image stack, the inhomogeneous illumination causes most of this variance making it most likely to be found in the first component.

4.4.5.3 Conclusion

As it can be seen, interpreting the PCA spectrum can be complex if the data is not clear itself due to the presence of negative values. Being variance-based, the algorithm strongly depends on the way of detection and the acquisition as we have seen when analyzing the nematodes. Nevertheless, it has been demonstrated that coherent Raman imaging can efficiently be utilized in the analysis of nematodes. Nematodes itself are very suitable as model organisms for studying the influence of environmental factors such as pollutants. They are predestined as early markers for pollutants or similar environmental factors e.g. nanoparticles that might affect the fertility or metabolism.

4.4.6 Following cell differentiation of alveolar epithelium cells with label-free microscopy

4.4.6.1 Introduction

Understanding the mechanisms within the lung alveolar epithelium is essential for exploiting therapeutic approaches to improve the recovery time of lung patients [124]. The tissue layer covering the alveolar surface area is composed of two kinds of cell types: The alveolar epithelial type I (AT1) and type II (ATII). The ATI cells are approximately covering 93% of the surface and are characterized by a flat cell shape while the ATII cells are cuboidal and are responsible for producing surfactants that might play an important role in the host defense of the lung. Moreover, it is widely accepted that the ATII is the sole progenitor of ATI cells [124]. Studies have indicated [125], that the ATII cells proliferate and differentiate into ATI cells, possibly by passing an intermediate stage (see also figure 4.31). During this stage, the cell is either moving on into becoming an ATI cell or is going back into the stage of an ATII cell. From observations it is assumed, that these ATII cells are restoring themselves as stem cell and can undergo many rounds of cell differentiation. Recent studies have indicated that the ATI cell is capable of reversion to type II cells and enter the cell cycle again [126][127]. The underlying mechanism of this reversion are yet to be evaluated [128]. Understanding this process of differentiation is essential for manipulating cell proliferation and improving the management of lung disorders. Identifying

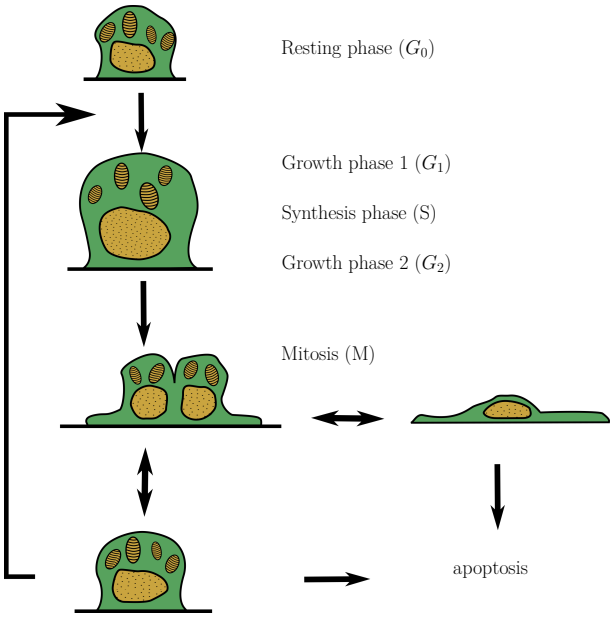

Figure 4.31: **Differentiation pathway for alveolar epithelial cells**
At the top, the ATII cell is in the resting phase G_0. By an external trigger it moves into an intermediate state that is described by the growth phase 1 (G_1), the synthesis phase (S) and the growth phase 2 (G_2). After mitosis (M), the cell is either differentiating into an ATI cell or going back to becoming an ATII cell. For the latter, the cell can go back to the state before the growth phase 1 where it either moves into the resting phase or to the growth phase again. Also the cell can undergo apoptosis and die. If the cell develops into an ATI cell after mitosis, the cell can die (apoptosis) or undergoes reversion to type II. As it can be seen from this figure, the ATII cell is only allowed to enter the cell cycle and is therefore acting as its own stem cell (image adapted from [124]).

the different cell types is possible due to their specific functions and morphology. As stated earlier, ATI cells exhibit a flattend cell form compared to the roundish cuboidal ATII cells [125]. In addition, there are more indicators than the appearance of the cell to identify the cell types. The ATII cell is the only on to expresses the surfactant protein SP-C [129] that can be specifically targeted with fluorescent agents. Targeting the structural protein Caveolin-1 (Cav-1) with fluorescent markers will indicate the ATI cells [130][131].
Many studies that have been performed on these cells involve fixation of the cell or labeling them with exogenous agents [125][132], the cells' environment is perturbed so that any reaction of the cells in terms of proliferation and differentiation might be affected by the utilized methods. Since isolated ATII cells lose their specific characteristics within a couple of days and acquire ATI characteristics instead, environmental factors are of great importance [125][133]. Our approach of utilizing (coherent) Raman scattering aims to be minimally invasive on the cells environment.
The results of this study have been published in *Journal of Biophotonics* under the title "Vibrational spectroscopic imaging and live cell video microscopy for studying differentiation of primary human alveolar epithelial cells" [134].
In the beginning, successful cultivation of ATII cells that evolve over time into ATI cells are verified by means of Laurdan staining as well as fluorescent labeling of SP-C and Cav-1. The cells are further analyzed by confocal spontaneous Raman scattering and coherent anti-Stokes Raman scattering microscopy. The goal of this investigation is to follow the differentiation over time, identify specific markers within the Raman spectrum and to be able to observe morphological changes more specifically compared to light microscopy techniques. Furthermore, the successful application of coherent Raman scattering will facilitate the analysis of alveolar epithelial cells.

4.4.6.2 Pre-experiments

The cells were isolated from human lung tissue following an established protocol [135]. In the following, those cells that have been cultivated ex-vivo will be called ATI-like and ATII-like cells, since there is still no evidence that the cells are behaving ex-vivo and in-vivo in the same way [125]. In order to verify the successful

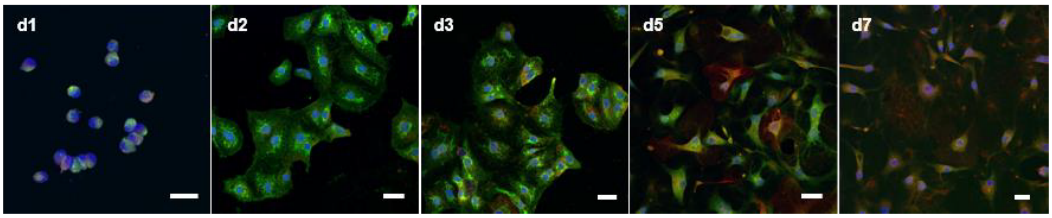

Figure 4.32: **Fluorescence images of evolving alveolar epithelial cells**
Staining of evolving alveolar epithelial cells proofs the successful differentiation of ATII-like into ATI-like cells. The cells are expressing SP-C (green) and Cav-1 (red) which are stained with fluorescent agents. The image impression shifts from green to red confirming the differentiation. Scale bars indicate 20 μm (images taken from [134]).

differentiation, the cells were stained against the surfactant protein C and Cav-1 for identifying ATII and ATI cells respectively. As it can be seen from figure 4.32, the expression of SP-C (green) is higher than of Cav-1 (red) in the first couple of days. Because of the differentiation process, the amount of fluorescence of SP-C decreases and of Cav-1 increases indicating the change in ratio of ATII and ATI-like cells. In addition to this verification, Laurdan staining was applied to the cells in order to follow the assumed decrease in lipid content throughout cell differentiation. The corresponding images that have been acquired with a confocal fluorescence microscope are displayed in figure 4.33. Here, the decrease in lipid levels is visible as is the change in morphology. The white arrow in the image of day 5 indicates the presence of an undifferentiated ATII-like cell supporting the assumption, that the ATI-like cell is not the sole route for an ATII-like cell to differentiate, as it is shown in figure 4.31 [125].

4.4.6.3 Imaging the evolution of ATI-like cells to ATII-like cells

After the verification of the protocol, confocal spontaneous Raman scattering was utilized to receive 3-dimensional images from ATI and ATII-like cells. Unlike fluorescence or electron microscopy, the advantage of Raman imaging techniques is the analysis of cells in their unperturbed environment. Figure 4.34(a) displays the characteristic spectra of the membrane, the nucleus, cytoplasm, lipid vesicles and cytochrome C and their distribution within the cell. Since the data was acquired by our collaboration partner, there is no in-depth analysis of these images (for

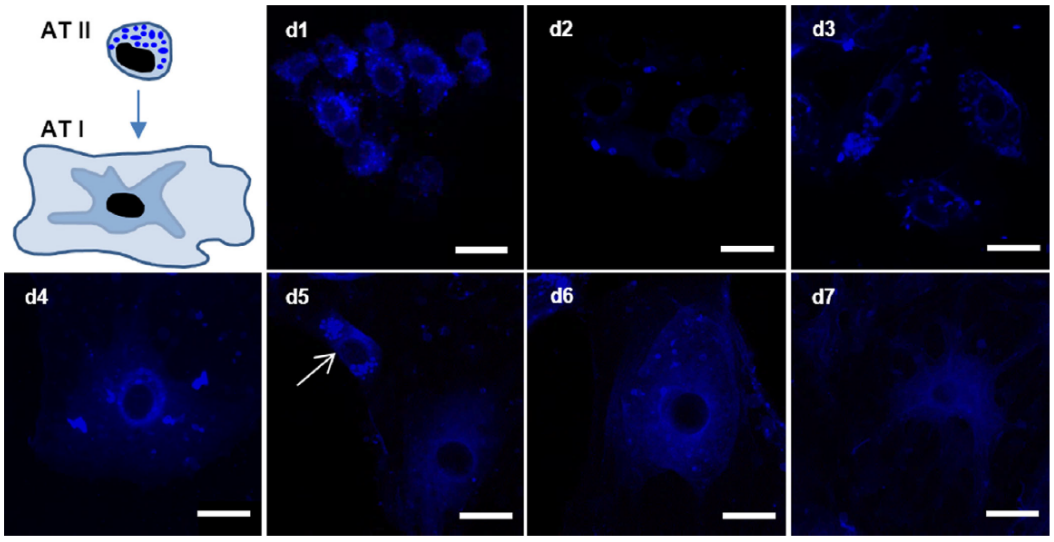

Figure 4.33: **Laurdan staining visualizes morphological changes upon differentiation** The sketch visualizes the cell differentiation that can be observed in the following images. The Laurdan staining visualizes the cell's morphology indicating an increase in the cell's diameter and a decrease in signal intensity. The arrow indicates a cell, that after 5 days is not differentiating and still possesses a cuboidal shape. Scale bar indicates 20 μm (images taken from [134]).

more details see [134]). However, it can be said that the observed cell initially is of cuboidal shape and evolves throughout the observed time span into a flattened cell. Furthermore, in the beginning the cell is filled with lipid vesicles that are vanishing over time. Since this observation shows the differentiation of an ATII-like cell into a ATI-like cell, it can be noted, that the ATII-like cell can be easily identified by imaging its lipid content and morphology. Since in most cases, CARS is restricted to the higher wavenumber region e.g. 2500 cm^{-1}, the spectral features of the nucleus and the lipid vesicles will be the main target within the CARS analysis.

Investigation of the alveolar epithelial-like cells by means of coherent Raman scattering techniques was accomplished by the custom-built coherent Raman scattering system described a previous section 3.8.2. The focal powers of the pump and Stokes beam were selected to be 20 mW and 10 mW respectively. The field of view of one image was 75 μm x 75μm with a pixel dwell time of 31.25 μs resulting in an acquisition time of roughly 6 minutes. All images undergo a correction algorithm that corrects for intensity fluctuations of up to 100 kHz (see also section

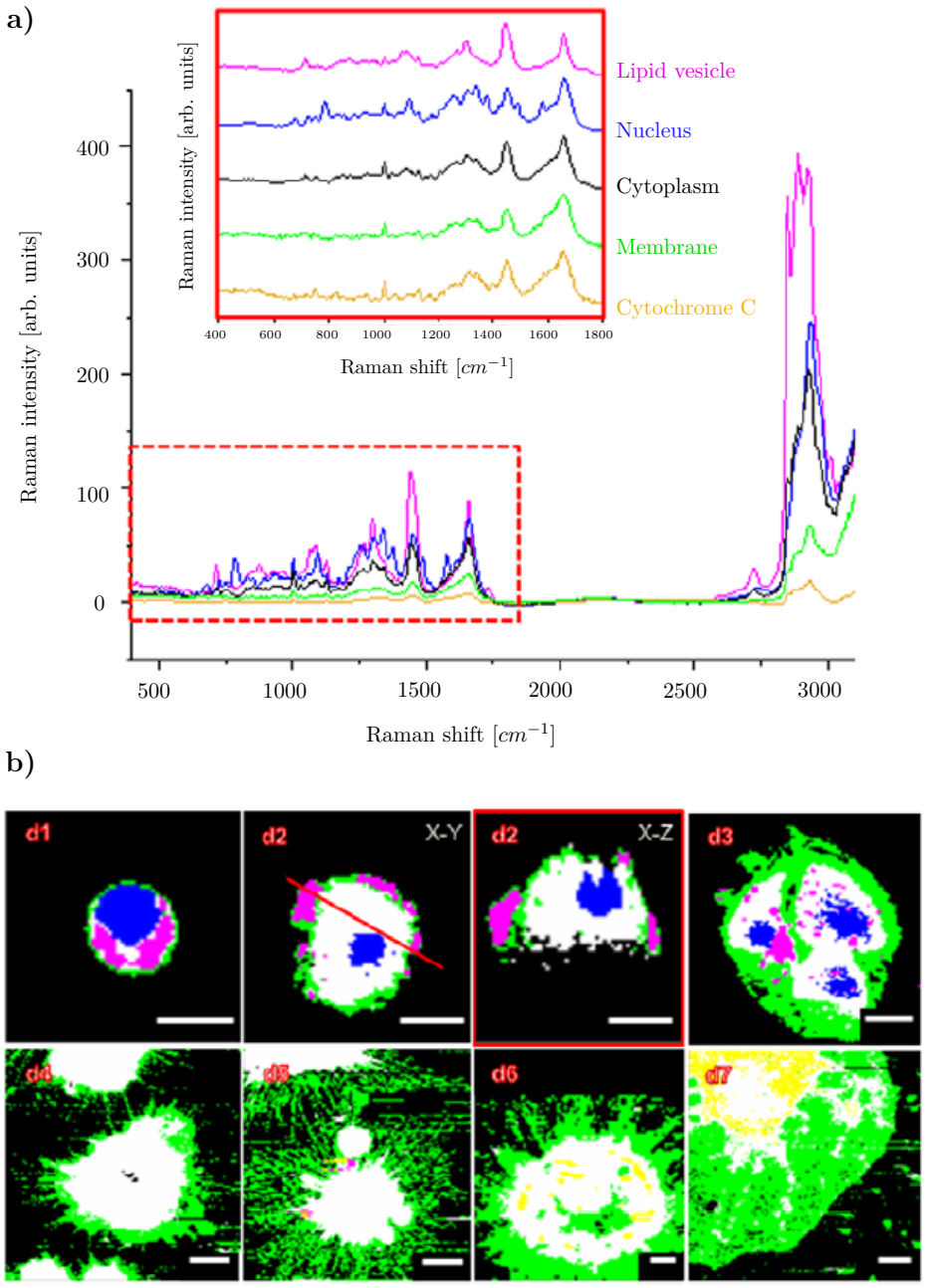

Figure 4.34: **Confocal spontaneous Raman scattering microscopy of evolving alveolar epithelial cells**
By identifying the characteristic Raman spectra from different cell compartments (a), the confocal spontaneous Raman scattering images can be color coded: lipid vesicles (magenta), nucleus (blue), cytoplasm (black), cellular membrane (green) and cytochrome c (yellow). The red line in the image of d2 indicates the plane utilized for the X-Z cross section. The scale bars indicate 10 μm (images taken from [134]).

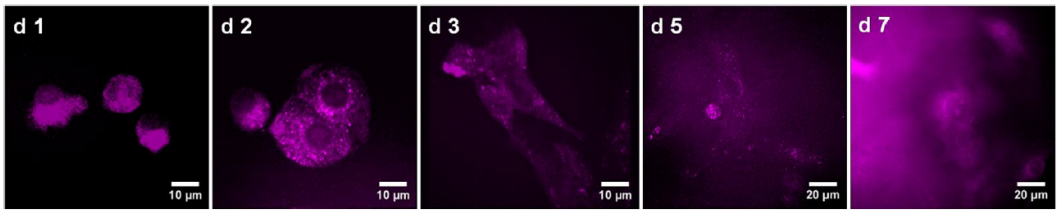

Figure 4.35: **Following cell differentiation with CARS microscopy**
The CARS image show the evolution of the cell on every observed day (e.g. 1, 2, 3, 5 and 7). The targeted resonance has been 2845 cm^{-1} which is predominantly associated with lipids. The morphological evolution of the cells can clearly be seen (images taken from [134]).

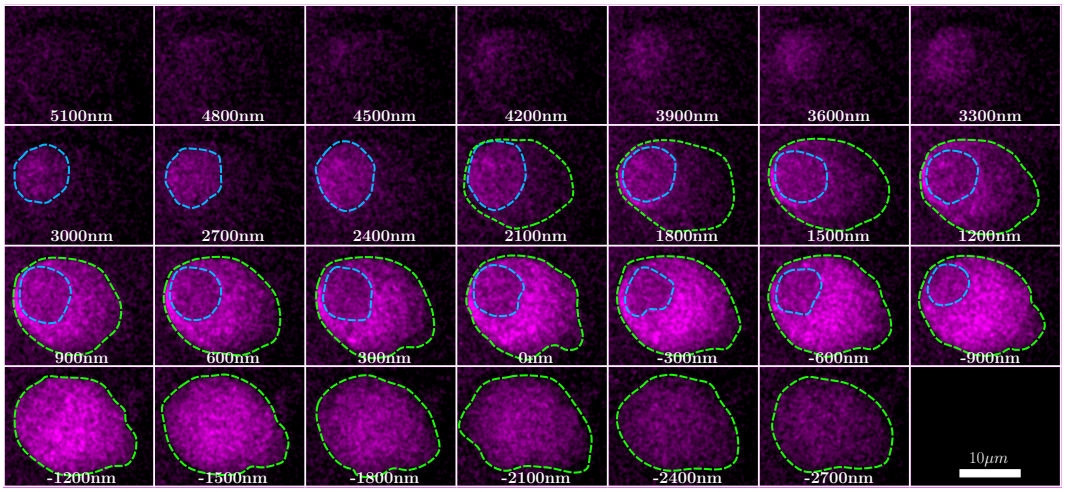

Figure 4.36: **3-dimensional CARS imaging of ATII-like cells**
3-dimensional CARS images were obtained from ATII-like cells on day 1. The targeted Raman resonance is 2845 cm^{-1}. As a guide to the eye blue and green dashed lines are introduced indicating the position of the nucleus and the membrane of the cell, respectively (images taken from [134]).

4.4.2). Figure 4.35 displays the acquisition of the cells at different time points for the 2845 cm^{-1} resonance that is predominantly associated with lipids. As it can be easily seen, the cell morphology is drastically changing from day 1 to day 5. It becomes apparent that through the different intensity levels the cell's nucleus can be clearly seen in the images. From these images two assumptions can be verified: Firstly, the morphology of the cells is changing throughout the time points and secondly the concentration of lipids within the cell is decreasing. In the next step, we analyzed individual cells on day 1 and 3 by acquiring a z-stack imaging the 2845 cm^{-1} resonance. Figures 4.36 and 4.37 are displaying the results of this

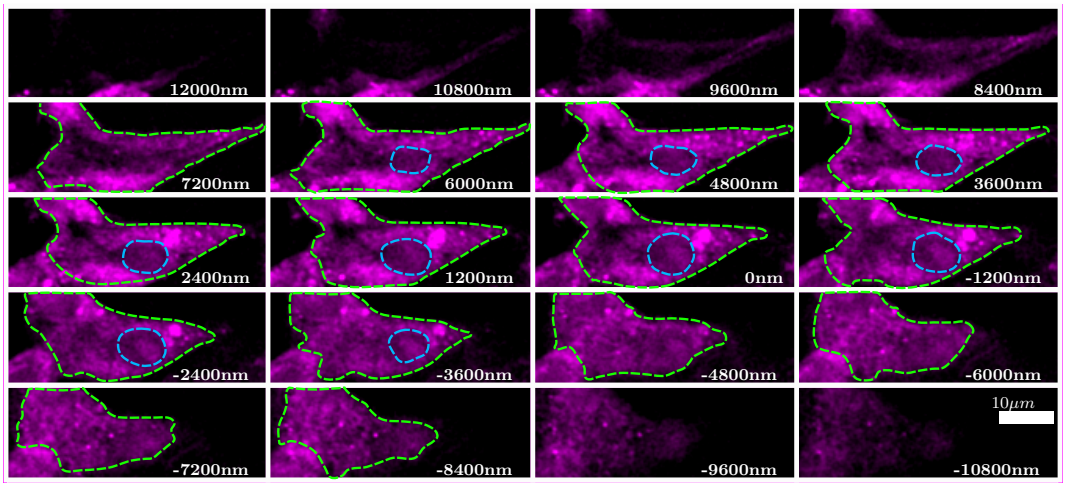

Figure 4.37: **3-dimensional CARS imaging of ATI-like cells**
In contrast to figure 4.36 a 3-dimensional CARS image was captured from an ATI-like cell on day 3. Blue and green dashed lines are inserted into the image in order to visualize the position of the nucleus and the membrane respectively. Compared to the ATII-like cell, the flattening of the cell is very prominent (images taken from [134]).

method. As a guide to the eye blue and green lines are added to the images in order to visualize the the nucleus and the cell borders. In order to reduce the influence of noise, a Gaussian filter was applied.

4.4.6.4 Resolving intracellular structures through the application of hyperspectral CARS imaging

Compared to spontaneous Raman scattering, coherent Raman scattering such as CARS and SRS trade in the huge amount of chemical information for live-cell imaging. To recover a certain amount of this chemical information, hyperspectral CARS is performed on one z-slice showing the cell's cross-section. Within this study, we tuned the target wavenumber from 2700 cm^{-1} to 3050 cm^{-1} and applied the previously presented NNMF algorithm on the data. Tuning was accomplished by altering the pump wavelength stepwise by 0.3 nm going from 803 nm to 826.5 nm. In order to reduce the computation time and also increase the signal levels, neighboring pixels are binned together (4x4) yielding a 2D image with reduced pixel count. Also a ROI was selected around individual cells and

an offset value was subtracted from the image. As earlier stated in the discussion about the NNMF algorithm, the key element for a successful algorithm is the choice of the seed values. Defining these seed values was accomplished by taking the hyperspectral data set, identifying the images corresponding to the 2845 cm^{-1} and 2920 cm^{-1} resonance and dividing both images from each other. Preceding this step is the assumption, that there is a cell located within this image that consists of lipids and a cell nucleus. Since lipids are mainly associated to the 2845 cm^{-1} resonance and the Raman spectrum of the nucleus shares both the 2845 cm^{-1} and the 2920 cm^{-1} resonance in a ratio of about 1:1, we took this criterion to identify two suitable sites within the image whose spectra are utilized as seed values. The remaining two seed values were arbitrarily chosen in order to not constrict the algorithm too much. The results for day 1 to 3 are displayed in figure 4.38. The false color images are visualizing the compartments with the corresponding spectra on the right side. Judged by the spectral features, the purple line corresponds to lipids, the blue line to proteins, mainly located within the nucleus and finally the background signal in black with no specific spectral features. Here, the black spectrum is the summation of the two remaining spectra of the algorithm. These images indicate the morphological change of the ATII-like cells into the flattened ATI-like cells. Comparing the distribution of lipids and proteins supports the interpretation of the confocal spontaneous Raman images. Attempts have been made for taking HS-CARS data sets from day 4 or later, however the signal intensity is decreasing in such a way, that the contribution of noise is higher than the actual CARS signal.

4.4.6.5 Conclusion

In summary, ATII-like and ATI-like cells have successfully been analyzed by means of label-free imaging techniques. Confocal spontaneous Raman microscopy and coherent Raman imaging have been utilized to characterize the morphology of these cells as well as their chemical composition. The application of confocal spontaneous Raman scattering microscopy yields a 3-dimensional image of the ATII-like cells undergoing differentiation into ATI-like cells. Here, it was found that ATII-like cells exhibit localized phospholipid vibrations while the ATI-like

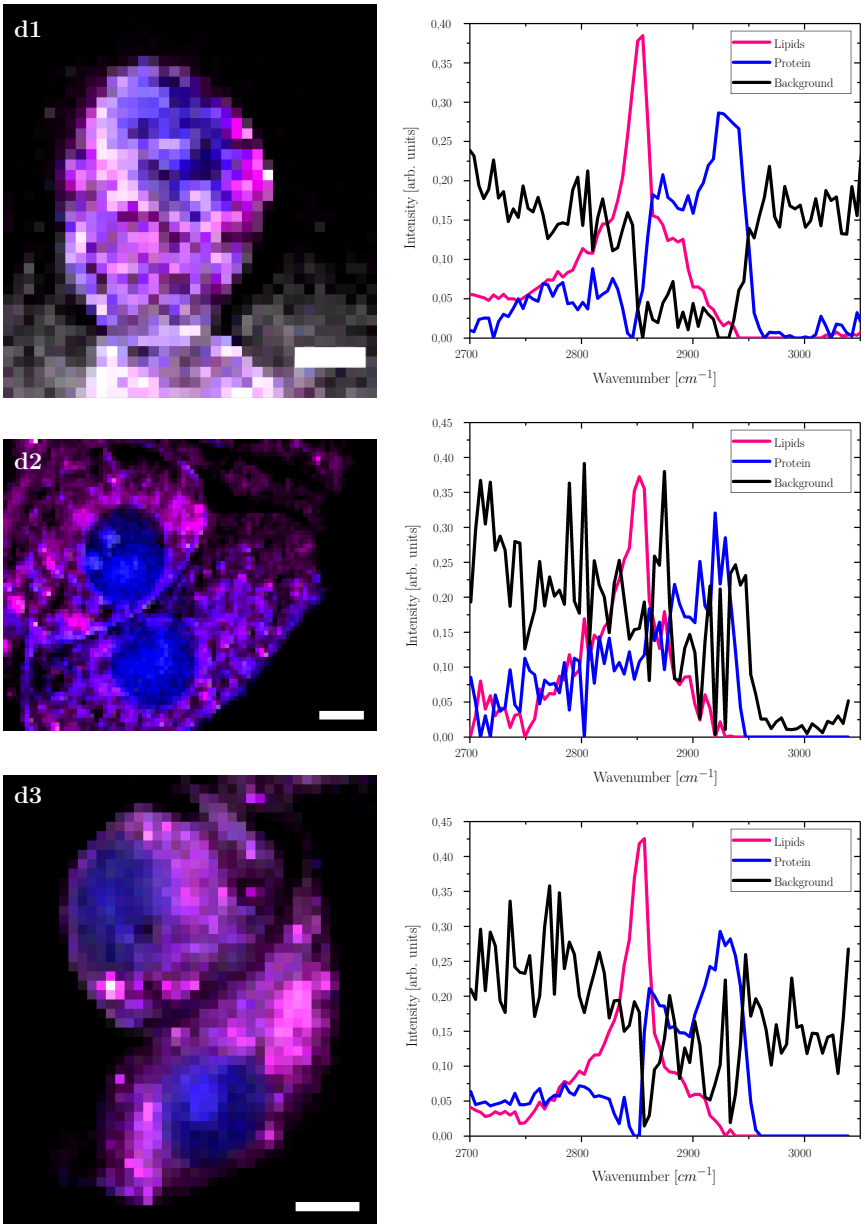

Figure 4.38: **Analyzing the hyperspectral CARS data set with NNMF**
The hyperspectral data set has been analyzed with NNMF algorithm. The resulting eigenvectors and the recalculated images are displayed for each of the three investigated days. On the right side, the three fundamental spectra of the image (eigenvectors) are displayed and on the left side an overlay image of the corresponding three recalculated images. As it can be seen, the magenta spectrum is referred to as the spectrum of lipid vesicles, the blue spectrum to the nucleus and the black spectrum to the background signal. The scale bar is 1 μm (adapted from [134]).

cells are characterized by a decreasing lipid content and the absence of vesicular structures. Since the acquisition of these information is very time consuming, the investigation was extended through the application of CARS. Here, the acquisition time was drastically reduced by the cost of chemical information. The application of HS-CARS in combination with the NNMF algorithm slightly compensates this drawback and expands the significance of the CARS images. The final computed images support the findings of confocal spontaneous Raman microscopy. That way CARS and HS-CARS are offering the time efficient possibility to perform this analysis on living cells and follow the differentiation of ATII-like cells into ATI-like cells live.

4.5 Compact fiber laser source for coherent Raman scattering

In the following chapter the approach of designing and testing a two-color fiber laser source for coherent Raman scattering will be highlighted and compared to recent approaches of fiber laser systems that satisfy the demanding requirements of coherent Raman microscopy. The most important challenges for fiber laser sources are the provision of laser pulses that are defined by low noise characteristics and superior temporal stability as well as their compactness. Finally, in order to be able to compete with optical systems utilizing solid-state lasers, they should be able to provide a relevant amount of laser power and a suitable wavelength tuning range.

4.5.1 Current state of the art

In general, one can divide the various fiber laser approaches into several categories utilizing different solutions in generating a suitable system. In the following, the hybrid fiber laser, the actively synchronized fiber laser and the supercontinuum (SC) fiber laser approach will be discussed in depth. A more detailed discussion about other fiber laser designs can be found in the published study in *Light: Science & Applications* with the title "High-contrast, fast chemical imaging by coherent Raman scattering using a self-synchronized two-colour fibre laser" [136]. The first fiber laser design, being discussed is the supercontinuum approach. Here, either the pump or the Stokes beam are being fed into a highly non-linear fiber (HNLF) producing a supercontinuum spectrum due to self-phase modulation (SPM). The newly generated spectrum is then filtered for the desired center wavelength with a suitable bandwidth for coherent Raman applications. Because of the supercontinuum generation itself, the process is prone to excessive noise. Reducing the fiber length can reduce the noise, however in terms of SRS, the utilization of balanced detection schemes is still inevitable. As an example, Freudiger et al. [48] demonstrated an all-fiber laser source utilizing a HNLF and balanced detection. The schematic SRS process and the experimental setup are displayed in figure 4.39. The laser pulses are generated in an Er-doped fiber os-

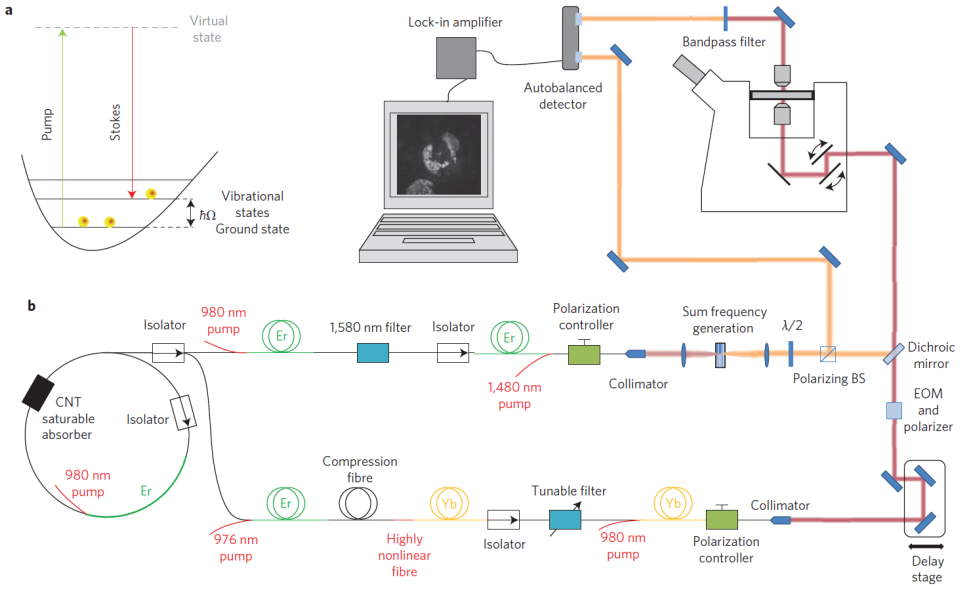

Figure 4.39: **Setup of a supercontinuum based all-fiber laser approach**
Figure (a) displays the SRS process while figure (b) presents the all-fiber based laser system. The system starts with a fiber oscillator whose output is split into two parts. The upper part is acting as the pump beam, the lower part as the Stokes beam. The supercontinuum generation takes place in the Stokes beam branch within the highly-nonlinear fiber. Both beams are combined in the end and directed into an inverted microscope. The detection of the signal is conducted via balanced detection (image taken from [48]).

cillator utilizing a carbon nanotube saturable absorber for mode locking. The center wavelength of the cavity is 1560 nm and its repetition rate is 60 MHz. The output of the cavity is then split into two parts and directed into the pump and Stokes beam generating branches. The upper branch is described as the pump beam branch. The incoming pulses are pre-amplified in an Er-doped amplifier and then filtered by a narrow-band filter. In order to avoid excessive spectrum broadening a low-nonlinearity Er-doped amplifier it utilized before the beam is frequency-doubled in a periodically-poled lithium niobate (PPLN) crystal. The tuning range of the pump beam goes from 765 nm to 795 nm. For the Stokes beam generation, the beam is pre-amplified, compressed, fed into a HNLF and is again amplified. In the HNLF, a supercontinuum is generated that ranges from 950 nm to at least 1700 nm. The authors noted that by keeping the length of the HNLF to a minimum, the generated noise is minimized as well. The output is then amplified with an ytterbium-doped amplifier before the spectrum is reduced by a tunable filter. After the filter, the beam is again amplified and then launched into free-space. The Stokes beam is modulated with a sinusoidal waveform of 10 MHz through an EOM. The output power of the Stokes beam is 120 mW and offers a tuning range going from 1010 nm to 1060 nm. This results in an overall accessible wavenumber region from 2800 cm^{-1} to 3100 cm^{-1}. Both beams are then overlapped and directed into the laser scanning microscope. For utilizing balanced detection, a portion of the pump beam is directed towards the auto-balanced detector together with the modulated pump beam. The authors noted, that commercially available balanced detectors are limited in speed which is why they developed a balanced detector that allows imaging speeds with 1 frame/s. According to the authors, this is the fastest demonstrated imaging speed with a fiber laser. However, the need of utilizing custom-built balanced detection schemes for high-speed imaging is rather challenging. According to Nose et al. [137], the application of balanced detection to (biological) samples suffers from the need to balance the intensity of signal and reference. Since the optical transmission of the signal varies with the focus position, particularly in tissue, the performance of balanced detection is limited.

Therefore, Nose et al. [137] proposed a different approach with actively synchronized laser cavities and collinear balanced detection (CBD). Active control of a

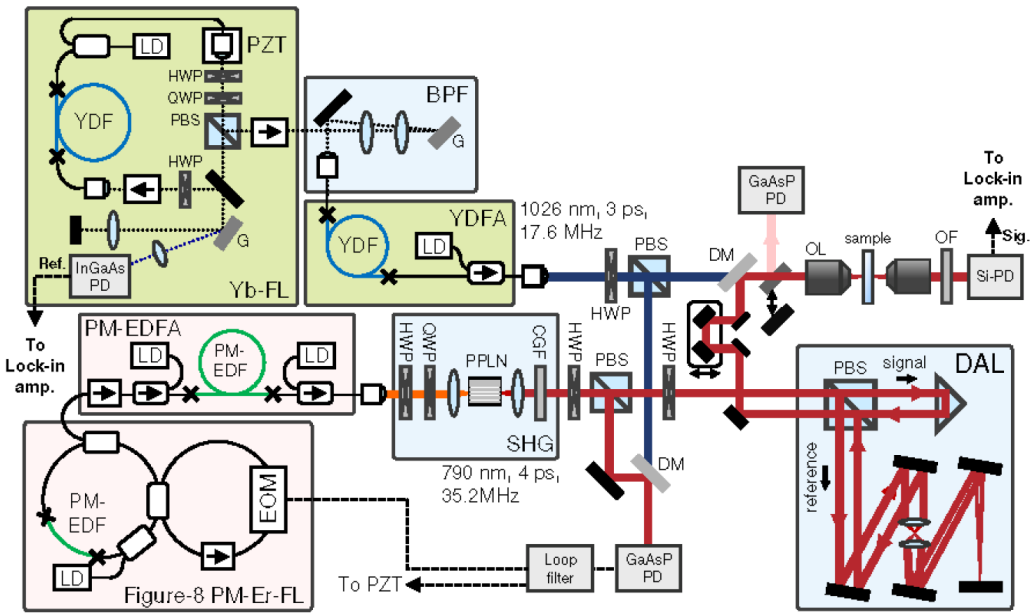

Figure 4.40: **All fiber-based laser system utilizing active synchronization**
The laser system consists of two fiber laser cavities which are actively synchronized. The master oscillator is located at the top, the slave oscillator in the lower left corner in a Figure-8 arrangement. The photodiodes TPA signal is utilized for active synchronization of the slave oscillator. The signal is then detected via a collinear balanced detection scheme (image taken from [137]).

laser cavity is often performed by defining one cavity as the master and the other as the slave. Within the slave cavity an element is introduced that modifies the repetition rate in order to synchronize itself with the master cavity. In Nose et al. this is being accomplished by measuring the two-photon absorption (TPA) of a GaAsP photodiode, calculating the jitter that feedbacks an EOM within the slave cavity. The experimental setup is shown in figure 4.40 and will only be briefly discussed. The laser system consists of the master cavity (YB-FL, green) and the slave cavity (Figure-8 PM-Er-FL, red). The EOM within the slave cavity is utilized for mode locking and for high-speed tuning of the cavity's repetition rate which is being exploited for synchronization. The polarization maintained (PM) cavity has a repetition rate of 35.2 MHz and has a center wavelength of 1560 nm with a bandwidth of 14 nm. After amplification and frequency doubling the pump beam, it yields an average power of 12 mW and a tuning range going from 760 nm to 810 nm. The master cavity utilized nonlinear polarization rotation as mode locking mechanism and operates with a repetition rate of 17.6 MHz and

a center wavelength of 1026 nm. The cavity comprises a grating for dispersion compensation. The grating's zeroth order is utilized as the reference for the SRS experiment. After spectral filtering and amplification, the average power of the Stokes beam was 15 mW and the bandwidth 0.3 nm. For active synchronization, the phase locked loop (PLL) was utilized by focusing the pump and Stokes beam on a photodiode detecting the TPA signal. This signal is then analyzed and fed back through a loop filter into the EOM. The achieved timing jitter was found to be in the order of 210 fs. For collinear balanced detection, the pump beam is split into two parts by the delay-and-add line (DAL). Here, two pulse trains are generated with a defined timing difference and opposite polarization e.g. s and p-polarized. The pulse train is then overlapped with the Stokes beam and send into the microscope. After passing through the sample and filtering out the Stokes beam, a silicon photodiode detects the pump pulse train. Compared to the previous presented balanced detection scheme, the reference e.g. the second pulse in the pump pulse train, also passes through the sample and thus experiences the same optical effects as the signal pump. Therefore, the balancing between the reference and signal is automatically achieved for every focus position within the sample. However, the presented laser system is limited in accessible power for both pump and Stokes beam and suffers from excessive noise making the need for balanced detection imperative.

The hybrid laser approach utilizes a fiber laser source and a solid-state laser in order to circumvent the necessity of balanced detection. Ozeki et al. [138] demonstrated the application of such a hybrid laser system for video-rate wavelength tuning of SRS signals. Figure 4.41 shows the experimental setup that consists of a solid-state Ti:Sapphire oscillator with a repetition rate of 76 MHz and a center wavelength of 797 nm. The fiber laser oscillator has a repetition rate of 38 MHz, a center wavelength of 1030 nm with a spectral bandwidth of 30 nm. Utilizing a fast tunable band-pass filter (TBPF) and subsequent amplification of the Stokes pulse to about 300 mW, the pump beam of the solid-state laser and the Stokes beam of the fiber laser can be overlapped and directed into the microscope. After passing through the sample, the Stokes beam is filtered out and the pump signal is detected with a photodiode, whose signal is fed into a lock-in amplifier. In order to optimize the timing jitter between the two laser sources, the same PPL mech-

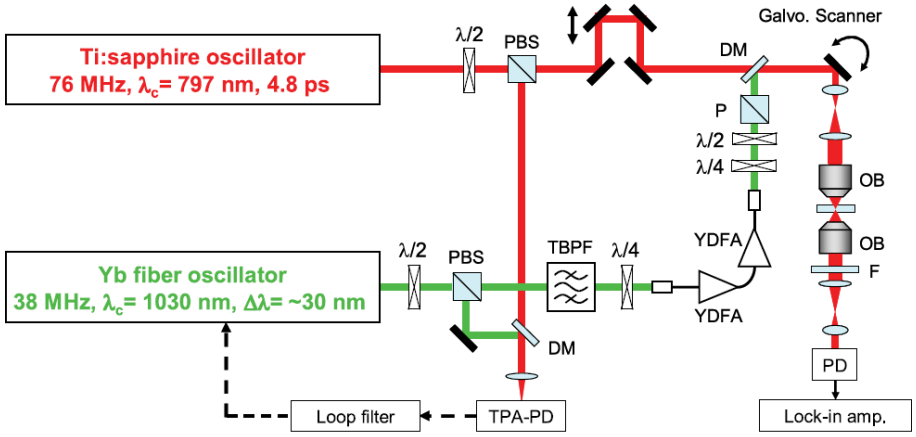

Figure 4.41: **Hybrid laser system approach utilizing a solid-state laser**
In addition to an all-fiber laser oscillator, a Ti:Sapphire laser acting as pump laser source is added to the system. Synchronization is achieved through active synchronization similar to Nose et. al. [137]. The SRS signal is detected via a photodiode without the need for balanced detection. Fast wavelength-tuning is accomplished by the tunable band-pass filter (TBPF) (image taken from [138]).

anism is applied as utilized in Nose et al. [137]. The herein presented tunable band-pass filter is capable of tuning the wavelength of the Stokes beam within a few ms resulting in a tuning rate of 1 kHz. Due to the shot-noise limited pulses of the Ti:Sapphire laser, the presented system's imaging speed is not limited by the use of balanced detection. The wavelength tuning speed of the TBPF can be directly exploited for creating hyperspectral SRS image stacks. However, the authors reported a shift in the temporal overlap resulting from the wavelength tuning. Due to dispersion within the fibers, a temporal shift factor of -75 fs/nm was found which led to less than 10 % decrease of the SRS signal over the entire tuning range. The main drawback of the system is of course the reduced portability and costs of the solid-state laser making clinical applications challenging.
In summary, the previous three presented fiber laser approaches are introducing fascinating methods for the generation and acquisition of SRS images e.g. fast acquisition of SRS images or video-rate wavelength tuning. However, each approach has its own short coming in terms of laser power, a complicated detection scheme based on balanced detection or expensive components such as Ti:Sapphire lasers. In the next section, I will present an approach of an all-fiber laser system that offers a superior noise level suitable to acquire SRS images without the need

of balanced detection.

4.5.2 General outline

The approach in focus differs fundamentally from the previously presented fiber laser schemes. Instead of utilizing a solid-state laser or relying on the stability of SC generation, the laser leverages the principle of an all normal dispersion (ANDi) laser [51] and pulse pattern manipulation [53][52]. After the presentation of the fiber laser source, its capabilities will be demonstrated by acquiring coherent Raman images of living human cells and multimodal images of mouse tissue.

4.5.3 Master laser cavity

The laser scheme that is depicted in figure 4.42 can be divided into two parts: the part of the laser that is responsible for generating the Stokes laser beam and the one for the pump laser. Since the pump beam generation directly depends on the generation of the Stokes beam, the Stokes beam generation will be highlighted first. The laser cavity for the Stokes beam is a passively modelocked femtosecond (fs) fiber laser cavity with a center wavelength of 1 μm. The cavity consists of a highly-doped ytterbium fiber, a drop-in polarization controller (PC), spectral filtering (SF) and a fiber-based integrated module (OIM). The OIM comprises the functions of polarization-sensitive isolation, pump/signal multiplexing and signal extraction. Since the laser cavity is based on an all-normal dispersion laser, passive mode locking is achieved by non-linear polarization rotation (NPR) [139][140]. NPR leverages the effect of intensity dependent polarization rotation. In order to explain this effect, figure 4.43 displays a Gaussian shaped laser pulse with linear polarization in the temporal regime. The intensity of the laser pulse in the middle is higher than at the edges of the pulse. Consequently, the polarization is shifted stronger in the mid position than at the edges. As a result, when traveling within the fiber cavity the overall polarization of the pulse is shifting from linear to elliptical. By carefully tuning the polarization controller, one can tune the polarization state of the middle in such a way, that the OIM only allows the highest portion of the pulse to pass and rejects the rest. That way, the laser pulse's edges are clipped and only the center of the pulse is allowed to circulate in

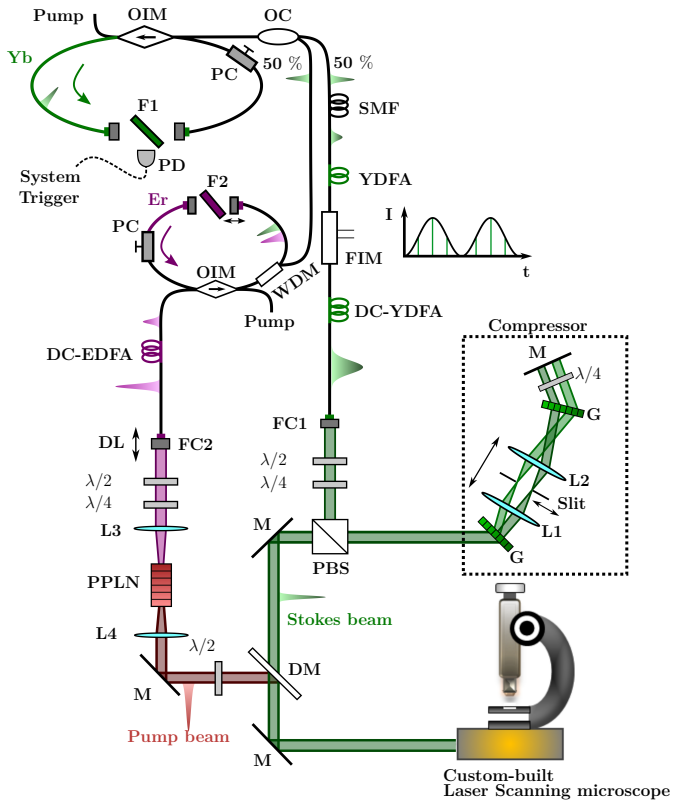

Figure 4.42: **Fiber laser scheme for SRS imaging**
The laser system consists of two fiber laser oscillator which are arranged in a master/slave configuration. The master oscillator consists of an optical isolator module (OIM), a ytterbium-doped (Yb) nonlinear fiber, a band-pass filter (F1), and a polarization controller (PC). The output is split into two parts. One part is serving as synchronization injection for the slave oscillator. The second part is introduced into the Stokes branch. Here, the pulse is stretched by introducing excessive amount of GVD by traveling through 50 m of singlemode fiber. The stretched pulse is then amplified in a ytterbium-doped fiber amplifier (YDFA) and intensity modulated with a fiber-based intensity modulator (FIM). The modulated pulse is then again amplified by a double-cladded (DC)-YDFA and launched into free-space. Finally, the beam is compressed by a grating compressor consisting of gratings (G), a $\lambda/4$ wave plate and a mirror (M). The pump oscillator is similarly build with the addition of a wavelength-division multiplexer (WDM) as the injection port. Instead of the highly-doped ytterbium fiber an erbium fiber is employed. The output of the pump oscillator is amplified by a DC-Erbium-doped fiber-amplifier (DC-EDFA). The beam is then launched into free-space and focused into a periodically-poled lithium-niobate (PPLN) crystal which frequency-doubles the beam. After combining the pump with the Stokes beam, they are coupled into the custom-built microscope. The leaked beam that originates from the reflection of the intra-cavity filter is utilized as system trigger for the modulation of the Stokes beam (adapted from [136]).

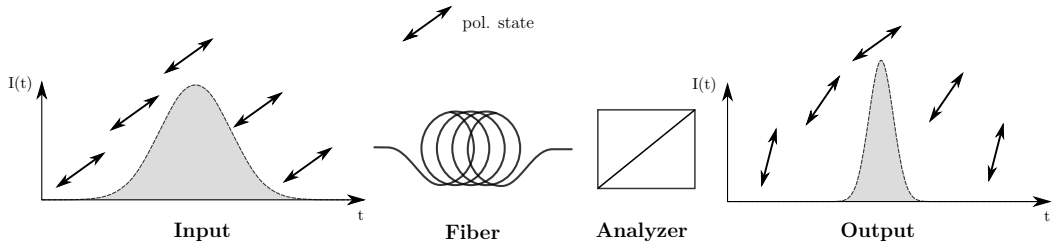

Figure 4.43: **Nonlinear polarization rotation**
The left diagram displays the temporal intensity of a Gaussian pulse. The arrows on top of the curve show the temporal polarization state. When traveling through a fiber, the polarization state is changed due to the nonlinear polarization rotation (NPR). The amount of change depends on the temporal intensity and is thus the highest in the center of the pulse. The effect of placing an analyzer at the exit of the fiber and the resulting pulse profile and temporal polarization state are shown in the right diagram. As it can be seen, due to the difference in polarization between the center and the edges, the pulse is shaped (adapted from [141]).

the cavity. Since no external control is necessary to achieve this state of operation, the laser cavity is self-starting and self-stabilized. The laser cavity is pumped by a 976 nm laser diode that is injected through the OIM. The center wavelength of the cavity is initially defined by the emission spectrum of the nonlinear fiber which can be tuned by the utilized length. In order to support oscillation away from the typical high-gain window and to suppress occurring amplified spontaneous emission (ASE), spectral filtering is exploited. Here, a free-space filter (F1) with a 4 nm band-pass located around the center wavelength is introduced into the cavity between two fiber collimators. By carefully turning the filter, the center wavelength can be shifted allowing coarse tuning of the laser cavity's center wavelength. Next to the filter, a $\frac{\lambda}{2}$ wave plate was inserted allowing reproducible fine tuning of the pulse's polarization state. Since the laser source should be suitable for coherent Raman applications in tissue and cells, the center wavelength was chosen to be 1010 nm exploiting the higher penetration depth of near-infrared light due to the low absorption coefficient of water. This cavity is from now on referred to as the master cavity. In order to perform high sensitivity measurements such as stimulated Raman scattering (SRS) with high-speed, the repetition rate of the laser cavity is designed to be 80 MHz allowing a theoretical maximum modulation frequency of 40 MHz. Finally, the cavity output is split into two parts utilizing a 50:50 fiber optic coupler. One portion is directed to the

pump cavity as an injection pulse and the second portion is fed into the Stokes branch.

4.5.4 Stokes branch

Within the Stokes branch, the pulses are amplified, modulated, spectrally filtered and finally temporally compressed yielding ideal pulse characteristics for coherent Raman applications. In order to efficiently amplify the Stokes pulse, the fiber chirped-pulse amplification (FCPA) scheme is exploited [142]. It is the fiber based version of the chirped pulse amplification (CPA) [55] which is one of the most important methods in modern laser technology. Amplifying the pulse by a typical amplification stage would yield such a high energy density inside the fiber that it facilitates the presence of higher-order effects. These are, however, not desirable since they strongly modify the spectral and temporal shape of the laser pulse as well as reduce the efficiency of the amplification stage. Thus, prior to amplifying the pulse, it has to travel through 50 m of SMF introducing sufficient chirp and thereby reducing the temporal energy density. Now, the pulse is amplified by a core-pumped Yb-doped fiber amplifier (YDFA). Since the ytterbium-dopded fiber (YDF) is backward pumped, the laser cavity has to be protected by a fiber isolator with high efficiency around 1100 nm. Otherwise, the backward-propagating light is entering the cavity producing ASE and lasing around 1300 nm destabilizing the self-starting operation of the cavity. After amplification, the pulses are optionally modulated by a 20 MHz sinusoidal waveform through a fiber-coupled intensity modulator (FIM). The reference frequency of the 20 MHz waveform is being generated from a photodiode signal of the master cavity. Here, the reflection of the utilized band-pass filter is directed onto the photodiode. This 80 MHz signal is then frequency divided and fed as the reference frequency into the frequency generator that provides the 20 MHz signal. Without a proper reference, the laser pulses would shift arbitrarily underneath the modulation resulting in an unstable and unoptimized SRS signal. The FIM is capable of achieving a modulation depth of >20 dB. After modulation, the pulse has to pass the final stage of amplification by traveling through a cladding-pumped doubled-cladded YDFA. The pumping is accomplished by a multimode fiber coupled pump laser diode

(MMFPLD) resulting in an amplified Stokes beam of >1 W. This pulse is then launched into free-space. Since the polarization of the beam is yet undefined, the beam's polarization can be controlled by a $\frac{\lambda}{2}$ and $\frac{\lambda}{4}$ wave plate.
Before overlapping the Stokes and the pump beam, the chirp of the Stokes beam has to be compensated for. Therefore, a grating compressor is introduced into the beam path. The grating compressor operates with the folded 4-f scheme. The beam hits the initial grating that disperses the beam into its spectral components. A second grating in a predefined distance is utilized to form a collinear beam so that the spectral components are spatially encoded. A mirror reflects all components back again and the beam then travels back through both gratings. Since the gratings introduce a path difference between the spectral components, the initial chirp mainly originating from the SMF is compensated. In order to achieve narrow-band filtering of the Stokes beam, two lenses and a slit are introduced between the two gratings. Here, the spectral dispersed beam is focused onto the slit. By closing and moving the slit, it operates as a tunable filter which can select the passing center wavelength and the width. Furthermore, a $\frac{\lambda}{4}$ wave plate is introduced before the mirror so that the beam polarization experiences a shift by 90°. The polarization shift is being exploited by the polarizing beam splitter cube (PBS) that splits its original Stokes beam from the compressed Stokes beam.

4.5.5 Pump branch

The second part of the Stokes beam, that is split from the master cavity output, is fed into the pump beam cavity and is referred to as slave cavity. In general, this cavity resembles the master cavity. It is also designed as an ANDi cavity and is comprised of an inline PC, OIM, SF, an OIM and a heavily-doped nonlinear fiber. In addition to that, a wavelength-division multiplexing (WDM) coupler is inserted into the cavity acting as the injection port of the Stokes beam. Without the external injection, the cavity would operate in the quasi-continuous wave (CW) regime at around 1.5 μm. Quasi-continuous wave regime describes the state of the cavity when it produces pulses with the width in the order of ns [50]. As the gain medium a double-cladded erbium/ytterbium fiber (DC-EY) is utilized. By carefully tuning the tunable narrow-band filter (F2) with a bandwidth

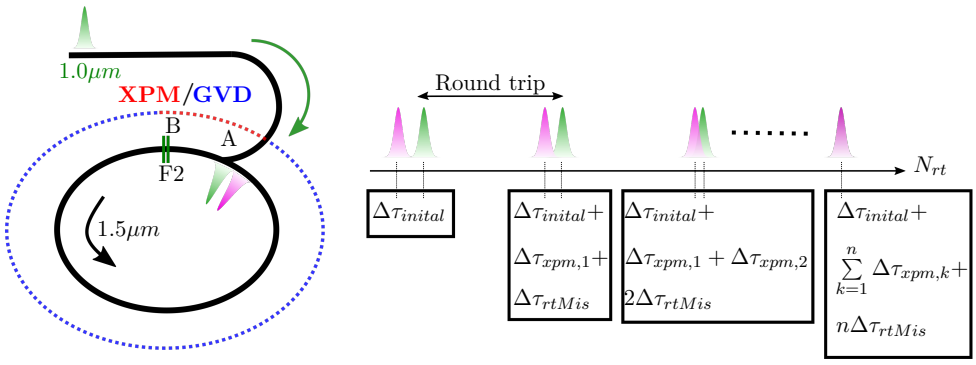

Figure 4.44: **Automatic synchronization of the slave cavity**
The sketch shows the principle of the automatic synchronization between the master and the slave cavity. The injection pulse enters the cavity through a WDM and then travels together with the pump pulse through the cavity. However, since the band-pass filter F2 blocks the injection pulse, the path on which both beams travel together is limited. Thus, the timing between the master and slave oscillator needs to be adjusted as fine as possible. Throughout a couple of round trips, the initial timing difference $\Delta\tau_{initial}$ is further reduced with every round trip. This is because the wavelength of both pulses is altered by cross-phase modulation. The timing mismatch is reduced with every round trip by the nonlinear effects until the mismatch is zero (adapted from [136]).

of <1nm, the center wavelength can be selected. When introducing the Stokes beam with a suitable power level into the cavity, the equilibrium within the cavity is perturbed resulting in pulses perfectly mimicking the incoming pulses. If the cavity mismatch between the master and slave cavity is small enough e.g. <200 μm, the slave cavity is self-synchronizing to the master cavity. This behavior is based on the combined effect of NPR, cross-phase manipulation (XPM), group velocity dispersion (GVD) as well as chromatic dispersion.

In order to illustrate the effect of auto-synchronization, figure 4.44 shows a schematic of the cavity. Here, the cavity itself is shown as the black ring which is divided into two parts that are either governed by the XPM effect or by GVD. For the sake of simplification, we assume that within the cavity there is already a pulse oscillating with a temporal mismatch $\Delta\tau_{initial}$ to the injected pulse train. Each round, the mismatch is increased or decreased further by the difference in the repetition rate between the two cavities t_{rtMIS}. Because of the naturally occurring dispersion, the interaction length on which both beams do co-propagate and may interact with each other is finite. This interaction length can be confined

additionally by introducing a filter (F2), that blocks the injected pulse. Thus, the interaction can only occur on the path between A and B and is thus governed by the XPM effect. XPM leads to the addition of a temporal phase to both pulses resulting in a timing-dependent wavelength shift. Depending on the timing, the 1.5 μm pulse is either blue-shifted or red-shifted. Because the center wavelength experiences a net anomalous dispersion, the wavelength shifting is directly translated into a temporal shifting $t_{xpm,n}$, where n stands for the number of round trips. A blue-shift results in a slower timing while a red shift means a faster timing. The maximum temporal mismatch that can still be compensated by this method is defined by the interaction length L_{AB}.

Figure 4.45 shows a simulation of the temporal mismatch with and without the injection of a pulse of the master cavity. The simulation is based on a split-step Fourier method [50] that derives the solution numerically. This method is based on the approximation that on a small distance the linear and nonlinear effects within the fiber act independently (further details can be found in [136]). Assuming an initial positive mismatch between the master and slave oscillator (a), the mismatch is evolving over the number of round trips in a linear manner when no interaction takes place. However, when injecting the pulse of the master cavity (b), the mismatch between the cavities is reduced until the mismatch equals zero. Within the simulation, it takes around 50 round trips in order to compensate for the initial mismatch. Since one round trip takes 12.5 ns (equaling a repetition rate of 80 MHz), the compensation is achieved after 625 ns. The situation is similar when assuming a negative temporal mismatch between the two cavities. Again, the temporal mismatch is linearly evolving over time when no synchronization takes place. When the pulse of the master cavity is injected (d), synchronization is achieved after 50 round trips.

XPM also plays a crucial role in the explanation of the mimic effect of the slave cavity. This effect is known as additive pulse mode locking and has already been demonstrated [52][53][143]. Here, the combination of SPM and XPM forces the polarization of the pulse to evolve depending on the temporal intensity. Thus, by carefully tuning the intra-cavity polarization and selecting only the high power pulses, the cavity is forced to reproduce the injected pulses. Exploiting this effect results in a low-noise cavity which in combination with the master oscillator is a

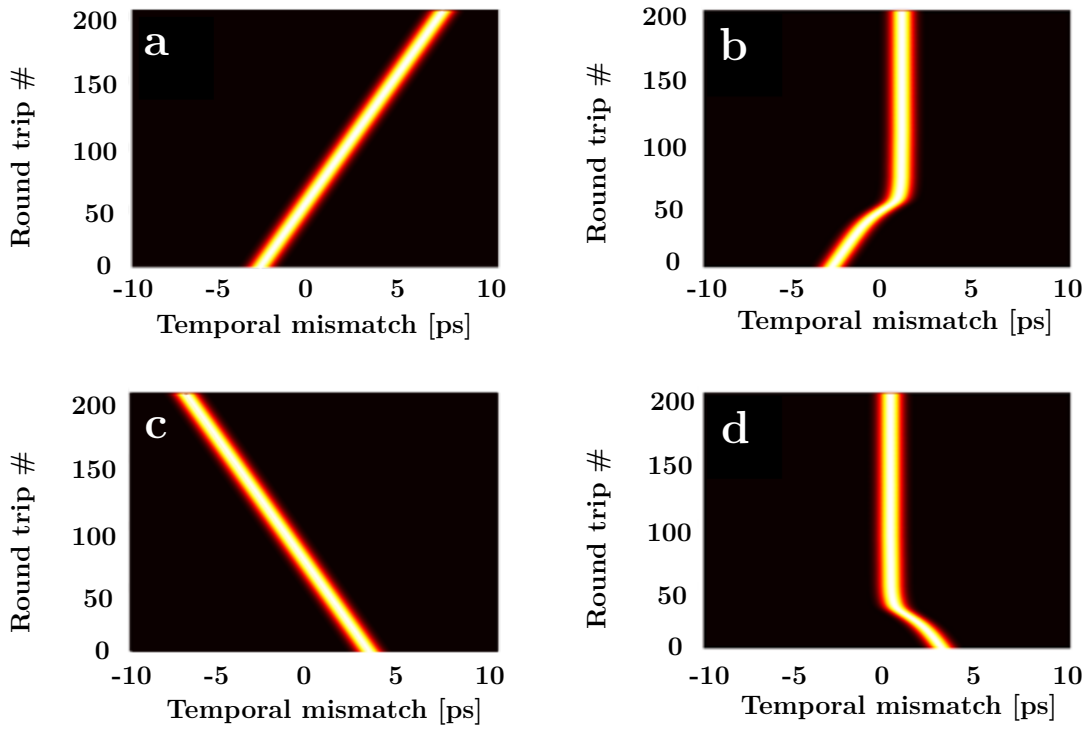

Figure 4.45: **Evolution of temporal mismatch between master and slave oscillator** The simulations show the temporal evolution between the master and the slave oscillator with and without injecting the synchronization pulse. In the first case (a), the temporal mismatch is positive and no synchronization is taking place. When a pulse is injected (b), the temporal mismatch is reduced to zero and stabilized after a couple of round trips. In the second case (c), the initial temporal mismatch is negative. With synchronization (d), the mismatch is again reduced to zero after a couple of round trips (images taken from [136]).

suitable source for SRS experiments.
The pump beam is coupled out of the cavity by the OIM. Centered at around 1.5 μm, the pulse is then amplified to 1 W in a double-cladding erbium/ytterbium-doped fiber amplifier (DC-EDFA). Since the output pulses are already in the ps regime, the occurrence of higher-order effects is reduced due to the low temporal intensity. Finally, the pump beam is launched into free-space by a fiber collimator. Now, it needs to be frequency-doubled in a periodically-poled lithium niobate (PPLN) crystal. Therefore, in order to optimize the doubling efficiency, the polarization of the pump beam is controlled via a $\frac{\lambda}{4}$ and $\frac{\lambda}{2}$ wave plate and focused into the PPLN crystal. The frequency-doubled part is then collected with a second lens. In order to match the polarization of the beam to the polarization of the Stokes beam, a $\frac{\lambda}{2}$ wave plate is utilized to turn the polarization by 90°.
The spatial overlap is accomplished by a dichroic mirror (DM). In addition the part of the pump beam that is not frequency-doubled is filtered out. The temporal overlap is optimized by mounting the fiber collimator of the pump beam, that launches the beam into free-space, on a delay stage (DL). Now, the combined beam is directed into the custom-built laser scanning microscope, that has been previously presented (see section 3.5).

4.5.6 Characterizing the laser source performance

Before starting the coherent Raman experiments, the laser source itself is characterized in terms of its stability, modulation depth and the timing jitter between the pump and Stokes beam. Figure 4.46 summarizes the characteristics of the two-color fiber laser source. Figure 4.46(a) shows the two pulse trains of the laser source. The Stokes beam in green, the pump beam in red. Analyzing the modulation depth of the Stokes beam with a radio-frequency (RF) spectrum results in a modulation depth of $> 99\%$ or 67 dB at 20 MHz. Figure 4.47 displays the RF spectra of the pump and Stokes beam as well as of the Stokes beam with active modulation. Here, the modulation depth of the fundamental 80 MHz signal is 74 dBm (a) and 73 dBm (c) for Stokes and pump beam, respectively. Analyzing the modulation depth of the modulation (b) shows the aforementioned 67 dBm. Note that there are no neighboring peaks or frequency components next to the

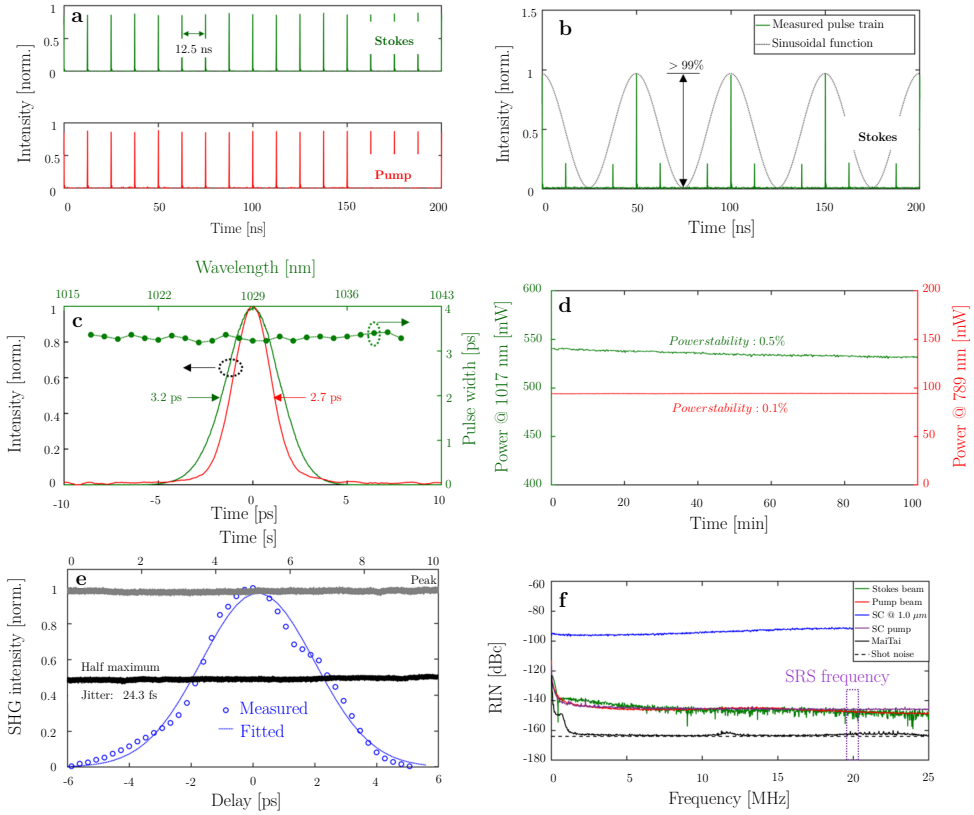

Figure 4.46: **Temporal characterization of the fiber laser source**
(a) The pulses of the pump and Stokes beam are shown on a timescale of 200 ns. The temporal distance between two pulses is 12.5 ns equaling a repetition rate of 80 MHz. (b) The modulation depth that is achieved with the fiber-based intensity modulator is about 99%. In green the Stokes laser pulses are depicted and in black the resulting sinusoidal waveform. (c) The temporal pulse profile of the Stokes and pump beam are depicted in green and red, respectively. When tuning the Stokes beam from 1015 nm to 1040 nm, the pulse length stays the same which plays an important role in the acquisition of hyperspectral data sets. (d) The long-term stability is shown for a time frame of 100 min. This time frame corresponds to the acquisition of a hyperspectral data set or an extensive 3D scan of a sample. (e) Characterization of the timing jitter was found to be in the order of 24.3 fs. Here, both beams are focused into a BBO crystal and the SFG signal is detected. (f) Visualization of the RIN noise in comparison with other laser systems that are utilized for SRS imaging. Since the modulation frequency is about 20 MHz, the RIN noise around this frequency is critical for SRS imaging (adapted from [136]).

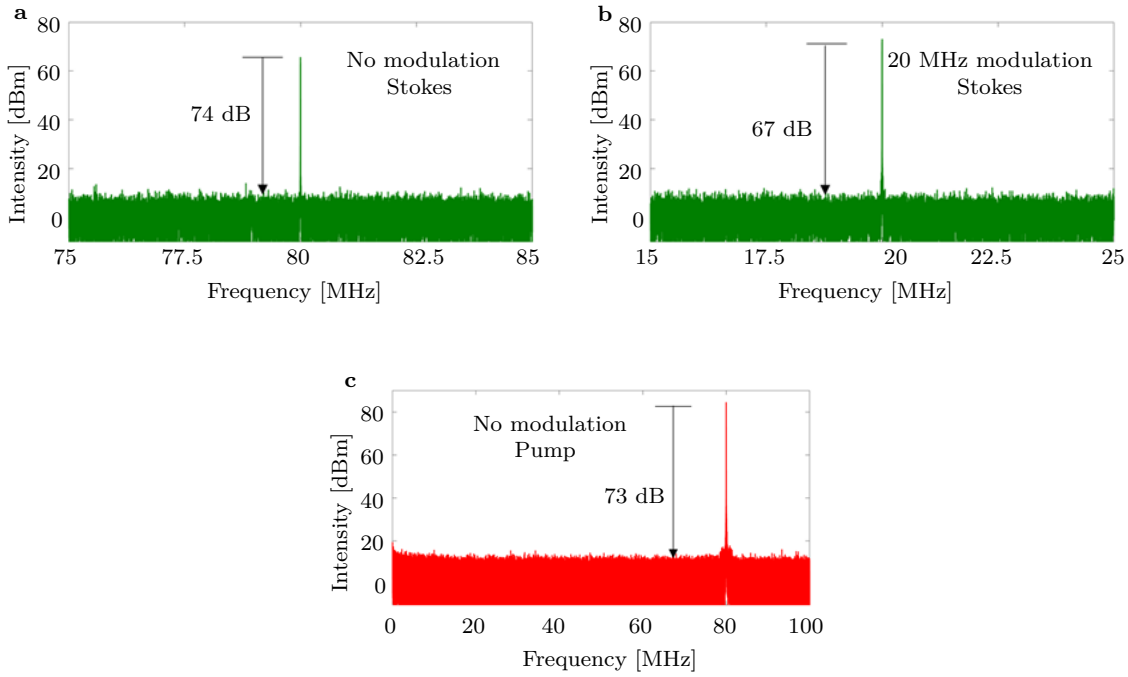

Figure 4.47: **RF spectrum of the pump and Stokes laser source**
(a) RF spectrum of the Stokes beam without modulation indicates a signal-to-noise ratio of 74 dB. (b) RF spectrum with modulation of the Stokes beam indicates a modulation depth of 67 dB. (c) RF spectrum of the pump laser beam with no modulation present (adapted from [136]).

fundamental 80 MHz or the modulation frequency. This is one of the key requirements for efficient SRS signal generation. The pulse widths of the Stokes and the pump beam are measured to be 2.7 ps and 3.2 ps, respectively. Surprisingly, when tuning the center wavelength of the Stokes beam, the pulse width is stable and changes only by a few tens of fs (3.2 ± 0.06 ps). This measurement indicates that this fiber laser source is superior to commonly utilized bulky OPO systems when it comes to pulse width stability. The power stability that is shown in figure 4.47(d) displays the excellent long term stability of the laser system. Even when longer measurements over the course of more than 100 min are performed, the power varies only by 0.5% and 0.1% of the initial power for the Stokes and pump beam, respectively.

An interesting parameter in terms of stability is the timing jitter of both laser cavities since they are passively synchronized without any feedback. Therefore, the pump and Stokes beam are both focused collinearly into a beta-barium borate (BBO) crystal and the sum frequency generation (SFG) signal is being monitored. By carefully tuning the temporal overlap between the Stokes and pump beam, a cross-correlation trace is being measured, displayed in figure 4.47(e) as the blue circles. Additionally, the temporal behavior of the SFG signal at t = 0 ps (gray curve) and t = 2 ps (black curve), resembling the half-maximum of the SFG signal, is measured. The timing jitter was then found to be approximately 24.3 fs.

The relative intensity noise (RIN) of a laser is a key parameter for high sensitivity measurements such as SRS and should ideally be as low as possible. Normally, in most fiber laser based approaches one of the two laser sources for coherent Raman measurements is contaminated with a high RIN e.g. resulting in the necessity of applying balanced detection schemes. Figure 4.47(f) compares the herein presented fiber laser source to a solid-state MaiTai laser (black line) symbolizing the shot-noise limit and a typical fiber based supercontinuum (SC) approach (blue line). As it can be seen, the SC approach possesses a RIN of >-100 dBc around 20 MHz while the MaiTai offers a RIN of >-160 dBc. Both laser cavities, pump and Stokes, exhibit a RIN close to -140 dBc. After the amplification stages, the RIN is slightly increased but is still improved by 50 dBc compared to the typical SC approach.

In the next step, the tuning capabilities of both laser cavities are tested. Figure

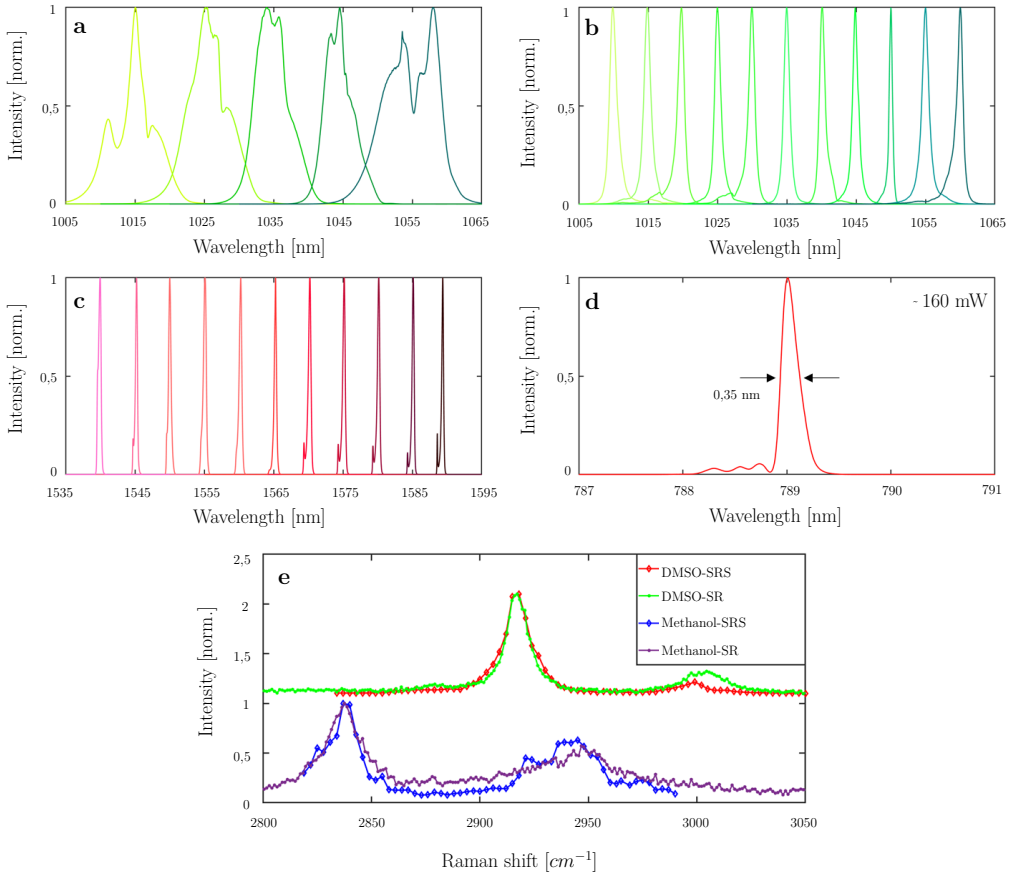

Figure 4.48: **Spectral characterization of the fiber laser source**
(a) Spectrum of the Stokes beam when coarsely tuning with the intra-cavity filter. (b) Tuning of the Stokes beam with the slit in the compressor results in finer tuning capabilities. (c) Tuning of the pump beam with the intra-cavity filter. (d) Spectrum of the frequency-doubled output of the pump branch results in a spectrum with a FWHM of 0.35 nm. (e) Comparison of spontaneous Raman measurements and hyperspectral SRS imaging of DMSO and Methanol. The DMSO spectrum has an offset for improved visibility (adapted from [136]).

4.48(a-c) illustrates the tuning behavior for the Stokes and pump beam. Figure 4.48(a) shows the tuning of the Stokes cavity by turning the intra-cavity filter. The tuning range is ranging from 1010 nm to 1060 nm with a bandwidth of 4 nm. Figure 4.48(b) displays the fine tuning capabilities of the Stokes branch when the slit in the grating compressor is utilized resulting in an effective bandwidth of 1 nm. In comparison, the pump beam cavity can be tuned from 1540 nm to 1690 nm by turning the intra-cavity filter (figure 4.48(c)). Figure 4.48(d) shows the SHG spectrum of the pump beam at 1578 nm. The spectral width is found to be 0.35 nm which results in a transform-limited Gaussian pulse width of 2.6 ps. This value is in good accordance with the prior measured pulse width of the pump beam (figure 4.48(c) - 2.7 ps). Combining the pump beam and the Stokes beam tuning capabilities results in a wavenumber tuning range of 2700 cm^{-1} to 3550 cm^{-1} covering the important higher wavenumber region. Figure 4.48(e) illustrates the spectral capabilities of the fiber laser source. Here, two hyperspectral SRS spectra were acquired and compared to their Raman spectrum. The upper spectrum belongs to dimethylsulfoxid (DMSO), the lower to Methanol. The red dotted and blue dotted lines belong to the hyperspectral SRS signal. The reference Raman measurements have been acquired on the previously presented Raman system (see section 3.8.2) and are depicted in green and purple. As it can be seen, both curves, hyperspectral SRS and Raman are in good accordance to each other.

4.5.7 Imaging performance of the new laser source

In the following, the imaging capabilities of this multimodal laser source are demonstrated by imaging living human cells and mouse tissue sections. Figure 4.49(a-d) displays CARS and SRS images of living osteosarcoma (U2OS) cells that have been simultaneously acquired. The targeted Raman resonance has been the CH_2 stretching mode that lies around 2845 cm^{-1} which is predominately associated with lipids. Thus, the images identify lipid-rich regions such as naturally occurring lipid droplets inside the cells. The focal powers for the pump and Stokes beam are set to 33 mW and 74 mW, respectively. The pixel dwell time has been 12.5 μs and the time constant of the lock-in amplifier (LIA) has been

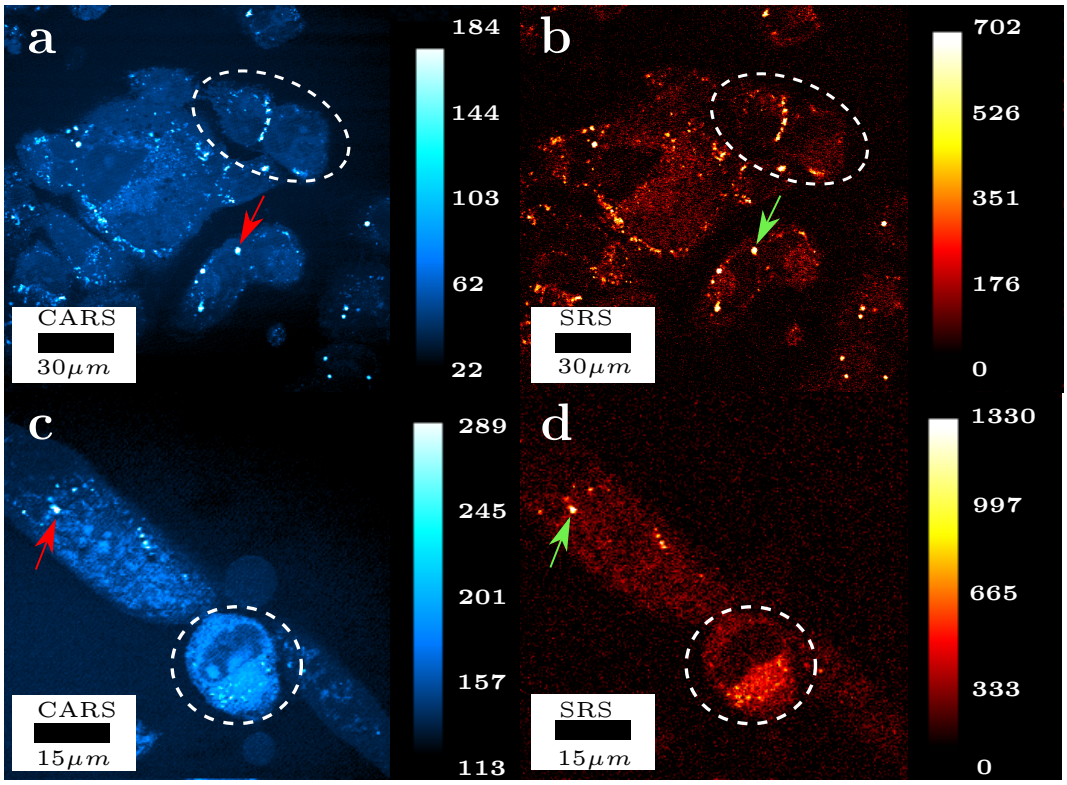

Figure 4.49: **CARS and SRS imaging of cells**
(a) & (b) are displaying the false-color coded CARS and SRS image of living U2OS cells respectively. The red/green arrow indicates an isolated lipid vesicle and the encircled region demonstrates the presence of the non-resonant background in the CARS image which is not present in the SRS image. (c) and (d) show images of living PMD cells. Imaging these cells is challenging due to the overall lower lipid content of the cells. Again, the arrow indicates an isolated lipid vesicle and the region demonstrates the background-free imaging quality of SRS (adapted from [136]).

2 μs. As it can be seen in figure 4.49(a), the CARS image is still showing the cell's structure and the inner compartments. The SRS image in figure 4.49(b) appears darker than the CARS image suggesting a lower contrast. However, comparing the background signal of the cell or the cell medium with the intensity of the lipid droplets (dashed white circle), the advantage of SRS becomes apparent. Since SRS is insensitive to the non-resonant background whereas in CARS the non-resonant background itself is emitting a signal, the contrast of the SRS image is higher and more specific to the targeted Raman resonance than the CARS image. Within the cells, individual lipid droplets (red/green arrow)

can be clearly identified. Figure 4.49(c-d) is showing the images of living differentiating primary myoblast (PMD) cells. Since it appears that the PMD cells contain a lower amount of lipid droplets the pixel dwell time is quadrupled to 51.2 μs. Accordingly, the time constant of the LIA was set to 20 μs. The focal power was set to 25 mW and 47 mW for pump and Stokes beam. Again, the SRS image shows a superior imaging contrast compared to the CARS image. Here, the contribution of the non-resonant background can be clearly seen in the area indicated by the white dashed circle. The inner parts of the nucleus can be seen in the CARS image resembling more a white light image, while the SRS images show no sign of its presence and only display the chemical contrast of the 2845 cm^{-1} resonance. Furthermore, the CARS image slightly suffers from the rolling ball effect seen by the decreasing intensity of the non-resonant background signal of the buffer going from high intensity next to the cell to low intensity at the edges of the image.

In the next step a cryo section of a 2-month old mouse's superior vena cava has been analyzed by acquiring CARS and SRS images simultaneously. The section has been embedded into paraffin and cut into 50 μm thick slices with a cryo microtome. The paraffin is protecting the delicate sample from rupture and overheating. The section is then placed on a glass coverslip. Figure 4.50(a) shows a bright-field image of the tissue with 4x magnification. The blue dashed line indicates the position of the superior vena cava. Within this area, two regions of interest (ROI) were selected that have been analyzed with CARS and SRS. Figure 4.50(b-c) is showing the CARS and SRS image of the red ROI. It consists of multiple images stitched together by utilizing Fiji. The power is set to 33 mW and 74 mW for pump and Stokes beam, respectively, and the targeted wavenumber was set to 2845 cm^{-1}. The pixel dwell time was set to 6.4 μs and the time constant of the LIA to 2 μs . The images are suitable for discriminating the different parts of the tunica by their amount of lipids, highlighted by the magenta dashed line: the tunica intima and the tunica media. Furthermore, it has been possible to identify a thrombus-like region adherent to the tunica intima. The yellow inset is a magnification of the dashed yellow encircled region. Here, the clustering of red blood cell can be easily detected by their characteristic shape.

The second ROI (figure 4.50(d-e)) is displaying the lipid-rich tunica media. Com-

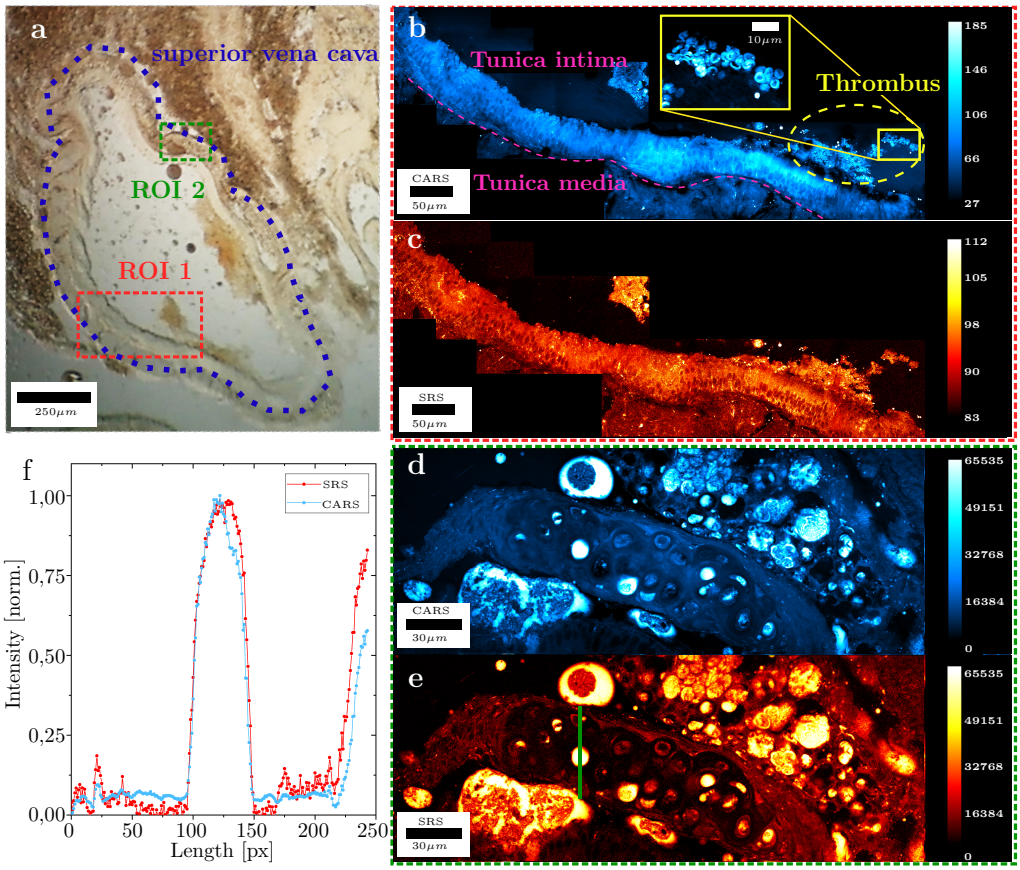

Figure 4.50: **CARS and SRS imaging of a cryo-section of a murin superior vena cava** (a) shows a bright light image with 4x magnification of the cryo section. The blue dashed line illustrates the location of the superior vena cava and the two ROIs we chose for coherent Raman imaging. (b) and (c) are displaying the CARS and SRS images of ROI 1, respectively. The images are consisting of multiple single images stitched together. The magenta line is a guide to the eye to discriminate between the tunica intima and the tunica media. The inset shows a magnification of the thrombus-like area. (d) and (e) are showing the CARS and SRS images of ROI 2. Again, multiple images were captured and stitched together. The green line indicates the position from which a line scan was taken (f). Here, it can be seen, that the SRS signal (red) shows more features and is thus more sensitive to lower concentrations than CARS (adapted from [136]).

pared to ROI 1, it seems that the local concentration of lipids caused the tunica media to collect lipids in abundance. The focal power and pixel dwell time is unchanged. The green line in figure 4.50(e) indicates the location of the line scan shown in figure 4.50(f). By normalizing the maximum intensity, small features e.g. lipid droplets can be seen in the SRS image that are not present in the CARS image confirming the higher molecular sensitivity of SRS.
In order to showcase the capability of the laser source to produce multimodal images with the Stokes beam, the slit within the grating compressor is removed. Thus by tuning the Stokes beam to 1025 nm with a bandwidth of 8 nm the beam has a pulse width of about 200 fs. Figure 4.51 (a) shows a SHG image of an unstained mouse tail on a glass coverslip. The polarization state is controlled via a $\frac{\lambda}{4}$ and $\frac{\lambda}{2}$ wave plate. The applied focal power was set to 20 mW. The SHG signal originates mainly from highly arranged collagen fibers within the tail (see also section 4.3.2). By turning the polarization of the Stokes beam, it can be seen, that different positions of the mouse tail were highlighted depending on the orientation of the collagen. Figure 4.51(b-c) is displaying two-photon excited fluorescence (TPEF) image of mouse kidney sections. The utilized fluorescent agents have been Alexa Fluor 568 phalloidin (b) and Alexa Fluor 488 (c). The focal power for generating these images has been 20 mW. Finally, a 200 μm thick mouse brain section was prepared between two glass coverslips. The mouse expresses yellow fluorescent protein (YFP) in layer-V pyriamidal neuron (Thy1-YFP H-line) that has been excited with a focal power of 50 mW. A z-scan of this sample is shown in figure 4.51(d) as a 3D constructed image. Here, every 1 μm a TPEF image was collected resulting in a 145 μm depth of the z-scan. Figure 4.51(e) illustrates one particular image plane of the z-scan visualizing the neurons and axons.

4.5.8 Conclusion

Compared to the previously presented approaches for an all-fiber laser source, the herein presented laser system offers superior suitable power levels, tuning range and noise performance. Apart from being able to generate multimodal images based on TPEF or SHG, the laser source is suitable as a laser source for CARS

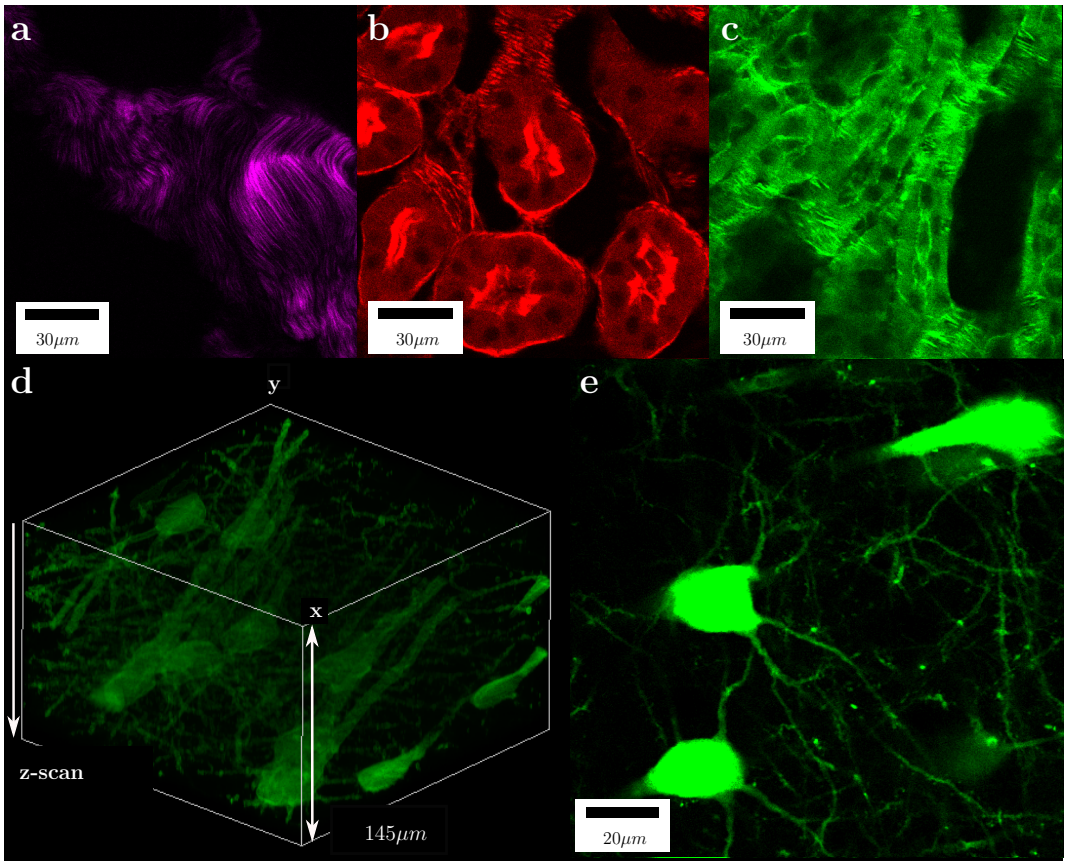

Figure 4.51: **Multimodal imaging capabilities illustrates the versatility of the fiber laser source**
(a) SHG image of highly oriented collagen fibers in an unstained mouse tail (b) and (c) show TPEF image of mouse kidney sections. The utilized fluorescent markers are Alexa Fluor 568 phalloidin (b) and Alex Fluor 488 (c). (d) shows the TPEF of YFP that was expressed within the neurons of a mouse brain sample in 3D constructed image. (e) is one particular plane of the constructed 3D image highlighting the neural network within the brain (adapted from [136]).

and SRS imaging without the need for balanced detection. Thus, it would be possible to attach this laser system to any (inverted) laser scanning microscope that has a suitable detector installed or even to an endoscopy system. This possibility facilitates the application of CARS and SRS to clinical applications. Note, that the previously described free-space components such as filters or the pulse compressor can be replaced by fiber based equals realizing a truly all-fiber based laser system.

5 Conclusion

The application of coherent Raman scattering techniques to biomedical questions enabled us to observe a well-defined system with minimal perturbation of the system's hidden dynamics. The presented advanced optical microscopy system is capable of multimodal imaging such as CARS, SHG and fluorescence imaging.
Multimodal imaging has been successfully showcased in the analysis of the osteogenic differentiation of stem cells. After initial verification of the successful induction of the stem cells through the application of rt-PCR, the differentiation was followed by CARS and SHG imaging of the sample as well as by staining with Alizarin Red S and spontaneous Raman spectroscopy. A unique sample holder was designed in order to satisfy the various requirements for Raman spectroscopy, CARS imaging utilizing a 4π arrangement as well as for the growth of stem cells. In a next step, the method could be applied to study other stem cells and their differentiation process.
The influence of a high background signal originating from laser induced fluorescence has been successfully reduced, as seen in subsection 4.2. In this study, a modulation approach was utilized in order to isolate the modulated CARS signal from the unaffected fluorescence signal. Thus, it was possible to study the lipid metabolism of an algae strand which is a promising candidate for upscaled biofuel production. Compared to other algae strands, the rigid cell walls were impenetrable for fluorophores such as Nile Red. The results of 3-dimensional CARS images were in good accordance with the gravimetric measurements illustrating the powerful capabilities of CARS. In an upcoming study it would be interesting to analyze the metabolism of genetically-modified algae and compare that to the original algae strand. Here, possible scenarios would be a modification that leads to an increase in the maximum oil content of the algae as well as an optimized oil production metabolism.

The recovery of chemical information from a sample by means of hyperspectral CARS has been demonstrated on a number of samples. In the initial step, the whole optical system has been analyzed in-depth in order to increase the reproducibility of the optical setup. As a consequence, the control software of the OPO and the post-processing steps have been optimized yielding a very stable system. This stability is one of the key elements for a successful image analysis by means of dimension-reducing algorithms such as PCA and NNMF. Thus, it has been possible to render the hyperspectral data set to an image highlighting the distribution of lipids and proteins.

The overall performance of the microscope could be enhanced further by implementing adaptive optics. The application of these methods would modify the wavefront of the lasers allowing faster z-scanning capabilities since the sample, objective lens or any other element is not moved. Therefore, the acquisition time for 3-dimensional images as well as possible changes of live-cells are reduced. In order to achieve a qualitative result of the hyperspectral data set, SRS should be employed to get rid of the non-resonant background that influences the results of the utilized algorithms.

In addition to the multimodal solid-state laser system, a fiber laser source was developed that is also capable of multimodal imaging. In a collaborative effort, this fiber laser source comprises a similar functional range to a solid-state laser system with the advantage of being low-cost and of a smaller footprint. As a preliminary stage of an all-fiber laser system fitting in a clinical environment, the system is comprised of fiber optical elements as well as free-space elements. Compared to other fiber-laser approaches that have been presented, the newly developed system is characterized by providing signals with high signal intensity and low RIN. Therefore, the signal acquisition is not subject to the limitations of a balanced detection scheme. In order to overcome the limitations of a confined tuning range, additional laser oscillators utilizing different active fiber materials can be attached to the existing fiber laser system. Such a laser source could extend the tuning range to the wavenumber region of 2100 cm^{-1} which would be interesting when utilizing deuterated Raman tags as labels [144][145][146]. The stability of the fiber laser can be improved by utilizing polarization-maintaining fibers and thus reducing the influence of room temperature changes [147] or in-

duced mechanical stress on the fibers. In addition, it has been reported [51][148] that utilizing a SESAM mirror inside the cavity would further increase the stability due to the improved spectral shape. Finally, the manual wavelength tuning can be optimized by introducing a fast moveable mirror as it has been demonstrated by Ozeki et al [138], enabling tuning speeds in the order of ms.

6 Publications

Label-free in vivo analysis of intracellular lipid droplets in the oleaginous microalga Monoraphidium neglectum by coherent Raman scattering microscopy
Jäger D, Pilger C, Hachmeister H, Oberlander E, Wördenweber R, Wichmann J, Mussgnug JH, Huser T, Kruse O (2016) Scientific Reports 6(1): 35340

Label-free nonlinear optical microscopy detects early markers for osteogenic differentiation of human stem cells
Hofemeier AD, Hachmeister H, Pilger C, Schürmann M, Greiner J, Nolte L, Sudhoff H, Kaltschmidt C, Huser T, Kaltschmidt B (2016) Scientific Reports 6(1): 26716

Compact fs ytterbium fiber laser at 1010 nm for biomedical applications
Kong C[§], Pilger C[§], Hachmeister H[§], Wei X, Cheung TH, Lai CSW, Huser T, Tsia KK, Wong KKY (2017) Biomedical Optics Express 8(11): 4921-4932
{ [§] : equal contributions}

Surface-Enhanced Raman Spectroscopy of Carbon Nanomembranes from Aromatic Self-Assembled Monolayers
Zhang X, Mainka M, Paneff F, Hachmeister H, Beyer A, Gölzhäuser A, Huser T (2018) LANGMUIR 34(8): 2692-2698.

Analyzing life-history traits and lipid storage using CARS microscopy for assessing effects of copper on the fitness of Caenorhabditis elegans
Füser H, Majdi N, Hägerbäumer A, Pilger C, Hachmeister H, Greife P, Huser T, Traunspurger W (2018) Ecotoxicology and Environmental Safety 156: 255-262

Pulse length variation causing spectral distortions in OPO-based hyperspectral coherent Raman scattering microscopy
Pilger C, Hachmeister H, Greife P, Weiß A, Wiebusch G, Huser T (2018) Optics Express 26(22): 28312-28322

Identification of a human adult cardiac stem cell population with neural crest origin
Höving A, Merten M, Schmidt KE, Faust I, Ruiz-Perera LM, Hachmeister H, Sommer S, Fujita B, Puehler T, Huser T, Greiner J, Kaltschmidt B, Gummert J, Knabbe C, Kaltschmidt C bioRxiv, 2019

Vibrational spectroscopic imaging and live cell video microscopy for studying differentiation of primary human alveolar epithelial cells.
Vukosavljevic B, Hittinger M, Hachmeister H, Pilger C, Murgia X, Gepp MM, Gentile L, Huwer H, Schneider-Daum N, Huser T, Lehr C-M, et al. (2019) Journal of Biophotonics 12(6): e201800052

High-contrast, fast chemical imaging by coherent Raman scattering using a self-synchronized two-colour fibre laser
Kong C[§], Pilger C[§], Hachmeister H[§], Wei X, Cheung TH, Lai CSW, Lee NP, Tsia KK, Wong KKY, Huser T (2020) Light: Science & Applications 9(1): 25
{ [§] : equal contributions }

7 Acknowledgements

First and foremost I would like to thank Prof. Dr. Thomas Huser for giving me the opportunity to construct this state-of-the-art microscope and providing me with a fantastic infrastructure. Thank you for all the support concerning the collaboration with the University of Hong Kong and throughout my studies in Berkeley. Your guidance and motivation have inspired me throughout my research.
Next, I thank Dr. Gerd Wiebusch for sharing his profound experience and counsel. Thank you for the numerous negotiations with our suppliers concerning technical issues that was always a tremendous help.
Special thanks go to Dr. Christian Pilger. We worked together side by side for more than a decade solving problems and finally designing our awesome microscope. I am grateful for your second view on things. It has been a very creative and motivating working atmosphere in the lab and the office throughout the whole time. Our sightseeing tours in Hong Kong and the badminton matches back home will stay in my memories.
Furthermore, I would like to thank Prof. Kenneth Wong and his research group for the enjoyable stay in Hong Kong and the fruitful discussions. Special thanks go to Dr. Sherry Kong and Dr. Xiaoming Wei for the very productive time in the lab and showing us all the fascinating places in Hong Kong.
In addition I thank Dr. Adam Schwartzberg, Dr. Christoph Kastl and Dr. Christopher Chen for the inspiring time at the Molecular Foundry. Many thanks for the introduction to the variety of indian restaurants around Berkeley, too.
I would also like to thank Dr. Daniel Jäger and Prof. Dr. Olaf Kruse for the very productive collaboration on the algae-related research. Daniel, I really enjoyed your positive view on things and your efficient working style.
For the collaboration on differentiating stem cells I am grateful to Arne Hofemeier

and Anna Höving. Arne, your drive has been really motivating and it was fun to work with you. For the many conversations, their constant interest in coherent Raman scattering and their expertise concerning the murine brain and stem cells, I would like to thank Prof. Dr. Barbara Kaltschmidt and Prof. Dr. Christian Kaltschmidt. It has always been great to have you two around.
Many thanks also go to Prof. Dr. Maike Windbergs and Dr. Branko Vukosavljevic for the fruitful study on alveolar epithelial cells. It has been quite a bit of work but we were finally rewarded with the accepted paper.
For all the studies involving C. elegans, I would like to thank Prof. Dr. Walter Traunspurger and Hendrik Füser for the great collaboration.
I would also like to thank Prof. Dr. Thorsten Glaser and Dr. Stephan Walleck for the collaboration on (hydro-)peroxo diferric complexes. Even though we had a few setbacks, we never gave up and believed in our success.
I also wish to thank Prof. Dr. Dario Anselmetti, Prof. Dr. Nicolas Borghini and Prof. Dr. Andreas Hütten for joining the examination committee.
I would like to express my gratitude to the German-American Fulbright Commission for supporting my research at the Molecular Foundry in Berkeley (CA,USA).
Many thanks go to Jan Lietz, Gian-Luca Anselmetti, Alex Weiß and Paul Greife for their efforts in the CARS lab throughout their theses.
In addition I would like to thank the members of the research group Biomolecular Photonics for the great atmosphere, the team spirit and the awesome Christmas parties.
I am grateful for the support of the mechanical and electronic workshop of the faculty of physics in designing custom-made solutions. Special thanks go to Dieter Gollay, Herbert Bergmeier, Wolfgang Gronemeier and Karl-Heinz Eichner without whom many results of this thesis would not have been possible.
Finally, I would like to thank my family for their continuous support and their patience, especially my wife Sabine and my son Henry. You two have been a true inspiration and moral support throughout every step of the way.

8 Statutory Declaration

I herewith declare that I have completed the present thesis independently making use only of the specific literature and aids. Sentences or parts of sentences quoted literally are marked as quotations; identification of other references with regard to the statement and scope of the work is quoted. The thesis in this form or in any other form has not been submitted to an examination body and has not been published.

Bielefeld, 30.3.2021

Henning Maximilian Hachmeister

Bibliography

[1] Eva Johanna Kubosch, Anke Bernstein, Laura Wolf, Tobias Fretwurst, Katja Nelson, and Hagen Schmal. Clinical trial and in-vitro study comparing the efficacy of treating bony lesions with allografts versus synthetic or highly-processed xenogeneic bone grafts. *BMC musculoskeletal disorders*, 17:77, 2016.

[2] Sacha de Carlo and J. Robin Harris. Negative staining and cryo-negative staining of macromolecules and viruses for tem. *Micron (Oxford, England : 1993)*, 42(2):117–131, 2011.

[3] Alan Merk, Alberto Bartesaghi, Soojay Banerjee, Veronica Falconieri, Prashant Rao, Mindy I. Davis, Rajan Pragani, Matthew B. Boxer, Lesley A. Earl, Jacqueline L. S. Milne, and Sriram Subramaniam. Breaking cryo-em resolution barriers to facilitate drug discovery. *Cell*, 165(7):1698–1707, 2016.

[4] Elizabeth Betts. An introduction to radiography. *Radiography*, 16(2):167, 2010.

[5] A. Delnevo, M. Bandirali, G. Di Leo, C. Messina, L. M. Sconfienza, A. Aliprandi, F. M. Ulivieri, and F. Sardanelli. Differences among array, fast array, and high-definition scan modes in bone mineral density measurement at dual-energy x-ray absorptiometry on a phantom. *Clinical radiology*, 68(6):616–619, 2013.

[6] Olesya V. Stepanenko, Olga V. Stepanenko, Irina M. Kuznetsova, Vladislav V. Verkhusha, and Konstantin K. Turoverov. Beta-barrel scaffold of fluorescent proteins: folding, stability and role in chromophore formation. *International review of cell and molecular biology*, 302:221–278, 2013.

[7] Jakub Chojnacki and Christian Eggeling. Super-resolution fluorescence microscopy studies of human immunodeficiency virus. *Retrovirology*, 15(1):41, 2018.

[8] Wolfgang Hübner, Gregory P. McNerney, Ping Chen, Benjamin M. Dale, Ronald E. Gordon, Frank Y. S. Chuang, Xiao-Dong Li, David M. Asmuth, Thomas Huser, and Benjamin K. Chen. Quantitative 3d video microscopy of hiv transfer across t cell virological synapses. *Science (New York, N.Y.)*, 323(5922):1743–1747, 2009.

[9] Yi Chen, Qi Shen, Sharla L. White, Yesim Gokmen-Polar, Sunil Badve, and Laurie J. Goodman. Three-dimensional imaging and quantitative analysis in clarity processed breast cancer tissues. *Scientific Reports*, 9(1):5624, 2019.

[10] James Jonkman and Claire M. Brown. Any way you slice it-a comparison of confocal microscopy techniques. *Journal of Biomolecular Techniques : JBT*, 26(2):54–65, 2015.

[11] Claudette M. St Croix, Stuart H. Shand, and Simon C. Watkins. Confocal microscopy: comparisons, applications, and problems. *BioTechniques*, 39(6 Suppl):S2–5, 2005.

[12] Giuseppe Vicidomini, Paolo Bianchini, and Alberto Diaspro. Sted super-resolved microscopy. *Nature Methods*, 15(3):173–182, 2018.

[13] Eric Betzig, George H. Patterson, Rachid Sougrat, O. Wolf Lindwasser, Scott Olenych, Juan S. Bonifacino, Michael W. Davidson, Jennifer Lippincott-Schwartz, and Harald F. Hess. Imaging intracellular fluorescent proteins at nanometer resolution. *Science (New York, N.Y.)*, 313(5793):1642–1645, 2006.

[14] M. G. Gustafsson. Surpassing the lateral resolution limit by a factor of two using structured illumination microscopy. *Journal of microscopy*, 198(Pt 2):82–87, 2000.

[15] Mike Heilemann, Emmanuel Margeat, Robert Kasper, Markus Sauer, and Philip Tinnefeld. Carbocyanine dyes as efficient reversible single-molecule

optical switch. *Journal of the American Chemical Society*, 127(11):3801–3806, 2005.

[16] Eva Wegel, Antonia Göhler, B. Christoffer Lagerholm, Alan Wainman, Stephan Uphoff, Rainer Kaufmann, and Ian M. Dobbie. Imaging cellular structures in super-resolution with sim, sted and localisation microscopy: A practical comparison. *Scientific Reports*, 6:27290, 2016.

[17] Rongwen Lu, Wenzhi Sun, Yajie Liang, Aaron Kerlin, Jens Bierfeld, Johannes D. Seelig, Daniel E. Wilson, Benjamin Scholl, Boaz Mohar, Masashi Tanimoto, Minoru Koyama, David Fitzpatrick, Michael B. Orger, and Na Ji. Video-rate volumetric functional imaging of the brain at synaptic resolution. *Nature Neuroscience*, 20(4):620–628, 2017.

[18] Sina Wäldchen, Julian Lehmann, Teresa Klein, Sebastian van de Linde, and Markus Sauer. Light-induced cell damage in live-cell super-resolution microscopy. *Scientific Reports*, 5:15348, 2015.

[19] Viola Mönkemöller, Cristina Øie, Wolfgang Hübner, Thomas Huser, and Peter McCourt. Multimodal super-resolution optical microscopy visualizes the close connection between membrane and the cytoskeleton in liver sinusoidal endothelial cell fenestrations. *Scientific Reports*, 5:16279, 2015.

[20] Lothar Schermelleh, Alexia Ferrand, Thomas Huser, Christian Eggeling, Markus Sauer, Oliver Biehlmaier, and Gregor P. C. Drummen. Super-resolution microscopy demystified. *Nature Cell Biology*, 21(1):72–84, 2019.

[21] Christian Matthäus, Susie Boydston-White, Milos Miljković, Melissa Romeo, and Max Diem. Raman and infrared microspectral imaging of mitotic cells. *Applied spectroscopy*, 60(1):1–8, 2006.

[22] N. Uzunbajakava, A. Lenferink, Y. Kraan, B. Willekens, G. Vrensen, J. Greve, and C. Otto. Nonresonant raman imaging of protein distribution in single human cells. *Biopolymers*, 72(1):1–9, 2003.

[23] Birthe Kann, Herman L. Offerhaus, Maike Windbergs, and Cees Otto. Raman microscopy for cellular investigations–from single cell imaging to

drug carrier uptake visualization. *Advanced drug delivery reviews*, 89:71–90, 2015.

[24] I. Notingher, S. Verrier, S. Haque, J. M. Polak, and L. L. Hench. Spectroscopic study of human lung epithelial cells (a549) in culture: living cells versus dead cells. *Biopolymers*, 72(4):230–240, 2003.

[25] Nicholas Stone, Catherine Kendall, Jenny Smith, Paul Crow, and Hugh Barr. Raman spectroscopy for identification of epithelial cancers. *Faraday discussions*, 126:141–57; discussion 169–83, 2004.

[26] Andrew Downes and Alistair Elfick. Raman spectroscopy and related techniques in biomedicine. *Sensors (Basel, Switzerland)*, 10(3):1871–1889, 2010.

[27] Andreas Zumbusch, Gary R. Holtom, and X. Sunney Xie. Three-dimensional vibrational imaging by coherent anti-stokes raman scattering. *Physical Review Letters*, 82(20):4142–4145, 1999.

[28] Xiaolin Nan, Ji-Xin Cheng, and X. Sunney Xie. Vibrational imaging of lipid droplets in live fibroblast cells with coherent anti-stokes raman scattering microscopy. *Journal of lipid research*, 44(11):2202–2208, 2003.

[29] Christian W. Freudiger, Wei Min, Brian G. Saar, Sijia Lu, Gary R. Holtom, Chengwei He, Jason C. Tsai, Jing X. Kang, and X. Sunney Xie. Label-free biomedical imaging with high sensitivity by stimulated raman scattering microscopy. *Science (New York, N.Y.)*, 322(5909):1857–1861, 2008.

[30] P. Nandakumar, A. Kovalev, and A. Volkmer. Vibrational imaging based on stimulated raman scattering microscopy. *New Journal of Physics*, 11(3):033026, 2009.

[31] Yasuyuki Ozeki, Fumihiro Dake, Shin'ichiro Kajiyama, Kiichi Fukui, and Kazuyoshi Itoh. Analysis and experimental assessment of the sensitivity of stimulated raman scattering microscopy. *Optics Express*, 17(5):3651–3658, 2009.

[32] Conor L. Evans, Eric O. Potma, Mehron Puoris'haag, Daniel Côté, Charles P. Lin, and X. Sunney Xie. Chemical imaging of tissue in vivo

with video-rate coherent anti-stokes raman scattering microscopy. *Proceedings of the National Academy of Sciences of the United States of America*, 102(46):16807–16812, 2005.

[33] Han-Wei Wang, Ning Bao, Thuc L. Le, Cheng Lu, and Ji-Xin Cheng. Microfluidic cars cytometry. *Optics Express*, 16(8):5782–5789, 2008.

[34] Li Li, Haifeng Wang, and Ji-Xin Cheng. Quantitative coherent anti-stokes raman scattering imaging of lipid distribution in coexisting domains. *Biophysical journal*, 89(5):3480–3490, 2005.

[35] Xueli Chen, Chi Zhang, Peng Lin, Kai-Chih Huang, Jimin Liang, Jie Tian, and Ji-Xin Cheng. Volumetric chemical imaging by stimulated raman projection microscopy and tomography. *Nature communications*, 8:15117, 2017.

[36] Ji-Xin Cheng, Andreas Volkmer, and X. Sunney Xie. Theoretical and experimental characterization of coherent anti-stokes raman scattering microscopy. *Journal of the Optical Society of America B*, 19(6):1363, 2002.

[37] Bernhard von Vacano, Lars Meyer, and Marcus Motzkus. Rapid polymer blend imaging with quantitative broadband multiplex cars microscopy. *Journal of Raman Spectroscopy*, 38(7):916–926, 2007.

[38] Thomas Hellerer, Annika M.K. Enejder, and Andreas Zumbusch. Spectral focusing: High spectral resolution spectroscopy with broad-bandwidth laser pulses. *Applied Physics Letters*, 85(1):25–27, 2004.

[39] Charles H. Camp, Young Jong Lee, John M. Heddleston, Christopher M. Hartshorn, Angela R. Hight Walker, Jeremy N. Rich, Justin D. Lathia, and Marcus T. Cicerone. High-speed coherent raman fingerprint imaging of biological tissues. *Nature Photonics*, 8(8):627–634, 2014.

[40] Romedi Selm, Martin Winterhalder, Andreas Zumbusch, Günther Krauss, Tobias Hanke, Alexander Sell, and Alfred Leitenstorfer. Ultrabroadband background-free coherent anti-stokes raman scattering microscopy based on a compact er:fiber laser system. *Optics Letters*, 35(19):3282–3284, 2010.

[41] Israel Rocha-Mendoza, Wolfgang Langbein, and Paola Borri. Coherent anti-stokes raman microspectroscopy using spectral focusing with glass dispersion. *Applied Physics Letters*, 93(20):201103, 2008.

[42] Alberto Lombardini, Vasyl Mytskaniuk, Siddharth Sivankutty, Esben Ravn Andresen, Xueqin Chen, Jérôme Wenger, Marc Fabert, Nicolas Joly, Frédéric Louradour, Alexandre Kudlinski, and Hervé Rigneault. High-resolution multimodal flexible coherent raman endoscope. *Light: Science & Applications*, 7(1):10, 2018.

[43] Aleksandar Lukic, Sebastian Dochow, Hyeonsoo Bae, Gregor Matz, Ines Latka, Bernhard Messerschmidt, Michael Schmitt, and Jürgen Popp. Endoscopic fiber probe for nonlinear spectroscopic imaging. *Optica*, 4(5):496, 2017.

[44] François Légaré, Conor L. Evans, Feruz Ganikhanov, and X. S. Xie. Towards cars endoscopy. *Optics Express*, 14(10):4427–4432, 2006.

[45] Ji-Xin Cheng and Xiaoliang Sunney Xie, editors. *Coherent raman scattering microscopy*. Series in cellular and clinical imaging. CRC Press, Boca Raton and London and New York, 2018.

[46] Geoffrey H. C. New. *Introduction to nonlinear optics*. Cambridge University Press, Cambridge and New York, 2011.

[47] Shuhua Yue, Mikhail N. Slipchenko, and Ji-Xin Cheng. Multimodal nonlinear optical microscopy. *Laser & photonics reviews*, 5(4), 2011.

[48] Christian W. Freudiger, Wenlong Yang, Gary R. Holtom, Nasser Peyghambarian, X. Sunney Xie, and Khanh Q. Kieu. Stimulated raman scattering microscopy with a robust fibre laser source. *Nature Photonics*, 8(2):153–159, 2014.

[49] Stephen Geoffrey Lipson, Henry Lipson, and David Stefan Tannhauser. *Optical physics*. Optical Physics. Cambridge University Press, Cambridge, 3. ed. edition, 1995.

[50] Govind Agrawal. *Nonlinear Fiber Optics*. Elsevier Science & Technology Books, San Diego, CA, USA, 2012.

[51] Andy Chong, Joel Buckley, Will Renninger, and Frank Wise. All-normal-dispersion femtosecond fiber laser. *Optics Express*, 14(21):10095–10100, 2006.

[52] G. Sucha. Self-starting of an additive-pulse mode-locked color-center laser. *Optics Letters*, 16(12):922–924, 1991.

[53] H. A. Haus, E. P. Ippen, and K. Tamura. Additive-pulse modelocking in fiber lasers. *IEEE Journal of Quantum Electronics*, 30(1):200–208, 1994.

[54] Fedor Mitschke. *Fiber Optics: Physics and Technology*. Springer Berlin Heidelberg and Imprint Springer, Berlin, Heidelberg, 2nd ed. 2016 edition, 2016.

[55] Donna Strickland and Gerard Mourou. Compression of amplified chirped optical pulses. *Optics Communications*, 56(3):219–221, 1985.

[56] Christoph Heinrich, Stefan Bernet, and Monika Ritsch-Marte. Wide-field coherent anti-stokes raman scattering microscopy. *Applied Physics Letters*, 84(5):816–818, 2004.

[57] Alex Soares Duarte, Christoph Schnedermann, and Philipp Kukura. Wide-field detected fourier transform cars microscopy. *Scientific Reports*, 6:37516, 2016.

[58] Thomas A. Pologruto, Bernardo L. Sabatini, and Karel Svoboda. Scanimage: flexible software for operating laser scanning microscopes. *BioMedical Engineering OnLine*, 2(1):13, 2003.

[59] Gian-Luca Anselmetti. *Korrektur von Laserfluktuationen in Bildern eines Kohärente Anti-Stokes-Raman-Streuung (CARS) Mikroskops: Bachelor Thesis*. Bielefeld, 2016.

[60] Elina Oberlander. *Raman-Spektroskopie in Biomedizin und an nahfeldgekoppelten Nanosystemen*. 2016.

[61] Walter Enns. *Raman- und Photolumineszenz-Spektroskopie an mechanisch exfolierten Mono- und Multilagen des van-der-Waals-Kristalls WSe2 sowie die Untersuchung der optischen Anistropie durch winkelaufgelöste Ellipsometrie am Volumen-Kristall: Master Thesis*. Bielefeld, 2017.

[62] Lina Mikoliunaite, Raul D. Rodriguez, Evgeniya Sheremet, Vladimir Kolchuzhin, Jan Mehner, Arunas Ramanavicius, and Dietrich R. T. Zahn. The substrate matters in the raman spectroscopy analysis of cells. *Scientific Reports*, 5(1):13150, 2015.

[63] Laura T. Kerr, Hugh J. Byrne, and Bryan M. Hennelly. Optimal choice of sample substrate and laser wavelength for raman spectroscopic analysis of biological specimen. *Analytical Methods*, 7(12):5041–5052, 2015.

[64] A. Ashkin, J. M. Dziedzic, J. E. Bjorkholm, and S. Chu. Observation of a single-beam gradient force optical trap for dielectric particles. *Optics letters*, 11(5):288, 1986.

[65] Xianghui Zhang, Marcel Mainka, Florian Paneff, Henning Hachmeister, André Beyer, Armin Gölzhäuser, and Thomas Huser. Surface-enhanced raman spectroscopy of carbon nanomembranes from aromatic self-assembled monolayers. *Langmuir*, 34(8):2692–2698, 2018.

[66] Neil J. Everall. Confocal raman microscopy: common errors and artefacts. *Analyst*, 135(10):2512–2522, 2010.

[67] Neil Everall, Jonathan Lapham, Fran Adar, Andrew Whitley, Eunah Lee, and Sergey Mamedov. Optimizing depth resolution in confocal raman microscopy: a comparison of metallurgical, dry corrected, and oil immersion objectives. *Applied spectroscopy*, 61(3):251–259, 2007.

[68] Ilia G. Denisov, Piotr J. Mak, Thomas M. Makris, Stephen G. Sligar, and James R. Kincaid. Resonance raman characterization of the peroxo and hydroperoxo intermediates in cytochrome p450. *The journal of physical chemistry. A*, 112(50):13172–13179, 2008.

[69] Yonghua Li-Beisson, Fred Beisson, and Wayne Riekhof. Metabolism of acyl-lipids in chlamydomonas reinhardtii. *The Plant Journal*, 82(3):504–522, 2015.

[70] Qiang Hu, Milton Sommerfeld, Eric Jarvis, Maria Ghirardi, Matthew Posewitz, Michael Seibert, and Al Darzins. Microalgal triacylglycerols as feedstocks for biofuel production: perspectives and advances. *The Plant Journal*, 54(4):621–639, 2008.

[71] Sheeja Jagadevan, Avik Banerjee, Chiranjib Banerjee, Chandan Guria, Rameshwar Tiwari, Mehak Baweja, and Pratyoosh Shukla. Recent developments in synthetic biology and metabolic engineering in microalgae towards biofuel production. *Biotechnology for Biofuels*, 11(1):185, 2018.

[72] Randor Radakovits, Robert E. Jinkerson, Al Darzins, and Matthew C. Posewitz. Genetic engineering of algae for enhanced biofuel production. *Eukaryotic Cell*, 9(4):486–501, 2010.

[73] Jilian Fan, Chengshi Yan, Carl Andre, John Shanklin, Jörg Schwender, and Changcheng Xu. Oil accumulation is controlled by carbon precursor supply for fatty acid synthesis in chlamydomonas reinhardtii. *Plant & cell physiology*, 53(8):1380–1390, 2012.

[74] Xiaobo Li, Eric R. Moellering, Bensheng Liu, Cassandra Johnny, Marie Fedewa, Barbara B. Sears, Min-Hao Kuo, and Christoph Benning. A galactoglycerolipid lipase is required for triacylglycerol accumulation and survival following nitrogen deprivation in chlamydomonas reinhardtii. *The Plant cell*, 24(11):4670–4686, 2012.

[75] Raphael Slade and Ausilio Bauen. Micro-algae cultivation for biofuels: Cost, energy balance, environmental impacts and future prospects. *Biomass and Bioenergy*, 53:29–38, 2013.

[76] Christian Bogen, Arwa Al-Dilaimi, Andreas Albersmeier, Julian Wichmann, Michael Grundmann, Oliver Rupp, Kyle J. Lauersen, Olga Blifernez-Klassen, Jörn Kalinowski, Alexander Goesmann, Jan H. Mussgnug, and

Olaf Kruse. Reconstruction of the lipid metabolism for the microalga monoraphidium neglectum from its genome sequence reveals characteristics suitable for biofuel production. *BMC Genomics*, 14(1):926, 2013.

[77] Daniel Jaeger, Christian Pilger, Henning Hachmeister, Elina Oberländer, Robin Wördenweber, Julian Wichmann, Jan H. Mussgnug, Thomas Huser, and Olaf Kruse. Label-free in vivo analysis of intracellular lipid droplets in the oleaginous microalga monoraphidium neglectum by coherent raman scattering microscopy. *Scientific Reports*, 6(1):35340, 2016.

[78] Judith Rumin, Hubert Bonnefond, Bruno Saint-Jean, Catherine Rouxel, Antoine Sciandra, Olivier Bernard, Jean-Paul Cadoret, and Gaël Bougaran. The use of fluorescent nile red and bodipy for lipid measurement in microalgae. *Biotechnology for Biofuels*, 8:42, 2015.

[79] Hong-Yu Ren, Bing-Feng Liu, Fanying Kong, Lei Zhao, and Nan-Qi Ren. Improved nile red staining of scenedesmus sp. by combining ultrasonic treatment and three-dimensional excitation emission matrix fluorescence spectroscopy. *Algal Research*, 7:11–15, 2015.

[80] Erik T. Garbacik, Roza P. Korai, Eric H. Frater, Jeroen P. Korterik, Cees Otto, and Herman L. Offerhaus. In planta imaging of δ^9-tetrahydrocannabinolic acid in cannabis sativa l. with hyperspectral coherent anti-stokes raman scattering microscopy. *Journal of biomedical optics*, 18(4):046009, 2013.

[81] J. FOLCH, M. LEES, and G. H. SLOANE STANLEY. A simple method for the isolation and purification of total lipides from animal tissues. *The Journal of biological chemistry*, 226(1):497–509, 1957.

[82] Arne D. Hofemeier, Henning Hachmeister, Christian Pilger, Matthias Schürmann, Johannes F. W. Greiner, Lena Nolte, Holger Sudhoff, Christian Kaltschmidt, Thomas Huser, and Barbara Kaltschmidt. Label-free nonlinear optical microscopy detects early markers for osteogenic differentiation of human stem cells. *Scientific Reports*, 6(1):26716, 2016.

[83] Maya Sieber-Blum and Yaofei Hu. Epidermal neural crest stem cells (epincsc) and pluripotency. *Stem cell reviews*, 4(4):256–260, 2008.

[84] Jm Gimble and F. Guilak. Adipose-derived adult stem cells: isolation, characterization, and differentiation potential. *Cytotherapy*, 5(5):362–369, 2003.

[85] Johannes F. W. Greiner, Lena-Marie Grunwald, Janine Müller, Holger Sudhoff, Darius Widera, Christian Kaltschmidt, and Barbara Kaltschmidt. Culture bag systems for clinical applications of adult human neural crest-derived stem cells. *Stem Cell Research & Therapy*, 5(2):34, 2014.

[86] Stefan Hauser, Darius Widera, Firas Qunneis, Janine Müller, Christin Zander, Johannes Greiner, Christina Strauss, Patrick Lüningschrör, Peter Heimann, Hartmut Schwarze, Jörg Ebmeyer, Holger Sudhoff, Marcos J. Araúzo-Bravo, Boris Greber, Holm Zaehres, Hans Schöler, Christian Kaltschmidt, and Barbara Kaltschmidt. Isolation of novel multipotent neural crest-derived stem cells from adult human inferior turbinate. *Stem Cells and Development*, 21(5):742–756, 2012.

[87] Robert D. Barber, Dan W. Harmer, Robert A. Coleman, and Brian J. Clark. Gapdh as a housekeeping gene: analysis of gapdh mrna expression in a panel of 72 human tissues. *Physiological genomics*, 21(3):389–395, 2005.

[88] Yulia Panina, Arno Germond, Shinji Masui, and Tomonobu M. Watanabe. Validation of common housekeeping genes as reference for qpcr gene expression analysis during ips reprogramming process. *Scientific Reports*, 8(1):8716, 2018.

[89] Cindy Grethel Fuentes-Corona, Jacob Licea-Rodriguez, Rebecca Younger, Raul Rangel-Rojo, Eric O. Potma, and Israel Rocha-Mendoza. Second harmonic generation signal from type i collagen fibers grown in vitro. *Biomedical Optics Express*, 10(12):6449–6461, 2019.

[90] J. E. Davies. In vitro modeling of the bone/implant interface. *The Anatomical Record*, 245(2):426–445, 1996.

[91] Christian Pilger, Henning Hachmeister, Paul Greife, Alex Weiß, Gerd Wiebusch, and Thomas Huser. Pulse length variation causing spectral distortions in opo-based hyperspectral coherent raman scattering microscopy. *Optics Express*, 26(22):28312–28322, 2018.

[92] Alex Weiß. *Background-Free Coherent Anti-Stokes Raman Scattering Microscopy by High Frequency Modulation: Master Thesis*. Bielefeld, 2017.

[93] Paul Greife. *Implementation of a Hyper-Spectral Image Scan Capability in a Coherent Anti-Stokes Raman Scattering (CARS) Microscope: Master Thesis*. Bielefeld, 2017.

[94] I. T. Jolliffe. *Principal Component Analysis*. Springer Series in Statistics. Springer-Verlag New York Inc, New York, NY, second edition edition, 2002.

[95] Svante Wold, Kim Esbensen, and Paul Geladi. Principal component analysis. *Chemometrics and Intelligent Laboratory Systems*, 2(1-3):37–52, 1987.

[96] D. D. Lee and H. S. Seung. Learning the parts of objects by non-negative matrix factorization. *Nature*, 401(6755):788–791, 1999.

[97] Todd K. Leen, editor. *Advances in neural information processing systems 13: Proceedings of the 2000 conference*. MIT Press, Cambridge, Mass., 2001.

[98] Michael W. Berry, Murray Browne, Amy N. Langville, V. Paul Pauca, and Robert J. Plemmons. Algorithms and applications for approximate nonnegative matrix factorization. *Computational Statistics & Data Analysis*, 52(1):155–173, 2007.

[99] Cédric Févotte and Jérôme Idier. Algorithms for nonnegative matrix factorization with the β-divergence. *Neural Computation*, 23(9):2421–2456, 2011.

[100] Andrzej Cichocki and Anh-Huy Phan. Fast local algorithms for large scale nonnegative matrix and tensor factorizations. *IEICE Transactions on Fundamentals of Electronics, Communications and Computer Sciences*, E92-A(3):708–721, 2009.

[101] Wilhelm His. *Untersuchungen über die erste Anlage des Wirbelthierleibes : die erste Entwickelung des Hühnchens im Ei / von Wilhelm His.* F.C.W. Vogel, Leipzig, 1868.

[102] Janine Müller, Christiana Ossig, Johannes F. W. Greiner, Stefan Hauser, Mareike Fauser, Darius Widera, Christian Kaltschmidt, Alexander Storch, and Barbara Kaltschmidt. Intrastriatal transplantation of adult human neural crest-derived stem cells improves functional outcome in parkinsonian rats. *Stem cells translational medicine*, 4(1):31–43, 2015.

[103] Oliver Clewes, Alla Narytnyk, Kevin R. Gillinder, Andrew D. Loughney, Alison P. Murdoch, and Maya Sieber-Blum. Human epidermal neural crest stem cells (hepi-ncsc)–characterization and directed differentiation into osteocytes and melanocytes. *Stem cell reviews and reports*, 7(4):799–814, 2011.

[104] Elisabeth Dupin and Lukas Sommer. Neural crest progenitors and stem cells: from early development to adulthood. *Developmental biology*, 366(1):83–95, 2012.

[105] Anna Höving, Madlen Merten, Kazuko Elena Schmidt, Isabel Faust, Lucia Mercedes Ruiz-Perera, Henning Hachmeister, Sebastian-Patrick Sommer, Buntaro Fujita, Thomas Pühler, Thomas Huser, Johannes Greiner, Barbara Kaltschmidt, Jan Gummert, Cornelius Knabbe, and Christian Kaltschmidt. Identification of a human adult cardiac stem cell population with neural crest origin. *bioRxiv*, page 590679, 2019.

[106] Anke M. Smits, Patrick van Vliet, Corina H. Metz, Tom Korfage, Joost Pg Sluijter, Pieter A. Doevendans, and Marie-José Goumans. Human cardiomyocyte progenitor cells differentiate into functional mature cardiomyocytes: an in vitro model for studying human cardiac physiology and pathophysiology. *Nature protocols*, 4(2):232–243, 2009.

[107] Antonio P. Beltrami, Laura Barlucchi, Daniele Torella, Mathue Baker, Federica Limana, Stefano Chimenti, Hideko Kasahara, Marcello Rota, Ezio

Musso, Konrad Urbanek, Annarosa Leri, Jan Kajstura, Bernardo Nadal-Ginard, and Piero Anversa. Adult cardiac stem cells are multipotent and support myocardial regeneration. *Cell*, 114(6):763–776, 2003.

[108] Thomas Eschenhagen, Roberto Bolli, Thomas Braun, Loren J. Field, Bernd K. Fleischmann, Jonas Frisén, Mauro Giacca, Joshua M. Hare, Steven Houser, Richard T. Lee, Eduardo Marbán, James F. Martin, Jeffery D. Molkentin, Charles E. Murry, Paul R. Riley, Pilar Ruiz-Lozano, Hesham A. Sadek, Mark A. Sussman, and Joseph A. Hill. Cardiomyocyte regeneration: A consensus statement. *Circulation*, 136(7):680–686, 2017.

[109] Jop H. van Berlo, Onur Kanisicak, Marjorie Maillet, Ronald J. Vagnozzi, Jason Karch, Suh-Chin J. Lin, Ryan C. Middleton, Eduardo Marbán, and Jeffery D. Molkentin. c-kit+ cells minimally contribute cardiomyocytes to the heart. *Nature*, 509(7500):337–341, 2014.

[110] Qing Liu, Chao Jiang, Jin Xu, Ming-Tao Zhao, Kevin van Bortle, Xun Cheng, Guangwen Wang, Howard Y. Chang, Joseph C. Wu, and Michael P. Snyder. Genome-wide temporal profiling of transcriptome and open chromatin of early cardiomyocyte differentiation derived from hipscs and hescs. *Circulation research*, 121(4):376–391, 2017.

[111] M. Bittel, C. B. Y. Cordella, A. Assaf, S. Jouanneau, M. J. Durand, and G. Thouand. Potential of raman spectroscopy to monitor arsenic toxicity on bacteria: Insights toward multiparametric bioassays. *Environmental science & technology*, 49(20):12324–12332, 2015.

[112] G. L. Anderson, W. A. Boyd, and P. L. Williams. Assessment of sublethal endpoints for toxicity testing with the nematode caenorhabditis elegans. *Environmental toxicology and chemistry*, 20(4):833–838, 2001.

[113] David C. Kennedy, Rodney K. Lyn, and John Paul Pezacki. Cellular lipid metabolism is influenced by the coordination environment of copper. *Journal of the American Chemical Society*, 131(7):2444–2445, 2009.

[114] Kelvin Yen, Thuc T. Le, Ankita Bansal, Sri Devi Narasimhan, Ji-Xin Cheng, and Heidi A. Tissenbaum. A comparative study of fat storage

quantitation in nematode caenorhabditis elegans using label and label-free methods. *PLOS ONE*, 5(9):e12810, 2010.

[115] Robert D. Kaiser and Erwin London. Determination of the depth of bodipy probes in model membranes by parallax analysis of fluorescence quenching. *Biochimica et Biophysica Acta (BBA) - Biomembranes*, 1375(1-2):13–22, 1998.

[116] Eyleen J. O'Rourke, Alexander A. Soukas, Christopher E. Carr, and Gary Ruvkun. C. elegans major fats are stored in vesicles distinct from lysosome-related organelles. *Cell metabolism*, 10(5):430–435, 2009.

[117] George V. Clokey and Lewis A. Jacobson. The autofluorescent "lipofuscin granules" in the intestinal cells of caenorhabditis elegans are secondary lysosomes. *Mechanisms of Ageing and Development*, 35(1):79–94, 1986.

[118] Thomas Hellerer, Claes Axäng, Christian Brackmann, Per Hillertz, Marc Pilon, and Annika Enejder. Monitoring of lipid storage in caenorhabditis elegans using coherent anti-stokes raman scattering (cars) microscopy. *Proceedings of the National Academy of Sciences of the United States of America*, 104(37):14658–14663, 2007.

[119] Yung-Hsiang Yi, Cheng-Hao Chien, Wei-Wen Chen, Tian-Hsiang Ma, Kuan-Yu Liu, Yu-Sun Chang, Ta-Chau Chang, and Szecheng J. Lo. Lipid droplet pattern and nondroplet-like structure in two fat mutants of caenorhabditis elegans revealed by coherent anti-stokes raman scattering microscopy. *Journal of biomedical optics*, 19(1):011011, 2014.

[120] Hendrik Fueser, Nabil Majdi, Arne Haegerbaeumer, Christian Pilger, Henning Hachmeister, Paul Greife, Thomas Huser, and Walter Traunspurger. Analyzing life-history traits and lipid storage using cars microscopy for assessing effects of copper on the fitness of caenorhabditis elegans. *Ecotoxicology and Environmental Safety*, 156:255–262, 2018.

[121] Daniel Muschiol and Walter Traunspurger. Life cycle and calculation of the intrinsic rate of natural increase of two bacterivorous nematodes, pana-

grolaimus sp. and poikilolaimus sp. from chemoautotrophic movile cave, romania. *Nematology*, 9(2):271–284, 2007.

[122] Johannes Schindelin, Ignacio Arganda-Carreras, Erwin Frise, Verena Kaynig, Mark Longair, Tobias Pietzsch, Stephan Preibisch, Curtis Rueden, Stephan Saalfeld, Benjamin Schmid, Jean-Yves Tinevez, Daniel James White, Volker Hartenstein, Kevin Eliceiri, Pavel Tomancak, and Albert Cardona. Fiji: an open-source platform for biological-image analysis. *Nature methods*, 9(7):676–682, 2012.

[123] Ho Yi Mak. Lipid droplets as fat storage organelles in caenorhabditis elegans: Thematic review series: Lipid droplet synthesis and metabolism: from yeast to man. *Journal of lipid research*, 53(1):28–33, 2012.

[124] B. D. Uhal. Cell cycle kinetics in the alveolar epithelium. *The American journal of physiology*, 272(6 Pt 1):L1031–45, 1997.

[125] Sabine Fuchs, Andrew John Hollins, Michael Laue, Ulrich Friedrich Schaefer, Klaus Roemer, Mark Gumbleton, and Claus-Michael Lehr. Differentiation of human alveolar epithelial cells in primary culture: morphological characterization and synthesis of caveolin-1 and surfactant protein-c. *Cell and tissue research*, 311(1):31–45, 2003.

[126] S. I. Danto, J. M. Shannon, Z. Borok, S. M. Zabski, and E. D. Crandall. Reversible transdifferentiation of alveolar epithelial cells. *American journal of respiratory cell and molecular biology*, 12(5):497–502, 1995.

[127] J. M. Shannon, S. D. Jennings, and L. D. Nielsen. Modulation of alveolar type ii cell differentiated function in vitro. *The American journal of physiology*, 262(4 Pt 1):L427–36, 1992.

[128] Lan Zhao, Min Yee, and Michael A. O'Reilly. Transdifferentiation of alveolar epithelial type ii to type i cells is controlled by opposing tgf-β and bmp signaling. *American Journal of Physiology - Lung Cellular and Molecular Physiology*, 305(6):L409–18, 2013.

[129] D. S. Phelps and J. Floros. Localization of pulmonary surfactant proteins using immunohistochemistry and tissue in situ hybridization. *Experimental lung research*, 17(6):985–995, 1991.

[130] M. Kalina, R. J. Mason, and J. M. Shannon. Surfactant protein c is expressed in alveolar type ii cells but not in clara cells of rat lung. *American journal of respiratory cell and molecular biology*, 6(6):594–600, 1992.

[131] M. F. Beers, C. Y. Kim, C. Dodia, and A. B. Fisher. Synthesis of type ii cell lamellar body lysozyme-15 kd protein (lbl-15) by perfused rat lung. *American journal of respiratory cell and molecular biology*, 11(2):240–248, 1994.

[132] Jeffrey M. Cheek, Michael J. Evans, and Edward D. Crandall. Type i cell-like morphology in tight alveolar epithelial monolayers. *Experimental Cell Research*, 184(2):375–387, 1989.

[133] H. Fehrenbach. Alveolar epithelial type ii cell: defender of the alveolus revisited. *Respiratory research*, 2(1):33–46, 2001.

[134] Branko Vukosavljevic, Marius Hittinger, Henning Hachmeister, Christian Pilger, Xabier Murgia, Michael M. Gepp, Luca Gentile, Hanno Huwer, Nicole Schneider-Daum, Thomas Huser, Claus-Michael Lehr, and Maike Windbergs. Vibrational spectroscopic imaging and live cell video microscopy for studying differentiation of primary human alveolar epithelial cells. *Journal of Biophotonics*, 12(6):e201800052, 2019.

[135] Nicole Daum, Anna Kuehn, Stephanie Hein, Ulrich F. Schaefer, Hanno Huwer, and Claus-Michael Lehr. Isolation, cultivation, and application of human alveolar epithelial cells. *Methods in molecular biology (Clifton, N.J.)*, 806:31–42, 2012.

[136] Cihang Kong, Christian Pilger, Henning Hachmeister, Xiaoming Wei, Tom H. Cheung, Cora S. W. Lai, Nikki P. Lee, Kevin K. Tsia, Kenneth K. Y. Wong, and Thomas Huser. High-contrast, fast chemical imaging by coherent raman scattering using a self-synchronized two-colour fibre laser. *Light: Science & Applications*, 9(1):25, 2020.

[137] Keisuke Nose, Yasuyuki Ozeki, Tatsuya Kishi, Kazuhiko Sumimura, Norihiko Nishizawa, Kiichi Fukui, Yasuo Kanematsu, and Kazuyoshi Itoh. Sensitivity enhancement of fiber-laser-based stimulated raman scattering microscopy by collinear balanced detection technique. *Optics Express*, 20(13):13958–13965, 2012.

[138] Yasuyuki Ozeki, Wataru Umemura, Kazuhiko Sumimura, Norihiko Nishizawa, Kiichi Fukui, and Kazuyoshi Itoh. Stimulated raman hyperspectral imaging based on spectral filtering of broadband fiber laser pulses. *Optics Letters*, 37(3):431–433, 2012.

[139] K. Tamura, E. P. Ippen, H. A. Haus, and L. E. Nelson. 77-fs pulse generation from a stretched-pulse mode-locked all-fiber ring laser. *Optics Letters*, 18(13):1080, 1993.

[140] Edwin Ding, William H. Renninger, Frank W. Wise, Philippe Grelu, Eli Shlizerman, and J. Nathan Kutz. High-energy passive mode-locking of fiber lasers. *International Journal of Optics*, 2012, 2012.

[141] Xiaoming Wei. *Robust laser sources for ultrafast imaging systems: PhD-Thesis*. 2015.

[142] J. Limpert, T. Clausnitzer, A. Liem, T. Schreiber, H. J. Fuchs, H. Zellmer, E. B. Kley, and A. Tünnermann. High-average-power femtosecond fiber chirped-pulse amplification system. *Optics letters*, 28(20):1984–1986, 2003.

[143] R. H. Stolen, J. Botineau, and A. Ashkin. Intensity discrimination of optical pulses with birefringent fibers. *Optics letters*, 7(10):512–514, 1982.

[144] Lu Wei, Zhixing Chen, Lixue Shi, Rong Long, Andrew V. Anzalone, Luyuan Zhang, Fanghao Hu, Rafael Yuste, Virginia W. Cornish, and Wei Min. Super-multiplex vibrational imaging. *Nature*, 544(7651):465–470, 2017.

[145] Lu Wei, Fanghao Hu, Yihui Shen, Zhixing Chen, Yong Yu, Chih-Chun Lin, Meng C. Wang, and Wei Min. Live-cell imaging of alkyne-tagged small biomolecules by stimulated raman scattering. *Nature methods*, 11(4):410–412, 2014.

[146] Senlian Hong, Tao Chen, Yuntao Zhu, Ang Li, Yanyi Huang, and Xing Chen. Live-cell stimulated raman scattering imaging of alkyne-tagged biomolecules. *Angewandte Chemie (International ed. in English)*, 53(23):5827–5831, 2014.

[147] Ádám Krolopp, Attila Csákányi, Dóra Haluszka, Dániel Csáti, Lajos Vass, Attila Kolonics, Norbert Wikonkál, and Róbert Szipőcs. Handheld nonlinear microscope system comprising a 2 mhz repetition rate, mode-locked yb-fiber laser for in vivo biomedical imaging. *Biomedical Optics Express*, 7(9):3531–3542, 2016.

[148] Matei Rusu, Robert Herda, and Oleg Okhotnikov. Passively synchronized two-color mode-locked fiber system based on master-slave lasers geometry. *Optics Express*, 12(20):4719–4724, 2004.